UNIVERSITÀ
DI PAVIA

Dipartimento di Biologia e Biotecnologie

"L. Spallanzani"

Multi-scale analysis of the Calcium Release Unit

From proteomic analysis of the junctional Sarcoplasmic Reticulum to biochemical characterization of CASQ2

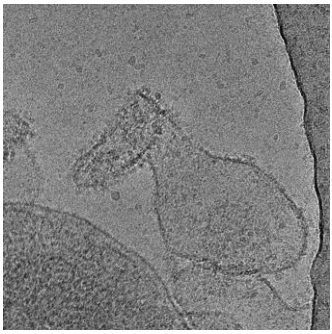

Chiara Di Antonio

Dottorato di Ricerca in
Genetica, Biologia Molecolare e Cellulare
Ciclo XXXVIII – A.A. 2022-2025

Summary

Abstract of the research

Catecholaminergic polymorphic ventricular tachycardia (CPVT) is an inherited arrhythmogenic disorder in which a structurally normal heart becomes prone to stress-induced ventricular tachycardia due to defective intracellular Ca^{2+} handling. Despite the genetic heterogeneity of the disease, the pathophysiological mechanisms of CPVT converge to dysfunction of a common hotspot, the junctional sarcoplasmic reticulum (jSR). At the dyadic junction, Ca^{2+} influx through L-type Ca^{2+} channels triggers Ca^{2+} induced Ca^{2+} release via Ryanodine receptor type 2 (RyR2). This process is finely tuned by the Calcium Release Unit (CRU), a regulatory protein network that includes Calsequestrin 2 (CASQ2), Triadin (TRDN) and Junctin (JNT), which collectively modulate the luminal Ca^{2+} buffering RyR2 refractoriness and the stability of diastolic Ca^{2+} control. Alteration of these mechanisms can promote spontaneous Ca^{2+} release that represents the substrate for delayed after depolarization and ventricular arrhythmias. However, the study of the jSR remains challenging, particularly in murine models where the starting material is limited; therefore, a compartment-specific enrichment protocol is required to enable molecular characterization.

This PhD thesis was designed to address these limitations by combining two complementary approaches to deepen our understanding of CPVT: (i) an *ex vivo* proteomic characterization of jSR-enriched vesicles isolated from mouse hearts, and (ii) an *in vitro* biochemical and biophysical study of CASQ2 assembly, both in its *wild-type* (WT) form and disease associated variants relevant to CPVT2.

In the first part of this thesis, I developed a workflow for the reproducible isolation of MS-compatible jSR-enriched vesicles from a single mouse heart. This preparation was then applied to compare three experimental conditions: WT mice, $RyR2^{R4496C/+}$ mice (a well-established CPVT1 model), and $RyR2^{R4496C/+}$ mice treated with AAV8-mediated gene therapy of human *CASQ2* (Inf AAV8-

h*CASQ2*), representing a therapeutic strategy for the restoring of Ca^{2+} regulation in the jSR (unpublished data). Method optimization showed that rapid flash-freezing of hearts immediately after excision improved the preservation of the proteins and, at the same time, the protocol yielded reproducible enrichment of key CRU components across independent single heart preparations. A sucrose density gradient step further improved selectivity by reducing contaminants, including cytoplasmic and plasma membrane proteins, while enriching the dense jSR-associated fraction. Co-enrichment of RyR2 with the dyadic proteins, such as $Ca_V1.2$ and Junctophillin2, is indicative of the good preservation of the native assemblies; additionally, qualitative Cryo-EM visualization of isolated vesicles was consistent with the maintenance of the integrity of vesicles and membrane-embedded protein complexes, suitable for downstream molecular investigation. On this basis, label free LC-MS/MS comparative analysis was performed, with the focus on proteins annotated to the ER/SR compartment. Within this compartment-focused view, the comparison between $RyR2^{R4496C/+}$ and WT samples revealed only limited quantitative differences, suggesting that the mutation does not translate into broad proteome remodeling of ER/SR compartment. In contrast, the AAV8-h*CASQ2* treated group showed a discrete and coherent signature, with CASQ2 emerging as the most prominent regulated signal, including detection of increased murine CASQ2 abundance. Additional changes were observed for proteins mapped to the Asph/JNT locus, suggesting that the effect of the therapy may extend beyond CASQ2 itself to include other CRU related components.

The second part of this thesis investigated CASQ2 as the major luminal Ca^{2+} buffer, with a specific focus on the relationship between ionic environment, protein stability and supra-molecular assembly of the protein itself. CASQ2 oligomerization and polymerization are indeed closely linked to its physiological role in Ca^{2+} storage in the jSR and to its pathological involvement in CPVT2. Using complementary biochemical and biophysical techniques including turbidimetry, thermal stability assays, dynamic light scattering and

size-exclusion chromatography, $CASQ2^{WT}$ behavior was characterized under specific ionic conditions. These experiments support the view that CASQ2 can populate stable oligomeric states even in the absence of Ca^{2+}. Indeed, physiological concentrations of monovalent ions, particularly K^{+}, promote conformational compaction and high-affinity Ca^{2+} dimerization. Ca^{2+} acts as a cooperative trigger shifting CASQ2 toward higher-order polymeric assemblies. Physiological quantities of Mg^{2+} further tune the properties of Ca^{2+}-dependent assemblies. Building on this framework, eight disease-associated CASQ2 mutants were studied under different experimental conditions. Rather than converging on a single common defect, the panel of mutants exhibited distinct, ion-dependent alterations in stability and quaternary assembly equilibrium, with subgroup-specific behaviors.

In conclusion, this thesis contributes to both methodological and mechanistic advances to the study of CPVT. By establishing a single heart preparation of jSR-enriched vesicles compatible with quantitative MS, it improves experimental accessibility of a master regulator compartment of Ca^{2+} handling and arrhythmogenesis. In parallel, the biochemical characterization of CASQ2 assembly properties provides an integrated framework linking ionic control of supra molecular states to mutation-specific dysfunction relevant for CPVT2. Together, these results lay the basis for future studies expanding jSR proteomic profiling beyond ER/SR compartment and for systematic genotype-phenotype investigations of CASQ2 mutants, ultimately leading to patient stratification and mutation-specific therapeutic strategies.

Chapter I: General Introduction

1. Anatomy and function of the heart

In mammals, the heart is a muscular organ located centrally in the thoracic cavity, posterior to the sternum. It is composed of four chambers: two atria positioned superiorly and two ventricles located inferiorly (Figure 1). Functionally, the right atrium and right ventricle form the right heart, while the left atrium and left ventricle constitute the left heart. These operate as two coordinated pumps that maintain blood circulation through the pulmonary and systemic circuits. The right atrium receives deoxygenated blood from the systemic circulation via the superior and inferior venae cavae. Venous return from the myocardium is directed into the right atrium through the coronary sinus. Acting as a reservoir, the right atrium channels blood through the tricuspid valve into the right ventricle, which functions as the primary contractile chamber of the right heart. The left atrium receives oxygenated blood from the lungs via the four pulmonary veins. It acts as a reservoir and conduit, directing blood through the mitral (bicuspid) valve into the left ventricle. The left ventricle, the primary contractile chamber of the left heart, generates high pressure to pump blood into the systemic circulation. During ventricular systole, blood is ejected through the aortic valve into the ascending aorta, which distributes oxygenated blood to the body. The mitral and aortic valves ensure one-way flow and prevent backflow into the left atrium and left ventricle. Cardiac contractility is governed by an intrinsic electrical conduction system that coordinates temporally the atrial and ventricular contractions. The sinoatrial (SA) node, located at the junction of the superior vena cava and right atrium, is the primary pacemaker and generates rhythmic action potentials at an average frequency of approximately 70 impulses per minute. The electrical impulse propagates to the left atrium via Bachmann's bundle and through the right atrium to the atrioventricular (AV) node. Upon receiving the electrical signal, the AV node introduces a physiological conduction delay before transmitting the impulse to the His bundle, a group of fibres located below the aortic valve, that conducts electrical

impulses from the atrioventricular node to the ventricles. This delay permits complete atrial emptying into the ventricle prior to initiation of the ventricular systole, thereby optimizing cardiac output [1].

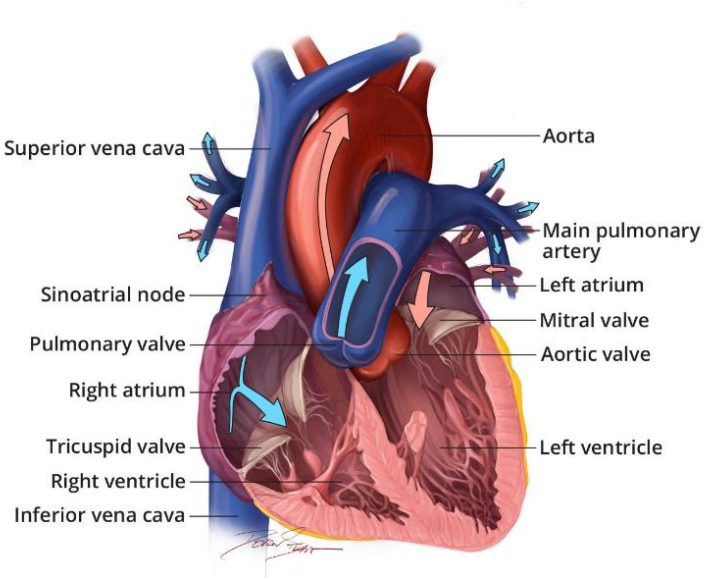

Figure 1: Anatomy of the interior of the heart (2).

2. The cardiomyocytes

The heart exhibits significant cellular diversity, comprising at least a dozen distinct cell types, among which cardiomyocytes, specialized smooth muscle cells, are the most abundant [2]. Although cardiomyocytes make up approximately 50% of the total cell population in the adult heart, their comparatively large size makes them occupy nearly two-thirds of the myocardial tissue volume [3]. Estimates suggest that the adult human heart contains several billion

cardiomyocytes. Other major cell types present in the heart are: fibroblasts, endothelial cells, pericytes, smooth muscle cells, resident and peripherally recruited immune cells, adipocytes, mesothelial cells and neuronal cells. The distribution of these cell types differs between the atrial tissue and the ventricular tissue [4].

The cell membrane of cardiomyocytes, called sarcolemma, presents 150 to 300 nm wide invaginations called T-tubules [5]. These are fundamental for the coordinated propagation of the electric signal throughout the entire volume of the cell [6].

While most of the cardiomyocytes function as force-generating units, a subset is dedicated to impulse initiation and conduction. Working ventricular myocytes are typically polynucleated (generally binucleated for large mammals), cylindrical or bifurcated in shape, and organized into a three-dimensional network through longitudinal and transverse connections[7]. They join at intercalated discs, mechanically and electrically coupled junctions that include desmosomes, fascia adherens, and gap junctions. Electrical conduction is anisotropic, hence not uniform in different directions, occurring more rapidly along the longitudinal axis of the cells than transversely[8]. Specialized conducting myocytes, such as those in the SA and AV nodes, display fewer and smaller gap junctions, reduced myofibrillar density, and increased glycogen content, reflecting their role in impulse propagation rather than contraction [9].

The fundamental unit for the contraction and relaxation, is the sarcomere [10]. Sarcomeres, are organized into distinct zones based on filament composition and ultrastructure (Figure 2).

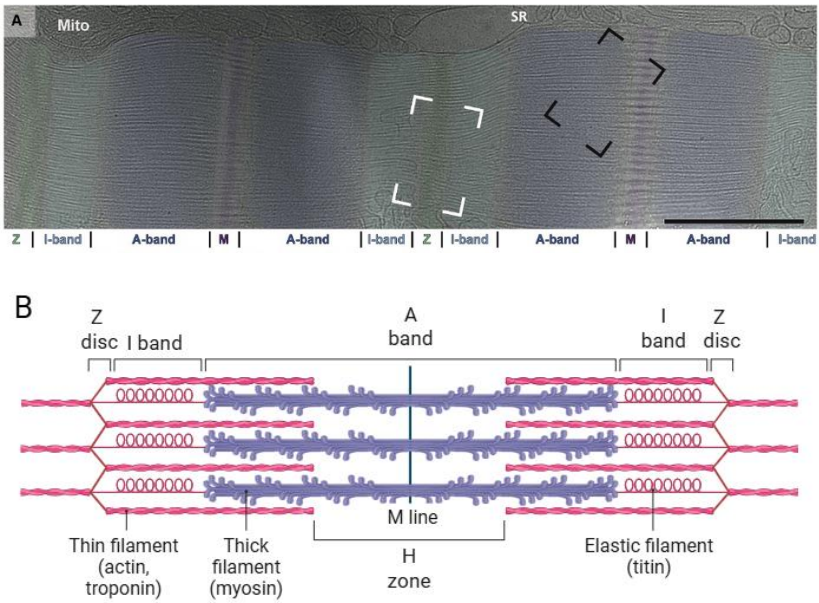

Figure 2: A) Image of mouse skeletal muscle, with Z-disc, I-, M-, and A-bands visible (green, light blue, dark blue, and purple, respectively). Image adapted from Wang et al [10]. B) Schematic representation of the sarcomere. Image created with Biorender.

The I-band contains only thin (actin and troponin) filaments, while the A-band includes regions of overlap between actin and thick (myosin) filaments. The Z-disc delineates the boundaries of each sarcomere, anchoring the barbed ends of actin filaments and providing lateral cross-linking through α-actinin [11] and other structural proteins such as titin, nebulin, and myotilin [10]. Centrally, the M-band contains cross-linked myosin filaments stabilized by titin other proteins, ensuring resistance to contractile stress. Connecting myosin and actin filaments, titin spans from the Z-disc to the M-band, also this protein contributes to sarcomere elasticity and alignment. Force generation arises from ATP-dependent interactions between actin and myosin, which slide past one another during contraction. Electron microscopy studies of transverse sarcomere sections have demonstrated the ordered

hexagonal filament lattice of thick and thin filaments, as well as the presence of myosin cross-bridges within the A-band [12]. A series of serially arranged sarcomeres form the myofibrils; these are cylindrical contractile structures that run longitudinally within the cell, whose coordinated shortening produces muscle contraction [13].

3. The cardiac sarcoplasmic reticulum

The sarcoplasmic reticulum (SR) in cardiomyocytes is essential for the homeostasis and transport of intracellular Ca^{2+}, in turn fundamental to proper cardiac performance. It is a specialized form of the endoplasmic reticulum (ER), which forms an elaborate three-dimensional network that closely associates with the myofibrils [13].

Despite the structural continuity, the ER and SR feature unique protein compositions: the SR harbours unique proteins specialized in Ca^{2+} buffering and transport. The majority of SR proteins do not contain the classical ER retrieval amino acid sequence KDEL [14], suggesting that additional mechanisms may have evolved for their retention in this organelle. Although numerous morphological and functional studies have demonstrated clear differences in protein composition [15], Ca^{2+} storage capacity [16], and spatial organization between the ER and the SR [17], the two organelles remain physically continuous and highly interconnected [18]. This continuity in the same membrane network makes the physical separation intrinsically challenging.

Structurally and functionally, the SR is subdivided into two main domains [19]: the longitudinal SR, composed by a series of interconnected tubules running parallel to the length of the sarcomeres, and the junctional SR (jSR), constituted by the SR terminal cisternae, adjacent to the Z-lines of the sarcomere [20]. T-tubules, when juxtaposed with the jSR, form a structural unit known as the dyad in cardiomyocytes (Figure 3). These structures are spatially organized at the nanometer-sized distances in order to allow

a rapid response to electrical stimuli traversing along the T-tubules' membrane.

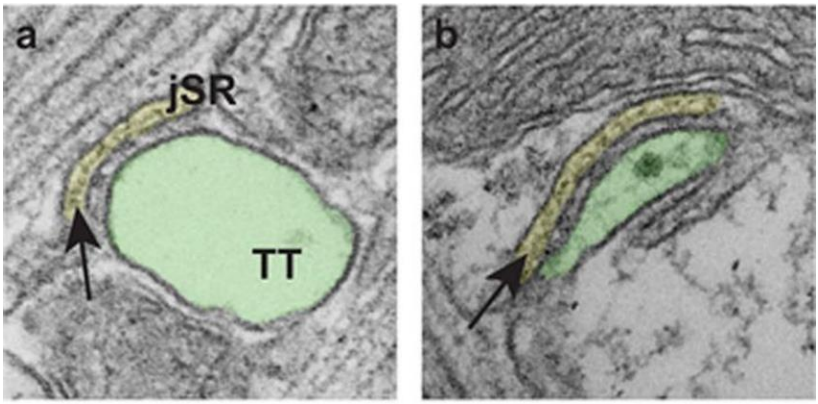

Figure 3: Electron micrographs of junctions between transverse tubules and jSR from WT mice. Image taken from Denegri et al [21].

Dyads are a critical hotspot for coordination and rhythmic contractions of the heart [22]. Indeed, they allow the translation of the electric signal membrane depolarization (from a resting potential state of -90 mV to the activation threshold of -50/-55 mV), propagated through T-tubules, to a synchronized cellular contraction. This mechanism is named Excitation-Contraction Coupling (ECC) [6]. It is mediated by conversion of the electrical stimulus into a chemical signal (Ca^{2+} release in the cytoplasm, necessary for sarcomere contraction). More specifically, the activation of voltage-gated calcium channels (L-type Ca^{2+} channels, i.e. $Ca_V1.2$) located in the membrane of T-tubules, in response to depolarization, allows Ca^{2+} influx from the extracellular space into the narrow dyadic cleft between the T-tubule membrane and the adjacent jSR. This localized rise in Ca^{2+} is generally believed to be the main trigger opening the ryanodine receptor type 2 (RyR2) channels situated on the jSR membrane, in close proximity to the L-type channels, through a mechanism named Calcium-Induced Calcium Release (CICR) [23]. RyR2 opening brings a substantial release of Ca^{2+} from the jSR into the cytosol of the cell, where Ca^{2+}-responsive

sarcomeric proteins (Figure 2) initiate contraction [24]. The Ca^{2+} release from the jSR increases the intracellular concentration of free Ca^{2+} from 100 nM to up to 100-fold [14]. At these concentrations, troponin is bound by the cytoplasmic free Ca^{2+} in the cytoplasm, opening the myosin binding sites on filamentous actin and allowing actin-myosin interactions. In this context, the jSR acts as the primary intracellular Ca^{2+} store [25]. In order to remove the excess of Ca^{2+} in the cytosol and to initiate relaxation, the closure of RyR2 is required first and then Ca^{2+} is pumped back into the SR by the action of the SarcoEndoplasmic Reticulum Ca^{2+} ATPase (SERCA2) which removes 70% or more of cytosolic Ca^{2+} present during systole. Ca^{2+} ions are also pumped out of the cell through the sodium–calcium exchanger (NCX). This membrane transporter couples the influx of three sodium ions (three positive charges enter the cell) with the efflux of one Ca^{2+} ion (two negative charges leave the cell) generating a ionic current ($I_{Na/Ca}$) (Figure 4). $I_{Na/Ca}$ exhibits a reversal potential, which is analogous to those of ion channels, basically a high concentration of Ca^{2+} (~0,6 μM)in the cell favor an inward $I_{Na/Ca}$, instead positive membrane potential (~ +30 mV) and high concentration of Na^{+} favour an outward $I_{Na/Ca}$ [14].

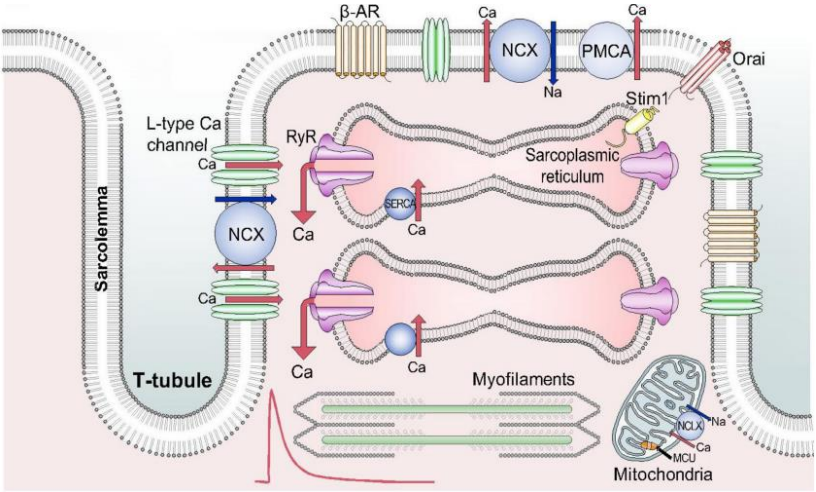

Figure 4: Elements involved in Ca^{2+} movement inside the SR. Image taken from Eisner et al [23].

4. The cardiac Ca^{2+} release unit (CRU)

The amount and duration of Ca^{2+} release from the jSR is controlled by the Ca^{2+} release units (CRU), which are supramolecular quaternary complexes arranged on the membrane of the jSR. These are clusters of about 100-200 RyR2 channels in size, where each RyR2 is believed to be accompanied by its protein partners associated from the jSR lumen: Calsequestrin 2 (CASQ2), Triadin (TRDN) and Junctin (JNT) (Figure 5).

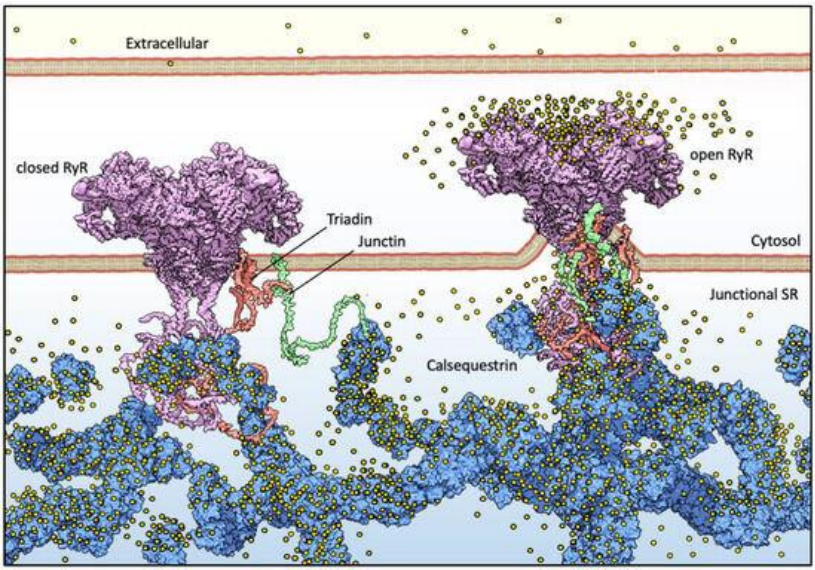

Figure 5: The fundamental elements of the machinery that release Ca^{2+}, located on the jSR. Image taken from Marabelli et al [26].

To further conceptualize the organization and coordinated function of these proteins within the CRU, also the term couplon was introduced [27]. A couplon is considered a functional unit comprising a cluster of $Ca_V1.2$ channels and adjacent RyR2 channels, along with auxiliary proteins that regulate their activity during ECC. The couplon framework helps to explain the discrete and stochastic nature of elementary and transient Ca^{2+} release events (calcium sparks), as well as their recruitment and summation into whole-cell calcium transients [28]. This concept is fundamental for the interpretation of how local control of Ca^{2+} release contributes to both normal ECC and arrhythmogenic dysfunctions in cardiac pathologies.

4.1. The Ryanodine receptor type 2 (RyR2)

RyR2s are massive protein channels, up to 2,7 MDa, expressed in the cardiac tissue of mammals [29,30]. They share ~70% of sequence homology [31] with isoforms RyR1, mainly found in skeletal muscle [32], and RyR3, originally found in the brain [33].

RyR2 modulates the duration and amplitude of Ca^{2+} release from jSR into the cytosol, consequently controlling muscle fiber contraction [34]. The human gene *RYR2* is localized on chromosome 1 (1q42-q43) [35] and codes for a 4967 aminoacids-long polypeptide. The functional channel is composed of four RyR2 proteins, each with a molecular weight of 565 kDa [36]. Each monomer features two main structural regions: the N-terminal nine tenths of the protein constitute the regulatory cytoplasmic domain, functioning as a platform of interaction with ligands, proteins, and enzyme modulators [37]; the C-terminal domain folds into six transmembrane helices that define the channel pore [38].

There are various accessory proteins that interact with RyR2: the cytosolic portion of the channel works alongside with Calstabin 2 (or FKBP12.6), Calmodulin, Protein Phosphatase 1, Protein Phosphatase 2A, Protein Kinase A and others; instead, at the intra-SR level, RyR2 interrelates with JNT, TRDN and CASQ2 (Figure 6).

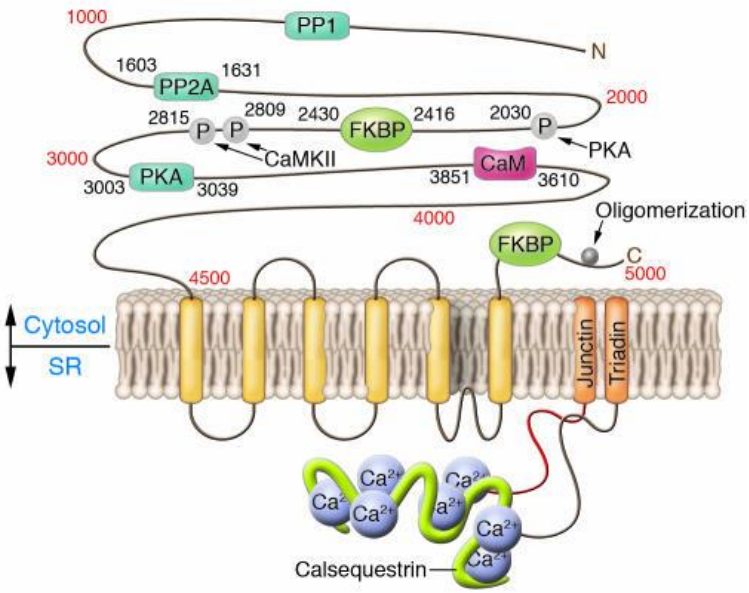

Figure 6: Schematic representation of cardiac RyR2 with sites of interaction and phosphorylation sites. Image taken from Zalk et al [36].

4.2. Cardiac calsequestrin (CASQ2)

CASQ2 is a 46 kDa glycoprotein which acts as the major Ca^{2+} storage present in the jSR lumen. CASQ2 has the ability to bind and release millimolar quantities of Ca^{2+} ions during each contraction and relaxation cycle of the heart through its high capacity (up to 60 mol of Ca^{2+} ion per molecule) and low affinity interactions with Ca^{2+} (K_d= 1mM) [39]. It maintains the free Ca^{2+} concentration within the jSR around 1.7 mM [14], while retaining up to 19 mM Ca^{2+}. CASQ2 is composed of three domains: an amino-terminal flexible domain, three thioredoxin domains and a disordered acid tail. Its high-capacity Ca^{2+}-binding is brought about by the high number of negatively charged acid residues exposed to the solution, as up to 26% of the residues of

human CASQ2 is represented by either Glutamates or Aspartates [40]. The abundance of negative charges makes CASQ2 an unusually conformationally unstable protein in low ionic strength conditions. The packing of the three thioredoxin domains into a globular tertiary structure is indeed stabilized Ca^{2+} ions, which mask the repulsing net negative charges of the polypeptide. CASQ2 features a Ca^{2+}-dependent polymerization, which is essential for its Ca^{2+}-related functions, as its Ca2+-binding capacity increases at each stage of polymer assembly. Each Ca^{2+} -driven quaternary state is indeed characterized by distinct Ca^{2+} binding and release properties [41]. In addition to its Ca^{2+}-buffering capacity, CASQ2 also regulates the open probability of the RyR2, mainly through indirect interaction mediated by TRDN and JNT [42], and possibly through direct interaction [43].

The biochemical properties of CASQ2, including oligomerization behavior and ionic sensitivity, will be discussed in greater detail in Chapter IV of this dissertation.

4.3. Triadin (TRDN) and Junctin (JNT)

TRDN regulates the activity of the RyR2 channel, and together with JNT anchors CASQ2 to the jSR [44]. TRDN is part of a family of proteins, all produced by the alternative splicing of the same transcript from a single gene, *TRDN*. In 1990, TRDN was first identified as a 95 kDa protein residing in the lumen of the jSR [45,46], but in 1994 it was also found as a 40 kDa protein [47]. Different mutations of TRDN cause a recessive form of cardiac arrhythmia [48].

JNT was identified as 26 kDa CASQ2-binding protein in both the cardiac and skeletal muscles [49]. The encoding transcript of JNT goes through alternative splicing, resulting in the production of three proteins: JNT, junctate and aspartyl β-hydroxylase[50–52]. During postnatal development of the rabbit heart, junction-specific mRNA levels increase markedly between the fetal stage and early postnatal days, in parallel with the progressive maturation of the jSR and of the

CICR process, which becomes functionally evident between 5 and 15 days after birth [53].

Both JNT and TRDN are composed of a short cytoplasmic N-terminal domain (47 aa for TRDN and 23 aa for JNT), a single transmembrane helix and a long, highly charged C-terminal domain located in the lumen of SR (660 aa for TRDN and 135 aa for JNT). Specific patterns of alternatively charged residues, mostly Lysines and Glutamates, shape the so-called KEKE motifs that decorate the C-termini of both proteins, and are essential for the interaction with CASQ2. TRDN and JNT both operate as "functional bridges" to tether CASQ2 close to RyR2 [54]. In addition, they support the structural stability of RyR2 channels during periods of intense activity [55].

5. Catecholaminergic Polymorphic Ventricular Tachycardia (CPVT)

Catecholaminergic Polymorphic Ventricular Tachycardia (CPVT), described for the first time in 1975 [56], is an inherited disease that predisposes to cardiac arrest and sudden death in patients with a structurally normal heart and normal baseline electrocardiogram (ECG) [57]. The incidence is estimated around 1:10.000. The typical feature of this disorder is the bidirectional/polymorphic ventricular tachycardia, triggered by emotional stress or physical exercise [44], often leading to sudden cardiac death. When untreated, CPVT has an elevated mortality rate, reaching 30-35% by 30 years of age [58]. Since the first identification of a CPVT causative mutation in the *RYR2* gene in 2001 [59], other mutations in RyR2 and its associated proteins CASQ2 and TRDN were discovered and associated with the disease. Most of the identified mutations related to this disease are single-base substitution, causing changes in a single conserved aminoacid.

The three main forms of the pathology are classified based on the affected gene: *RYR2*, *CASQ2*, or *TRDN*. CPVT type 1 (CPVT1), which represents up to 70% of diagnosed cases of CPVT, is associated with dominantly inherited mutations in the *RYR2* gene [58]. Nearly 300

mutations in the *RYR2* gene have been recognized as critical contributors to the pathogenesis of various cardiac disorders [60], including arrhythmias and cardiomyopathies such as catecholaminergic polymorphic ventricular tachycardia (CPVT), idiopathic ventricular fibrillation (IVF) and atrial fibrillation (AF). These mutations often lead to dysregulated Ca^{2+} release from the jSR, thereby compromising both the electrical stability and contractile function of the heart [61–63]. For most of the characterized mutations, namely the gain-of-function mutations (GOF), the open probability of RyR2 is enhanced, as they increase the sensitivity of the channel to luminal Ca^{2+} activation [64], specifically promoting spontaneous Ca^{2+} release from the SR under conditions of Ca^{2+} overload. This aberrant release can manifest as calcium sparks, oscillations in Ca^{2+} concentrations, or propagating waves of Ca^{2+} transient increases. The phenomenon by which RyR2 opens as a consequence of the excessive concentration of free Ca^{2+} in the jSR lumen (either real or perceived by RyR2) is referred to as store overload-induced calcium release (SOICR) [63,65,66]. SOICR can in turn, lead to arrhythmic episodes such as ventricular tachycardia. Structural analyses of RyR2 have demonstrated that many pathogenic CPVT mutations destabilize the interdomain interfaces that normally keep the channel closed [67–69], leading to an increased probability of opening. These have been classified as gain-of-function (GOF) mutations. More recently, also loss-of-function (LOF) RyR2 mutations have been identified as the underlying cause of a distinct inherited arrhythmia disorder (RyR2 Ca^{2+} release deficiency syndrome) [70,71].

In 2005, our group developed the first conditional knock-in mouse model carrier of the GOF *RYR2*^{R4496C} mutation [72]. This mutation is homologous to the autosomal dominant *RYR2*^{R4497C} mutation present in humans. In terms of severity and clinical manifestation, this animal model present remarkable similarity with patient carriers of the R4497C mutation: the anatomically preserved heart is prone to the onset of bidirectional and polymorphic ventricular tachycardia (VT) combined with the administration of caffeine and of adrenergic

agonists. There are more than 170 heterozygous missense GOF mutations that lead to the disease.

CPVT type 2 (CPVT2) results from mutations in CASQ2 and may follow either a dominant or recessive mode of inheritance [26,73], as it will be explained in more detail in Chapter IV. The rarest form, CPVT type 5 (CPVT5), is caused by loss-of-function mutations in TRDN and is inherited in an autosomal recessive manner [74]. It is interesting to note that a common defect characterizes both CASQ2-related and TRDN-related CPVT forms: as for most of the CASQ2 pathological variants, also TRDN pathological mutations, either in homozygosis or heterozygosis, lead to the loss of protein in the jSR compartment [75]. The lack of the protein, in turn, results in functional alterations in Ca^{2+} homeostasis and dynamics [76].

Despite genetic heterogeneity, all forms of CPVT share a common pathophysiological mechanism involving abnormal Ca^{2+} handling in the SR. Following adrenergic stimulation, there is an excessive accumulation of Ca^{2+} in the jSR, accompanied by an increased RyR2 channel sensitivity or leakiness. The prevailing model for CPVT1, suggests that Ca^{2+} leakage through a subset of RyR2 channels can initiate a regenerative, positive-feedback activation of neighbouring channels, leading to spontaneous and uncoordinated Ca^{2+} release. This uncontrolled Ca^{2+} cycling induces delayed, non-electrically driven contractions of cardiomyocytes, ultimately progressing to ventricular arrhythmias (VT) [44]. From a mechanistic point of view, the onset of arrhythmias can be conceptualized as a two-hit process. Experimental evidence suggests that mutations affecting the function of the SR Ca^{2+} release complex, such as those increasing the open probability of RyR2 channels, represent a necessary but insufficient condition for arrhythmogenesis [77]. Under baseline conditions, individual cardiomyocytes may compensate for these altered channel properties by reducing their SR Ca^{2+} load. However, adrenergic stimulation disrupts this compensatory mechanism by simultaneously enhancing RyR2 phosphorylation and relieving SERCA inhibition via phospholamban phosphorylation, leading to SR calcium overload. This coordinated effect satisfies both conditions required to trigger

spontaneous Ca^{2+} release events, such as delayed after depolarizations (DADs) and triggered activity (TA) [78].

Chapter II: Aims of the Research

This work combines targeted proteomics *in vivo* with mechanistic biochemistry *in vitro* to address the mechanism of Ca^{2+}-handling dysfunction in both CPVT1 and CPVT2, and an additional insight on the therapeutic potential of a DNA therapy for CPVT1 based on an adeno-associated viral vector (AAV) construct.

In the first part of this work, the aim is to define how the protein landscape of the jSR is remodeled in CPVT1 murine model $RyR2^{R4496C/+}$, in comparison with the wild-type one and the pathological model treated with the AAV-based therapy. A comparative proteomic approach was applied to test whether the DNA-based therapy, already shown to improve physiological phenotype (unpublished results), also produces a measurable molecular normalization at the protein level. In order to achieve this result, it was necessary to develop a jSR vesicles enrichment workflow capable of isolating reproducible, MS-compatible samples from single mouse hearts. This methodological effort addressed two critical needs: enhancing the signal in MS of low-abundance membrane jSR proteins, and reducing the number of animals required, both to limit the costs associated with the gene therapy and to adhere to the 3Rs principles in animal research.

The second part of this work focuses on the CASQ2 protein as the molecular determinant of luminal Ca^{2+} buffering with direct implications for CPVT2. First, we aimed to refine the biochemical framework describing $CASQ2^{WT}$ by investigating its ion-dependent stability, oligomerization and polymerization through biochemical and biophysical methods. Building on this knowledge, we then started the investigation of a panel of disease-associated CASQ2 mutants to understand how alterations in the same protein can lead to heterogeneous outcomes. By relating mutation-specific biochemical

phenotypes to differences in penetrance, this work aims to generate principles that may support future patient stratification within a precision medicine perspective.

Together, these two lines of investigation converge on a common goal: connect the molecular mechanisms of the CRU protein complex to their pathophysiological and clinically relevant aspects.

Chapter III: A proteomic profiling of a CPVT1 therapy

The first part of this work focuses on the establishment of a reliable protocol for the enrichment of jSR vesicles from a single murine heart [79]. This approach enables the recovery of intact membrane proteins under native conditions, thus avoiding the use of detergents that could otherwise disrupt physiological protein conformations and protein-protein interactions. The method proves robust and reproducible, allowing the identification of well-known low-abundance proteins, such as RyR2, TRDN, and JNT, as well as proteins tightly associated, including junctophilin-2 and the L-type calcium channel $Ca_V1.2$. Building on this methodological foundation, the second part of the project (currently unpublished) extends the use of this protocol to a comparative proteomic analysis. Specifically, I here present the data obtained from jSR-enriched vesicles isolated from three distinct models: WT mice, $RyR2^{R4496C}$ heterozygous mutants, and $RyR2^{R4496C}$ mutants treated through therapeutic viral gene transfer of the wild-type human *CASQ2* gene. This approach aims to elucidate how the pathological dominant RyR2 ^{R4496C} mutation and CASQ2 over-expression in the pathological context influence the proteomic composition of the jSR. The reported results provide new insights into the pathophysiological mechanisms of CPVT1 and the therapeutic possibilities.

1. Introduction

1.1. Mass Spectrometry – Proteomics

"Omics" in biology involves the high-throughput study of complete sets of biological molecules and how they function together in a biological system. The past century was characterized by the effort in genome sequencing of multiple organisms, culminating in the Human Genome Project completed in April 2003 [80]. Genomics provides sequence information of an organism's complete DNA sequence, comprising coding and non-coding sequences. Transcriptomics, on the other hand, studies the sequence and abundances of coding and non-coding RNA transcripts. The large complexity and diversity of the information carried by DNA and RNA molecules in a cell determines the specific set of proteins that are expressed and their abundances. Proteins are multi-purpose tools for the wealth of dynamic processes or specific mechanical properties that are needed at defined times and locations in a cell: from transient signaling events to structural support. Proteomics, the third major "omics" field, is a unique and potent tool to define the characteristics that define any given tissue (or even cell) by analyzing the entire set of proteins expressed, along with their interactions and post-translational modifications. Nowadays, multiple examples demonstrate that mass spectrometry is a highly effective analytical technique employed for the identification, quantification, and even structural characterization of proteins in their native context.

In the course of the past decades, mass spectrometry (MS) has become the principal method for protein identification from complex biological samples. This was due to the instrumental advances that allowed analysis of polar compounds, such as peptides in complex mixtures. Also, the parallel rapid growth of genomic databases that can be used to analyze MS data, was fundamental to the establishment of this technique. Although MS was initially developed for the detection of chemical compounds, from the late 1980s onwards, its evolution into a powerful analytical tool for multiple purposes has

largely been driven by the development of methods for quantitative analysis of molecules from complex samples

In MS, molecules are ionized, usually with electrospray ionization (ESI) or matrix-assisted laser desorption/ionization (MALDI), and then separated according to their mass-to-charge ratio (m/z) (m: molecular weight of the ion; z: number of charges) using different types of mass analyzers, such as quadrupole, time-of-flight (TOF), or Orbitrap systems [81]. The introduction of soft ionization techniques in the late 1980s revolutionized protein analysis, allowing the identification of a much larger number of proteins and ultimately giving rise to the field of proteomics [82]. In proteomics applications, especially when working with high-complexity samples for large-scale analysis, a bottom-up approach is frequently preferred: in this method, proteins are enzymatically cleaved and the fragments are separated by liquid chromatography (LC) before analysis by tandem mass spectrometry (MS/MS), in which peptides are subjected to collision-activated dissociation (CID). CID is a fragmentation technique in which a selected precursor ion undergoes multiple low-energy collisions with an inert gas, which produces characteristic ionized fragments that allow molecular identification. The data identification of the bottom-up approach relies on the database search, where MS data are equated to the fragmentation of the peptides investigated generated *in silico*.

There are a variety of approaches for the quantification of proteins and peptides, classified into two groups based on the information that provide [83]:

- Absolute quantification: providing information about the absolute quantity (expressed as mass, mole number or copy number) of a protein within a sample.
- Relative quantification: providing information about the quantitative ratio or relative change of a protein or whole proteomes among multiple samples.

An alternative classification of the methods is based on the methodology used [82]:

- Label-based: involving the artificial chemical labelling of proteins or peptides with a stable isotope, facilitating the detection of the target molecules.
- Label-free (also called subtractive proteomics): comparing separate measurements while retaining their native isotope composition, to obtain a relative abundance.

Label-free quantification allows the relative quantification of a virtually unlimited number of samples. There are principally two categories of experiments that fall in this group:

- Methods that compare the signal intensities of LC-MS analysis [84] by cross correlating the signal intensities of ions with their concentration. In other terms, the extracted peak areas from the chromatogram are used for relative quantification of the same peptide (or protein) from different samples. In recent years, intensity-based quantification has become the most widely adopted approach due to its improved accuracy.
- Methods that count the number of identified peptides or acquired fragment spectra [85]. In an MS experiment, abundant peptides are more likely to be observed, but since large proteins are prone to give rise to more peptides, additional normalization factors should be applied to improve the general results. However, Liu and colleagues [85] didn't find a correlation between the relative amount of protein and its peptide number. Instead, their model assumes that the relationship between spectral counts and abundance has been shown to be linear over a dynamic range of about 100-fold.

The label-free quantitation offers several advantages such as simplicity, broad applicability and flexibility on the number of comparable samples.

An important distinction must be made between two different data acquisition approaches: data-dependent acquisition (DDA) and data-independent acquisition (DIA) [82,86]. The DDA method subjects the most abundant peaks observed in the MS scan to an additional

fragmentation step, producing a spectrum of their constituent peptides. The selected ionized fragments are picked only based on their intensity, with the most abundant ions being prioritized for the fragmentation. For this reason, the principal limitation of DDA is that when many peptides are eluting at the same time, many low-abundance proteins are lost and not quantified. On the other hand, DIA involves the comprehensive fragmentation of each analyte present in the sample and hence does not need to be selected as individual precursors in the MS1 scan to be quantified. This approach provides a global view, ensuring that all potential analytes in a predetermined m/z range are captured and analysed.

1.2. A proteomic profiling of the jSR compartment in CPVT1

The jSR is a crucial subdomain of the cardiac sarcoplasmic reticulum, playing a central role in excitation–contraction coupling and Ca^{2+} handling. Despite its recognized physiological and clinical importance, the molecular composition and organization of this compartment remain only partially understood. In part, this may be due to the fact that the isolation and characterization of the jSR is particularly challenging. The enrichment of this membrane domain is hindered by several intrinsic features: the predominance of integral membrane proteins over lipids, which compromises the membrane stability in vesicles; the sensitivity of its luminal protein network to small ionic changes, which can lead to disassembly of CRU complexes for changes in buffer osmolarity or pH; and its complex spatial and structural arrangement at the interface between T-tubules and mitochondria to which it is tightly associated. These factors collectively complicate the preservation of native protein-protein interactions during enrichment steps. To enable proteomic investigation of jSR, we established an enrichment protocol that allows the isolation of jSR vesicles from a single WT murine heart while preserving membrane proteins in their native state. The robustness of the preparation is demonstrated by the reproducible

detection of low abundance jSR components, including RyR2, TRDN and JNT, from a single murine heart. The combination of this enrichment strategy with qualitative mass spectrometry enables sensitive profiling of jSR membrane proteins, providing a reliable basis for downstream proteomic analysis of jSR composition and organization.

1.3. Comparison with previous jSR/SR purification strategies

Early efforts on the isolation and characterization of the SR compartment laid the foundation for our current understanding of muscle Ca^{2+} handling. Studies from the 70s and 80s demonstrated that the SR could be partially separated and enriched from other cellular compartments using fractionation and biochemical approaches. In a work from 1983 by Mitchell and colleagues [87] morphologically intact triad structures were isolated from skeletal muscle (60 grams for each preparation). By combining centrifugation step with density gradient fractionation, this work provided the evidence for the preservation of junctional complexes between transverse tubules and terminal cisternae. However, this study relied on very large amounts of starting material (whole skeletal muscles from large animals). Similarly, Jones and collaborators in 1979 [88] developed a protocol to separate sarcolemmal vesicles from cardiac sarcoplasmic reticulum vesicles. Also, later in 1981 the same group have demonstrated that different SR subfractions differ in enzymatic activities, Ca^{2+} uptake capacity and protein composition [89]. However, also these works rely on substantial amounts of tissue and were based on indirect biochemical readouts. More recently, a work from Staunton and Ohlendieck characterized the SR proteome from rabbit skeletal muscle with the "on-membrane digestion" technique [90]. Although this work represents an important step toward regarding the proteomic profiling of the SR, it still relied on bulk muscle preparations, limiting its applicability to smaller organisms of wider interest, such as murine models.

Collectively, these pioneering studies rely on large quantities of starting material (at least 60 grams) and on protocols not compatible with modern analytic methods. Nowadays, these limitations are particularly relevant, as genetically engineered mouse models for cardiac diseases are central in many laboratory, yet their proteomic analysis remains a challenging step. A recent and technically rigorous work from Eckhardt and colleagues applied quantitative proteomics to murine skeletal muscle, yielding an in-depth characterization of Ca^{2+}-handling and ECC proteins. Nevertheless, this work is limited to the skeletal muscle and did not investigate the cardiac SR [91]. These motivations led us to update this enrichment strategy, capable of obtaining samples enriched in cardiac jSR vesicles, suitable for MS analysis, from a quantity of biological material that meets the possibilities of the multiple laboratories working on murine models.

2.Materials and methods

2.1. Animal studies

All animal studies were conducted in compliance with the EU Directive 2010/63/EU and according to the Committee for animal well-being of the University of Pavia. The animal study protocol was approved by the Italian Ministry of Health; protocol code 223/2023-PR; date of approval 17/03/2023.

2.2. Tissue preparation

The mouse heart tissue was flash-frozen by placing it in a reinforced tube pre-loaded with six zirconium oxide beads and immediately immersing the tube in liquid nitrogen. After at least five minutes, the tube was retrieved and placed on ice to preserve tissue integrity. Tissue homogenization was carried out using a Minilys® bead-beater at 5000 rpm for four cycles of 30 seconds, with 30-second intervals on ice between each cycle.

2.3. Centrifugation and ultracentrifugation

The homogenate, including the zirconium oxide beads, was centrifuged at 9,000 × g for 20 minutes at 4°C using a pre-cooled HERMLE Z 216 MK mini centrifuge. Following centrifugation, the resulting supernatant (SNT) was filtered with a 100 μm cell strainer. The filtered SNT was then ultracentrifuged at 4°C for 1 hour at 200,000 x g (Beckman Coulter OPTIMA MAX-XP, TLA-120.2 rotor).

2.4. Pellet resuspension and protein quantification

The resulting pellet after ultracentrifugation was carefully resuspended in the Resuspension buffer using 500 µl Hamilton syringe; Pierce BCA Protein Assay Kit (Thermo Scientific) was used to determine the protein concentration following manufacturer instructions. Before performing the procedure 5 µl sample was mixed with 5 µl of SDS 10% (w/v) to allow protein solubilization.

2.5. Sucrose density gradient

A discontinuous sucrose density gradient was prepared by layering, 1 ml of each Sucrose-Phase Buffer, starting from the 50% (w/v) sucrose solution. The sample, previously resuspended in buffer containing 10% sucrose, was then gently layered on top of the gradient. The tube was subjected to ultracentrifugation at 100,000 × g for 1 hour at 4°C in a swinging-bucket rotor (OPTIMA XPN 90; SW 41 Ti rotor). After centrifugation, fractionation of the gradient was performed by collecting successive 1 ml layers from the top of the tube. To remove sucrose, each fraction was subjected to a second ultracentrifugation step at 200,000 × g for 1.5 hours at 4°C using an OPTIMA MAX-XP ultracentrifuge with a TLA-120.2 rotor. Following this step, the supernatants were discarded and the pellets were separately resuspended in 200 µl of Dilution Buffer each, using a 500 µl Hamilton syringe. All steps carried out on ice to preserve sample integrity.

2.6. SDS-Page and Western blot

A total of 30 µg of each protein sample was separately mixed with Laemmli Sample Buffer in a 1:3 ratio and then incubated at 90°C for 5 minutes to allow protein denaturation. The samples were subsequently loaded onto a precast acrylamide gel, which was run until the dye front reached the reference line.

For protein transfer, a PVDF Mini membrane and the bottom transfer stack were placed on the cassette base of the Trans-Blot Turbo system. The gel was carefully placed on top of the membrane, followed by the second pre-wetted transfer stack. The transfer was initiated using the following program: 25 V (limit); 1.3 A (constant); 7 minutes (duration).

Once the transfer was complete, the membrane was blocked for 1 hour in 5% (w/v) non-fat milk prepared in Tris-buffered saline with 1% Tween-20 (TBS-T), to prevent non-specific binding.

Subsequently, the membrane was washed three times for 5 minutes each with TBS-T. Then, it was incubated with the primary antibody, diluted with TBS-T at the concentration indicated by the manufacturer. For detection of calcium release unit (CRU) proteins, RyR2, CASQ2, TRDN and JNT, an overnight incubation at 4°C is recommended to enhance signal resolution.

The membrane was then washed with TBS-T for a total of 2 hours, with at least three buffer changes. Following this, the membrane was incubated with the appropriate secondary antibody for 1 hour at room temperature. Finally, a last washing step with TBS-T for 1 hour was performed, again with at least three buffer changes, to ensure removal of unbound antibodies.

2.7. MS sample processing and measurement

A total of 30 µg of protein was processed by resuspension in 50 mM ammonium bicarbonate (AmBic). After verifying the basic pH using pH test strips, enzymatic digestion was carried out in sequential steps. First, dithiothreitol (DTT) was added to obtain a final concentration of 5 mM, and the sample was incubated at 55°C for 30 minutes to reduce disulfide bonds. Then, iodoacetamide (IAA) was added to a final concentration of 5 mM, followed by incubation in the dark for 20 minutes to alkylate free cysteine residues. Digestion was then initiated by adding trypsin (0.2 µg/µl final concentration) and the sample was incubated overnight at 37°C. To quench the reaction, 1 µl of 100% trifluoroacetic acid (TFA) was added.

Following digestion, peptide mixtures were purified using a ZipTip® according to the manufacturer's protocol. The eluate was then dried by SpeedVac centrifugation at 30°C and subsequently resuspended in 20 µl of 0.1% formic acid for mass spectrometry analysis.

2.8. High resolution mass spectrometry analysis (nLC-HRMS)

All samples here reported have been analyzed at UNITECH OMICs (University of Milano, Italy) using: Dionex Ultimate 3000 nano-LC system (Sunnyvale CA, USA) connected to Orbitrap Exploris™ 240 Mass Spectrometer (Thermo Scientific, Bremen, Germany) equipped with nano electrospray ion source. Peptide mixtures were pre-concentrated onto an Acclaim PepMap 100 – 0.3 x 5 mm C18 (Thermo Scientific) and separated on EASY-Spray column ES902, 25 cm x 75 µm ID packed with Thermo Scientific Acclaim PepMap RSLC C18, 3 µm, 100 Å using mobile phase A (0.1 % formic acid in water) and mobile phase B (0.1% formic acid in acetonitrile 20/80, v/v) at a flow rate of 0.300 µL/min. The temperature was set to 35°C and the sample were injected in triplicates. The sample injection volume is 5 µL.

2.9. Data processing

The measured results were processed using Proteome Discoverer 3.2 software, setting the search database to Mus musculus (sp_tr_incl_isoforms, TaxID=10090_and_subtaxonomies, version 2025-06-18) and specifying trypsin as the digestion enzyme.

Within the *Mus musculus* database, the following additional sequences were included, since the infected mice had undergone gene therapy with the human calsequestrin (CASQ2) gene:

>sp|O14958|CASQ2_HUMAN Calsequestrin-2 OS=Homo sapiens OX=9606 GN=CASQ2 PE=1 SV=2
MKRTHLFIVGIYFLSSCRAEEGLNFPTYDGKDRVVSLSEKNFKQVLKKYDLLCLYYHE
PVSSDKVTQKQFQLKEIVLELVAQVLEHKAIGFVMVDAKKEAKLAKKLGFDEEGSLY
ILKGDRTIEFDGEFAADVLVEFLLDLIEDPVEIISSKLEVQAFERIEDYIKLIGFFKSEDSE
YYKAFEEAAEHFQPYIKFFATFDKGVAKKLSLKMNEVDFYEPFMDEPIAIPNKPYTEE
ELVEFVKEHQRPTLRRLRPEEMFETWEDDLNGIHIVAFAEKSDPDGYEFLEILKQVAR
DNTDNPDLSILWIDPDDFPLLVAYWEKTFKIDLFRPQIGVVNVTDADSVWMEIPDDDD
LPTAEEL EDWIEDVLSGKINTEDDDEDDDDDDNSDEEDNDDSDDDDDE
>sp|O14958-2|CASQ2_HUMAN Isoform 2 of Calsequestrin-2 OS=Homo sapiens OX=9606 GN=CASQ2
MKRTHLFIVGIYFLSSCRAEEGLNFPTYDGKDRVVSLSEKNFKQVLKKYDLLCLYYHE
PVSSDKVTQKQFQLKEIVLELVAQVLEHKAIGFVMVDAKKEAKLAKKLDYKAFEEA
AEHFQPYIKFFATFDKGVAKKLSLKMNEVDFYEPFMDEPIAIPNKPYTEEELVEFVKE
HQRPTLRRLRPEEMFETWEDDLNGIHIVAFAEKSDPDGYEFLEILKQVARDNTDNPD
LSILWIDPDDFPLLVAYWEKTFKIDLFRPQIGVVNVTDADSVWMEIPDDDDLPTAEEL
EDWIEDVLSGKINTEDDDEDDDDDDNSDEEDNDDSDDDDDE

>sp|P31415|CASQ1_HUMAN Calsequestrin-1 OS=Homo sapiens OX=9606 GN=CASQ1 PE=1 SV=3
MSATDRMGPRAVPGLRLALLLLLVLGTPKSGVQGQEGLDFPEYDGVDRVINVNAKN
YKNVFKKYEVLALLYHEPPEDDKASQRQFEMEELILELAAQVLEDKGVGFGLVDSEK
DAAVAKKLGLTEVDSMYVFKGDEVIEYDGEFSADTIVEFLLDVLEDPVELIEGERELQ
AFENIEDEIKLIGYFKSKDSEHYKAFEDAAEEFHPYIPFFATFDSKVAKKLTLKLNEIDF
YEAFMEEPVTIPDKPNSEEEIVNFVEEHRRSTLRKLKPESMYETWEDDMDGIHIVAFA
EEADPDGFEFLETLKAVAQDNTENPDLSIIWIDPDDFPLLVPYWEKTFDIDLSAPQIGV
VNVTDADSVWMEMDDEEDLPSAEELEDWLEDVLEGEINTEDDDDDDDD

Dynamic Modifications:

- Max. Dynamic Modifications Per Peptide: 3
- 1. Dynamic Modification: Oxidation / +15.995 Da (M)

Static Modifications:

- 1. Static Modification: Carbamidomethyl / +57.021 Da (C)

Parameters used for Label Free Quantification (LFQ) are the following:

- Prediction Model: inferys_4.7.0_fragmentation
- Processing node: CHIMERYS

General Quantification Settings:

- Peptides to Use: Unique + Razor

Precursor Quantification:

- Precursor Abundance Based On: Intensity

Normalization and Scaling:

- Normalization Mode: Total Peptide Amount
- Scaling Mode: None

Exclude Peptides from Protein Quantification:

- For Normalization: Use All Peptides
- For Protein Roll-Up: Use All Peptides
- For Pairwise Ratios: Exclude Modified

Quan Rollup and Hypothesis Testing:

- Protein Abundance Calculation: Summed Abundances
- N for Top N: 3
- Protein Ratio Calculation: Pairwise Ratio Based
- Maximum Allowed Fold Change: 100
- Imputation Mode: None
- Hypothesis Test: t-test (Background Based)

Protein and Peptide FDR Validator, Confidence Thresholds:

- Target FDR (Strict): 0.01

- Target FDR (Relaxed): 0.05

Protein and Peptide Filters:

- Peptide Confidence At Least: High
- Minimum Number of Peptide Sequences: 1
- Count Only Rank 1 Peptides: False
- Count Peptides Only for Top Scored Protein: False

3. Results

3.1. Rapid flash-freezing is more suited to preserve jSR proteins

The initial and most delicate step in obtaining high-quality jSR vesicles is the method of collection of cardiac tissue. For this purpose, hearts (each weighing approximately 100 - 120 mg) were isolated from adult C57BL/6N mice, immediately after euthanasia by cervical dislocation. I compared the RyR2 signal in western blot (WB) between freshly excised hearts, immediately lysed and treated, and hearts rapidly frozen in liquid nitrogen immediately after isolation, prior to any subsequent treatment (Figure 7). A pronounced degradation of RyR2 in fresh tissue was evident from WB analyses (Figure 7). All subsequent preparations were thus performed starting from hearts that had been rapidly frozen in liquid nitrogen right after excision.

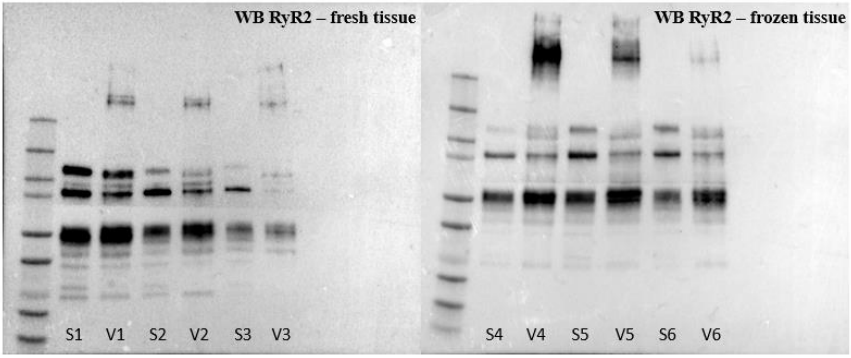

Figure 7: Anti RyR2 WB comparison of 3 fresh hearts vs 3 frozen hearts. All the samples were treated separately and simultaneously. Our data demonstrate that the best results are obtained with frozen samples. S=supernatant; V=vesicles.

3.2. Reproducibility of the protocol

To evaluate the reliability and reproducibility of the developed enrichment procedure, I analysed the protein content of nine independent preparations, each obtained from a single mouse heart, by WB. All samples were processed in parallel under identical experimental conditions to minimize technical variability. The analysis of key proteins involved in ECC revealed a highly consistent enrichment pattern across biological replicates (Figure 8). The reproducibility of the results was particularly evident for the soluble luminal protein CASQ2 and for the small transmembrane components TRDN and JNT, confirming the robustness of the isolation procedure even when working with such a limited amount of starting material.

As expected, RyR2 showed greater variability among the different samples. This observation likely reflects its intrinsic biochemical nature, as RyR2 is a very large, multi-subunit membrane complex known for its low stability once extracted from the native membrane environment. These difficulties are well documented in the literature and are a common challenge in studies focusing on RyR2 purification and analysis. Nevertheless, the protocol consistently enabled the recovery of RyR2 across all biological replicates, supporting the effectiveness of the enrichment in maintaining key jSR components and providing a reliable experimental basis for subsequent molecular investigations of the jSR organization.

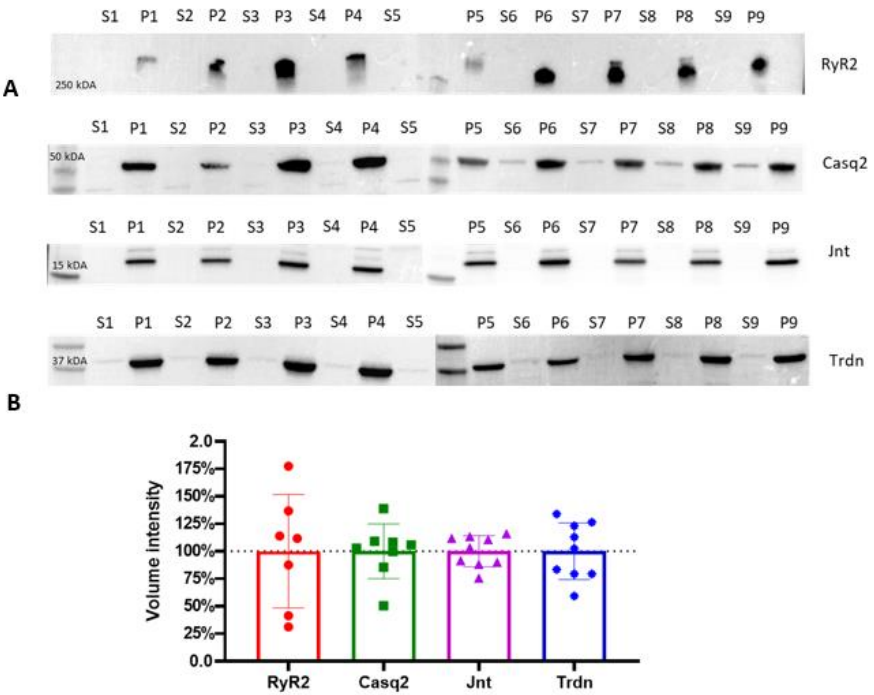

Figure 8: A) Western blot analyses of vesicle fractions obtained from the final pelleting step, compared with the relative discarded supernatant. Key jSR and SR proteins, including RyR2, CASQ2, JNT, TRDN, are analyzed across each preparation. The four horizontal blot panels correspond to different molecular weight protein targets, as indicated by the molecular weight markers on the left (250 kDa, 50 kDa, 35 kDa, and 17 kDa). B) Quantitative analysis of the Western blots is presented in the form of bar plots, summarizing the statistical variance in protein levels across the nine biological replicates. Band intensities were quantified and normalized, and data are represented as mean ± standard deviation.

3.3. Fractionation of the SR vesicles by density gradient and Cryo-EM quality evaluation

To achieve a more refined separation of the SR subdomains, I performed an additional purification step based on sucrose density gradient centrifugation (Figure 9).

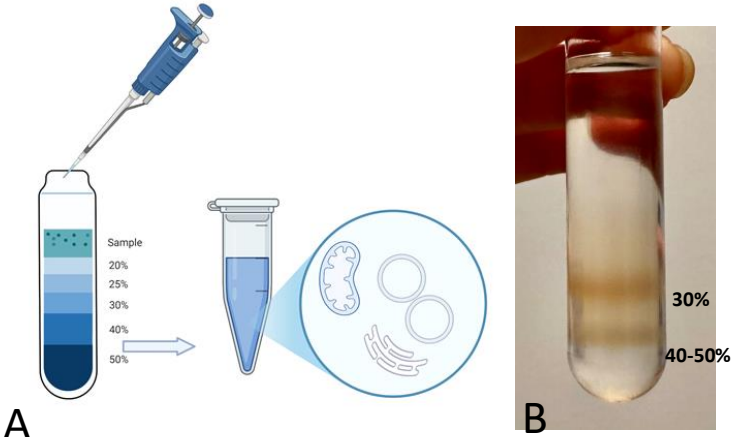

Figure 9: A) Schematic representation of the sucrose density gradient. B) Picture of the sucrose density gradient with two evident bands in the bottom sucrose phases. The uppermost band corresponds to the 30% sucrose phase, while the lower band corresponds to the 30% sucrose phase, while the lower band corresponds to the interface between the 40% and 50% sucrose densities.

While the initial enrichment already allowed the identification of key jSR proteins, the gradient approach provides a finer distinction between the longitudinal and junctional regions of the SR, thereby minimizing the presence of contaminating proteins from other cellular compartments such as the cytosol or plasma membrane. Because the material recovery from each gradient fraction is inherently limited, four murine hearts were pooled to obtain sufficient biological material for a single jSR-enriched preparation.

When exposed to high centrifugal forces, each vesicle migrates through the gradient until reaching the position where its density matches that of the surrounding sucrose solution. At this equilibrium point, particles of different lipid and protein composition accumulate at distinct interfaces within the gradient.

Previous studies on muscle-derived microsomal fractions have shown that vesicles originating from the longitudinal SR typically settle in the 30% (w/v) sucrose region, whereas those derived from the junctional SR are recovered between the 40% and 50% (w/v) sucrose layers [87,88]. This distribution reflects their compositional differences: jSR vesicles, characterized by a higher protein-to-lipid ratio, are denser than those from the longitudinal SR, which contain relatively more membrane lipids.

In my preparations, the junctional SR components were predominantly concentrated at the 40–50% (w/v) sucrose interface, consistent with previous observations. Notably, the soluble luminal protein CASQ2 followed the same enrichment profile as the membrane proteins RyR2 and TRDN, confirming that it remained tightly associated with the jSR vesicles during the entire procedure (Figure 10). This suggests that the vesicular structures were preserved in their native state, maintaining the integrity of the underlying protein complexes.

To further validate the identity and quality of the enriched fractions, I examined the distribution of additional SR and T-tubule proteins by Western blotting. SERCA, the Ca^{2+}-ATPase responsible for cytosolic Ca^{2+} reuptake, was found broadly distributed across the gradient fractions, as expected for this abundant enzyme present throughout the SR network. Conversely, $Ca_V1.2$ and JPH2, two key proteins of the dyadic junction, located at the interface between the T-tubule and the jSR, were detected together with RyR2 in the denser fractions of the gradient. This co-enrichment provides strong evidence that the physiological interactions among these proteins were retained throughout the procedure, further supporting the structural and molecular integrity of the isolated junctional SR vesicles.

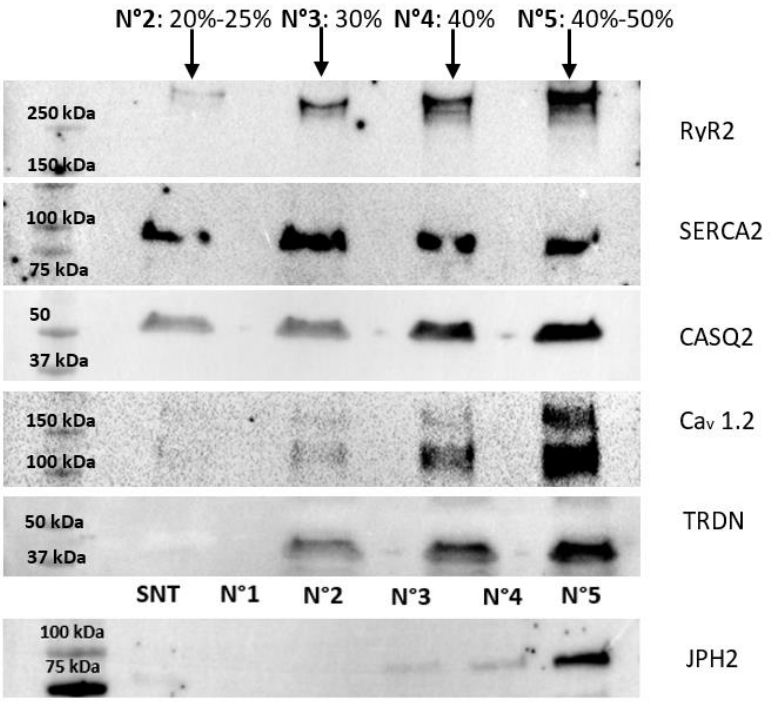

Figure 10: Western blot analysis of fractions 2, 3, 4, and 5 from the sucrose density gradient. The analysis highlights the distribution of proteins across the gradient, with the highest enrichment of the target proteins observed in fraction 5, consistent with the expected localization of SR-derived vesicles containing junctional SR components. These results confirm the efficacy of the isolation protocol in separating SR subdomains and concentrating the proteins of interest in fraction 5. The JPH2 membrane was loaded differently from the others, specifically with the supernatant (S) from the vesicle preparation and fraction N° 1, which does not contain any proteins. The total protein content of the fractions are: n°2= 119 µg; n°3= 182 µg; n°4= 219 µg; n°5= 350 µg.

Cryo-electron microscopy (Cryo-EM) was employed to evaluate vesicles' morphology and detect possible contaminants (such as collagen or actin fibers). Qualitative Cryo-EM imaging (Figure 11) shows features that are consistent with RyR2 channels, with their expected shape and massive dimension (27–28 nm) in multiple vesicles [22].

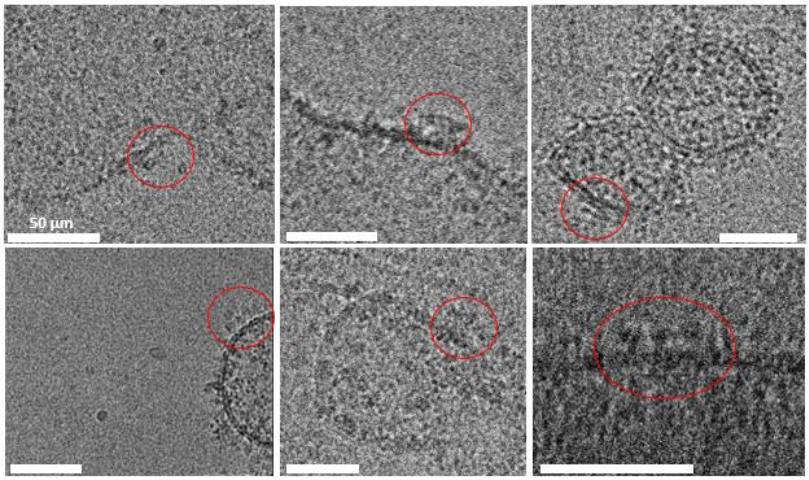

Figure 11: Cryo-electron microscopy images of jSR vesicles. The well-preserved membrane integrity indicates successful isolation and preparation, highlighting the suitability of the protocol for structural studies of jSR-associated proteins. RyR2 channels are circled in red, scale bar for all pictures is 50 µm.

3.4. Relative quantification of jSR vesicles

I analysed by MS the protein content of fraction 5, corresponding to the region enriched in jSR components, and compared it to three independent SR-enriched samples obtained from individual mouse hearts that had not undergone the gradient separation (Figure 12).

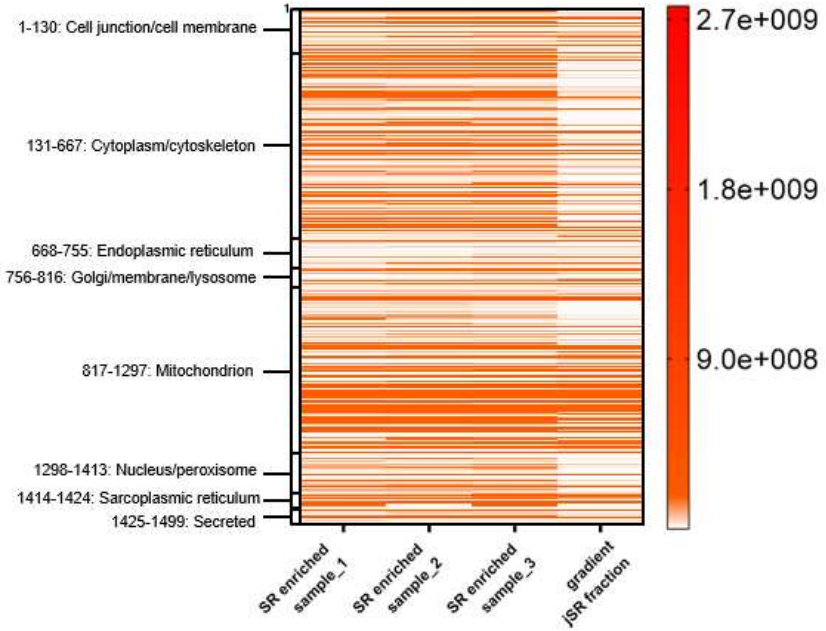

Figure 12: Heat map of protein intensity across three SR-enriched samples (each from n=1 mouse heart) and the sucrose gradient fraction (from n=4 mouse hearts). Proteins were grouped according to their annotated subcellular localization. Each row represents a protein, and the colour intensity reflects MS-based quantification (label-free intensities), according to the colour legend bar. The fourth column ("gradient") corresponds to Fraction 5 of the sucrose density gradient.

This comparison allowed me to assess the actual contribution of the gradient step to the purification efficiency. The analysis revealed that the proteins identified in fraction 5 displayed a decrease in cytoplasmic and plasma membrane contaminants, confirming that the gradient centrifugation effectively improved the selectivity of the enrichment. In parallel, the relative abundance of typical jSR markers increased, indicating that this additional step not only enhanced sample purity but also provided a preparation more specifically representative of the junctional SR domain.

To provide a more detailed view of the enrichment of SR components, we inspected a subset of selected proteins of interest from both jSR and lSR (Figure 13).

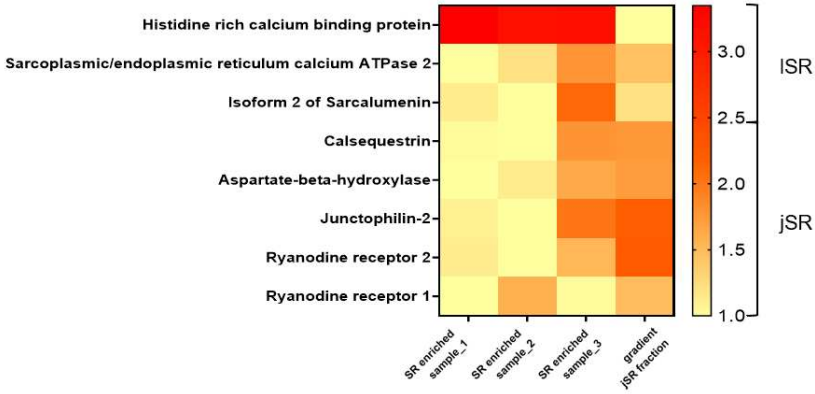

Figure 13: Heat map showing the relative abundance of selected junctional SR proteins across SR-enriched samples and the sucrose gradient fraction. The heat map includes key proteins localized to the jSR and lSR. Values represent intensities from MS analysis normalized over the minimum value.

According to the data presented in Figure 13, proteins specifically localized to the jSR are clearly enriched in the corresponding sucrose gradient fraction. In contrast, the relative abundance of other SR proteins, such as HRC and Sarcalumenin, is reduced in this fraction.

3.5. CPVT1 mouse models: RyR$^{R4496C7/+}$ mutation and CASQ2 based gene therapy

In addition to the proteomic characterization of jSR-enriched vesicles of WT mice, the present work expands this analysis to two additional experimental models: RyR$^{R4496C/+}$ (hereafter Mut) and the same heterozygous model treated with the human *CASQ2* gene (RyR2$^{R4496C/+}$ Inf AAV8-h*CASQ2*, hereafter Inf). These results have not been previously published and provide a novel insight into these physiological and pathological conditions. The murine model carrying the RyR2$^{R4496C/+}$ mutation is one of the most characterized CPVT1 models, showing high homology of the phenotype with the clinical consequences of the human RYR2^{R4497C} mutation, originally identified in a large Italian family[92].

To evaluate the relative abundance of CRU proteins in these two mice models, four Mut mice and three Inf mice were treated with the already published protocol in order to have a sample enriched in jSR vesicles. After the procedure the samples were analysed through WB with RyR2, TRDN, CASQ2 and JNT antibodies (Figure 14). WB analysis of CASQ2 expression in the Inf mice revealed an inter individual variability, with one animal displaying lower levels of CASQ2 overexpression. This difference is consistent with the variability associated with tail vein injection of the gene therapy, which typically results in heterogeneous efficiency across animals [93]. It is also important to note that the antibody used for CASQ2 detection recognizes both the murine and human CASQ2 proteins, because the two isoforms are highly conserved, differencing only in the C-terminal region. Despite this, the levels of the other CRU proteins, RyR2, TRDN and JNT were comparable among the three animals, indicating high reproducibility in sample preparation. These results confirm that the observed differences in CASQ2 levels are specific for the gene therapy rather that reflecting technical variability.

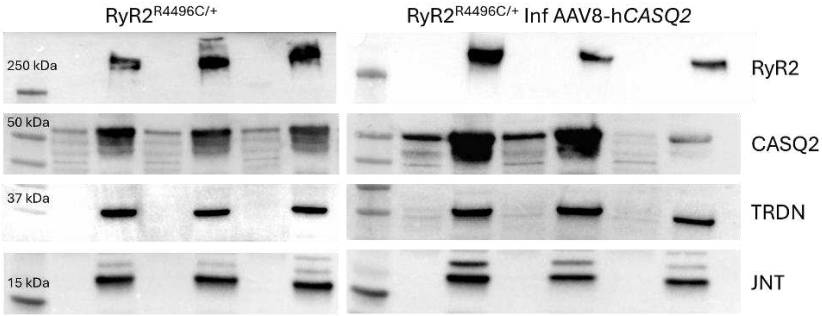

Figure 14: Western blot analyses of vesicle obtained from the two different mouse models: RyR2$^{R4496C/+}$ and RyR2$^{R4496C/+}$ Inf AAV8-hCASQ2, compared with the relative discarded supernatant. Key jSR and SR proteins, including RyR2, CASQ2, JNT, TRDN, are analysed across each preparation. 30 µg of protein was injected in each well.

3.6. Comparative proteomic analysis across different mice models

To investigate how the mutation and the treatment with AAV8-h*CASQ2* impact the proteome composition of the sample, we performed a comparative quantitative mass spectrometry analysis across the three mice models: WT, Mut and Inf. The proteomic analysis was carried out using three biological replicates for each condition (N=3 mice per group). Every biological sample was injected in triplicates in the LC-MS/MS system, to ensure technical reproducibility. Proteins were considered differentially expressed when showing an absolute log2 fold change ≥ 0.585 (corresponding to a 1.5-fold change). For the comparative analysis, only proteins annotated as belonging to the "endoplasmic reticulum" and "sarcoplasmic reticulum" were taken in consideration, because these

are the organelles enriched in the sample and represent the primary focus of this study. The three physiological and pathological conditions were then analyzed and compared with each other. The full lists of significantly up- and down- regulated proteins for each pairwise conditions are provided in Tables 1-6; the distribution of fold-changes and significance is represented as volcano plots (Figures 15 –17).

3.6.1. Comparison of Mut vs WT mice models

The proteomic comparison between Mut and WT samples revealed minimal differences, with only few proteins belonging to the ER/SR showing statistical changes in abundances (Tables 1-2). This suggests that the mutation $RyR2^{R4496C/+}$, although functional disruptive for Ca^{2+} handling [59], does not trigger significant proteome changes at least in the ER/SR compartment. It is worth noting that in the group of proteins upregulated in the Mut model with respect to the WT, the Aspartyl/asparaginyl beta-hydroxylase or Aspartate-beta-hydroxylase (Asph) is found. This protein originates from the same genetic locus that encodes also for JNT via alternative splicing. These isoforms are annotated under the same gene entry in databases such as Uniprot, even if they have different functions and structures. Therefore, the detection of Asph in SR enriched samples may reflect the JNT isoform, which is known to interact with RyR2, CASQ2 and TRDN.

Table 1: List of downregulated proteins in the comparison Mut vs WT.

Uniprot ID	Name	Abundance Ratio (log2): (Mut) / (WT)	-LOG10 p-value
B9EHY2	CAAX prenyl protease	-6,6439	15,5908
Q3U3R4-3	Isoform 3 of Lipase maturation factor 1	-6,6439	15,5908
Q07456	Protein AMBP	-6,6439	15,5908
O08795-2	Isoform 2 of Glucosidase 2 subunit beta	-2,2042	15,5908
A0A1S6GWK0	Dolichyl-diphosphooligosaccharide--protein glycosyltransferase subunit STT3A	-0,8314	2,5266
P50172	11-beta-hydroxysteroid dehydrogenase 1	-0,7250	1,8570

Table 2: List of upregulated proteins in the comparison of Mut vs WT.

Uniprot ID	Name	Abundance Ratio (log2): (Mut) / (WT)	-LOG10 p-value
F8VQC7	Kinectin 1	0,5840	0,5459
Q99L43	Phosphatidate cytidylyltransferase 2	0,6116	0,6196
Q8BSY0	Aspartyl/asparaginyl beta-hydroxylase	0,7251	1,0054
Q7TQ95	Endoplasmic reticulum junction formation protein lunapark	0,8875	1,7951

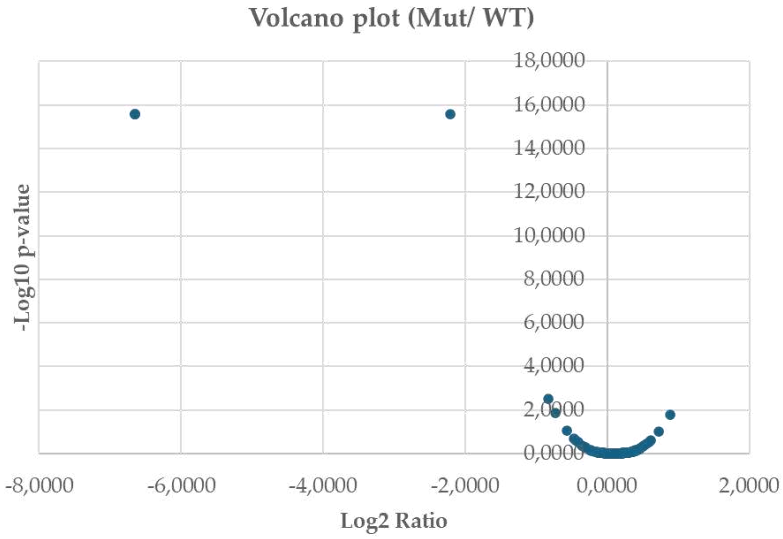

Figure 15: Volcano plot showing differential protein abundance between Mut and WT conditions. The x-axis shows the log_2 fold change, and the y-axis displays the $-log_{10}$ adjusted p-value. Proteins passing the significance thresholds ($|log_2FC| \geq 0.58$ and $FDR \leq 0.05$) are considered differentially regulated.

3.6.2. Comparison of Inf vs Mut mice models

The Inf vs Mut comparison highlights a subset of proteins completely depleted in the Inf group, and vice versa a distinct subset of proteins expressed only in the Inf group compared to the Mut. In the list of proteins upregulated in the Inf model there is, along with human CASQ2 (which is expected as hCASAQ2 mRNA is provided via AAV infection), also the murine CASQ2 protein. The increase in CASQ2 abundance is likely associated with successful transduction and expression of the exogenous human CASQ2, which may trigger compensatory upregulation of the endogenous protein, thereby amplifying total CASQ2 signal in the jSR sample. Differently from the comparison Mut vs WT, here Asph/JNT protein is highly downregulated in the treated model (Inf) with respect to the untreated one (Mut), which suggests this is a consequence of the therapy.

Table 3: List of downregulated proteins in the comparison Inf vs Mut.

Uniprot ID	Name	Abundance Ratio (log2): (Inf) / (Mut)	-LOG10 p-value
P33267	Cytochrome P450 2F2	-6,644	15,486
P61804	Dolichyl-diphosphooligosaccharide--protein glycosyltransferase subunit DAD1	-6,644	15,486
Q0VGQ1	Very-long-chain 3-oxoacyl-CoA reductase	-6,644	15,486
P50285	Flavin-containing monooxygenase 1	-1,014	1,464
A2AL76	Aspartate-beta-hydroxylase	-0,921	1,142
Q8R5J9	PRA1 family protein 3	-0,808	0,783
Q9D1G3	Protein-cysteine N-palmitoyltransferase HHAT-like protein	-0,756	0,633

Table 4: List of upregulated proteins in the comparison of Inf vs Mut.

Uniprot ID	Name	Abundance Ratio (log2): (Inf) / (Mut)	-LOG10 p-value
O09161	Calsequestrin-2	0,5878	0,2145
Q9DCY1	Peptidyl-prolyl cis-trans isomerase	0,6636	0,3180
P19324	Serpin H1	0,9107	0,8987
B9EHY2	CAAX prenyl protease	6,6439	15,4863
O14958	Calsequestrin-2 OS=Homo sapiens	6,6439	15,4863
Q07456	Protein AMBP	6,6439	15,4863

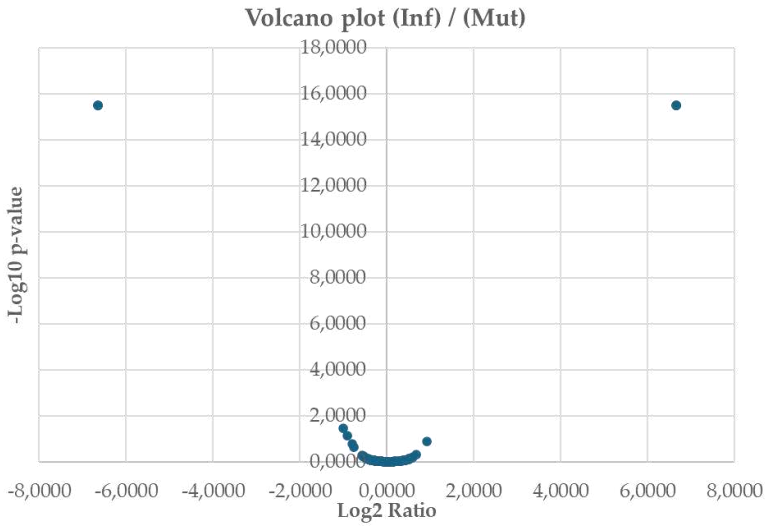

Figure 16: Volcano plot showing differential protein abundance between Inf and Mut conditions. The x-axis shows the log_2 fold change, and the y-axis displays the $-log_{10}$ adjusted p-value. Proteins passing the significance thresholds ($|log_2FC| \geq 0.58$ and $FDR \leq 0.05$) are considered differentially regulated.

3.6.3. Comparison of Inf vs WT mice models

Following the promising effect of the AAV-based therapy, that is the downregulation of Asph/JNT, a protein upregulated in the Mut model versus the WT one, the comparative proteomic analysis of Inf vs WT samples again revealed a set of ER/SR proteins that are not repristinated by the therapy to the WT levels. As expected from previous data on the Inf Vs Mut comparison, the murine CASQ2 is again consistently upregulated in the Inf group with respect to the WT one. Functionally, increased CASQ2 levels at the jSR would expectedly enhance intra Ca^{2+} buffering and strengthen the CASQ2-RyR2 interaction. Therefore, RyR2 would be stabilized in diastole and the spontaneous Ca^{2+} release is altered. The proteomic observation of CASQ2 upregulation is thereby concordant with the therapeutic effect observed in Inf model (data not shown).

Table 5: List of downregulated proteins in the comparison Inf vs WT.

Uniprot ID	Name	Abundance Ratio (log2): (Inf) / (WT)	-LOG10 p-value
P33267	Cytochrome P450 2F2	-6,6439	15,4396
P61804	Dolichyl-diphosphooligosaccharide--protein glycosyltransferase subunit DAD1	-6,6439	15,4396
Q3U3R4-3	Isoform 3 of Lipase maturation factor 1	-6,6439	15,4396
Q0VGQ1	Very-long-chain 3-oxoacyl-CoA reductase	-6,6439	15,4396
O08795-2	Isoform 2 of Glucosidase 2 subunit beta	-1,2828	1,6766
Q99J47	Dehydrogenase/reductase SDR family member 7B	-1,2345	1,5685
A0A1S6GWK0	Dolichyl-diphosphooligosaccharide--protein glycosyltransferase subunit STT3A	-1,1203	1,2351
Q3U944	L-type lectin-like domain-containing protein	-0,9379	0,7825
Q3TL33	Calumenin	-0,7735	0,4705
Q8R5J9	PRA1 family protein 3	-0,7274	0,3893
O55143-2	Isoform 2 of Sarcoplasmic/endoplasmic reticulum calcium ATPase 2	-0,6920	0,3451
Q8R1X1	Long-chain-fatty-acid--CoA ligase	-0,6620	0,3139
P50172	11-beta-hydroxysteroid dehydrogenase 1	-0,6349	0,2805

Table 6: List of upregulated proteins in the comparison of Inf vs WT.

Uniprot ID	Name	Abundance Ratio (log2): (Inf) / (WT)	-LOG10 p-value
P20029	Endoplasmic reticulum chaperone BiP	0,6480	0,1488
Q3TFU8	GOLD domain-containing protein	0,6617	0,1614
Q9CZI5	Small ribosomal subunit protein uS12	0,7312	0,2207
Q9CQS8	Protein transport protein Sec61 subunit beta	0,7579	0,2518
Q99PL5	Ribosome-binding protein 1	0,7908	0,2829
P19324	Serpin H1	0,8520	0,3542
Q9DCY1	Peptidyl-prolyl cis-trans isomerase	0,8631	0,3675
Q8K1N1	Calcium-independent phospholipase A2-gamma	1,0014	0,6098
F8VQC7	Kinectin 1	1,0115	0,6296
Q7TQ95	Endoplasmic reticulum junction formation protein lunapark	1,1583	0,9410
O09161	Calsequestrin-2	1,1661	0,9581
O14958	Calsequestrin-2 OS=Homo sapiens	6,6439	15,4396

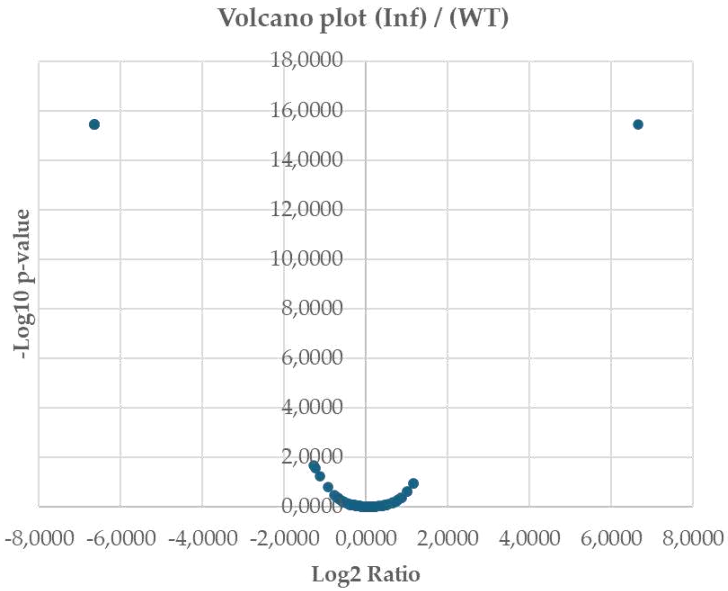

Figure 17: Volcano plot showing differential protein abundance between Inf and WT conditions. The x-axis shows the $\log_2$ fold change, and the y-axis displays the $-\log_{10}$ adjusted p-value. Proteins passing the significance thresholds ($|\log_2 FC| \geq 0.58$ and FDR ≤ 0.05) are considered differentially regulated.

3.7. Main outcomes of the comparative proteomic analysis

Overall, the first achievement of the proteomics approach to CPVT1 has been to make the jSR experimentally accessible to quantitative proteomics. The enrichment strategy here proves to be both feasible and reproducible, even starting from a limited amount of material, one mouse heart (approximately 100-120 mg), which is a major practical improvement compared to previous approaches. In addition to being technically advantageous, reducing the starting material is also relevant in the context of in vivo AAV-based gene therapy, where costs and inter-individual variability can be substantial as discussed before. Secondly, this protocol allowed me to perform a comparative quantitative LC-MS/MS analysis across the three conditions of murine models relevant to the study of CPVT1 pathophysiology: WT mice, $RyR2^{R4496C/+}$, and $RyR2^{R4496C/+}$ Inf AAV8-h*CASQ2*. The analysis intentionally focused onto proteins annotated as belonging to ER/SR. What emerges from these data is that there are minimal differences in the ER/SR proteome between WT and $RyR2^{R4496C/+}$ mice models. Although the $RyR2^{R4496C/+}$ mutation is functionally impactful on Ca^{2+} handling, these data suggest that it does not necessarily translate into broad quantitative remodelling of the ER/SR proteome in the enriched sample. In contrast, the $RyR2^{R4496C/+}$ Inf AAV8-h*CASQ2* condition presents a signature that is more directly aligned with the therapeutic goal. In this sample, both human CASQ2 and endogenous murine CASQ2 emerge among the upregulated proteins, supporting the effective transgene expression and indicating that the overall CASQ2 load in the jSR is increased after the therapy. A particularly interesting point emerges from the protein annotated under the Asph/JNT locus. The downregulation observed in the $RyR2^{R4496C/+}$ Inf AAV8-h*CASQ2* vs. $RyR2^{R4496C/+}$ mice models comparison may indicate that the therapy, while increasing CASQ2 levels, shifts the relative representation of other CRU components.

Taken together, the results obtained in this chapter support two main outcomes: first, the enrichment workflow developed provides a reliable tool to study the proteome of a challenging microdomain, while at the same time reducing the animal usage; and second, the comparative dataset suggests that the ER/SR proteomic landscape remains largely conserved across the three mice models, with the most coherent signature being the increase of CASQ2 in treated animals. This provides a reference molecular framework for future targeted and non-targeted MS-based analysis.

Chapter IV: Biochemical characterization of CASQ2 mutations in CPVT2

In this chapter I will discuss the data on the biochemical characterization of the pathological mutations of CASQ2 relative to the WT protein. The first part of this chapter reports data from our paper submitted with the title "The functionally active unit of Calsequestrin is the dimer" and describes the characterization of the ionic dependency of the Ca^{2+}-dependent polymerization of the WT protein. This work stems from the question of how CASQ2 assembles into functional polymers within the jSR. In particular, the intrinsic ability of CASQ2 to form dimers even in the absence of Ca^{2+} appears to play a crucial role in its proper trafficking and polymerization. Building on these concepts, the following section describes the experimental approaches employed to characterize the biochemical properties of the clinically relevant mutants of CASQ2, with the aim of understanding the physiopathology of CASQ2 disfunction on CPVT2.

1. Introduction

1.1. CASQ2 biochemical features

CASQ2 is the major Ca^{2+}-binding protein of the jSR, concentrated up to 100 mg/ml in the lumen of this organelle [39]. It features three thioredoxin-like domains, each composed of approximately 100 residues and exposing multiple acidic residues on the exterior, highly electronegative surface [41]. Thioredoxin domains are composed of five-stranded β-sheet and two pairs of α-helices, positioned at the opposite site of a hydrophobic core. A particular feature of CASQ2 (and its skeletal counterpart, CASQ1) is the amino acid composition of the C-terminal flexible tail, prevalently composed of acidic residues, mostly Asp and Glu[94].

The folding of CASQ is influenced by several factors (Figure 18). At concentrations of monovalent cations lower than physiological (i.e. [KCl] <150-220 mM [95]), CASQ polypeptide is a random coil, due to the presence of the abundant negative charges, repelling each other and impeding packing of the polypeptide. These non-acidic residues can be masked by either monovalent (Na^+ or K^+) or divalent ions (Ca^{2+} or Mg^{2+}), so that the increasing ionic strength generates the same secondary structures, with divalent cations being orders of magnitude more efficient than monovalent cations[26].

CASQ supra-molecular assembly, a critical and physiological relevant feature, is triggered by Ca^{2+}. The first step in CASQ2 quaternary assembly is generally believed to identify with the crystallographic "front-to-front" dimer, stabilized by N-terminal swapping between the monomers. Further increase in Ca^{2+} concentration promotes the "back-to-back" polymerization process, governed by the C-terminal tail. The Ca^{2+} binding capacity of each CASQ2 molecule increases along with polymerization, up to 60 Ca^{2+} ions per CASQ2. The attributes of Ca^{2+}-dependent multimerization of CASQ are related to the trafficking and also the retainment of this protein into the jSR lumen [96,97]. In cardiomyocytes, proper glycosylation ensures both efficient Ca^{2+}

buffering within the SR and the correct localization of CASQ2 at its functional site [98].

Module 1 of this chapter will focus on the biochemical characterization of wild-type CASQ2, providing insights into its dimerization and polymerization behavior.

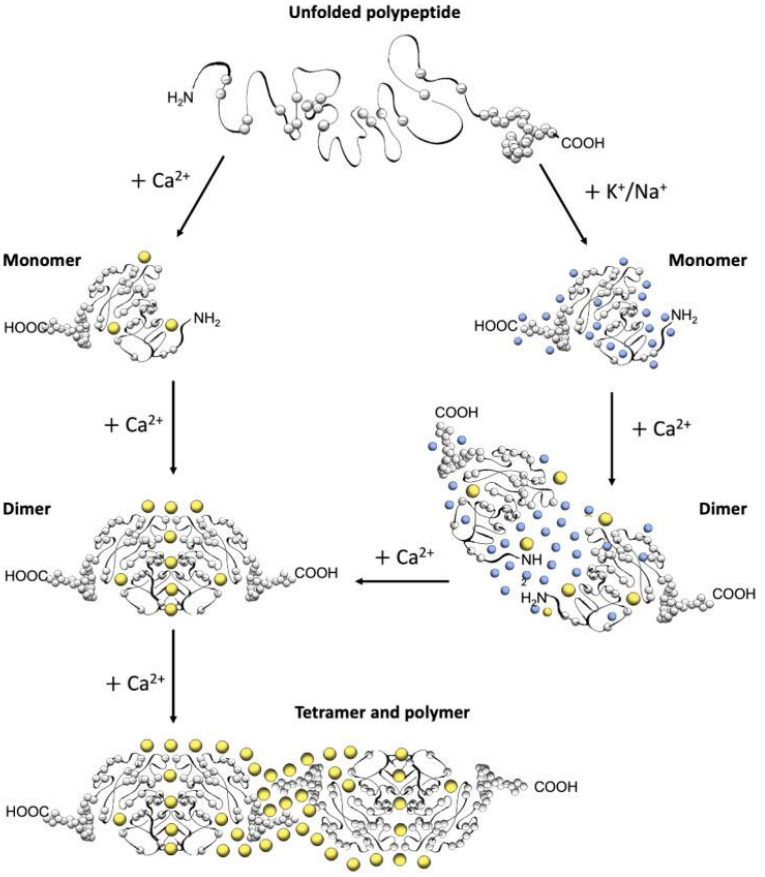

Figure 18: Schematic representation of CASQ2 multimerization driven by divalent and monovalent cations [26].

1.2. CASQ2 pathological mutations

CPVT2 is caused by mutations in the *CASQ2* gene; this disease features an impaired Ca^{2+} release refractoriness, with a premature activation of the RyR2 complex. Release refractoriness refers to the transient period following a Ca^{2+} release event during which RyR2 remains temporarily unable to trigger a new release. This condition may be caused by an impairment of CASQ2-RyR2 interactions [74]. For example, the mutant $CASQ2^{R33Q}$ is ineffective in inhibiting RyR2 channels when SR luminal Ca^{2+} concentrations are low.

CASQ2 missense mutations are spread all over the protein; the different mutants do not share common defects in their properties; indeed they are also difficult to classify and interpret [99]. Also, until 2016, CPVT2 was thought to be an autosomal recessive disease, but later findings identified a new autosomal dominant form of this disease, co-segregating with the $CASQ2^{K180R}$ variant[100]. For this reason, a re-evaluation of CASQ2-related pathogenic mechanisms has been done, with the hypothesis that distinct molecular processes may underlie the recessive and dominant forms of the disease: a functional classification of pathological CASQ2 mutations has been proposed, based on their predicted impact on the stability of different structural states [26]. More specifically, mutations that prevent dimer formation are expected to lead to the mislocalization or degradation of CASQ2, ultimately resulting in a loss of protein with recessive pathological effects. In contrast, dominant mutants would preserve their dimerization ability and thus be retained in the jSR and interact with WT CASQ2, thereby generating defective polymeric assemblies with impaired Ca^{2+} buffering dynamics.

1.3 CASQ2 polymerization model

Traditionally, CASQ2 polymerization has been conceived as a Ca^{2+}-driven, stepwise assembly in which specific interaction interfaces mediate the progressive formation of a linear polymer. This picture, however, struggles to account for the observation that numerous single-residue substitutions dispersed across the highly charged surface of CASQ2 can produce severe clinical phenotypes such as CPVT, as discussed above. The linear polymer model is supported mainly through turbidity assays, which monitor light scattering in colloidal suspensions as an indirect readout of multimer formation. In such assays, increases in scattering intensity are taken to reflect greater abundance of nanoscale particles or aggregates. Crucially, turbidimetry does not distinguish between different morphological classes of scattering species [101]. Overlapping contributions from heterogeneous species therefore introduce ambiguity about the actual nature and size distribution of the assemblies present in solution.

These methodological limitations have likely biased our view of CASQ2 assembly toward a simple, Ca^{2+}-centric, linear pathway [102–104]. At the same time, published studies have hinted at a more complex, ion-sensitive behaviour: for example, physiological concentrations of Mg^{2+} modulate CASQ2's response to Ca^{2+} and can unmask differences between variants that remain invisible in standard turbidity assays. Such findings raise the possibility that focusing exclusively on Ca^{2+} may obscure other important determinants of CASQ2 quaternary structure.

To address these issues, we systematically explored how ionic conditions, protein concentration, and the presence of divalent cations shape the oligomerization landscape of cardiac CASQ2. By combining different techniques, such as turbidimetry, mass photometry (MP), size-exclusion chromatography (SEC), dynamic light scattering (DLS), microscale thermophoresis (MST) and thermal stability assays, we provide a more detailed description of CASQ2 assembly. Our results indicate that dimer formation is an intrinsic property of CASQ2 that can occur independently of Ca^{2+}, and that Ca^{2+}

acts rather as a switch that promotes a transition from an ensemble of oligomeric species to larger oligomers and polymers. This view contrasts with the conventional notion of a strictly sequential, Ca^{2+}-only driven polymerization, and suggests that the functional unit of CASQ2 in the biological setting may be the dimer.

2. Materials and methods

2.1. Expression and Purification of Cardiac Calsequestrin

Expression constructs pET28a vector were transformed into *E. coli* BL21 (DE3) cells. Overnight starter cultures were used to inoculate large-scale cultures (750 mL of medium per 2.8 L flask), which were grown at 37 °C until reaching an optical density (OD_{600}) of approximately 0.5. Protein expression was then induced by adding 1 mM IPTG, followed by incubation for 3 hours at 30 °C. Cultures were grown in standard LB medium supplemented with 25 µg/mL kanamycin and 50 µg/mL chloramphenicol. Cells were harvested by centrifugation at 4,000 × g for 20 minutes, and the resulting pellets were collected and stored at −80 °C until use.

Frozen cell pellets were resuspended in lysis buffer (20 mM potassium phosphate, pH 7.4, 500 mM NaCl, 1 mM EDTA, 5 mM imidazole, and 1 mM β-mercaptoethanol) and disrupted mechanically using a Minilys® bead-beater (Bertin Technologies) at maximum speed (5000 rpm) for four 30-second cycles. The lysate was clarified by centrifugation at 8,900 × g for 1 hour at 4 °C, and the supernatant was filtered through a 0.45 µm membrane. His-tagged CASQ2 was purified by immobilized metal affinity chromatography (IMAC) on a 5 mL HisTrap FF column using an ÄKTA go FPLC system. The IMAC buffers consisted of Buffer A (20 mM potassium phosphate, pH 7.4, 300 mM NaCl, 20 mM imidazole) and Buffer B (20 mM potassium phosphate, pH 7.4, 300 mM NaCl, 300 mM imidazole). The protein was eluted in a single step with 100% Buffer B and dialyzed overnight at 4 °C against 2 L of dialysis buffer (20 mM HEPES, pH 7.3, 100 mM NaCl, 5 mM EDTA, 1 mM β-mercaptoethanol).

Anion-exchange chromatography was subsequently carried out using a 5 mL HiTrap Capto Q column with Buffer A (20 mM HEPES, pH 7.3, 100 mM NaCl) and Buffer B (20 mM HEPES, pH 7.3, 1 M NaCl). Protein elution was achieved through a continuous salt gradient up to

100% Buffer B, with CASQ2 typically eluting between 40–50%. Fractions containing CASQ2 were pooled and concentrated using an Amicon® centrifugal filter unit (10 kDa MWCO).

For size-exclusion chromatography (SEC), the sample was loaded into a 10 mL loop using a 5 mL syringe and passed through a HiLoad 26/600 Superdex 200 pg column equilibrated with gel filtration buffer (20 mM HEPES, pH 7.3, 50 mM KCl). Fractions enriched in CASQ2 were combined, concentrated, aliquoted, and stored at −80 °C.

2.2. Turbidity Assays

Turbidity measurements were used to assess CASQ2 polymerization in response to $CaCl_2$ or $MgCl_2$ (0.01–100 mM) in the presence of 10 mM or 50 mM KCl. Assays were performed in a 96-well plate using a Tecan Infinite 200® Pro plate reader to measure absorbance at 350 nm. Each well contained 140 µL of sample, with CASQ2 previously buffer-exchanged into 20 mM HEPES (pH 7.3) and the desired KCl concentration. Before salt addition, samples were equilibrated at room temperature for 20 minutes and baseline readings were recorded. $CaCl_2$ or $MgCl_2$ was then manually added using a multichannel pipette, and samples were mixed gently by pipetting five times to avoid air bubbles. Absorbance was recorded immediately after salt addition. Each condition was tested in triplicate at room temperature.

2.3. Mass Photometry

Mass photometry experiments were conducted using a Refeyn TwoMP instrument (Refeyn Ltd). CASQ2 was buffer-exchanged into 20 mM HEPES (pH 7.3) containing KCl concentrations between 25 mM and 500 mM. Samples were incubated on ice for 45 minutes and then diluted to 100 nM CASQ2 for the first dilution and 10 nM for the

final measurement. After loading the sample onto the coverslip, data acquisition began immediately and continued for 60 seconds. Individual molecular landing events were detected as changes in interferometric scattering and automatically quantified using AcquireMP software. Calibration curves generated from known protein standards were used to convert contrast values to molecular mass. Data were processed in DiscoverMP software to produce mass distribution histograms and determine mean molecular weights through Gaussian fitting. All measurements were performed at room temperature.

2.4. Size-Exclusion Chromatography

Analytical SEC experiments were performed using a Superdex 75 10/300 GL column (Cytiva) connected to an ÄKTA go FPLC system. The column was equilibrated with 20 mM HEPES (pH 7.3) containing different KCl concentrations (50–200 mM). CASQ2 (1 mg/mL) preincubated with the respective KCl concentration was injected (100 µL) into a 500 µL loop immediately after adding 1 mM $CaCl_2$.

To assess concentration-dependent effects, the same buffer composition (20 mM HEPES, pH 7.3, 50 mM KCl) was used, and CASQ2 samples ranging from 5.6 µM to 225 µM were injected under identical conditions. Elution profiles were recorded using the integrated UV–Vis detector. All runs were performed at 4 °C.

2.5. Thermal Stability Assay

Thermal unfolding of CASQ2 was assessed using a Tycho NT.6 instrument (NanoTemper Technologies). Samples (2.5 µM CASQ2) were prepared in 20 mM HEPES (pH 7.3) containing KCl concentrations ranging from 25 mM to 500 mM. Approximately 10

µL of each sample was loaded into disposable Tycho capillaries (cat. #TY-C001). Temperature was increased from 35 °C to 95 °C at a rate of 30 °C/min, while intrinsic tryptophan fluorescence was monitored at 330 nm and 350 nm. The fluorescence ratio (350/330 nm) was used to generate unfolding profiles, and inflection temperatures (T_i) were automatically determined using Tycho software. Each condition represents the average of three independent experiments.

2.6. Microscale Thermophoresis (MST)

Binding experiments were carried out on a Monolith NT.115 instrument (NanoTemper Technologies) using premium capillaries. Labeling of His-tagged CASQ2 was performed with the RED-tris-NTA 2nd Generation labeling kit (cat. #MO-L018) according to the manufacturer's instructions. Labeled protein was diluted in PBS-T buffer, and samples were incubated at room temperature for 30 minutes to reach equilibrium prior to measurement. All experiments were conducted at 25 °C, and data were analyzed using the MO.Affinity Analysis software.

2.7. Dynamic Light Scattering (DLS) and Zeta Potential Measurements

Particle size distributions were determined using a NANOTRAC Flex instrument (Microtrac), which employs dynamic light scattering with a flexible probe in batch mode. CASQ2 samples were diluted in 20 mM HEPES (pH 7.3) containing either 50 mM or 150 mM KCl to a final concentration of 2.5 µM. A blank buffer measurement was collected before each run. CASQ2 particle size was then recorded after stepwise additions of $CaCl_2$, with the sample continuously mixed by a piston during acquisition. At least six independent readings were taken per each $CaCl_2$ concentration.

ζ-potential was determined using a STABINO ZETA analyzer (Microtrac). CASQ2 samples (2.5 μM) were prepared in 20 mM HEPES (pH 7.3) with varying KCl and $CaCl_2$ concentrations. For ionic strength analysis, independent samples were prepared for each condition. A piston with a 200 nm cutoff was used for these measurements.

3. Results module 1

3.1. K^+ ions support CASQ2 folding and hydrophobic collapse

In the cytosol of cardiomyocytes, the physiological concentration of K^+ is around 120-225 mM range [95], instead the concentration of the second most abundant monovalent cation Na^+ is in the 5-15 mM range[95]. However, as the concentration of monovalent cations in the jSR compartment is not known, we inspected the compaction of CASQ2 tertiary structure with mass photometry (MP) in presence of varying KCl concentrations, at first in absence of Ca^{2+}. Rising potassium concentrations, particularly within the 150–200 mM range, induce a noticeable compaction of the CASQ2 monomer, resulting in a reduction of its apparent molecular volume by approximately 6.4 ± 2.4 kDa compared to the more extended conformation observed at 25 mM KCl (Figure 19).

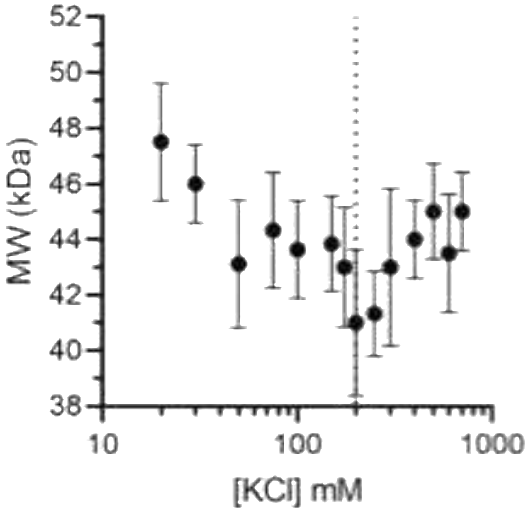

Figure 19: CASQ2 size distribution at varying KCl concentrations as determined by Mass Photometry.

Interestingly, the inverse linear correlation between ionic strength and the hydrodynamic size of CASQ2 does not persist across all KCl concentrations. Above 200 mM, the apparent molecular volume begins to increase with rising ionic strength. This observation suggests that at higher salt levels, excessive screening of negatively charged residues may disrupt the native conformation of CASQ2 and/or alter its surrounding hydration layer, ultimately affecting its apparent volume in solution.

To further investigate these ionic strength–dependent conformational changes we employed thermal denaturation assay to inspect CASQ2 thermal stability, at different KCl concentrations (Figures 20, 21).

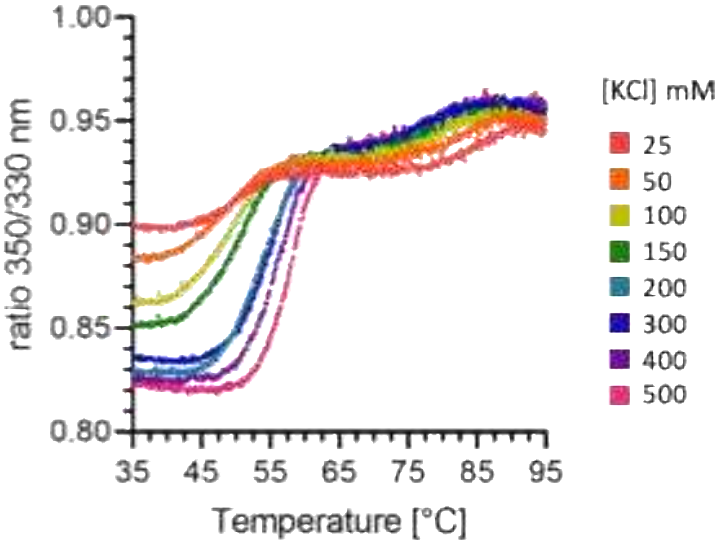

Figure 20: Thermal denaturation curves for CASQ2 samples under varying KCl concentrations, from which the melting temperatures are extrapolated. Data are presented as mean from three independent measurements.

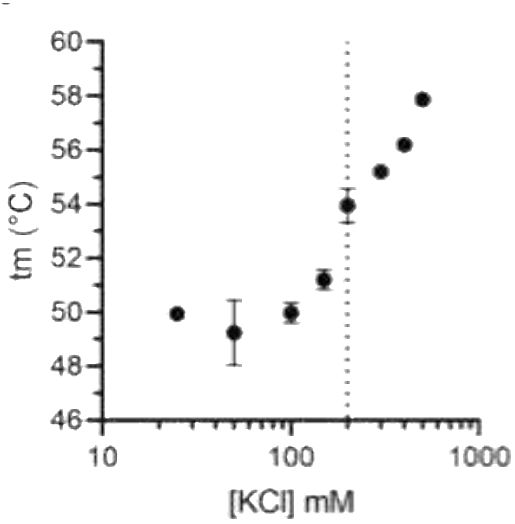

Figure 21: The value of CASQ2 melting temperature increases rapidly with KCl concentrations up to 200 mM (dotted line). At concentrations higher than 200 mM KCl the melting temperature increases further because the formation of a thicker ionic shell around CASQ2 monomers.

The thermal stability of CASQ2 shows a progressive increase as KCl concentration rises from 25 mM to 200 mM. Notably, an inflection point is observed at 200 mM KCl, where the T_m is approximately 4 °C higher than that measured at 50 mM KCl. Overall, the reduction in apparent molecular volume detected by mass photometry (MP), together with the observed thermal stabilization, indicates that K^+ ions promote the formation of a more compact and stable CASQ2 tertiary structure, with the most pronounced effect occurring at 200 mM KCl.

Both the apparent molecular volume of CASQ2 and the degree of hydrophobic core compaction increase when the ionic strength exceeds 200 mM KCl. To clarify these seemingly divergent observations, we analyzed the ζ-potential of CASQ2 to evaluate how

the protein's solvation shell responds to varying KCl concentrations (Figure 22).

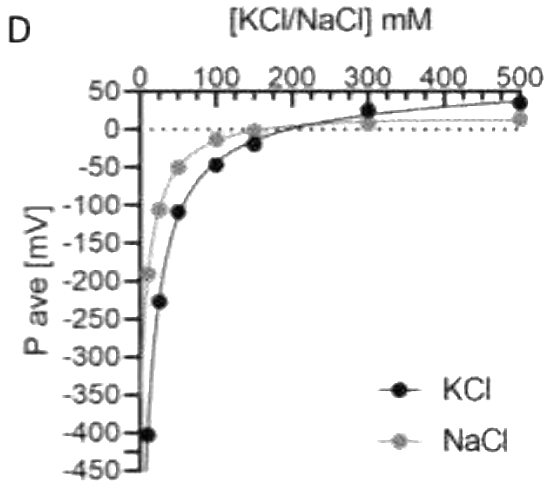

Figure 22: ζ-potential measurements of CASQ2 at increasing KCl and NaCl concentrations show a progressive reduction in surface charge. Data are presented as mean ±SD from three independent measurements.

Remarkably, 200 mM KCl again represents a critical condition: at which CASQ2 surface charges become effectively neutralized (ζ-potential approaches 0 mV). At 10 mM KCl, CASQ2 exhibits a highly negative ζ-potential of approximately –400 mV, whereas at near-physiological ionic strength (150 mM KCl), this value decreases to –19 mV. Functionally, this suggests that under cellular conditions, even in the absence of Ca^{2+}, most of CASQ2's negative surface charges are screened, thereby facilitating hydrophobic collapse and the formation of a compact tertiary structure.

3.2. CASQ2 forms Ca^{2+}-independent dimers

ζ-potential measurements indicate that at physiological K^+ concentrations of 140 – 220 mM K^+, the strong negative charges of CASQ2 are largely shielded, reducing both local and long-range electrostatic repulsion. Under these conditions, charge screening by K^+ ions may promote inter-monomer interactions even in the absence of Ca^{2+}. Supporting this idea, MP analysis revealed that in 150-200 mM KCl, CASQ2 can form stable dimers at very low protein concentrations (Figure 23). Below this ionic strength range, incomplete charge neutralization likely enhances non-specific electrostatic interactions between oppositely charged surface patches, whereas higher K^+ concentrations exert no further effect on dimer stability. These findings suggest that K^+ alone may support the formation of a Ca^{2+}-independent CASQ2 dimeric state.

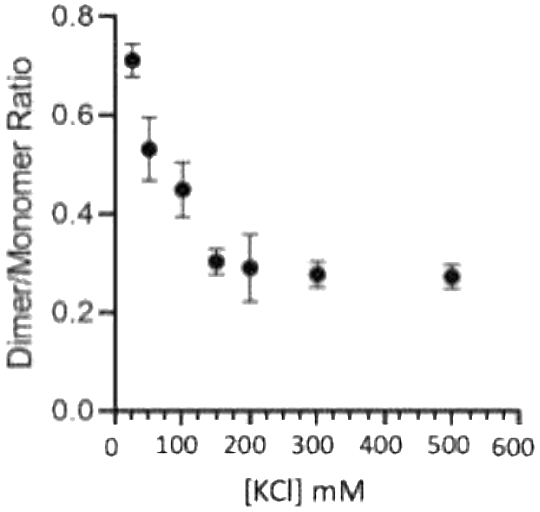

Figure 23: Quantification of dimer-to-monomer ration from MP across increasing KCl concentrations.

We next analysed the quaternary state of CASQ2 in varying ionic strength conditions at higher protein concentration (45 µM) than in MP through size-exclusion chromatography (SEC) (Figure 24).

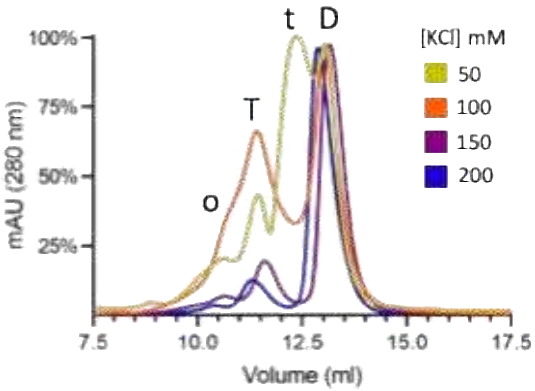

Figure 24: SEC analysis of CASQ2 (45 µM) (Superdex 200 10/300 GL column) at increasing KCl concentrations. The identity of elution peaks to dimer (D), trimers (t), tetramers (T) and oligomers (o), is based on the expected molecular weight of the eluted species, calculated from the column size calibration curve.

These experiments demonstrate the presence of several Ca^{2+}-independent oligomeric forms of CASQ2, including dimers, trimers, and tetramers, each displaying a distinct response to ionic strength. The dimeric assembly remains stable even at 200 mM KCl, whereas higher-order oligomers are progressively destabilized as salt concentration increases, supporting the notion that these supra-dimeric species are mainly stabilized by electrostatic interactions.

The properties of CASQ2 self-assembly were further dissected by MST (Figure 25).

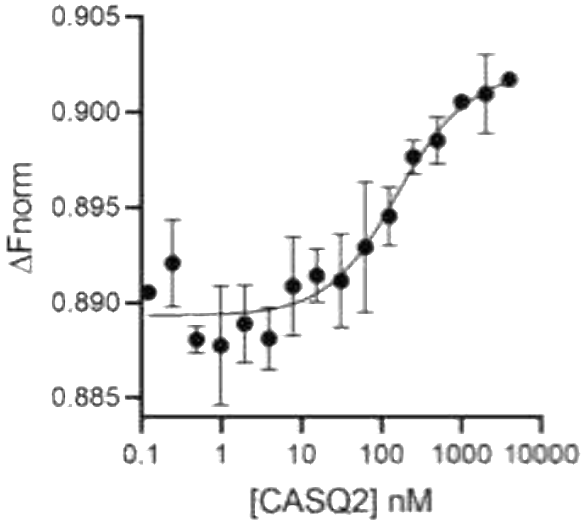

Figure 25: MST analysis of concentration-dependent self-association of CASQ2 in PBS buffer (137 mM NaCl and 2,7 mM KCl).

The gradual nature of the signal shift argues against a single, binary dimerization event mediated by specific binding interfaces. Instead, it indicates that CASQ2 self-association involves multiple weak and partially overlapping interaction sites. This process likely occurs as a continuous series of additive inter-monomer contacts rather than through distinct, stepwise binding events, with the likelihood of productive associations increasing almost linearly with protein concentration.

3.3. The CASQ2 Ca^{2+}-independent oligomers compete with Ca^{2+}-driven quaternary assemblies

The discovery of a Ca^{2+}-independent, electrostatic stable dimeric form led us to examine whether Ca^{2+}, and thus the Ca^{2+}-dependent polymerization, competes with or instead relies on the formation of

such assemblies. We added increasing amounts of Ca^{2+} to 10 nM CASQ2 in a 50 mM KCl buffer and measured the oligomeric state of the protein by MP. Ca^{2+} shifted the equilibrium toward dimerization (Figure 26). The effect became particularly evident at 20 mM and higher Ca^{2+} concentrations, where the proportion of the dimer exceeds that of the monomer.

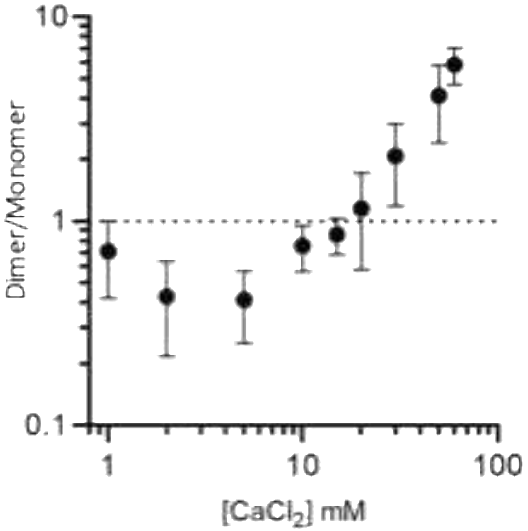

Figure 26: Dimer-to-monomer ratio of 10 nM CASQ2 as a function of increasing Ca^{2+} concentrations as measured by MP. Data are presented as mean ± SD from at least two independent measurements performed with the same sample preparation and diluted in the same buffer.

At 150 mM KCl however, where electrostatic interactions are screened, the positive effect of Ca^{2+} on dimer formation became less

evident (Figure 27), indicating a competition between electrostatically supported and Ca^{2+}-dependent assemblies.

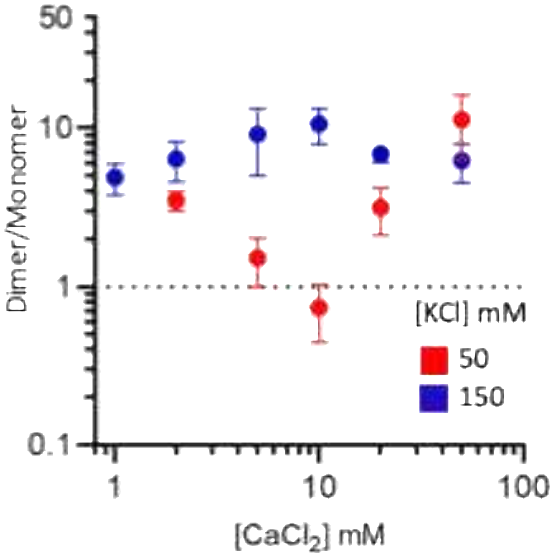

Figure 27: Dimer-to-monomer ratio of 25 nM CASQ2 as a function of increasing Ca^{2+} concentrations, in 50 and 150 mM KCl as measured by MP. Data are presented as mean ± SD from at least two independent measurements performed with the same sample preparation and diluted in the same buffer.

Complementary SEC analyses confirmed that, under physiological ionic conditions, Ca^{2+} promotes higher-order oligomerization, while suppressing non-specific electrostatic aggregates such as trimers (Figure 28). Altogether, these results demonstrate that Ca^{2+}-dependent polymerization does not build upon pre-existing electrostatic assemblies, but rather occurs in competition with them.

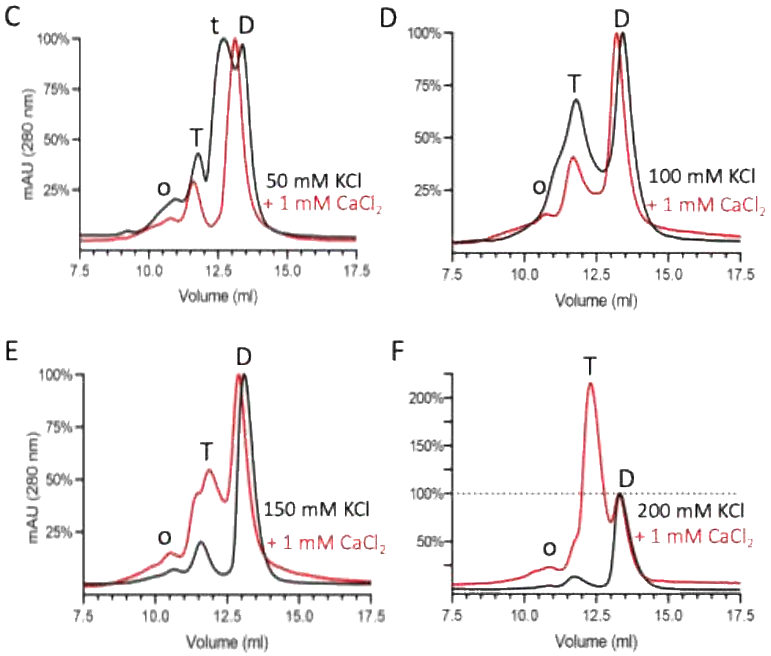

Figure 28: SEC chromatograms of CASQ2 injected at 2 mg/ml in buffer containing either 50, 100, 150 or 200 mM KCl (black chromatograms). After 1 h incubation in each ionic condition with 1 mM $CaCl_2$, the sample was injected at 2 mg/ml into the SEC running in the respective buffer (containing either 50, 100, 150 or 200 mM KCl and 1 mM $CaCl_2$, red chromatograms). The curves were normalized to the height of the peak of the dimer to facilitate comparison across species: dimer (D), trimer (t), tetramer (T) and oligomer (o).

3.4. A complex interplay between K^+-driven and Ca^{2+}-specific effects shapes CASQ2 polymerization

To investigate how electrostatics contribute to Ca^{2+}- dependent CASQ2 polymerization, we examined the turbidity response of the protein to Ca^{2+} at two different ionic strengths, 10 and 50 mM KCl (Figure 29). Increasing the salt concentration shifted the onset of polymerization to lower Ca^{2+} levels: 0.1 mM in 50 mM KCl vs 0,4 mM in 10 mM KCl, indicating that K^+ ions sensitize CASQ2 to Ca^{2+}. This effect likely reflets the combined action of K^+ and Ca^{2+} in promoting compaction of the tertiary structure (and thus the ability to chelate Ca^{2+} ions), together with the ability of both K^+ and Ca^{2+} cations to reduce long-range electrostatic repulsion between monomers, thereby accelerating the rate at which Ca^{2+}-mediated assemblies form (data not shown).

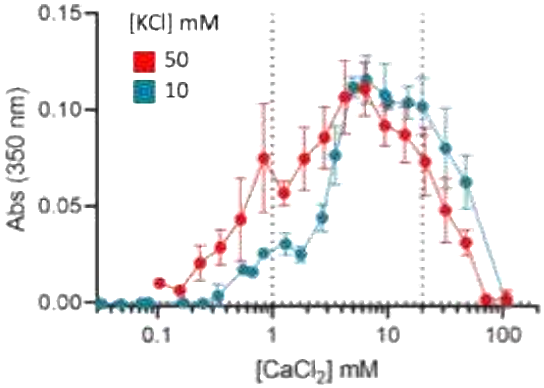

Figure 29: Turbidimetric measurements of CASQ2 samples after 40 minutes since the exposure to varying concentrations of Ca2+ (0,01-100 mM) in buffers containing 10 mM (red) and 50 mM (blue) KCl. Data are presented as mean ± SD from three independent experiments. The estimates for the physiological concentration of free (1 mM) and total (20 mM) Ca^{2+} ions in the jSR are indicated by dotted lines.

At higher than 5 mM Ca^{2+} concentration, turbidity decreases in both 50 mM KCl and 10 mM KCl conditions, suggesting that excessive Ca^{2+} ions can destabilize large CASQ2 polymers under conditions where electrostatic charge is heavily compensated. Our ζ-potential measurements support this interpretation (Figure 30). Similarly to K^+, progressive Ca^{2+} binding first neutralizes and then overcompensates CASQ2's negative surface charge, leading to charge reversal, suggesting that Ca^{2+}-dependent polymerization is strongly governed by electrostatics. Ca^{2+} is markedly more effective than K^+ in neutralizing the protein surface charge, probably this is mainly due to its divalency.

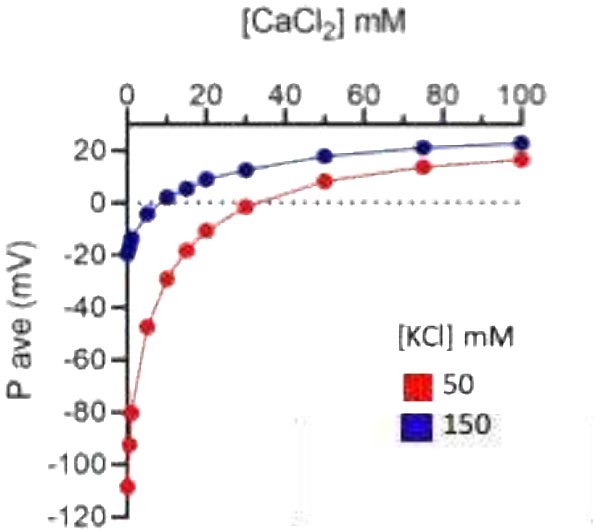

Figure 30: ζ-potential (expressed in mV) of CASQ2 as a function of $CaCl_2$ concentration. Data are presented as mean ± SD from at least three independent measurements. ζ-potential provides an estimate of the net surface charge of CASQ2 in a solution and therefore reflects the extent of electrostatic repulsion between protein particles.

3.5. CASQ2 polymerization is an ion-sensitive, Ca^{2+} triggered switch

Using a custom DLS method capable of analysing turbid samples, we found that in both 50 and 150 mM KCl, and in the absence of Ca^{2+}, CASQ2 exists as small oligomers (6-12 nm), with dimensions compatible with dimers, tetramers and possibly octamers (Figure 31A) . In each ionic condition, a defined Ca^{2+} threshold triggers an abrupt transition from these oligomers to much larger polymeric structures. The Ca^{2+} concentration at which this switch occurs depends on ionic strength: polymerization is induced at 0.5-1 mM Ca^{2+} in 50 mM KCl and at 5-10 mM Ca^{2+} in 150 mM KCl. This behaviour contradicts the linear, stepwise model of assembly till now hypothesized in literature [41]; while ionic strength tunes the sensitivity of CASQ2 to Ca^{2+}, CASQ2 itself acts as a Ca^{2+}-dependent binary switch between an oligomeric and a polymeric phase.

Additional experiments of thermal shift assays showed a sudden increase in thermal stability upon exposure to low-millimolar Ca^{2+}, consistent with a major rearrangement of the forces packing the protein's hydrophobic core in parallel with polymer formation (Figure 31B-D).

This transition, similarly to what occurs in DLS, occurs over a narrow Ca^{2+} range and is attenuated by increasing K^+ concentrations: in 1mM Ca^{2+} the melting temperature of CASQ2 is 8°C lower at 150 mM KCl relative to 50 mM KCl, and the effect disappears entirely at KCl concentrations ≥300 mM. Together, thermal shift and particle size-distribution indicate that CASQ2 polymerization is a highly cooperative process, possibly involving simultaneous engagement of multiple interaction interfaces in a tightly cross-linked polymeric network.

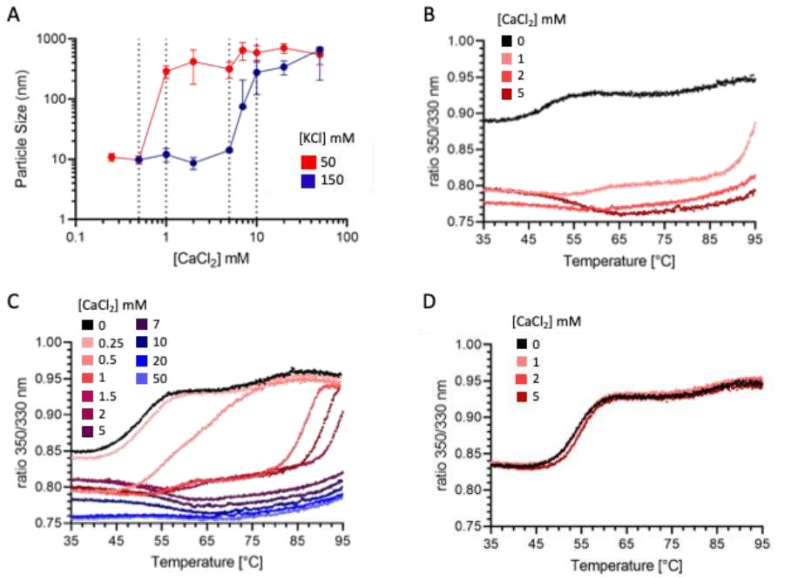

Figure 31: A) Average size of CASQ2 particles in solutions of varying Ca^{2+} and K^{+} concentrations, as determined by Dynamic Light Scattering (DLS). Data are presented as mean ± SD from at least three independent measurements. B-C-D) Thermal denaturation curves, monitored by intrinsic tryptophan fluorescence (350/320 nm ratio), for CASQ2 samples in varying $CaCl_2$ concentrations, and either 50 mM KCl, 150 mM KCl, or 300 mM KCl. Data are presented as mean from three independent measurements.

3.6. Mg^{2+} modulates Ca^{2+}-dependent polymerization

Recent work conducted by Titus and colleagues [40], challenges this Ca^{2+}-centric view. They showed that preincubating CASQ2 with Mg^{2+} modifies its subsequent response to Ca^{2+}, revealing kinetic and structural differences. Notably, these Mg^{2+}-dependent effects also distinguish WT CASQ2 from the dominant-negative K180R mutant,

highlighting Mg^{2+} as an influential modulator [40]. Together with the established regulatory role of Mg^{2+} in jSR, where it helps the stabilization of the closed state of RyR2 [105–107], these findings provide a strong rationale for investigating CASQ2 behavior in the presence of both divalent ions, Ca^{2+} and Mg^{2+}. Understanding how these two interact with CASQ2 is therefore essential to obtain a more complete picture of jSR Ca^{2+} handling under physiological and pathological conditions.

Starting from the notion that free Ca^{2+} in the jSR cyclically varies in the 0.3 to 1.7 mM range, while free Mg^{2+} remains stable in the 0.7-0.8 mM range, we examined how preincubation of CASQ2 with physiological levels of Mg^{2+} influences its subsequent response to Ca^{2+} [95].As we can understand from the turbidity response in Figure 32, preincubation with 2mM Mg^{2+} enhanced the amplitude of CASQ2 polymerization at low Ca^{2+} concentrations, while unexpectedly dampening the response when Ca^{2+} exceeded 4 mM.

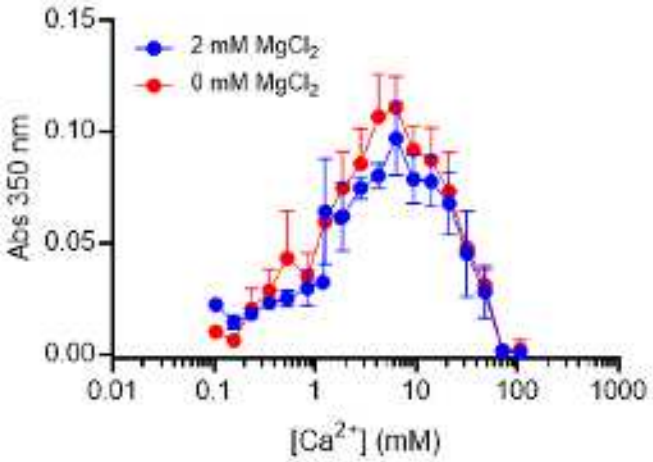

Figure 32: Turbidity response of CASQ2 to varying Ca^{2+} concentrations with (blue) or without (red) preincubation in 2 mM Mg^{2+}.

This dual action resembles the biphasic effect previously described for K^+, where moderate amounts facilitate Ca^{2+}-dependent assembly, but higher concentrations suppress it (Figure 29). To further explore this interplay, we monitored CASQ2 turbidity response at fixed Ca^{2+} concentration (5 mM) after preincubation with increasing Mg^{2+} levels (Figure 33).

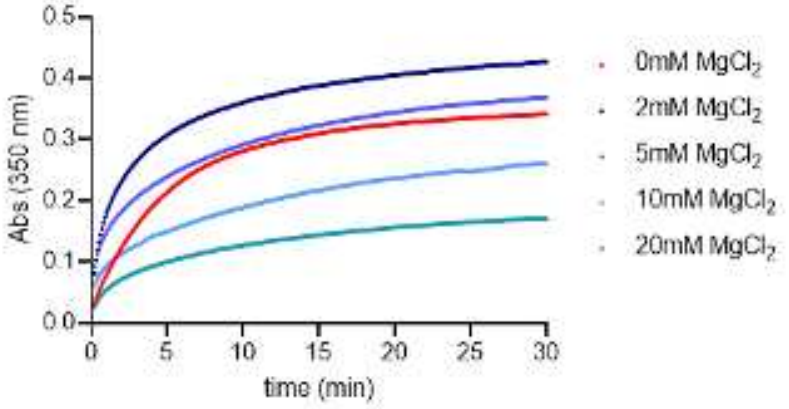

Figure 33: In 50 mM KCl, CASQ2 preincubation with varying concentrations of Mg^{2+} leads to either a reduced (for 5 to 10 mM Mg^{2+}) or emphasized (for Mg^{2+} concentrations below 5 mM) Ca^{2+}-dependent CASQ2 multimerization, highlighting the dual role of Mg^{2+} in regulation of Ca^{2+}-dependent polymerization of CASQ2

The result confirms the existence of an optimal Ca^{2+} /Mg^{2+} ratio that favors polymerization: 2-5 mM Mg^{2+} concentrations produced the strongest enhancement of CASQ2 response to 5 mM Ca^{2+}, despite inducing only minimal turbidity on their own (data not shown), whereas Mg^{2+} levels higher than 5 mM shift the balance toward inhibition of CASQ2 Ca^{2+}-dependent polymerization.

We performed thermal denaturation assays to verify whether the presence of Mg^{2+} alters the properties of Ca^{2+}-dependent polymers previously described (Figure 31). CASQ2 was measured after

incubation with either 2 mM $MgCl_2$, 1 mM $CaCl_2$, or preincubation with 2 mm $MgCl_2$ followed by addition of 1 mM $CaCl_2$ (Figure 34).

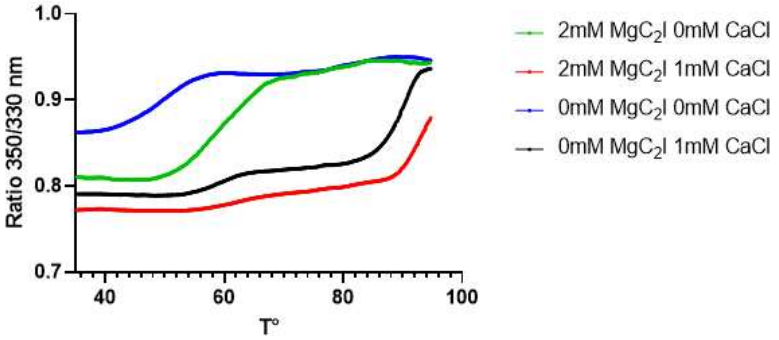

Figure 34: Thermal denaturation curves for CASQ2 either alone or preincubated with 2 mM Mg^{2+} or 1 mM Ca^{2+}.

The presence of 2 mM Mg^{2+} induces a substantial stabilization of the hydrophobic core packing, shifting the melting temperature by approximately 10°C. Still, this effect is significantly lower than that of Ca^{2+}. The presence of Mg^{2+} and Ca^{2+} leads to a cumulative stabilizing effect, with T_m higher than 90°C.

4. Results module 2

4.1. CASQ2 mutants: alteration in Ca^{2+}-dependent assembly and function

To gain a mechanistic insight into how mutations affect CASQ2 structure and quaternary assembly, we investigated a panel of disease-associated CASQ2 mutants through multiple biochemical and biophysical methods. More specifically, we combined thermal stability measurements, turbidity assays and analytical SEC as preliminary work to evaluate mutant-specific alterations. A total of eight CASQ2 mutants were studied in this preliminary work.

4.2. Thermal stability of CASQ2 mutants

To compare the thermal stability of CASQ2 mutants, thermal shift assays were employed. Four ionic conditions were tested: 0 or 2 mM Mg^{2+} in the presence or absence of 1 mM Ca^{2+}, in 150 mM KCl.

In the 150 mM KCl (Ca^{2+}- and Mg^{2+}-free) condition, the CASQ2 mutant panel separates into two groups with a WT-like behaviour or markedly non-canonical profiles. Some CASQ2 mutants ($CASQ2^{R33Q}$, $CASQ2^{L167H}$, $CASQ2^{D351G}$ and $CASQ2^{K180R}$) feature a delayed thermal denaturation and a lower 350/330 nm fluorescence ratio, suggesting a more compact structure in the native state (Figure 35A). A second subset of CASQ2 mutants ($CASQ2^{G332R}$, $CASQ2^{S173I}$, $CASQ2^{D325E}$ and $CASQ2^{R251H}$) is clearly mostly unfolded in absence of divalent cations (Figure 35B).

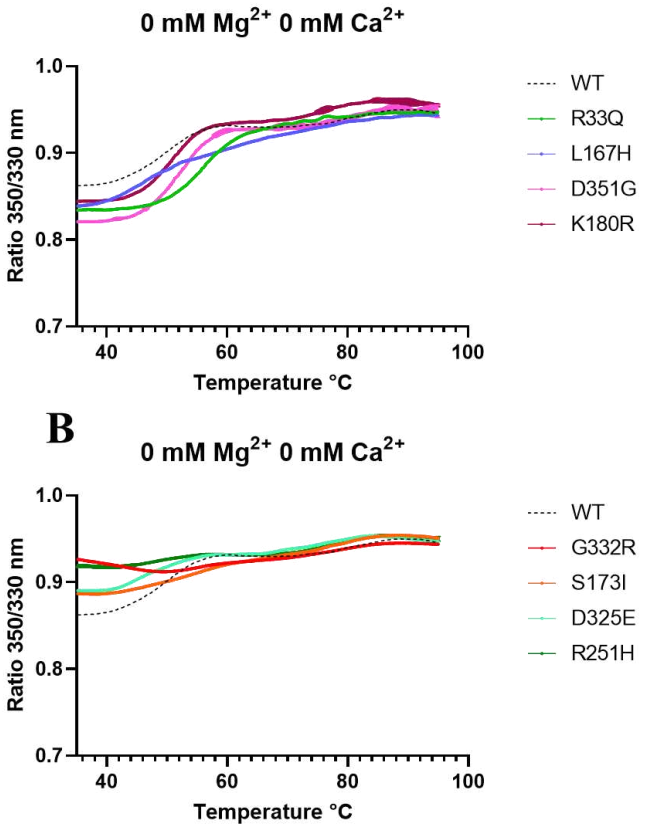

Figure 35: Thermal denaturation curves for CASQ2^{WT} and CASQ2 mutants in 0 mM Mg^{2+} 0 mM Ca^{2+} condition. A) CASQ2 mutants showing enhanced thermal stability with respect to the CASQ2^{WT}. B) CASQ2 mutants showing lower thermal stability with respect to the CASQ2^{WT}.

In presence of 1 mM Ca^{2+}(Figure 36) the CASQ2^{WT} profile has a pronounced late transition, consistent with a more stable conformation state triggered by Ca^{2+} (see Figure 34). All CASQ2 mutants exhibit an earlier large shift in the 350/330 ratio, particularly CASQ2^{G332R},

$CASQ2^{S173I}$ and $CASQ2^{L167H}$ which display a markedly reduced cooperativity of the denaturation curve compared to $CASQ2^{WT}$, suggesting a reduced thermal stability. Notably, for $CASQ2^{K180R}$, $CASQ2^{D351G}$ and $CASQ2^{R251H}$ mutants, the initial 350/330 baseline is lower than $CASQ2^{WT}$, compatible with a more compact structure in the tested condition.

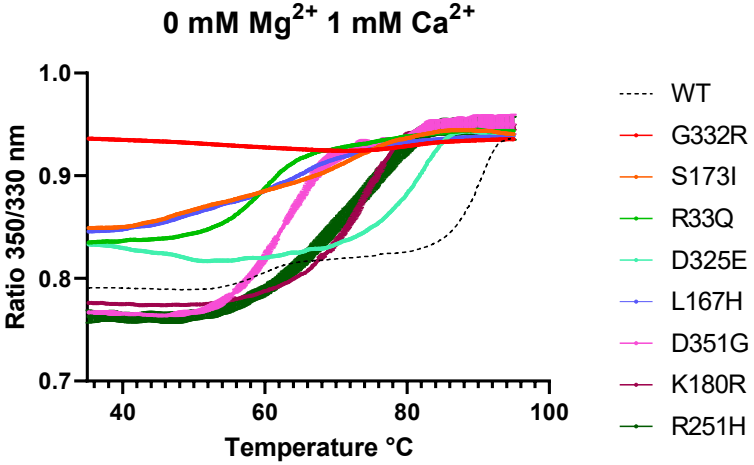

Figure 36: Thermal denaturation curves for $CASQ2^{WT}$ and CASQ2 mutants in 0 mM Mg^{2+} 1 mM Ca^{2+} condition. The line of $CASQ2^{WT}$ is shown as dashed line, while CASQ2 mutants are reported as solid traces.

In the condition 150 mM KCl 2 mM Mg^{2+} 0 mM Ca^{2+}, the difference between two types of CASQ2 mutants is evident at most. In Figure 37A are reported CASQ2 mutants that are less stable then or equally stable as the WT protein ($CASQ2^{G332R}$, $CASQ2^{S173I}$, $CASQ2^{R33Q}$, $CASQ2^{D325E}$, $CASQ2^{L167H}$ and $CASQ2^{R251H}$). Instead, $CASQ2^{D351G}$ and $CASQ2^{K180R}$ display substantial rightward shifts of the melting temperature (Figure 37B), underscoring that Mg^{2+} alone can stabilize the structure of the mutated protein more than the WT one.

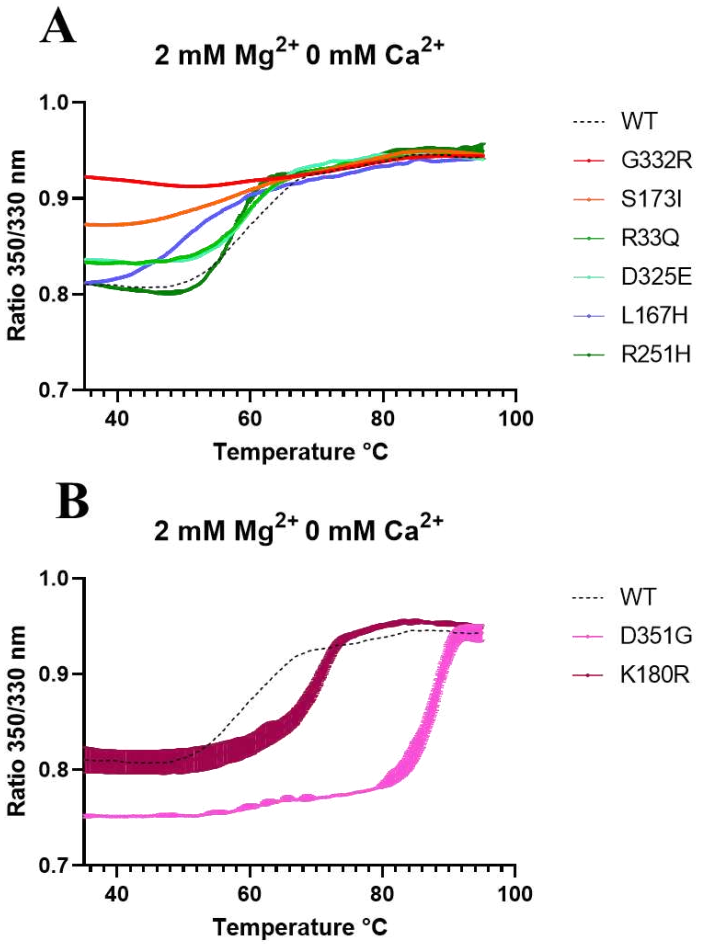

Figure 37: Thermal denaturation curves for $CASQ2^{WT}$ and CASQ2 mutants in 2 mM Mg^{2+} 0 mM Ca^{2+} condition. A) CASQ2 mutants showing lower thermal stability with respect to the $CASQ2^{WT}$. B) CASQ2 mutants showing enhanced thermal stability with respect to the $CASQ2^{WT}$.

When 2 mM Mg^{2+} is added in the presence of 1 mM Ca^{2+} (Figure 38), many traces (i.e. $CASQ2^{D351G}$, $CASQ2^{K180R}$, $CASQ2^{R251H}$ and $CASQ2^{D325E}$) on the other hand converge toward a more WT-like transitions, suggesting that the presence of Mg^{2+} can at least partially sustain the polymeric-associated packing of the hydrophobic core. However, a subset of CASQ2 mutants ($CASQ2^{L167H}$, $CASQ2^{R33Q}$, $CASQ2^{S173I}$ and $CASQ2^{G332R}$) still features a visible destabilization in the tested condition.

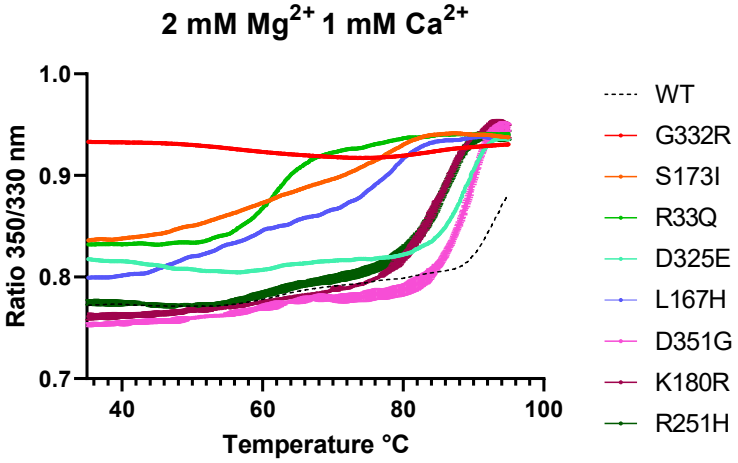

Figure 38: Thermal denaturation curves for $CASQ2^{WT}$ and CASQ2 mutants in 2 mM Mg^{2+} 1 mM Ca^{2+} condition.

4.3. Altered Ca^{2+}-dependent polymerization of CASQ2 mutants

We then investigated the impact of CASQ2 mutations on the kinetics and magnitude of Ca^{2+}-dependent polymerization via turbidity measurements: we compared the kinetics of formation of light-scattering bodies in solution between $CASQ2^{WT}$ and mutant proteins in 50 mM KCl, again under different ionic conditions: 1 mM Ca^{2+}, 2mM Mg^{2+}, and 2 mM Mg^{2+} followed by 1 mM Ca^{2+} addition.

Results from turbidity experiments in the 1 mM Ca^{2+}, 50 mM KCl condition are presented in Figure 39. All CASQ2 mutants exhibit lower turbidity response to $Ca2^{+}$ with respect to $CASQ2^{WT}$. A subset of CASQ2 mutants ($CASQ2^{K180R}$, $CASQ2^{R251H}$ and $CASQ2^{L167H}$) present a moderate response to Ca^{2+}, presenting an intermediate plateau around 0.2 mAU. All the other CASQ2 mutants tested instead, show a stronger reduction in their ability to form light-scattering polymers in response to Ca^{2+}, with $CASQ2^{R33Q}$ unable to show any detectable variation from the baseline.

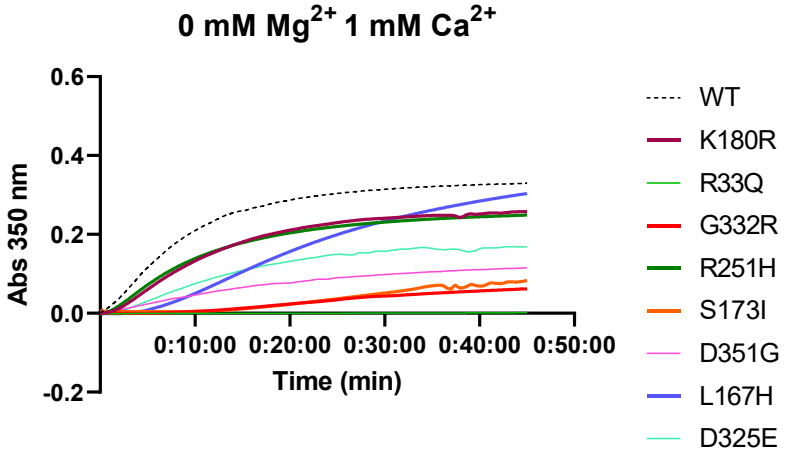

Figure 39: Turbidimetric measurements of CASQ2 mutants in presence of 0 mM Mg^{2+} 1 mM Ca^{2+}. Data are presented as mean from three independent experiments.

In presence of 2 mM Mg^{2+}, 50 mM KCl (Figure 40), $CASQ2^{WT}$, as reported in Module 1, is still capable of developing a clear turbidity increase over time. On the other hand, all CASQ2 mutants show a reduced response when compared to $CASQ2^{WT}$. $CASQ2^{K180R}$, $CASQ2^{R33Q}$, $CASQ2^{G332R}$, $CASQ2^{S173I}$, $CASQ2^{D351G}$ and $CASQ2^{D325E}$ remain close to the baseline. Instead, the only mutants exhibiting a detectable increase in turbidity, despite lower then $CASQ2^{WT}$, are $CASQ2^{L167H}$ and $CASQ2^{R251H}$. No mutant exhibited a higher turbidity response to Mg^{2+} with respect to $CASQ2^{WT}$.

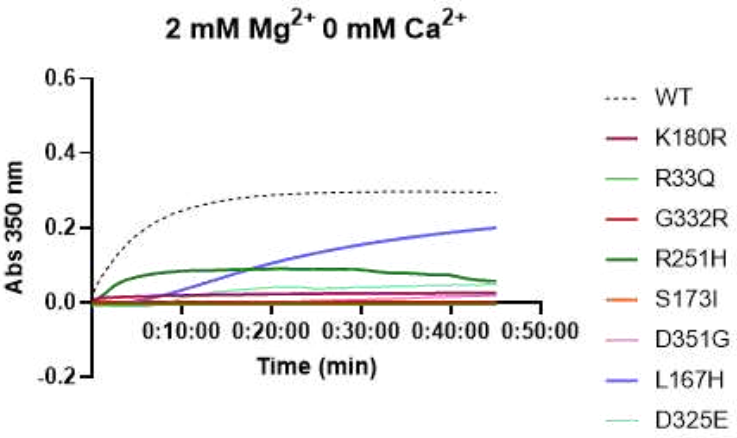

Figure 40: Turbidimetric measurements of CASQ2 mutants in presence of 2 mM Mg^{2+} 0 mM Ca^{2+}. Data are presented as mean from three independent experiments.

Under the 2 mM Mg^{2+} 1 mM Ca^{2+} condition (Figure 41), the panel of CASQ2 mutants separates into three clearly distinct groups. $CASQ2^{K180R}$ presents the largest increase in turbidity. The mutant $CASQ2^{R251H}$ instead, shows a response identical to $CASQ2^{WT}$, suggesting a preserved Ca^{2+}-dependent polymerization ability. The other CASQ2 mutants ($CASQ2^{R33Q}$, $CASQ2^{G332R}$, $CASQ2^{S173I}$ and $CASQ2^{D351G}$) show markedly reduced turbidity, with $CASQ2^{L167H}$ and $CASQ2^{D325E}$ remaining at baseline throughout the experimental time course.

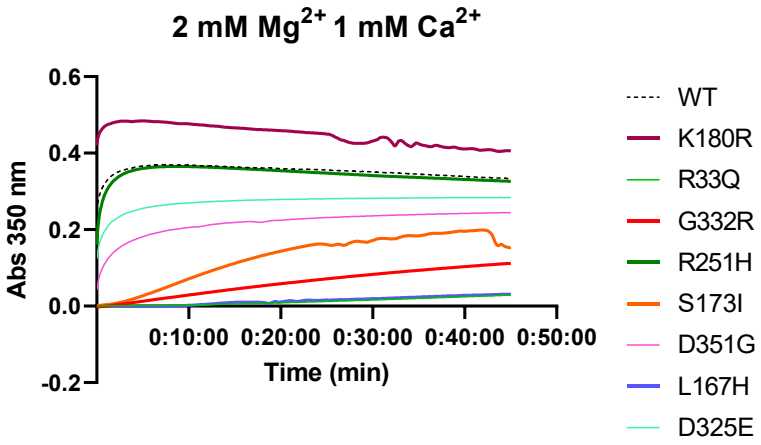

Figure 41: Turbidimetric measurements of CASQ2 mutants in presence of 2 mM Mg^{2+} 1 mM Ca^{2+}. Data are presented as mean from three independent experiments.

4.4. Oligomeric state of CASQ2 mutants assessed by size-exclusion chromatography

We performed SEC analyses of CASQ2 mutants to assess whether mutations also affect the relative proportions among dimeric, trimeric, and tetrameric species with respect to the WT (Figure 28). To facilitate a direct visual comparison of SEC profiles among CASQ2 variants, the chromatograms were normalized relative to the dimer peak (assigned to the species eluting at 13 ml). In absence of divalent ions, $CASQ2^{WT}$ features a dominant dimer peak along with trimer and tetramer species. A group of CASQ2 mutants (Figure 42A: $CASQ2^{G332R}$, $CASQ2^{R251H}$ and $CASQ2^{D325E}$) shows a marked attenuation of the trimeric and tetrameric species abundancies. $CASQ2^{S173I}$, shows a trimer-to-dimer ratio almost identical to the CASQ2WT, except that the tetramer shoulder is markedly reduced, which suggests a lower stability for of higher-order assemblies than the electrostatically induced, aspecific trimer (Figure 42B). $CASQ2^{L167H}$ (Figure 42C) stands out for its heterogeneous profile, characterized by broadened features across the pre-dimer region and a reproducible signal close to the void volume, consistent with the presence of very large species or aggregates, already in the absence of divalent ions. $CASQ2^{K180R}$ (Figure 42D) mutant overall has the most similar chromatogram when compared to $CASQ2^{WT}$, differing only for a slightly decrease in the trimer and tetramer region. The most atypical behaviour is exhibited by $CASQ2^{D351G}$ (Figure 42E), as the trimeric species is more abundant than the dimeric one. $CASQ2^{R33Q}$ precipitated prior to injection in the experimental buffer.

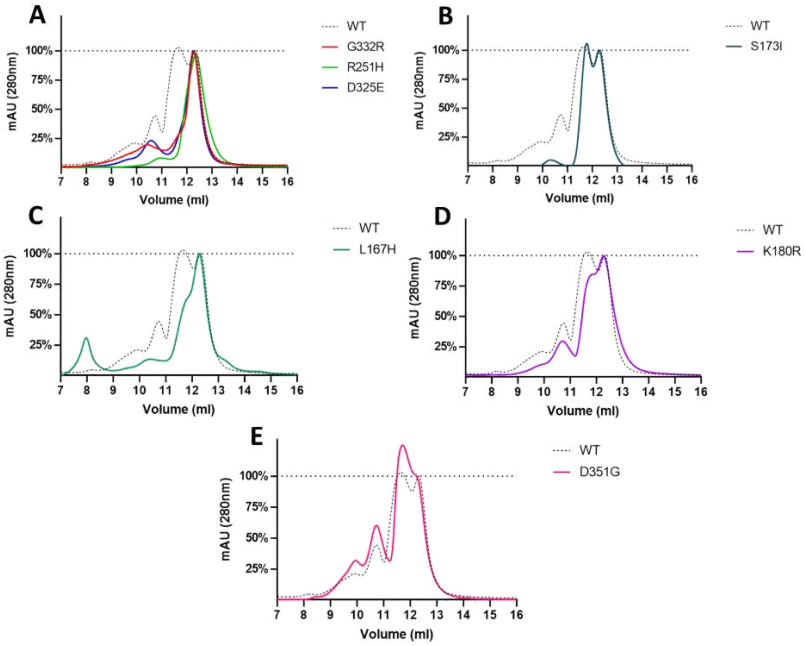

Figure 42: SEC chromatograms of CASQ2 mutants injected at 2 mg/ml in 0 mM Mg^{2+} 0 mM Ca^{2+} condition. The curves were normalized to the height of the peak of the dimer to facilitate comparison across species. $CASQ2^{WT}$ is represented with dashed line, CASQ2 mutants are represented with solid lines.

After incubation in 1 mM Ca^{2+} the distribution of CASQ2 species shifts towards earlier-eluting assemblies (Figure 43). The same subset of CASQ2 mutants that eluted mostly as dimeric species in absence of divalent cations, ($CASQ2^{D325E}$, $CASQ2^{R251H}$ and $CASQ2^{G332R}$), also in 1 mM Ca^{2+} shows substantially a dimer peak with a strongly reduced abundance of the trimeric and tetrameric species (Figure 43A). The $CASQ2^{K180R}$ mutants, which ability to trimerize and tetramerize was only slightly affected in absence of divalent ions, shows a marked

reduction of supra-dimeric species when Ca^{2+} is present in solution (Figure 43A). The propensity of the $CASQ2^{D351G}$ mutant to form electrostatic assemblies, detected in Figure 42E, is reduced by the presence of Ca^{2+}, up to the point that the protein almost uniquely populates the dimeric state (Figure 43B). On the contrary, the elution profile of the $CASQ2^{S173I}$ protein remains unvaried by the presence of Ca^{2+} (Figure 43C), hence characterized by the absence of supra-trimeric species, and a relative higher abundance of the trimer with respect to $CASQ2^{WT}$. In line with the chromatogram profile in absence of divalent ions, $CASQ2^{L167H}$ (Figure 43D), features an aggregation-prone behavior, with the largest species eluting soon after the void volume.

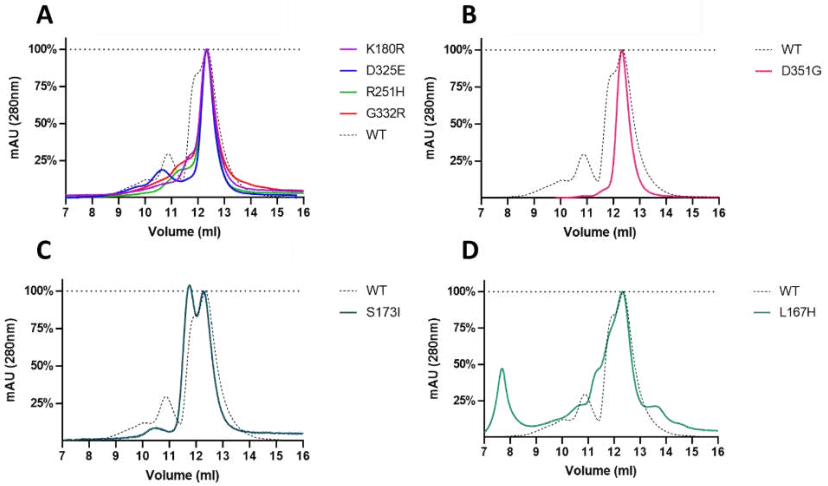

Figure 43: SEC chromatograms of CASQ2 mutants injected at 2 mg/ml in 0 mM Mg^{2+} 1 mM Ca^{2+} condition. The curves were normalized to the height of the peak of the dimer to facilitate comparison across species. $CASQ2^{WT}$ is represented with dashed line, CASQ2 mutants are represented with solid lines.

The third condition tested, i.e. after incubation with 2 mM Mg^{2+} in 50 mM KCl for 45 minutes, additional shifts in the distribution of CASQ2 quaternary states emerges (Figure 44). The distribution of $CASQ2^{WT}$ in presence of 2 mM Mg^{2+} closely matches the divalent-free condition, with a dominant dimer peak and a trimer-like structure of comparable relative amplitude (Figure 44A). This similarity indicates that Mg^{2+} alone does not markedly alter the $CASQ2^{WT}$ assembly equilibrium, so the landscape is largely comparable to the basal condition.

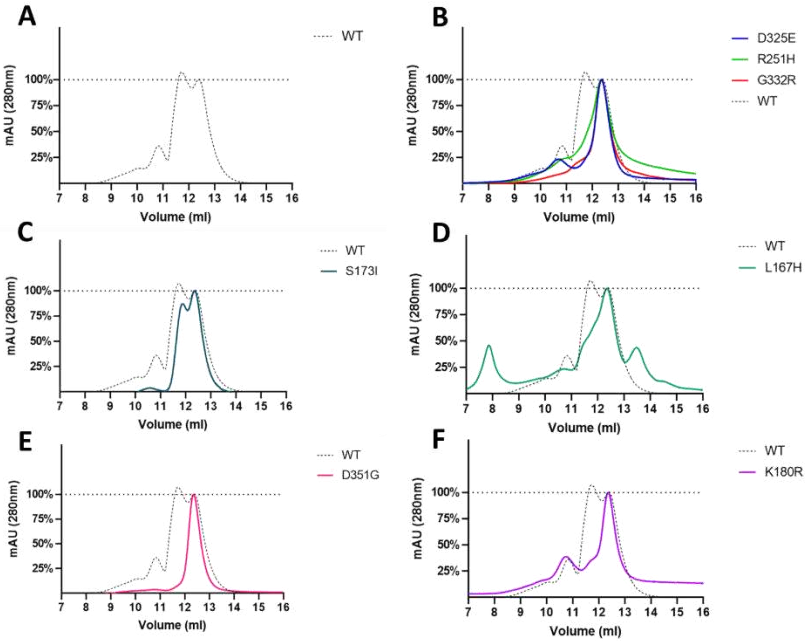

Figure 44: SEC chromatograms of CASQ2 mutants injected at 2 mg/ml in 2 mM Mg^{2+} 0 mM Ca^{2+} condition. The curves were normalized to the height of the peak of the dimer to facilitate comparison across species. $CASQ2^{WT}$ is represented with dashed line, CASQ2 mutants are represented with solid lines.

Once again, CASQ2^{D325E}, CASQ2^{R251H} and CASQ2^{G332R} constitute a unique group, where the propensity of the protein to form electrostatic trimers is inhibited, following the same trend shown in absence of divalent ions (Figure 44B). Also, the profile of CASQ2^{S173I} is unvaried by the presence of Mg^{2+} (Figure 44C). As in all other conditions tested, CASQ2^{L167H} (Figure 44D) retains a markedly heterogeneous chromatographic profile, and shows consistently the very large species close to the void volume. Instead, the CASQ2^{D351G} (Figure 44E), shows a notable difference from the Ca^{2+}/Mg^{2+}-free condition, but a strong similarity to the 1 mM Ca^{2+} one: as the protein almost only falls into a dimeric state. The CASQ2^{K180R} mutant (Figure 44F), as in other conditions, shows a loss in the trimer-like structure with respect to the CASQ2^{WT} protein, and retained ability to form tetramers in presence of Mg^{2+}.

4.5. Discussion: CASQ2 mutants across different ionic conditions

Taken together, the thermal stability, turbidity and SEC datasets indicate that CASQ2 mutants reshape the ion-dependent equilibrium of CASQ2 assemblies in a way that is strongly dependent on the ionic environment. In the baseline condition (50 mM KCl, 0 mM Mg^{2+}, 0 mM Ca^{2+}), SEC profiles of $CASQ2^{G332R}$, $CASQ2^{R251H}$ and $CASQ2^{D325E}$ show a reduced abundance of trimer- and tetramer-like structures compared to $CASQ2^{WT}$. $CASQ2^{K180R}$ and $CASQ2^{S173I}$ overall feature a reduced stability of higher-order assemblies. This baseline condition also highlights mutation-specific extremes, with the example of $CASQ2^{L167H}$ which exhibits here and in all the other conditions, an heterogeneous chromatographic distribution, with species eluting close to the void volume. On the other hand, $CASQ2^{D351G}$ shows the most atypical behaviour in this baseline condition, with an accentuated trimer-like structure, but a completely different profile, more comparable to the dimer peak, when exposed either to Ca^{2+} or Mg^{2+}.

When 2 mM Mg^{2+} is introduced, the $CASQ2^{WT}$ and also CASQ2 mutants (except for $CASQ2^{D351G}$ as discussed above) chromatograms remain largely comparable to the divalent-free condition. On the other hand, thermal shift experiments accentuate the differences among CASQ2 mutants. Most of them remain close to $CASQ2^{WT}$ trajectory, except for $CASQ2^{D351G}$ and $CASQ2^{K180R}$ showing a pronounced stabilization, supporting the fact that Mg^{2+} can differentially stabilize specific mutant conformations even in the absence of Ca^{2+}. Consistently, turbidity measurements performed under this condition show that all CASQ2 mutants exhibit a reduced response compared to $CASQ2^{WT}$.

In 0 mM Mg^{2+} 1 mM Ca^{2+} condition, $CASQ2^{WT}$ display the expected stabilizing effect in its thermal profile. In contrast, all CASQ2 mutants show deviation from $CASQ2^{WT}$, with a markedly altered transition

shape, and loss of cooperative conformational rearrangement upon heating, indicating that Ca^{2+} is not able to fully restore the thermal stability across the mutant panel. This trend is parallel in turbidity experiments, where all CASQ2 mutants exhibit a lower Ca^{2+}-dependent light scattering response than $CASQ2^{WT}$. Importantly, SEC profiles indicate that in 1 mM Ca^{2+} condition several mutants ($CASQ2^{D325E}$, $CASQ2^{R251H}$, $CASQ2^{G332R}$ and $CASQ2^{K180R}$) remain largely dimer-dominates, closely resembling their behaviour in the 2 mM Mg^{2+} condition, whereas $CASQ2^{S173I}$ consistently preserves the trimer-like population and $CASQ2^{L167H}$ retains its classical heterogeneous profile.

The last combined condition (2 mM Mg^{2+} 1 mM Ca^{2+}) tested only in thermal shift assays and turbidity, emerges as the environment in which mutants separated into distinct functional behaviour. The thermal shift profiles of $CASQ2^{D351G}$, $CASQ2^{K180R}$, $CASQ2^{R251H}$ and $CASQ2^{D325E}$ converge more closely toward a WT-like transition compared to the Ca^{2+}-only condition, suggesting that together the two divalent ions can partially stabilize the conformation of this subset of mutants. In contrast, $CASQ2^{L167H}$, $CASQ2^{R33Q}$, $CASQ2^{S173I}$ and $CASQ2^{G332R}$ retained visibly distinct thermal profiles, with their perturbation that are not compensated in this ionic condition. Turbidity experiments provide also a clear phenotypic separation: $CASQ2^{K180R}$ displays the largest turbidity increase, $CASQ2^{R251H}$ overlaps with $CASQ2^{WT}$ profile, while the other CASQ2 mutants have markedly reduced response, almost close to the baseline throughout the time course.

Taken together, these data support the view that CASQ2 pathogenic mutations do not simply abolish assembly but rather change the equilibrium of supra-molecular assemblies in an ion-dependent manner, generating distinct biochemical subgroups that can be resolved only by integrating many biochemical and biophysical approaches.

Chapter V: Conclusion and future perspectives

This work provides an overview of Ca^{2+}-handling dysfunction at the jSR, by integrating ex vivo proteomics of jSR vesicles from CPVT1 murine models, treated and untreated with a DNA-based therapy (Chapter III) with in vitro biochemical dissection of CASQ2 variants relevant for the human CPVT2 disease (Chapter IV). Although CPVT1 and CPVT2 originate from distinct mutations in different genes (*RYR2* and *CASQ2* respectively), both converge on the unstable control of diastolic Ca^{2+} release from the RyR2-CASQ2-TRDN-JNT complex.

A primary outcome of this thesis is the establishment of a workflow that yields, from a single murine heart, jSR vesicles of sufficient enrichment and preservation of native interactions that allow the study of the CRU proteins by MS. This protocol, applied to three different murine models (WT, $RyR2^{R4496C/+}$, $RyR2^{R4496C/+}$ Inf AAV8-h*CASQ2*) led to the first comparative proteomic analysis of a CPVT1 murine model pre- and post-therapeutic treatment. From the analysis of this dataset a first conclusion is that there is a limited difference in the SR/ER annotated proteins between the WT and $RyR2^{R4496C/+}$ mouse models. Secondly, the $RyR2^{R4496C/+}$ Inf AAV8-h*CASQ2* group displayed a discrete set of differentially regulated proteins when compared to WT and $RyR2^{R4496C/+}$. As expected, the prominent signal in protein detection was CASQ2, which is aligned with the therapeutic rationale of increasing luminal buffering capacity and reinforcing CASQ2-RyR2 functional coupling at the jSR.

The second part of this work is focused on the luminal protein CASQ2. The first module is centred on $CASQ2^{WT}$, which behaviour is described using complementary biophysical approaches (including turbidimetry, thermal stability, dynamic light scattering and SEC) to connect stability and assembly under controlled ionic conditions. We have demonstrated that CASQ2 can form quaternary assemblies even in absence of its canonical ligand Ca^{2+}. In particular, physiological concentrations of K^+ ions promote conformational compaction of the

monomer and support a Ca^{2+}-independent dimerization process that occurs with high affinity. This dimeric state appears to be structurally stable across a broad range of ionic conditions and expectedly facilitates Ca^{2+}-responsiveness. On these bases, it is therefore likely that the CASQ2 dimer represents a native assembly intermediate of physiological relevance. We revealed a dual role for monovalent cations, which can either facilitate or destabilize Ca^{2+}-dependent polymerization. Importantly, our particle size distribution and T_m data indicate that CASQ2 polymerization does not proceed through a linear assembly pathway; Ca^{2+} instead acts as a switch that drives cooperative transition to a high-order polymeric state. Beyond the relevance for $CASQ2^{WT}$ behaviour, these findings provide a conceptual and experimental framework to study the effects of pathological CASQ2 mutations. Following these insights, we dissected the ionic-dependent dimerization and polymerization properties of eight CASQ2 mutants. The experimental results show that mutations do not perturb the protein in a unique mode; instead, they may either affect the conformational stability and/or the ion-dependent manner kinetics of Ca^{2+}-dependent polymerization, and/or the sensitivity of this process to the ionic conditions.

The insights obtained in this work open to several questions and future investigations. First, the comparative proteomic analysis among WT, $RyR2^{R4496C/+}$, $RyR2^{R4496C/+}$ Inf AAV8-h*CASQ2* mice models may be expanded to include other cellular compartments, in order to capture adaptive or compensatory pathological responses and therapeutic mechanisms that extend beyond the SR proteome. Second, the biochemical characterization of CASQ2 mutants provides a foundation to a more systematic dissection of the genotype – phenotype relationships. Extending this analysis with other biophysical methods (such as MP and DLS) and also with *in vivo* experiments will be critical to understand how distinct mutations translate into variable disease penetrance. This approach will lead ultimately to a patient stratification and mutation-based therapeutic strategies.

By combining comparative proteomics with mechanistic insight into CASQ2 assembly, this work contributes to a more integrated understanding of CPVT pathogenesis, moving from a descriptive approach toward a more translatable information for the design of innovative therapeutic strategies for both CPVT1 and CPVT2.

References

1. Rehman, I. & Rehman, A. Anatomy, Thorax, Heart. in *StatPearls* (StatPearls Publishing, Treasure Island (FL), 2025).
2. The Editors. Circulation Research Thematic Synopsis Cardiac Myocyte Biology and Function. *Circulation Research* **111**, e232–e251 (2012).
3. Banerjee, I., Fuseler, J. W., Price, R. L., Borg, T. K. & Baudino, T. A. Determination of cell types and numbers during cardiac development in the neonatal and adult rat and mouse. *Am J Physiol Heart Circ Physiol* **293**, H1883-1891 (2007).
4. Litviňuková, M. *et al.* Cells of the adult human heart. *Nature* **588**, 466–472 (2020).
5. Forbes, M. S. & van Neil, E. E. Membrane systems of guinea pig myocardium: ultrastructure and morphometric studies. *Anat Rec* **222**, 362–379 (1988).
6. Bers, D. M. & Shannon, T. R. Calcium movements inside the sarcoplasmic reticulum of cardiac myocytes. *J Mol Cell Cardiol* **58**, 59–66 (2013).

7. Miyamoto, T., Zhang, L., Sekiguchi, A., Hadama, T. & Shimada, T. Structural differences in the cytoarchitecture and intercalated discs between the working myocardium and conduction system in the human heart. *Heart Vessels* **16**, 232–240 (2002).

8. Spach, M. S. *et al.* The discontinuous nature of propagation in normal canine cardiac muscle. Evidence for recurrent discontinuities of intracellular resistance that affect the membrane currents. *Circ Res* **48**, 39–54 (1981).

9. Canale, E. D., Campbell, G. R., Smolich, J. J. & Campbell, J. H. Morphology of Cardiac Muscle. in *Cardiac Muscle* (eds. Canale, E. D., Campbell, G. R., Smolich, J. J. & Campbell, J. H.) 8–51 (Springer, Berlin, Heidelberg, 1986). doi:10.1007/978-3-642-50115-9_2.

10. Wang, Z. *et al.* The molecular basis for sarcomere organization in vertebrate skeletal muscle. *Cell* **184**, 2135-2150.e13 (2021).

11. Ribeiro, E. de A. *et al.* The structure and regulation of human muscle α-actinin. *Cell* **159**, 1447–1460 (2014).

12. Huxley, H. E. The double array of filaments in cross-striated muscle. *J Biophys Biochem Cytol* **3**, 631–648 (1957).

13. Flucher, B. E., Takekura, H. & Franzini-Armstrong, C. Development of the excitation-contraction coupling apparatus in skeletal muscle: association of sarcoplasmic reticulum and transverse tubules with myofibrils. *Dev Biol* **160**, 135–147 (1993).

14. Bers, D. M. Cardiac excitation-contraction coupling. *Nature* **415**, 198–205 (2002).

15. Jorgensen, A. O., Kalnins, V. I., Zubrzycka, E. & MacLennan, D. H. Assembly of the sarcoplasmic reticulum. Localization by immunofluorescence of sarcoplasmic reticulum proteins in differentiating rat skeletal muscle cell cultures. *J Cell Biol* **74**, 287–298 (1977).

16. Robert, V., De Giorgi, F., Massimino, M. L., Cantini, M. & Pozzan, T. Direct monitoring of the calcium concentration in the sarcoplasmic and endoplasmic reticulum of skeletal muscle myotubes. *J Biol Chem* **273**, 30372–30378 (1998).

17. Villa, A. *et al.* The endoplasmic reticulum-sarcoplasmic reticulum connection. II. Postnatal differentiation of the sarcoplasmic reticulum in skeletal muscle fibers. *Exp Cell Res* **209**, 140–148 (1993).

18. Michalak, M. & Opas, M. Endoplasmic and sarcoplasmic reticulum in the heart. *Trends Cell Biol* **19**, 253–259 (2009).

19. Franzini-Armstrong, C. Structure of sarcoplasmic reticulum. *Fed Proc* **39**, 2403–2409 (1980).

20. Fleischer, S. & Inui, M. Biochemistry and biophysics of excitation-contraction coupling. *Annu Rev Biophys Biophys Chem* **18**, 333–364 (1989).

21. Denegri, M. *et al.* Single delivery of an adeno-associated viral construct to transfer the CASQ2 gene to knock-in mice affected by catecholaminergic polymorphic ventricular tachycardia is able to cure the disease from birth to advanced age. *Circulation* **129**, 2673–2681 (2014).

22. The Assembly of Calcium Release Units in Cardiac Muscle - FRANZINI-ARMSTRONG - 2005 - Annals of the New York

Academy of Sciences - Wiley Online Library. https://nyaspubs.onlinelibrary.wiley.com/doi/10.1196/annals.1341.007.

23. Eisner, D. A., Caldwell, J. L., Kistamás, K. & Trafford, A. W. Calcium and Excitation-Contraction Coupling in the Heart. *Circ Res* **121**, 181–195 (2017).

24. Ríos, E., Ma, J. J. & González, A. The mechanical hypothesis of excitation-contraction (EC) coupling in skeletal muscle. *J Muscle Res Cell Motil* **12**, 127–135 (1991).

25. Eisner, D. A., Caldwell, J. L., Kistamás, K. & Trafford, A. W. Calcium and Excitation-Contraction Coupling in the Heart. *Circ Res* **121**, 181–195 (2017).

26. Marabelli, C., Santiago, D. J. & Priori, S. G. The Structural-Functional Crosstalk of the Calsequestrin System: Insights and Pathological Implications. *Biomolecules* **13**, 1693 (2023).

27. Stern, M. D., Pizarro, G. & Ríos, E. Local control model of excitation-contraction coupling in skeletal muscle. *J Gen Physiol* **110**, 415–440 (1997).

28. Stern, M. D. *et al.* Local control models of cardiac excitation-contraction coupling. A possible role for allosteric interactions between ryanodine receptors. *J Gen Physiol* **113**, 469–489 (1999).

29. Nakai, J. *et al.* Primary structure and functional expression from cDNA of the cardiac ryanodine receptor/calcium release channel. *FEBS Lett* **271**, 169–177 (1990).

30. Otsu, K. *et al.* Molecular cloning of cDNA encoding the Ca2+ release channel (ryanodine receptor) of rabbit cardiac muscle sarcoplasmic reticulum. *J Biol Chem* **265**, 13472–13483 (1990).

31. Rossi, D. & Sorrentino, V. Molecular genetics of ryanodine receptors Ca2+-release channels. *Cell Calcium* **32**, 307–319 (2002).

32. Inui, M., Saito, A. & Fleischer, S. Purification of the ryanodine receptor and identity with feet structures of junctional terminal cisternae of sarcoplasmic reticulum from fast skeletal muscle. *J Biol Chem* **262**, 1740–1747 (1987).

33. Hakamata, Y., Nakai, J., Takeshima, H. & Imoto, K. Primary structure and distribution of a novel ryanodine receptor/calcium release channel from rabbit brain. *FEBS Lett* **312**, 229–235 (1992).

34. Chen, W. & Kudryashev, M. Structure of RyR1 in native membranes. *EMBO Rep* **21**, e49891 (2020).

35. Swan, H. *et al.* Arrhythmic disorder mapped to chromosome 1q42-q43 causes malignant polymorphic ventricular tachycardia in structurally normal hearts. *J Am Coll Cardiol* **34**, 2035–2042 (1999).

36. Priori, S. G. & Napolitano, C. Cardiac and skeletal muscle disorders caused by mutations in the intracellular Ca2+ release channels. *J Clin Invest* **115**, 2033–2038 (2005).

37. Zalk, R., Lehnart, S. E. & Marks, A. R. Modulation of the ryanodine receptor and intracellular calcium. *Annu Rev Biochem* **76**, 367–385 (2007).

38. Ma, J., Hayek, S. M. & Bhat, M. B. Membrane topology and membrane retention of the ryanodine receptor calcium release channel. *Cell Biochem Biophys* **40**, 207–224 (2004).

39. Park, H. *et al.* Comparing skeletal and cardiac calsequestrin structures and their calcium binding: a proposed mechanism for coupled calcium binding and protein polymerization. *J Biol Chem* **279**, 18026–18033 (2004).

40. Titus, E. W. *et al.* The structure of a calsequestrin filament reveals mechanisms of familial arrhythmia. *Nat Struct Mol Biol* **27**, 1142–1151 (2020).

41. Park, H., Wu, S., Dunker, A. K. & Kang, C. Polymerization of calsequestrin. Implications for Ca2+ regulation. *J Biol Chem* **278**, 16176–16182 (2003).

42. Kobayashi, Y. M., Alseikhan, B. A. & Jones, L. R. Localization and characterization of the calsequestrin-binding domain of triadin 1. Evidence for a charged beta-strand in mediating the protein-protein interaction. *J Biol Chem* **275**, 17639–17646 (2000).

43. Herzog, A., Szegedi, C., Jona, I., Herberg, F. W. & Varsanyi, M. Surface plasmon resonance studies prove the interaction of skeletal muscle sarcoplasmic reticular Ca(2+) release channel/ryanodine receptor with calsequestrin. *FEBS Lett* **472**, 73–77 (2000).

44. Cacheux, M. *et al.* Interplay between Triadin and Calsequestrin in the Pathogenesis of CPVT in the Mouse. *Mol Ther* **28**, 171–179 (2020).

45. Brandt, N. R., Caswell, A. H., Wen, S. R. & Talvenheimo, J. A. Molecular interactions of the junctional foot protein and dihydropyridine receptor in skeletal muscle triads. *J Membr Biol* **113**, 237–251 (1990).

46. Kim, K. C., Caswell, A. H., Talvenheimo, J. A. & Brandt, N. R. Isolation of a terminal cisterna protein which may link the dihydropyridine receptor to the junctional foot protein in skeletal muscle. *Biochemistry* **29**, 9281–9289 (1990).

47. Peng, M., Fan, H., Kirley, T. L., Caswell, A. H. & Schwartz, A. Structural diversity of triadin in skeletal muscle and evidence of its existence in heart. *FEBS Lett* **348**, 17–20 (1994).

48. Roux-Buisson, N. *et al.* Absence of triadin, a protein of the calcium release complex, is responsible for cardiac arrhythmia with sudden death in human. *Hum Mol Genet* **21**, 2759–2767 (2012).

49. Jones, L. R., Zhang, L., Sanborn, K., Jorgensen, A. O. & Kelley, J. Purification, primary structure, and immunological characterization of the 26-kDa calsequestrin binding protein (junctin) from cardiac junctional sarcoplasmic reticulum. *J Biol Chem* **270**, 30787–30796 (1995).

50. Dinchuk, J. E. *et al.* Aspartyl beta -hydroxylase (Asph) and an evolutionarily conserved isoform of Asph missing the catalytic domain share exons with junctin. *J Biol Chem* **275**, 39543–39554 (2000).

51. Hong, C. S., Kwak, Y. G., Ji, J. H., Chae, S. W. & Kim, D. H. Molecular cloning and characterization of mouse cardiac

junctate isoforms. *Biochem Biophys Res Commun* **289**, 882–887 (2001).

52. Treves, S., Feriotto, G., Moccagatta, L., Gambari, R. & Zorzato, F. Molecular cloning, expression, functional characterization, chromosomal localization, and gene structure of junctate, a novel integral calcium binding protein of sarco(endo)plasmic reticulum membrane. *J Biol Chem* **275**, 39555–39568 (2000).

53. Wetzel, G. T., Ding, S. & Chen, F. Molecular cloning of junctin from human and developing rabbit heart. *Mol Genet Metab* **69**, 252–258 (2000).

54. Terentyev, D. *et al.* Triadin overexpression stimulates excitation-contraction coupling and increases predisposition to cellular arrhythmia in cardiac myocytes. *Circ Res* **96**, 651–658 (2005).

55. Zhang, L., Kelley, J., Schmeisser, G., Kobayashi, Y. M. & Jones, L. R. Complex formation between junctin, triadin, calsequestrin, and the ryanodine receptor. Proteins of the cardiac junctional

sarcoplasmic reticulum membrane. *J Biol Chem* **272**, 23389–23397 (1997).

56. Reid, D. S., Tynan, M., Braidwood, L. & Fitzgerald, G. R. Bidirectional tachycardia in a child. A study using His bundle electrography. *Br Heart J* **37**, 339–344 (1975).

57. Denegri, M. *et al.* Viral gene transfer rescues arrhythmogenic phenotype and ultrastructural abnormalities in adult calsequestrin-null mice with inherited arrhythmias. *Circ Res* **110**, 663–668 (2012).

58. Henriquez, E. *et al.* Catecholaminergic Polymorphic Ventricular Tachycardia and Gene Therapy: A Comprehensive Review of the Literature. *Cureus* **15**, e47974 (2023).

59. Priori, S. G. *et al.* Mutations in the cardiac ryanodine receptor gene (hRyR2) underlie catecholaminergic polymorphic ventricular tachycardia. *Circulation* **103**, 196–200 (2001).

60. Kobayashi, T. *et al.* Molecular basis for gating of cardiac ryanodine receptor explains the mechanisms for gain- and loss-of function mutations. *Nat Commun* **13**, 2821 (2022).

61. Bers, D. M. Cardiac sarcoplasmic reticulum calcium leak: basis and roles in cardiac dysfunction. *Annu Rev Physiol* **76**, 107–127 (2014).

62. Mohamed, U., Napolitano, C. & Priori, S. G. Molecular and electrophysiological bases of catecholaminergic polymorphic ventricular tachycardia. *J Cardiovasc Electrophysiol* **18**, 791–797 (2007).

63. Priori, S. G. & Chen, S. R. W. Inherited dysfunction of sarcoplasmic reticulum Ca2+ handling and arrhythmogenesis. *Circ Res* **108**, 871–883 (2011).

64. Jiang, D. *et al.* RyR2 mutations linked to ventricular tachycardia and sudden death reduce the threshold for store-overload-induced Ca2+ release (SOICR). *Proc Natl Acad Sci U S A* **101**, 13062–13067 (2004).

65. Lakatta, E. G. Functional implications of spontaneous sarcoplasmic reticulum Ca2+ release in the heart. *Cardiovasc Res* **26**, 193–214 (1992).

66. Venetucci, L. A., Trafford, A. W., O'Neill, S. C. & Eisner, D. A. The sarcoplasmic reticulum and arrhythmogenic calcium release. *Cardiovasc Res* **77**, 285–292 (2008).

67. Efremov, R. G., Leitner, A., Aebersold, R. & Raunser, S. Architecture and conformational switch mechanism of the ryanodine receptor. *Nature* **517**, 39–43 (2015).

68. Chi, X. *et al.* Molecular basis for allosteric regulation of the type 2 ryanodine receptor channel gating by key modulators. *Proc Natl Acad Sci U S A* **116**, 25575–25582 (2019).

69. Kimlicka, L., Lau, K., Tung, C.-C. & Van Petegem, F. Disease mutations in the ryanodine receptor N-terminal region couple to a mobile intersubunit interface. *Nat Commun* **4**, 1506 (2013).

70. Sun, B. *et al.* Cardiac ryanodine receptor calcium release deficiency syndrome. *Sci Transl Med* **13**, eaba7287 (2021).

71. Zhong, X. *et al.* Identification of loss-of-function RyR2 mutations associated with idiopathic ventricular fibrillation and sudden death. *Biosci Rep* **41**, BSR20210209 (2021).

72. Cerrone, M. *et al.* Bidirectional ventricular tachycardia and fibrillation elicited in a knock-in mouse model carrier of a mutation in the cardiac ryanodine receptor. *Circ Res* **96**, e77-82 (2005).

73. Lahat, H. *et al.* A missense mutation in a highly conserved region of CASQ2 is associated with autosomal recessive catecholamine-induced polymorphic ventricular tachycardia in Bedouin families from Israel. *Am J Hum Genet* **69**, 1378–1384 (2001).

74. Priori, S. G. *et al.* Precision Medicine in Catecholaminergic Polymorphic Ventricular Tachycardia: JACC Focus Seminar 5/5. *J Am Coll Cardiol* **77**, 2592–2612 (2021).

75. Marty, I. Triadin regulation of the ryanodine receptor complex. *J Physiol* **593**, 3261–3266 (2015).

76. Manno, C., Tammineni, E., Figueroa, L., Marty, I. & Ríos, E. Quantification of the calcium signaling deficit in muscles devoid of triadin. *PLoS One* **17**, e0264146 (2022).

77. Venetucci, L. A., Trafford, A. W. & Eisner, D. A. Increasing ryanodine receptor open probability alone does not produce arrhythmogenic calcium waves: threshold sarcoplasmic reticulum calcium content is required. *Circ Res* **100**, 105–111 (2007).

78. Marx, S. O. *et al.* PKA phosphorylation dissociates FKBP12.6 from the calcium release channel (ryanodine receptor): defective regulation in failing hearts. *Cell* **101**, 365–376 (2000).

79. Di Antonio, C., Marabelli, C., Bongianino, R. & Priori, S. G. Protocol for Enrichment of Murine Cardiac Junctional Sarcoplasmic Reticulum Vesicles for Mass Spectrometry Analysis. *Int J Mol Sci* **26**, 8602 (2025).

80. Green, E. D., Watson, J. D. & Collins, F. S. Human Genome Project: Twenty-five years of big biology. *Nature* **526**, 29–31 (2015).

81. Urban, P. L. Quantitative mass spectrometry: an overview. *Philos Trans A Math Phys Eng Sci* **374**, 20150382 (2016).

82. Rotello, R. J. & Veenstra, T. D. Mass Spectrometry Techniques: Principles and Practices for Quantitative Proteomics. *Curr Protein Pept Sci* **22**, 121–133 (2021).

83. Bantscheff, M., Schirle, M., Sweetman, G., Rick, J. & Kuster, B. Quantitative mass spectrometry in proteomics: a critical review. *Anal Bioanal Chem* **389**, 1017–1031 (2007).

84. Wiener, M. C., Sachs, J. R., Deyanova, E. G. & Yates, N. A. Differential mass spectrometry: a label-free LC-MS method for finding significant differences in complex peptide and protein mixtures. *Anal Chem* **76**, 6085–6096 (2004).

85. Liu, H., Sadygov, R. G. & Yates, J. R. A model for random sampling and estimation of relative protein abundance in shotgun proteomics. *Anal Chem* **76**, 4193–4201 (2004).

86. Aebersold, R. & Mann, M. Mass-spectrometric exploration of proteome structure and function. *Nature* **537**, 347–355 (2016).

87. Mitchell, R. D., Palade, P. & Fleischer, S. Purification of morphologically intact triad structures from skeletal muscle. *J Cell Biol* **96**, 1008–1016 (1983).

88. Jones, L. R., Besch, H. R., Fleming, J. W., McConnaughey, M. M. & Watanabe, A. M. Separation of vesicles of cardiac sarcolemma from vesicles of cardiac sarcoplasmic reticulum. Comparative biochemical analysis of component activities. *J Biol Chem* **254**, 530–539 (1979).

89. Jones, L. R. & Cala, S. E. Biochemical evidence for functional heterogeneity of cardiac sarcoplasmic reticulum vesicles. *J Biol Chem* **256**, 11809–11818 (1981).

90. Staunton, L. & Ohlendieck, K. Mass spectrometric characterization of the sarcoplasmic reticulum from rabbit skeletal muscle by on-membrane digestion. *Protein Pept Lett* **19**, 252–263 (2012).

91. Eckhardt, J. *et al.* Quantitative proteomic analysis of skeletal muscles from wild-type and transgenic mice carrying recessive Ryr1 mutations linked to congenital myopathies. *Elife* **12**, e83618 (2023).

92. Priori, S. G. *et al.* Mutations in the cardiac ryanodine receptor gene (hRyR2) underlie catecholaminergic polymorphic ventricular tachycardia. *Circulation* **103**, 196–200 (2001).

93. Prabhakar, S., Lule, S., da Hora, C. C., Breakefield, X. O. & Cheah, P. S. AAV9 transduction mediated by systemic delivery of vector via retro-orbital injection in newborn, neonatal and juvenile mice. *Exp Anim* **70**, 450–458 (2021).

94. Bal, N. C. *et al.* The C-terminal calcium-sensitive disordered motifs regulate isoform-specific polymerization characteristics of calsequestrin. *Biopolymers* **103**, 15–22 (2015).

95. Bers, D. M. *Excitation-Contraction Coupling and Cardiac Contractile Force*. (Kluwer Academic Publishers, Dordrecht, Boston, 2001).

96. Houle, T. D., Ram, M. L., McMurray, W. J. & Cala, S. E. Different endoplasmic reticulum trafficking and processing pathways for calsequestrin (CSQ) and epitope-tagged CSQ. *Exp Cell Res* **312**, 4150–4161 (2006).

97. Milstein, M. L., Houle, T. D. & Cala, S. E. Calsequestrin isoforms localize to different ER subcompartments: evidence for polymer and heteropolymer-dependent localization. *Exp Cell Res* **315**, 523–534 (2009).

98. Lewis, K. M. *et al.* Characterization of Post-Translational Modifications to Calsequestrins of Cardiac and Skeletal Muscle. *Int J Mol Sci* **17**, 1539 (2016).

99. Wang, Q. *et al.* Phylogenetic and biochemical analysis of calsequestrin structure and association of its variants with cardiac disorders. *Sci Rep* **10**, 18115 (2020).

100. Gray, B. *et al.* A novel heterozygous mutation in cardiac calsequestrin causes autosomal dominant catecholaminergic polymorphic ventricular tachycardia. *Heart Rhythm* **13**, 1652–1660 (2016).

101. Zhao, R. *et al.* Measurement of amyloid formation by turbidity assay-seeing through the cloud. *Biophys Rev* **8**, 445–471 (2016).

102. Perni, S., Close, M. & Franzini-Armstrong, C. Novel details of calsequestrin gel conformation in situ. *J Biol Chem* **288**, 31358–31362 (2013).

103. Bal, N. C. *et al.* The catecholaminergic polymorphic ventricular tachycardia mutation R33Q disrupts the N-terminal structural motif that regulates reversible calsequestrin polymerization. *J Biol Chem* **285**, 17188–17196 (2010).

104. Bal, N. C. *et al.* The C-terminal calcium-sensitive disordered motifs regulate isoform-specific polymerization characteristics of calsequestrin. *Biopolymers* **103**, 15–22 (2015).

105. Nayak, A. R. *et al.* Interplay between Mg2+ and Ca2+ at multiple sites of the ryanodine receptor. *Nat Commun* **15**, 4115 (2024).

106. Laver, D. R. Regulation of the RyR channel gating by Ca2+ and Mg2. *Biophys Rev* **10**, 1087–1095 (2018).

107. Laver, D. R. & Honen, B. N. Luminal Mg2+, a key factor controlling RYR2-mediated Ca2+ release: cytoplasmic and

luminal regulation modeled in a tetrameric channel. *J Gen Physiol* **132**, 429–446 (2008).

Published/submitted articles

International Journal of
Molecular Sciences

MDPI

Article

Protocol for Enrichment of Murine Cardiac Junctional Sarcoplasmic Reticulum Vesicles for Mass Spectrometry Analysis

Chiara Di Antonio [1], Chiara Marabelli [1,2,3,*], Rossana Bongianino [2] and Silvia G. Priori [1,2,3]

[1] Department of Molecular Medicine, University of Pavia, 27100 Pavia, Italy; chiara.diantonio01@universitadipavia.it (C.D.A.)
[2] Laboratory of Molecular Cardiology, IRCCS ICS Maugeri, 27100 Pavia, Italy; rossana.bongianino@icsmaugeri.it
[3] Centro Nacional de Investigaciones Cardiovasculares Carlos III (CNIC), 28029 Madrid, Spain
* Correspondence: chiara.marabelli02@universitadipavia.it

Abstract

The junctional sarcoplasmic reticulum (jSR) is a critical organelle in cardiomyocytes, regulating calcium homeostasis and Excitation–Contraction Coupling (ECC). A quantitative understanding of its protein composition is essential for investigating cardiac physiology and related pathologies. However, isolating intact jSR vesicles, particularly those enriched in membrane proteins, remains a challenging task. Here, we describe our optimized protocol for reproducible enrichment of jSR vesicles from a single murine heart, without the use of antibodies. The protocol enables the recovery of low-abundance membrane proteins while preserving their native interactions with partners. This strategy facilitates the straightforward identification by Mass Spectrometry of highly relevant yet challenging jSR proteins, including the cardiac Ryanodine Receptor and calsequestrin. Our protocol provides a robust tool for studying the structural and stoichiometric organization of the cardiac jSR components in a widely used animal model.

Keywords: sarcoplasmic reticulum; membrane protein; proteostasis; mass spectrometry; cardiac pathologies

Academic Editor: Massimo Iacoviello

Received: 18 July 2025
Revised: 30 August 2025
Accepted: 2 September 2025
Published: 4 September 2025

Citation: Di Antonio, C.; Marabelli, C.; Bongianino, R.; Priori, S.G. Protocol for Enrichment of Murine Cardiac Junctional Sarcoplasmic Reticulum Vesicles for Mass Spectrometry Analysis. *Int. J. Mol. Sci.* **2025**, *26*, 8602. https://doi.org/10.3390/ijms26178602

1. Introduction

1.1. The Pathophysiological Relevance of the Cardiac jSR Compartment

The terminal portion of the sarcoplasmic reticulum (SR), namely the junctional SR (jSR), is a highly specialized compartment enriched in Ca^{2+}, crucial for the function of skeletal and cardiac myocytes [1,2]. Different from the longitudinal SR (lSR), which extends along the entire length of the sarcomeres, this specialized region is only found at the sarcomere Z-lines, in physical proximity (less than 20 nm) to the sarcolemmal invaginations, known as T-tubules [1,3,4], and mitochondria [5,6]. As the action potential is uniformly and quickly propagated throughout the entire volume of the cell by T-tubules, it triggers the coordinated release of Ca^{2+} ions from the jSR into the cytosol, and thus synchronized myofilament contraction [7]. This process, known as Excitation–Contraction Coupling (ECC), is initiated by the voltage-gated calcium channels (L-type Ca^{2+} channels, i.e., $Ca_V1.2$) in the T-tubules, which open in response to membrane depolarization [2,7]. In the cardiac setting, the local Ca^{2+} concentration increases in the narrow dyadic space between the T-tubule and the jSR, which in turn opens the nearby RyR2 Ca^{2+} channels (cardiac Ryanodine Receptor) [7,8].

RyR2 is organized in clusters so that Ca^{2+} release events can be amplified and coordinated, spatially and temporally, to generate an efficacious cytosolic Ca^{2+} transient. Overall,

the complex composed of a RyR2 cluster and a related modulator protein membrane is named the Ca^{2+} release unit (CRU). Along with those proteins directly modulating RyR2 activity, the proteome machinery of the jSR also supports the high-capacity storage of Ca^{2+} ions [9]. Of the luminal Ca^{2+} binding proteins, while cardiac calsequestrin (CASQ2) is known to be a jSR-specific component, the histidine-rich Ca^{2+}-binding protein (HRC) has been found either in proximity to RyR2 or the sarco(endo)plasmic reticulum Ca^{2+}-ATPase (SERCA) pumps for Ca^{2+} reuptake, distributed along the lSR membrane [10].

The precise spatial organization of these proteins at the nanometer scale, and more critically of the CRU machineries, allows the highly coordinated and rhythmic contractions of the heart [11]. Within the CRU, the single-pass transmembrane proteins Tradin (TRDN) and Junctin (JNT) [12,13], and the luminal CASQ2, are known to modulate RyR2 opening and refractoriness. Non-sense or missense mutations in any of these CRU components affect ECC. Among the multiple hereditary diseases associated with genetic mutations of the cardiac CRU components, Catecholaminergic Polymorphic Ventricular Tachycardia (CPVT) is one of the most severe. The bidirectional/polymorphic ventricular tachycardia typical of CPVT is triggered by emotional stress or physical exercise in patients with a structurally normal heart [14–17]. Since the first identification of a CPVT causative mutation in RyR2 in 2001 [18], dozens of mutations in proteins of the CRU have been discovered and associated with the disease. The three most prevalent forms of the pathology are distinguished according to the mutated gene: either RYR2, CASQ2, or TRDN. The dominantly inherited CPVT type 1, related to mutations of the RYR2 gene, accounts for up to 70% of CPVT cases [19]. CPVT type 2 is caused by a genetic defect on CASQ2 [20], and can show either a dominant or recessive inheritance [21]. CPVT type 5 is the rarest form. It is recessively inherited and caused by the loss of function of TRDN [22]. All CPVT forms feature Ca^{2+} overload within the jSR and increased RyR2 permeability to Ca^{2+}. The most accredited hypothesis is that Ca^{2+} leakage from a few RyR2 channels triggers spontaneous Ca^{2+} release from the neighboring ones in a positive-loop cascade. This, in turn, leads to non-electrically triggered contraction of the cardiomyocyte, degenerating to ventricular arrhythmia (VT) [17].

1.2. A Protocol for the Enrichment of Cardiac jSR Vesicles in Their Native State

Despite the extreme clinical relevance of the jSR compartment, its molecular composition and organization are poorly described. Among the technical difficulties that the study of this specialized domain poses, its isolation and separate characterization remain one of the most limiting challenges. The relatively high proportion of transmembrane proteins with respect to membrane lipids [23], the high sensitivity to subtle ionic variations in the soluble protein machinery [21], and its architectural complexity at the boundary between T-tubules and mitochondria [5,6] complicate the procedures for enrichment of the jSR components and the maintenance of protein complexes in their native form.

In this study, we present an enrichment protocol to obtain jSR vesicles from a single wild-type (WT) murine heart. This method enables the efficient recovery of intact membrane proteins in their native state, hence without the need for detergents (often required to solubilize such proteins, but can disrupt native interactions). The robustness of the enrichment and the preservation of the molecular interactions are proven by the reproducible detection of notorious low-abundance membrane proteins, such as RyR2, TRDN, and JNT, and other proteins physically tethered to the jSR compartment, such as JPH2 and $Ca_V1.2$. The qualitative MS technique allowed us to profile SR membrane proteins with high sensitivity, overcoming traditional limitations in detecting these hydrophobic proteins. This study aims to demonstrate the protocol's suitability for proteomic investigations on the structural organization of the jSR.

1.3. Interspecies Differences in the Cardiac jSR Compartment

While the protocol here described for the enrichment of native jSR vesicles from WT murine samples is rapidly transferable to any of the multiple murine models of cardiac pathologies, it is imperative to acknowledge the nuances when analyzing other animal models or extrapolating findings to human settings, particularly concerning membrane lipid composition and the composition and stability of CRU components.

More specifically, it is well-established that murine RyR2 is more prone to spontaneous Ca^{2+} release events than human ones, indicating a less stable closed state or higher intrinsic leakiness. Among the other species, it is rabbit RyR2 that, particularly under diastole-like conditions, best replicates the functional attributes of human RyR2 [24]. Notably, these species differences persist even when isolated RyR2 is studied under identical in vitro conditions, suggesting that they are consequences of intrinsic differences in partnering proteins (such as FKBP12.6) [25] and membrane lipid composition [23,26,27]. Known differences in CASQ2 abundance and its vulnerability to loss during isolation explain the significantly lower levels of CASQ2 recovered in SR vesicles in sheep with respect to samples obtained from murine or rat tissues [28]. Regarding the membrane lipid milieu, the heart of small rodents has strikingly more polyunsaturated fatty acids and polyunsaturated cardiolipin acyl chains than larger animals [26,27]. These differences in the membrane fluidity directly affect the open/closure equilibrium of membrane proteins such as SERCA [29] and, by extension, it is expected to influence RyR2 function and clustering.

Beyond the properties of individual proteins, the architecture and protein composition of the CRU widely differ between mice, pigs, and humans. Compared to pigs and humans, rodents feature a higher density of RyR2 and SERCA2 to support their rapid 600+ bpm heart rates, as well as other accessory jSR proteins like junctophilin-2 (JPH2), TRDN, and JNT [30].

In conclusion, while our protocol provides a valuable foundation for murine jSR proteomics, translating these insights to human cardiac ECC necessitates a rigorous consideration of species-specific molecular landscapes. Future investigations leveraging this protocol should diligently account for these potential disparities in membrane composition, protein stability, and quantificational challenges, employing cross-validation with human cellular models where feasible to bridge the translational gap.

2. Results

2.1. Protocol for jSR Vesicles Preparation

2.1.1. Sample Homogenization and Isolation of the Microsomal Fraction

Collection of the Heart Tissue

The first step, critical for the quality of the prepared sample, is the collection of the mouse heart (about 100–120 mg of tissue). Hearts are excised from C57BL/6N mice after euthanasia performed by cervical dislocation. Comparison of the results obtained after direct treatment of freshly isolated tissues, or instead freshly fast-frozen in liquid nitrogen, clearly indicates a major degradation of the proteins of interest for the fresh, unfrozen samples (Figure S1). Thus, it is recommended to use fresh tissues that have been immediately fast-frozen in liquid nitrogen just after isolation, as this minimizes degradation processes that may otherwise hamper the enrichment reproducibility and the physiological integrity of the enriched portion. A scheme of the entire protocol for the preparation of jSR vesicles is shown (Figure 1).

Homogenization of the Heart Tissue

In total, 1.5 mL of Homogenization Buffer was added to each flash-frozen mouse heart before homogenization with a bead-beater (see Methods Section 4.2.2) [31]. Unlike our

enrichment protocol, the standard homogenization procedure involved grinding frozen tissue using a pestle and mortar in liquid nitrogen vapors, followed by resuspension in a Homogenization Buffer and a sonication cycle for a minimum of 4–5 min. This approach introduces several sources of variability, including heat generation, inconsistent lysis efficiency, and potential cross-contamination when multiple samples are processed in parallel. In our case, we opted for an alternative method using the Minilys® bead-beater instrument, which processes each sample individually in a sealed tube and applies a standardized motion that improves reproducibility and reduces contamination risk.

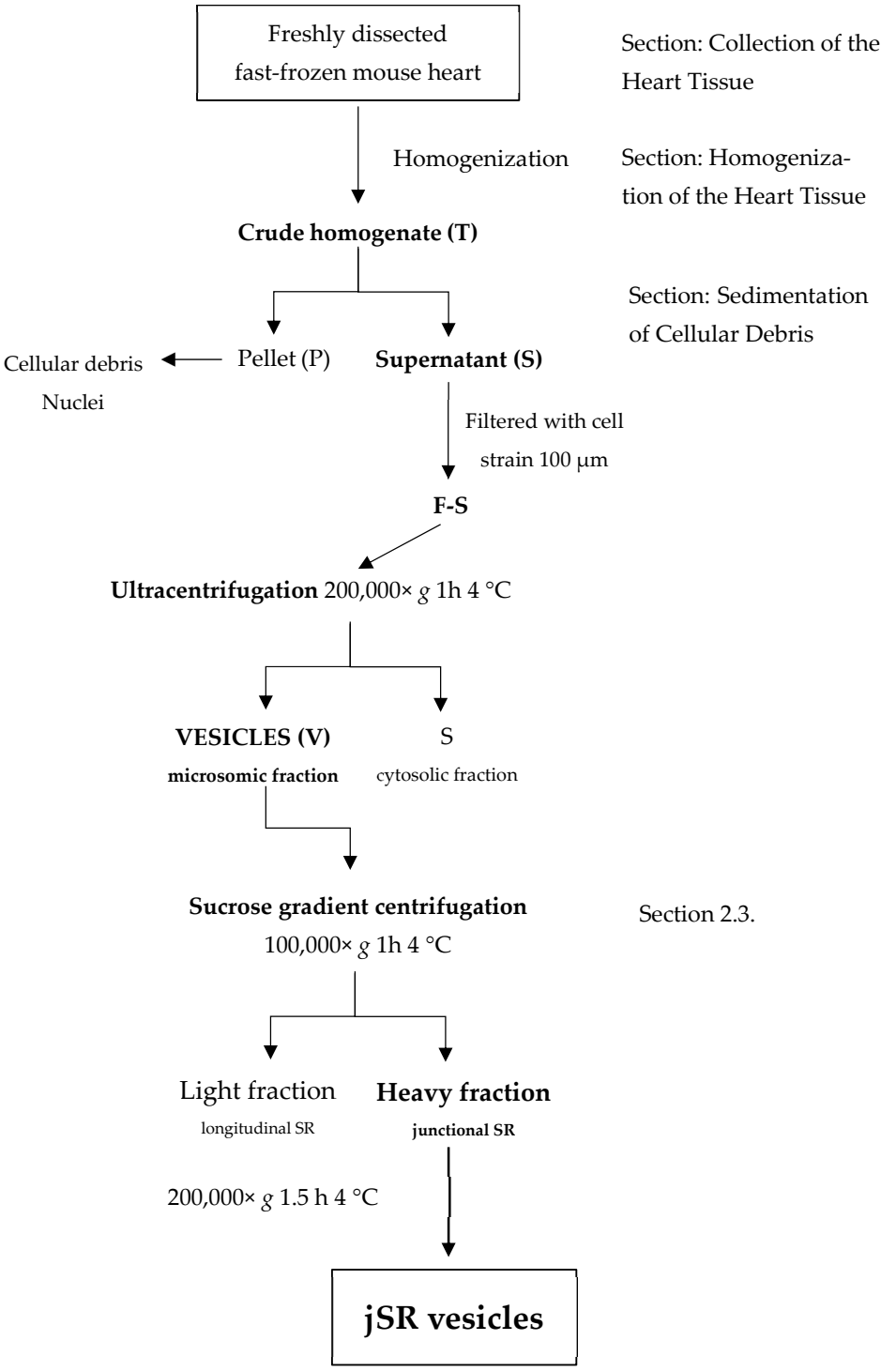

Figure 1. A schematic visualization of the enrichment protocol.

Sedimentation of Cellular Debris

The homogenate is subjected to a centrifugation step at 9000× *g* in order to remove cellular debris and major organelles, such as nuclei and mitochondria. Beads are also collected at the bottom of the tube. The supernatant (S) is separated from the rest of the sample and is then filtered with a 100 µm cell strainer for the removal of the fatty layer, composed of unbroken cells or large membrane debris. The filtered supernatant is subjected to ultracentrifugation at 4 °C for 1 h at 200,000× *g* to allow the recovery of cellular material (microsomal fraction) containing SR vesicles. The ultracentrifugation step was incorporated after evaluating different centrifugation protocols. Although published methods [31] recommend 20,000× *g* for the collection of SR vesicles, in our experience, higher sedimentation velocities yielded a more consistent pellet composition and volume, allowing reproducible loading for WB analysis of samples derived from single murine hearts and resulting in clearer detection of jSR protein bands.

Quantification of the Protein Content of the SR-Enriched Sample

In the end, the pellet containing SR vesicles is separated from the supernatant and resuspended in 200 µL of Resuspension Buffer. Resuspension with a thin syringe needle and the high ionic conditions prevent membrane aggregation and help maintain the stability of the overall sample. Protein concentration is determined using the Pierce BCA Protein Assay Kit (Thermo scientific, Waltham, MA, USA). To provide a clear evaluation of the enrichment process, we included additional WB analyses at different stages of the preparation (Figure 2; raw images of WB are presented in the Supplementary Materials: Figures S2–S6).

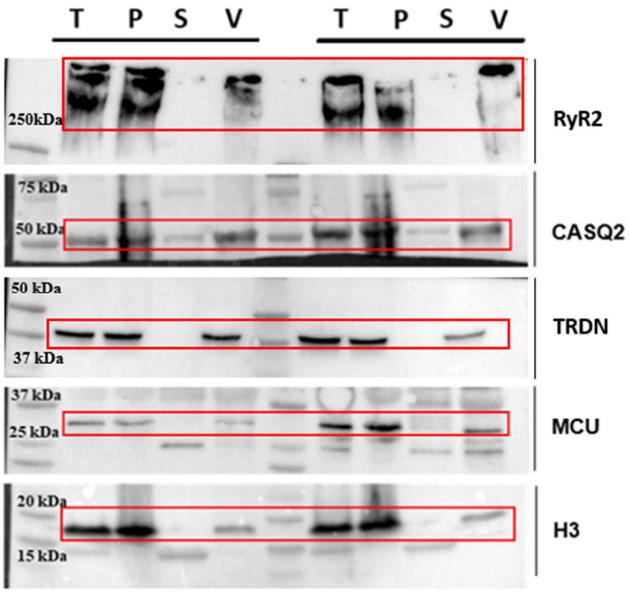

Figure 2. Western blot analysis performed at different stages of preparation. Analyzed steps include total heart lysate (T), membrane pellet (P) obtained after the first centrifugation, supernatant (S) of the ultracentrifugation step, and final vesicle pellet (V) obtained after ultracentrifugation. The antibodies used are sarcoplasmic reticulum proteins RyR2, CASQ2, TRDN; mitochondrial protein MCU; and nuclear protein H3. Red frames indicate the specific band for each protein.

Here, we show the total heart lysate (T), the membrane pellet obtained after the first centrifugation (P), the supernatant from the ultracentrifugation step (S), and the final vesicle pellet (V, Figure 2). To assess the distribution of different cellular components, we used a representative protein from each compartment: mitochondria (MCU), nucleus (Histone H3), and sarcoplasmic reticulum (RyR2 and CASQ2). For each lane, we loaded 30 µg of total protein to ensure a comparable representation of the different fractions. The Western

blot analysis here shows samples derived from two independent preparations, meaning that the samples were obtained from two distinct mouse hearts processed simultaneously yet independently.

We recognize that RyR2 is partially lost during homogenization, which is an inherent limitation of the separation process. This loss is primarily due to the mild homogenization conditions we deliberately employ to preserve protein integrity and minimize overall degradation. These conditions result in a fraction of cells remaining intact, thereby retaining some of the RyR2 within non-disrupted cells. Harsher homogenization protocols, while potentially increasing the overall yield, have been observed to cause extensive protein loss (Figure S1). Our approach prioritizes the enrichment of high-quality, CRU proteins, maintaining their native conformations and interactions, which is critical for downstream structural studies.

Regarding the mitochondrial and nuclear proteins, their presence is reduced but not completely eliminated in our final vesicle fraction. While the enrichment factor relative to these contaminants is moderate, it is important to emphasize that the goal of this protocol is not absolute purification but rather an increased representation of CRU-associated proteins compared to total homogenates.

Unlike previous studies, typically starting from larger amounts of tissue obtained from multiple animals [32,33], our approach is optimized for enrichment from a single murine heart (~100 mg). The main limitation to jSR protein enrichment indeed lies in the fact that the jSR compartments in ventricular cardiomyocytes represent the 0.22% of the cellular volume [34] and thus CRU proteins are inherently low in abundance within the total cardiac proteome. A key strength of our protocol is that it balances enrichment with protein integrity, allowing for the isolation of CRU components in a physiologically relevant state from a single murine heart.

2.2. Quality Evaluation of the Protocol

2.2.1. Reproducibility Evaluation of the Protocol

To assess the accuracy and reproducibility of the enrichment protocol, we inspected by WB the proteins enriched across nine independent samples, each derived from a distinct mouse heart.

Samples were treated separately and simultaneously. WB analysis of the key proteins involved in ECC (following the protocol described in the Materials and Methods Section 4.2.11) reveals the variance in the protein levels across biological replicates (Figure 3).

The consistent protein expression patterns across biological replicates demonstrate the robustness of this enrichment method in isolating CRU proteins, yielding reproducible results for the soluble protein Casq2, and the small transmembrane proteins Trdn and Jnt, despite the limited starting material (i.e., a single mouse heart). Expectedly, RyR2 exhibits higher variability across biological replicates, reflecting its intrinsic biochemical properties as an MDa-sized transmembrane protein complex with low stability. Indeed, the challenges associated with isolating and maintaining RyR2 channels in their native state due to their large size and poor stability have already been discussed [31,35]. Despite these inherent challenges, our protocol successfully enriches RyR2 in all tested samples, providing valuable insight into the molecular composition of the jSR while preserving key protein interactions.

2.2.2. Mass Spectrometry Analysis (nLC-HRMS)

Three samples, each derived from a single mouse heart, were analyzed by a relatively simple experimental procedure of Mass Spectrometry to conduct a qualitative protein characterization. The samples were analyzed using a nano-LC system connected to an

Orbitrap ExplorisTM 240 Mass Spectrometer equipped with a nano-electrospray ion source. Samples were injected in three technical triplicates (see details in Section 4.2.13).

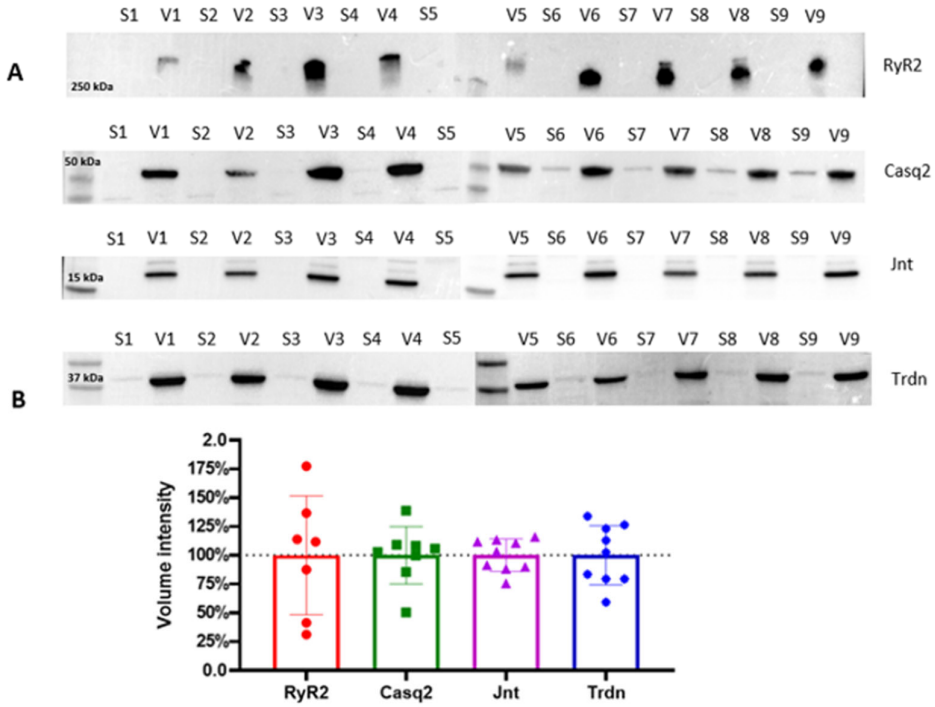

Figure 3. (**A**) Western blot analyses of vesicle fractions (V) obtained from the final pelleting step, compared to the relative discarded supernatant (S). Key jSR and SR proteins, including RyR2, Casq2, Jnt, and Trdn, are analyzed across each preparation. The four horizontal blot panels correspond to different molecular weight protein targets, as indicated by the molecular weight markers on the left (250 kDa, 50 kDa, 35 kDa, and 17 kDa). (**B**) Quantitative analysis of the Western blots is presented in the form of bar plots, summarizing the statistical variance in protein levels across the nine biological replicates. Band intensities were quantified and normalized, and data are represented as mean ± standard deviation. Dotted line represents the mean total volume intensity for each protein.

Despite the typical low abundance of RyR2 in the total cellular proteome, our protocol enabled its identification via MS without the need for detergent-assisted extraction. Table S1 lists the identified proteins from the endoplasmic and sarcoplasmic reticulum with a threshold of at least two peptides per hit. The total of the peptides obtained from all three technical replicates was considered.

2.3. Fractionation of the SR Vesicles by Density Gradient

Although identification of key jSR proteins is achievable at this level of enrichment, further purification from lSR components can be performed through sucrose gradient fractionation. This approach enables a more refined separation between longitudinal and junctional SR, and allows additional enrichment of the jSR fraction by reducing the abundance of contaminating proteins, such as those from the cytoplasm or plasma membrane. Since the recovery of the gradient fraction is very low, our protocol using jSR vesicle separation employs $n = 4$ murine hearts for a single jSR enrichment.

Sucrose density gradient centrifugation is a gentle method for separating particles in an aqueous solution. The distinct densities of the membranous and protein particles in aqueous solution determine their distribution among differently concentrated sucrose phases when subjected to high centrifugal forces (Figure 4).

Under the effect of acceleration forces toward the tube bottom, each particle or vesicle moves through the sucrose layers until it reaches a point where its density matches that

of the surrounding sucrose. Once this equilibrium is achieved, components of different densities, i.e., with distinct lipid and protein composition, will have sedimented at different positions [36].

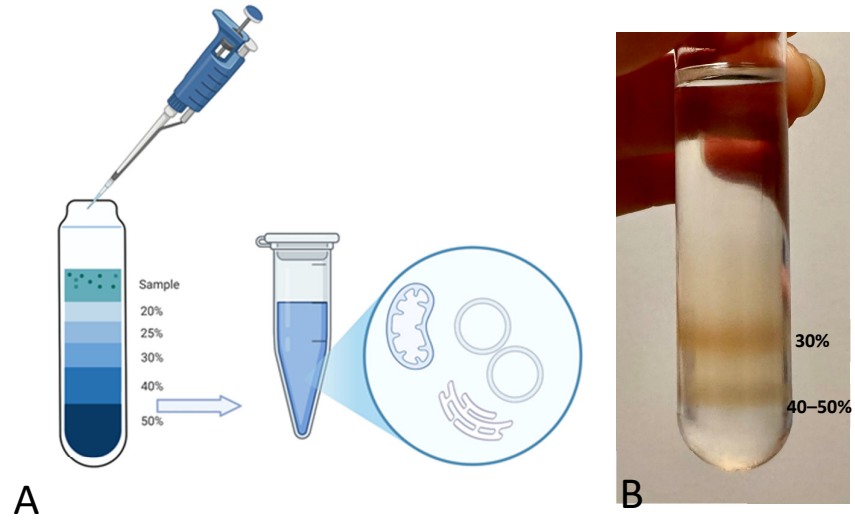

Figure 4. (**A**) Schematic representation of the sucrose density gradient. (**B**) Picture of the sucrose density gradient with two evident bands in the bottom sucrose phases. The uppermost band corresponds to the 30% sucrose phase, while the lower band corresponds to the interface between the 40% and 50% sucrose densities.

Previously published density gradients of muscle-derived samples [35,37] already identified vesicles from the longitudinal SR in the 30% (w/v) sucrose density fractions, whereas vesicles from the junctional SR have been located at the interface between 40% and 50% (w/v) sucrose phases. Vesicles from the jSR indeed feature a higher protein content with respect to the wet weight of the organelle, whereas longitudinal SR vesicles are characterized by a higher membrane-to-protein proportion [38].

In our case, the jSR protein components display a density-dependent distribution, accumulating primarily at the 40–50% (w/v) sucrose interface (Figure 5). The fact that the soluble protein CASQ2 follows the same enrichment trend as the membrane-bound CRU RyR2 and TRDN indicates its tight association with them, and hence that the jSR vesicles are preserved under these experimental conditions. Assessment of additional SR proteins is employed as a further confirmation of the quality of the obtained sample. SERCA (a Ca^{2+} ATPase that pumps Ca^{2+} from the cytosol back into the SR), $Ca_V1.2$ (an L-type Ca^{2+} channel), and Junctophilin 2 (JPH2), a membrane-bound protein that anchors the plasma membrane to the SR membrane, are also inspected by WB. SERCA is broadly detected across fractions, as expected for this highly abundant SR protein, consistent with its known role in Ca^{2+} reuptake along the length of the sarcomere. In contrast, the $Ca_V1.2$ (a Ca^{2+}-channel of the T-tubule, known to lie in close proximity with the jSR Ca^{2+}-channel RyR2 [8]) and JPH2, which tether jSR and T-tubule membranes, are identified along with RyR2 within the denser sucrose fractions. This provides an additional confirmation of the retained stability of physiological protein–protein interactions of the dyadic structure.

Non-SR elements, such as the sarcomeric contractile fibrils and mitochondria, are also fractionated by the sucrose density gradient. Mitochondrial contaminants, instead, are much larger and denser than SR vesicles due to their double-membrane structure and the presence of mitochondrial proteins and sediment within the 50% (w/v) sucrose fraction.

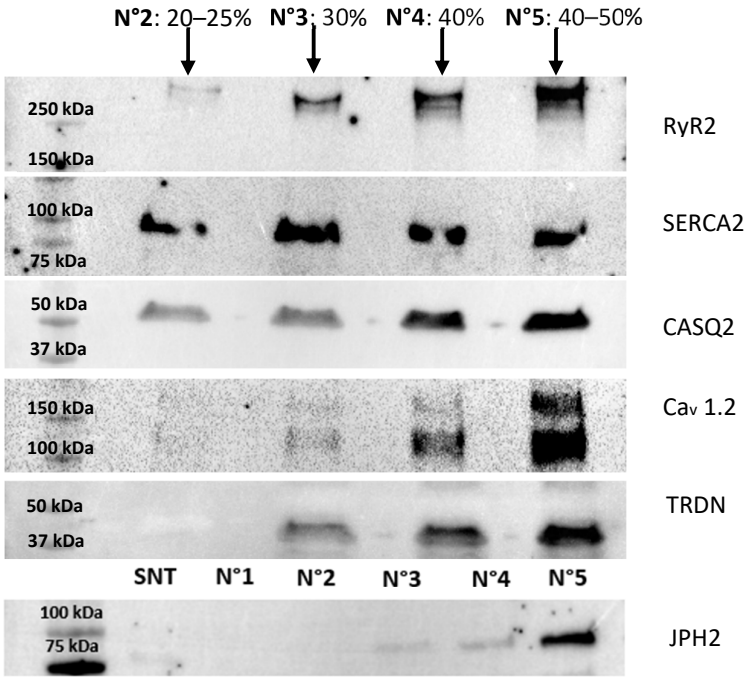

Figure 5. Western blot analysis of fractions 2, 3, 4, and 5 from the sucrose density gradient. The analysis highlights the distribution of proteins across the gradient, with the highest enrichment of the target proteins observed in fraction 5, consistent with the expected localization of SR-derived vesicles containing junctional SR components. These results confirm the efficacy of the isolation protocol in separating SR subdomains and concentrating the proteins of interest in fraction 5. The JPH2 membrane was loaded differently from the others, specifically with the supernatant (S) from the vesicle preparation and fraction N°1, which does not contain any proteins. The total protein content of the fractions is n°2 = 119 µg; n°3 = 182 µg; n°4 = 219 µg; and n°5 = 350 µg.

2.3.1. Cryo-EM Analysis

Cryo-electron microscopy (Cryo-EM) was employed to evaluate vesicles' morphology, detect possible contaminants (such as collagen or actin fibers) (see methodological details in Section 4.2.15). Qualitative Cryo-EM imaging shows features that are consistent with RyR2 channels, with their expected shape and massive dimension (27–28 nm) in multiple vesicles [11] (Figure 6).

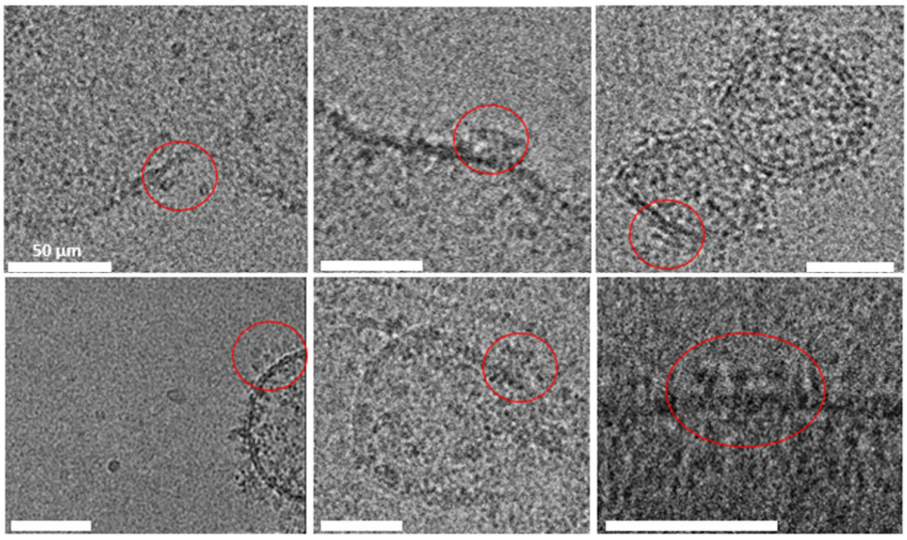

Figure 6. Cryo-electron microscopy images of jSR vesicles. The well-preserved membrane integrity indicates successful isolation and preparation, highlighting the suitability of the protocol for structural studies of jSR-associated proteins. RyR2 channels are circled in red; the scale bar for all pictures is 50 µm.

2.3.2. Relative Quantification of jSR Vesicles

Fraction 5 of the sucrose density gradient, enriched in jSR components, was subjected to MS analysis as previously described (see Section 2.2.2). To evaluate the degree of enrichment, we compared this fraction to three SR-enriched samples, each derived from an individual mouse heart (not subjected to sucrose gradient fractionation). MS data reveal a general reduction in contaminant proteins, such as cytoplasmic and plasma membrane-associated proteins (Figure 7). These results suggest that the sucrose density gradient can serve to further enrich the sample for the jSR subcellular compartment.

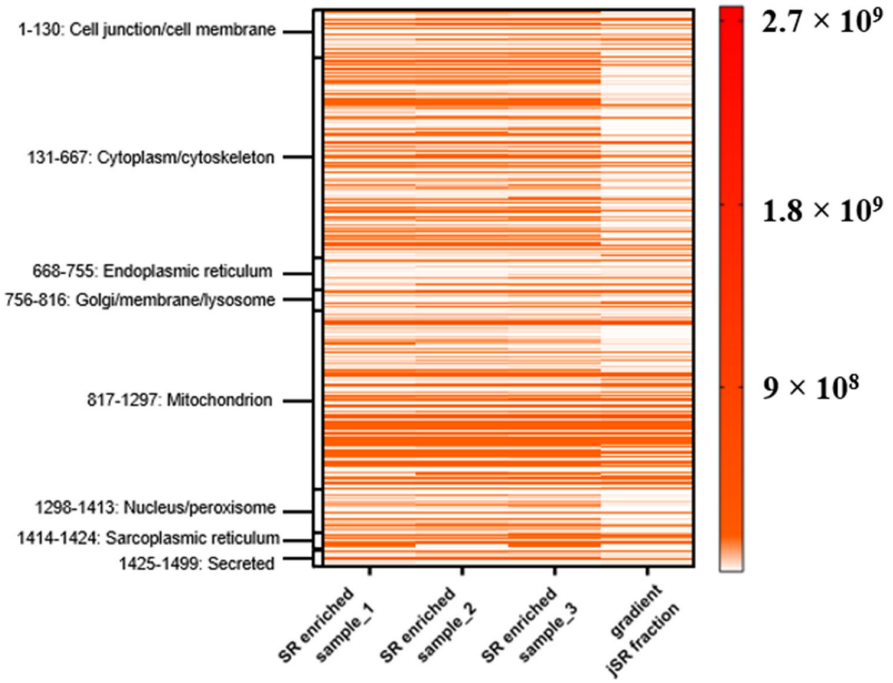

Figure 7. Heat map of protein intensity across three SR-enriched samples (each from n = 1 mouse heart) and the sucrose gradient fraction (from n = 4 mouse hearts). Proteins were grouped according to their annotated subcellular localization. Each row represents a protein, and the color intensity reflects MS-based quantification (label-free intensities), according to the color legend bar. The fourth column ("gradient") corresponds to fraction 5 of the sucrose density gradient.

To provide a more detailed view of the enrichment of SR components, we inspected a subset of selected proteins of interest from the jSR and lSR (Figure 8).

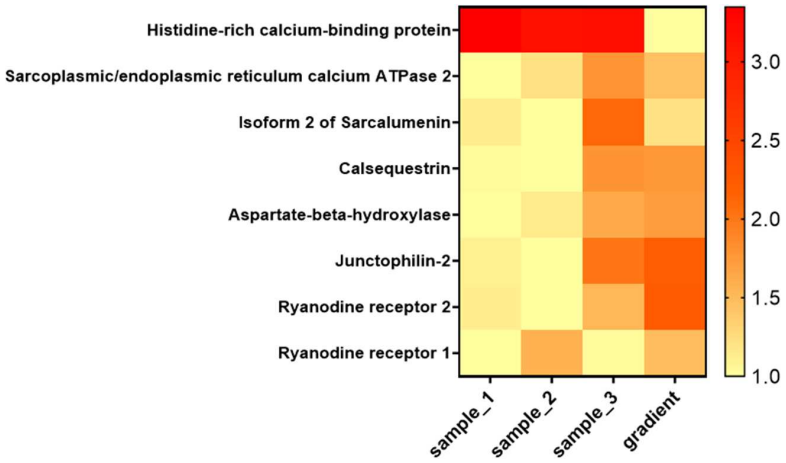

Figure 8. Heat map showing the relative abundance of selected junctional SR proteins across SR-enriched samples and the sucrose gradient fraction. The heat map includes key proteins localized to the jSR and lSR. Values represent intensities from MS analysis normalized over the minimum value.

According to the data presented in Figure 8, proteins specifically localized to the jSR are clearly enriched in the corresponding sucrose gradient fraction. In contrast, the relative abundance of other SR proteins, such as HRC and Sarcalumenin, is reduced in this fraction.

3. Discussion

We here present a protocol for the enrichment of jSR vesicles from a single murine heart, achieving a purity and reproducibility that allow quantification of low-abundance jSR proteins with Mass Spectrometry. Our approach addresses key limitations of traditional methods, such as variability in homogenization and insufficient resolution of vesicle subtypes, resulting in a robust technique for preparing jSR-enriched fractions suitable for downstream proteomic analyses.

Compared to previous protocols, our method introduces critical improvements that enhance preservation of membrane stability. Indeed, as this enrichment protocol employs a single murine heart, it significantly reduces the amount of biological material usually required [39,40].

These vesicles also preserve the structural integrity of jSR proteins, which is a fundamental step for the study of membrane protein complexes. The observed distribution of key SR proteins, such as RyR2, CASQ2, SERCA, TRDN, and JNT, aligns with their known localization in junctional and longitudinal SR subdomains, validating the efficiency of the protocol in maintaining protein co-assembly and native membrane associations.

We expect this protocol will set the basis for future studies to address the characterization of the SR or jSR proteome across different animal models, either for a comparison of the physiological scenario across different species, or to identify alterations associated with specific genetic or physiological conditions.

Integrating this protocol with more advanced MS and imaging techniques may help uncover novel protein interactions and regulatory pathways within the jSR. Such investigations could ultimately lead to the identification of novel therapeutic targets among these jSR resident proteins.

4. Materials and Methods

4.1. Materials

- Minilys® beads-beater (Bertin technologies, Montigny-le-Bretonneux, France)
- 2.8 mm zirconium oxide beads (Bertin technologies)
- 2 mL reinforced tubes (Bertin technologies)
- HERMLE Z 216 MK mini centrifuge
- 100 µm cell strainer
- OPTIMA MAX-XP Beckman Coulter; TLA-120.2 rotor
- Hamilton syringe 500 µL
- Pierce BCA Protein Assay Kit (Thermo scientific)
- OPTIMA XPN 90; SW 41 Ti rotor
- Ultra-clear centrifuge tubes (14 × 89 mm) (Beckman Coulter, Brea, CA, USA)
- Polycarbonate centrifuge tubes (11 × 34 mm) (Beckman Coulter)
- Primo multiwell plate 96 well, flat bottom (Euroclone, Milan, Italy)
- NanoQuant spectrophotometer (infinite F200 pro, Tecan, Männedorf, Switzerland)
- Laemmli sample buffer 4× (BIORAD, Hercules, CA, USA)
- Mini-PROTEAN TGX Stain-Free Gels (BIORAD)
- Trans-Blot Turbo Transfer Pack (Mini format 0.2 µm PVDF) (BIORAD)
- Trans-blot turbo (BIORAD)
- 10× TBS (BIORAD)
- Tween 20 (BIORAD)

- Precision Plus Protein Standards (Dual Color) (BIORAD)
- Homogenization Buffer:
  - 0.5 mM EDTA
  - 20 mM $Na_4O_7P_2$
  - 20 mM NaH_2PO_4
  - 1 mM $MgCl_2$
  - 10% (w/v) sucrose
  - EDTA-free protease inhibitors (Sigma Aldrich, Saint Louis, MO, USA)
- Sucrose-Phase buffers:
  - 0.5 mM EDTA
  - 20 mM $Na_4O_7P_2$
  - 20 mM NaH_2PO_4
  - 1 mM $MgCl_2$
  - 20–25–30–40–50% (w/v) sucrose
- Resuspension Buffer:
  - 0.5 mM EDTA
  - 20 mM $Na_4O_7P_2$
  - 20 mM NaH_2PO_4
  - 1 mM $MgCl_2$
  - 10% (w/v) sucrose
  - 400 mM KCl
  - EDTA-free protease inhibitors (Sigma Aldrich)
- Dilution Buffer:
  - 0.5 mM EDTA
  - 20 mM $Na_4O_7P_2$
  - 20 mM NaH_2PO_4
  - 1 mM $MgCl_2$
  - 400 mM KCl
  - EDTA-free protease inhibitors (Sigma Aldrich)

4.2. Methods

4.2.1. Animal Studies

All animal studies were conducted in compliance with the EU Directive 2010/63/EU and according to the Committee for animal well-being of the University of Pavia.

The animal study protocol was approved by the Italian Ministry of Health; protocol code 223/2023-PR; date of approval 17 March 2023.

4.2.2. Tissue Preparation

- Flash-freeze the tissue (mouse heart) by placing it in a reinforced tube already containing 6 zirconium oxide beads and then rapidly place it into liquid nitrogen.
- Extract the tube after at least 5 min and place it on ice.
- Homogenize for 4 cycles of 30 s (with 30 s of pause in between on ice) at 5000 rpm using a Minilys® beads-beater in 1.5 mL of Homogenization Buffer. Tubes shall be filled to their maximum volume to minimize the formation of air bubbles, which could compromise tissue integrity during homogenization.

4.2.3. Centrifugation

- Centrifuge homogenate (including the beads) in a pre-cooled mini-centrifuge at 4 °C at 9000× g (HERMLE Z 216 MK mini centrifuge) for 20 min.

- Pipette the supernatant through a 100 μm cell strainer positioned on top of a 50 mL Falcon, positioned on ice.

4.2.4. Ultracentrifugation

- Move the filtered supernatant to a 1.5 mL polycarbonate centrifuge tube and ultracentrifuge it at 4 °C for 1 h at 200,000× *g* (Beckman Coulter OPTIMA MAX-XP, TLA-120.2 rotor).

4.2.5. Pellet Resuspension

- Remove about 1 mL of supernatant with a 200 μL micropipette, without touching the pellet. Always keep the sample on ice.
- Resuspend the remaining pellet carefully in 200 μL of Resuspension Buffer using a 500 μL Hamilton syringe.

4.2.6. Protein Quantification

- To determine the protein concentration of each sample using Pierce BCA Protein Assay Kit (Thermo Scientific), mix 5 μL of sample with 5 μL of SDS 10% (*w*/*v*) in a dedicated 0.5 mL tube.
- Prepare a serial 1:1 dilution of albumin (BSA) standards, starting from a maximum concentration of 2 mg/mL.
- Prepare BCA working reagents (WR) according to manufacturer instructions: Use the following formula to determine the total volume of WR required for the assay: (# standards + # unknowns) × (# replicates) × (volume of WR per sample) = total volume WR required.
- Prepare WR by mixing 50 parts of BCA reagent A with 1 part of BCA reagent B (50:1, Reagent A:B).
- Put 190 μL of WR and 10 μL of BSA standards and sample into a 96 multiwell plate, flat-bottom.
- Cover the plate and incubate at 37 °C for 20 min.
- Set the spectrophotometer (NanoQuant) to 595 nm absorbance.
- Prepare a standard curve by plotting the 595 nm measurement for each BSA standard vs. its concentration in μg/mL. Use the standard curve to determine the protein concentration of each unknown sample.

4.2.7. Sucrose Density Gradient

- Starting from the 50% (*w*/*v*) sucrose buffer, layer with a P200 micropipette 1 mL of each Sucrose-Phase Buffer in decreasing sucrose percentage order (i.e., the order is 50%, 40%, 30%, 25%, and 20% (*w*/*v*) sucrose). Each sucrose-containing buffer has to be layered with care, avoiding mixing with other phases, in an ultra-clear centrifuge tube. The interfaces between the phases should be visible under a source of light.
- The sample (previously resuspended in 10% sucrose buffer, as specified for Resuspension Buffer) is layered on top of the sucrose gradient.
- Ultracentrifuge at 4 °C for 1 h at 100,000× *g* in a swinging-bucket rotor (OPTIMA XPN 90; SW 41 Ti rotor).

4.2.8. Fractionation

- Fractionate the sucrose density gradient by carefully removing successive layers from the top of the tube with a micropipette. The volume of each fraction is 1 mL for a total of N = 6 fractions. Position each fraction within a 1.5 mL polycarbonate centrifuge tube.

4.2.9. Sucrose Removal

- Ultracentrifuge all fractions at 4 °C for 1.5 h at 200,000× g using an OPTIMA MAX-XP ultracentrifuge (TLA-120.2 rotor) in a polycarbonate centrifuge tube. This step is critical because residual sucrose could interfere with downstream processes or analyses, such as Mass Spectrometry.

4.2.10. jSR Vesicles Resuspension

- Remove the supernatant of all fractions with a micropipette, without touching the pellet.
- Resuspend the resulting pellet in 200 µL of Dilution Buffer with a 500 µL Hamilton syringe on ice. Samples can be flash-frozen in liquid nitrogen and then stored at −80 °C, before further analysis.
- The total protein content from each fraction is measured using the Pierce BCA Protein Assay Kit (Thermo Scientific). The first and last fractions of the gradient (the lightest contains 10% of sucrose; the heaviest contains 50% of sucrose) should be devoid of proteins, and thus can be discarded after protein quantification.

4.2.11. SDS-PAGE and Western Blot

- Take 30 µg of the total protein sample. Mix with Laemmli Sample Buffer with 1 part of buffer and 3 parts of sample, then incubate at 90 °C for 5 min.
- Run the acrylamide precast gel until the dye front reaches the reference line.
- Place the PVDF Mini membrane and bottom stack on the cassette base for the transfer.
- Place gel on top of the membrane.
- Place the second wetted transfer stack on top of the gel.
- Close and lock the cassette lid and insert it into the instrument (Trans-blot Turbo, BIO-RAD, Hercules, CA, USA) and begin transfer with the following program: 25 limit (V); 1.3 const (A); 7 time (min).
- Carefully transfer the membrane to a suitable container to proceed with the following steps.
- Leave the membrane for 1 h with 5% milk in Tris-buffered saline with 1% of Tween 20 (TBS-T) (w/v).
- Wash the membrane at least 3 times, 5 min each, with a suitable amount of TBS-T buffer.
- Incubate the membrane with the desired primary antibody. We suggest, especially for the CRU primary antibody, overnight incubation for a good resolution.
- Wash the membrane with TBS-T for 2 h, changing the buffer at least 3 times.
- Incubate the membrane with the secondary antibody for 1 h.
- Wash the membrane with TBS-T for 1 h, changing the buffer at least 3 times.

4.2.12. MS Sample Processing and Digestion

The sample (30 µg of proteins, quantified with Pierce BCA Protein Assay Kit Thermo Scientific), according to the procedure provided in Section 4.2.6, was processed with 45.5 µL of 50 mM ammonium bicarbonate. After confirming that the pH was basic, with pH test strips, digestion was carried out by adding the following:

- A total of 3 µL of 100 mM dithiothreitol (DTT) (final concentration: 5 mM), incubated at 55 °C for 30 min.
- A total of 6 µL of 150 mM iodoacetamide (IAA) (final concentration: 5 mM), incubated in the dark for 20 min.
  NB. Excessive IAA may affect the subsequent step of trypsin digestion, and hence any variation in the amount of IAA used may keep this effect into account.
- A total of 5 µL of 0.2 µg/µL trypsin, incubated at 37 °C overnight.

- A total of 1 µL of 100% trifluoroacetic acid (TFA).

After digestion, the sample was purified using a ZipTip (5 µg capacity) as follows:

- A total of 35 µL of the peptide mixture;
- ZipTip purification according to the manufacturer's protocol;
- SpeedVac centrifugation at 30 °C;
- Elution in 20 µL of 0.1% formic acid.

4.2.13. MS Measurement

The samples have been analyzed at UNITECH OMICs (University of Milano, Milan, Italy) using a Dionex Ultimate 3000 nano-LC system (Sunnyvale, CA, USA) connected to an Orbitrap ExplorisTM 240 Mass Spectrometer (Thermo Scientific, Bremen, Germany) equipped with a nano-electrospray ion source. Peptide mixtures were pre-concentrated onto an Acclaim PepMap 100—0.3 × 5 mm C18 (Thermo Scientific) and separated on an EASY-Spray column ES902, 25 cm × 75 µm ID packed with Thermo Scientific Acclaim PepMap RSLC C18, 3 µm, 100 Å using mobile phase A (0.1% formic acid in water) and mobile phase B (0.1% formic acid in acetonitrile 20/80, v/v) at a flow rate of 0.300 µL/min. The temperature was set to 35 °C, and samples were injected in three technical triplicates. The injection volume was 5 µL.

One blank was run between each technical replicate to prevent sample carryover. MS spectra were collected over an m/z range of 375–1500 Da at 120,000 resolution, operating in the data-dependent mode, with a cycle time of 3 sec between master's scans. HCD was performed with a collision energy set to 35 eV. Polarity: positive.

4.2.14. MS Data Processing and Evaluation

Three technical replicates of the same sample were processed with the software Proteome Discoverer 2.5 with the database Mus musculus (sp_tr_incl_isoforms TaxID = 10090_and_subtaxonomies) (v2024-10-02).

Filters applied to the analysis were as follows:

Dynamic Modifications:

- Max. Equal Modifications Per Peptide: 3.
- Max. Dynamic Modifications Per Peptide: 4.
- Dynamic Modification: Oxidation/+15.995 Da (M).

Static Modifications:

- Static Modification: Carbamidomethyl/+57.021 Da (C).

Dynamic Modifications (protein terminus):

- N-Terminal Modification: Acetyl/+42.011 Da (N-Terminus).
- N-Terminal Modification: Met-loss/−131.040 Da (M).
- N-Terminal Modification: Met-loss + Acetyl/−89.030 Da (M).

Filters applied to the results are as follows:

- Protein level: peptide $\geq$ 2.
- Peptide level: Xcorr $\geq$ 2.2; Rank = 1; Confidence = high.
- PSMs level: Xcorr $\geq$ 2.2.

4.2.15. Cryo-EM Imaging

A 3 µL drop of concentrated sample (fraction 5 of the sucrose gradient after buffer exchange) was deposited onto a QuantiFoil copper R2/2 grid and plunge-frozen in liquid ethane. The sample was imaged with a FEI, Talos Artica 200 kV equipped with a FEG and a Falcon 3 camera (FEI).

Supplementary Materials: The following supporting information can be downloaded at: https://www.mdpi.com/article/10.3390/ijms26178602/s1.

Author Contributions: Conceptualization C.D.A. and C.M.; methodology C.D.A., C.M. and R.B.; investigation C.D.A., C.M. and R.B.; writing—original draft preparation C.D.A., C.M. and R.B.; writing—review and editing C.D.A., C.M. and R.B.; supervision S.G.P.; funding acquisition S.G.P. All authors have read and agreed to the published version of the manuscript.

Funding: This research was funded by European Union Next Generation EU, Missione 4 Componente 2—Investimento 1.4—1 CUP CN00000041.

Institutional Review Board Statement: The animal study protocol was approved by the Italian Ministry of Health; protocol code 223/2023-PR; date of approval 17 March 2023.

Informed Consent Statement: Not applicable.

Data Availability Statement: Data from this protocol are available upon request to the authors.

Acknowledgments: Part of this work was carried out in UNITECH OMICs, an advanced core facility established by the Università degli Studi di Milano; the instrument used for this study was funded by Regione Lombardia, regional law n° 9/2020, resolution n° 3776/2020.

Conflicts of Interest: The authors declare no conflicts of interest.

Abbreviations

The following abbreviations are used in this manuscript:

CASQ2	Calsequestrin 2
CICR	Calcium-Induced Calcium-Release
CPVT	Catecholaminergic Polymorphic Ventricular Tachycardia
CRU	Ca^{2+} Release Unit
ECC	Excitation–Contraction Coupling
HRC	Histidine-Rich Calcium-Binding Protein
JNT	Junctin
JPH2	Junctophilin 2
jSR	Junctional Sarcoplasmic Reticulum
lSR	Longitudinal Sarcoplasmic Reticulum
MS	Mass Spectrometry
RyR2	Ryanodine Receptor type 2
SDS	Sodium Dodecyl Sulfate
SERCA	Sarco(endo)plasmic Reticulum Ca2—ATPase
S	Supernatant
SR	Sarcoplasmic Reticulum
TBS	Tris-Buffered saline
TRDN	Triadin
VT	Ventricular Arrhythmia
WB	Western Blot
WT	Wild-Type

References

1. Flucher, B.E.; Takekura, H.; Franzini-Armstrong, C. Development of the excitation-contraction coupling apparatus in skeletal muscle: Association of sarcoplasmic reticulum and transverse tubules with myofibrils. *Dev. Biol.* **1993**, *160*, 135–147. [CrossRef] [PubMed]
2. Franzini-Armstrong, C. Structure of sarcoplasmic reticulum. *Fed. Proc.* **1980**, *39*, 2403–2409. [PubMed]
3. Fleischer, S.; Inui, M. Biochemistry and biophysics of excitation-contraction coupling. *Annu. Rev. Biophys. Biophys. Chem.* **1989**, *18*, 333–364. [CrossRef] [PubMed]

4. Sorrentino, V. Sarcoplasmic reticulum: Structural determinants and protein dynamics. *Int. J. Biochem. Cell Biol.* **2011**, *43*, 1075–1078. [CrossRef] [PubMed]
5. Rossini, M.; Filadi, R. Sarcoplasmic Reticulum-Mitochondria Kissing in Cardiomyocytes: Ca^{2+}, ATP, and Undisclosed Secrets. Front. *Cell Dev. Biol.* **2020**, *8*, 532. [CrossRef] [PubMed]
6. Guttipatti, P.; Saadallah, N.; Ji, R.; Avula, U.M.R.; Goulbourne, C.N.; Wan, E.Y. Quantitative 3D Electron Microscopy Characterization of Mitochondrial Structure, Mitophagy, and Organelle Interactions in Murine Atrial Fibrillation. *J. Struct. Biol.* **2024**, *216*, 108110. [CrossRef] [PubMed]
7. Bers, D.M.; Shannon, T.R. Calcium movements inside the sarcoplasmic reticulum of cardiac myocytes. *J. Mol. Cell Cardiol.* **2013**, *58*, 59–66. [CrossRef] [PubMed] [PubMed Central]
8. Eisner, D.A.; Caldwell, J.L.; Kistamás, K.; Trafford, A.W. Calcium and Excitation-Contraction Coupling in the Heart. *Circ. Res.* **2017**, *121*, 181–195. [CrossRef] [PubMed] [PubMed Central]
9. Ríos, E.; Ma, J.J.; González, A. The mechanical hypothesis of excitation-contraction (EC) coupling in skeletal muscle. *J. Muscle Res. Cell Motil.* **1991**, *12*, 127–135. [CrossRef] [PubMed]
10. Arvanitis, D.A.; Vafiadaki, E.; Sanoudou, D.; Kranias, E.G. Histidine-Rich Calcium Binding Protein: The New Regulator of Sarcoplasmic Reticulum Calcium Cycling. *J. Mol. Cell Cardiol.* **2011**, *50*, 43–49. [CrossRef]
11. Franzini-Armstrong, C.; Protasi, F.; Tijskens, P. The assembly of calcium release units in cardiac muscle. *Ann. N. Y. Acad. Sci.* **2005**, *1047*, 76–85. [CrossRef] [PubMed]
12. Rossi, A.E.; Dirksen, R.T. Sarcoplasmic reticulum: The dynamic calcium governor of muscle. *Muscle Nerve* **2006**, *33*, 715–731. [CrossRef] [PubMed]
13. Rani, S.; Park, C.S.; Sreenivasaiah, P.K.; Kim, D.H. Characterization of Ca^{2+}-Dependent Protein-Protein Interactions within the Ca^{2+} Release Units of Cardiac Sarcoplasmic Reticulum. *Mol. Cells* **2016**, *39*, 149–155. [CrossRef] [PubMed] [PubMed Central]
14. Reid, D.S.; Tynan, M.; Braidwood, L.; Fitzgerald, G.R. Bidirectional tachycardia in a child. A study using His bundle electrography. *Br. Heart J.* **1975**, *37*, 339–344. [CrossRef] [PubMed]
15. Coumel, P.F.J.; Lucet, V.; Attuel, P. Catecholamine-induced severe ventricular arrhythmias with Adams-Stokes syndrome in children: Report of four cases. *Br. Heart J.* **1978**, *40*, 28–37.
16. Denegri, M.; Avelino-Cruz, J.E.; Boncompagni, S.; De Simone, S.A.; Auricchio, A.; Villani, L.; Volpe, P.; Protasi, F.; Napolitano, C.; Priori, S.G. Viral gene transfer rescues arrhythmogenic phenotype and ultrastructural abnormalities in adult calsequestrin-null mice with inherited arrhythmias. *Circ. Res.* **2012**, *110*, 663–668. [CrossRef] [PubMed]
17. Cacheux, M.; Fauconnier, J.; Thireau, J.; Osseni, A.; Brocard, J.; Roux-Buisson, N.; Brocard, J.; Fauré, J.; Lacampagne, A.; Marty, I. Interplay between Triadin and Calsequestrin in the Pathogenesis of CPVT in the Mouse. *Mol. Ther.* **2020**, *28*, 171–179. [CrossRef] [PubMed] [PubMed Central]
18. Priori, S.G.; Napolitano, C.; Tiso, N.; Memmi, M.; Vignati, G.; Bloise, R.; Sorrentino, V.; Danieli, G.A. Mutations in the cardiac ryanodine receptor gene (hRyR2) underlie catecholaminergic polymorphic ventricular tachycardia. *Circulation* **2001**, *103*, 196–200. [CrossRef] [PubMed]
19. Henriquez, E.; Hernandez, E.A.; Mundla, S.R.; Wankhade, D.H.; Saad, M.; Ketha, S.S.; Penke, Y.; Martinez, G.C.; Ahmed, F.S.; Hussain, M.S. Catecholaminergic Polymorphic Ventricular Tachycardia and Gene Therapy: A Comprehensive Review of the Literature. *Cureus* **2023**, *15*, e47974. [CrossRef] [PubMed] [PubMed Central]
20. Lahat, H.; Pras, E.; Olender, T.; Avidan, N.; Ben-Asher, E.; Man, O.; Levy-Nissenbaum, E.; Khoury, A.; Lorber, A.; Goldman, B.; et al. A missense mutation in a highly conserved region of CASQ2 is associated with autosomal recessive catecholamine-induced polymorphic ventricular tachycardia in Bedouin families from Israel. *Am. J. Hum. Genet.* **2001**, *69*, 1378–1384. [CrossRef] [PubMed] [PubMed Central]
21. Marabelli, C.; Santiago, D.J.; Priori, S.G. The Structural-Functional Crosstalk of the Calsequestrin System: Insights and Pathological Implications. *Biomolecules* **2023**, *13*, 1693. [CrossRef] [PubMed] [PubMed Central]
22. Priori, S.G.; Mazzanti, A.; Santiago, D.J.; Kukavica, D.; Trancuccio, A.; Kovacic, J.C. Precision Medicine in Catecholaminergic Polymorphic Ventricular Tachycardia: JACC Focus Seminar 5/5. *J. Am. Coll. Cardiol.* **2021**, *77*, 2592–2612. [CrossRef] [PubMed]
23. Sanslone, W.R.; Bertrand, H.A.; Yu, B.P.; Masoro, E.J. Lipid Components of Sarcotubular Membranes. *J. Cell. Physiol.* **1972**, *79*, 97–101. [CrossRef]
24. Carvajal, C.; Yan, J.; Nani, A.; DeSantiago, J.; Wan, X.; Deschenes, I.; Ai, X.; Fill, M. Isolated Cardiac Ryanodine Receptor Function Is Species Specific. *J. Membr. Biol.* **2024**, *257*, 25–36. [CrossRef]
25. Zissimopoulos, S.; Seifan, S.; Maxwell, C.; Williams, A.J.; Lai, F.A. Disparities in the Association of the Ryanodine Receptor and the FK506-Binding Proteins in Mammalian Heart. *J. Cell Sci.* **2012**, *125*, 1759–1769. [CrossRef]
26. Gross, R.W. Identification of Plasmalogen as the Major Phospholipid Constituent of Cardiac Sarcoplasmic Reticulum. *Biochemistry* **1985**, *24*, 1662–1668. [CrossRef] [PubMed]
27. Maulik, N.; Bagchi, D.; Ihm, W.J.; Cordis, G.A.; Das, D.K. Fatty Acid Profiles of Plasmalogen Choline and Ethanolamine Glycerophospholipids in Pig and Rat Hearts. *J. Pharm. Biomed. Anal.* **1995**, *14*, 49–56. [CrossRef]

28. Murphy, R.M.; Mollica, J.P.; Beard, N.A.; Knollmann, B.C.; Lamb, G.D. Quantification of Calsequestrin 2 (CSQ2) in Sheep Cardiac Muscle and Ca^{2+}-Binding Protein Changes in CSQ2 Knockout Mice. *Am. J. Physiol. Heart Circ. Physiol.* **2011**, *300*, H595–H604. [CrossRef]
29. Giroud, S.; Frare, C.; Strijkstra, A.; Boerema, A.; Arnold, W.; Ruf, T. Membrane Phospholipid Fatty Acid Composition Regulates Cardiac SERCA Activity in a Hibernator, the Syrian Hamster (*Mesocricetus auratus*). *PLoS ONE* **2013**, *8*, e63111. [CrossRef]
30. Linscheid, N.; Santos, A.; Poulsen, P.C.; Mills, R.W.; Calloe, K.; Leurs, U.; Ye, J.Z.; Stolte, C.; Thomsen, M.B.; Bentzen, B.H.; et al. Quantitative Proteome Comparison of Human Hearts with Those of Model Organisms. *PLoS Biol.* **2021**, *19*, e3001144. [CrossRef]
31. Chen, W.; Kudryashev, M. Structure of RyR1 in native membranes. *EMBO Rep.* **2020**, *21*, e49891. [CrossRef] [PubMed] [PubMed Central]
32. Lai, F.A.; Erickson, H.P.; Rousseau, E.; Liu, Q.Y.; Meissner, G. Purification and reconstitution of the calcium release channel from skeletal muscle. *Nature* **1988**, *331*, 315–319. [CrossRef] [PubMed]
33. Maurya, S.; Mills, R.W.; Kahnert, K.; Chiang, D.Y.; Bertoli, G.; Lundegaard, P.R.; Duran, M.P.-H.; Zhang, M.; Rothenberg, E.; George, A.L.; et al. Outlining Cardiac Ion Channel Protein Interactors and Their Signature in the Human Electrocardiogram. *Nat. Cardiovasc. Res.* **2023**, *2*, 673–692. [CrossRef] [PubMed]
34. Bers, D. *Excitation-Contraction Coupling and Cardiac Contractile Force*, 2nd ed.; Springer-Science: Berlin/Heidelberg, Germany, 2001.
35. Jones, L.R.; Besch, H.R., Jr.; Fleming, J.W.; McConnaughey, M.M.; Watanabe, A.M. Separation of vesicles of cardiac sarcolemma from vesicles of cardiac sarcoplasmic reticulum. Comparative biochemical analysis of component activities. *J. Biol. Chem.* **1979**, *254*, 530–539. [CrossRef] [PubMed]
36. Raschke, S.; Guan, J.; Iliakis, G. Application of alkaline sucrose gradient centrifugation in the analysis of DNA replication after DNA damage. *Methods Mol. Biol.* **2009**, *521*, 329–342. [CrossRef] [PubMed]
37. Mitchell, R.D.; Palade, P.; Fleischer, S. Purification of morphologically intact triad structures from skeletal muscle. *J. Cell Biol.* **1983**, *96*, 1008–1016. [CrossRef] [PubMed] [PubMed Central]
38. Jones, L.R.; Cala, S.E. Biochemical evidence for functional heterogeneity of cardiac sarcoplasmic reticulum vesicles. *J. Biol. Chem.* **1981**, *256*, 11809–11818. [CrossRef] [PubMed]
39. Rosemblatt, M.; Hidalgo, C.; Vergara, C.; Ikemoto, N. Immunological and biochemical properties of transverse tubule membranes isolated from rabbit skeletal muscle. *J. Biol. Chem.* **1981**, *256*, 8140–8148. [CrossRef] [PubMed]
40. Ohlendieck, K.; Ervasti, J.M.; Snook, J.B.; Campbell, K.P. Dystrophin-glycoprotein complex is highly enriched in isolated skeletal muscle sarcolemma. *J. Cell Biol.* **1991**, *112*, 135–148. [CrossRef] [PubMed] [PubMed Central]

THE FUNCTIONAL UNIT OF CARDIAC CALSEQUESTRIN IS THE DIMER

Marabelli C.[1,2,3*], Di Antonio C.[1], Santiago D.J.[3], Pirana E.[4], Forneris F.[4], Priori S.G.[1,2,3]

[1] Department of Molecular Medicine, University of Pavia, 27100 Pavia, Italy;
[2] Laboratory of Molecular Cardiology, IRCCS ICS Maugeri, 27100 Pavia, Italy;
[3] Centro Nacional de Investigaciones Cardiovasculares Carlos III (CNIC), 28029 Madrid, Spain
[4] Department of Biology and Biotechnology, University of Pavia, 27100 Pavia, Italy.
* Correspondence: chiara.marabelli02@universitadipavia.it

Introduction

Calsequestrin (CASQ) is critical to the Ca^{2+}-mediated process of excitation-contraction coupling (ECC) in skeletal and cardiac muscle cells. It is the principal Ca^{2+}-binding protein in the lumen of the junctional Sarcoplasmic Reticulum (jSR), where it regulates -either directly and indirectly- the opening and refractoriness of the ryanodine receptor (RyR) Ca^{2+} release channel, and thereby controlling contraction initiation and termination. In vivo, CASQ function is intimately linked to its Ca^{2+}-dependent assembly into filamentous electron-dense structures within the jSR[1–3], that disassemble upon Ca^{2+} depletion. Loss of these luminal jSR polymeric structures is a characteristic of pathological conditions [1,3,4].

CASQ Ca^{2+}-driven polymerization pairs with its low-millimolar affinity, high-capacity Ca^{2+}-binding properties (up to 60 or 80 Ca^{2+} ions per molecule, depending on the isoform)[5]. Unlike typical Ca^{2+}-binding proteins, CASQ lacks EF-hand motifs, or defined acidic Ca^{2+}-binding sites. At least one fourth of CASQ residues are glutamates or aspartates, whose charge neutralization by Ca^{2+} ions allows the compaction of CASQ thioredoxin-fold globular core (Figure 1A). This globular core features a highly negative surface, and is flanked by two flexible terminal regions that are functionally essential (Figure 1). The N-terminal portion enables domain swapping and locks CASQ in the crystallographic dimeric (Figure 1B)[3,6–8]. In the traditional model of CASQ2 polymerization, this "front-to-front" dimer forms via Ca^{2+} -mediated bridges. Additional "back-to-back" inter-dimer contacts observed in some crystal lattices have been proposed to drive Ca^{2+}-dependent polymerization. The highly acidic and flexible C-terminal tail (Figure 1C), shapes the isoform-specific kinetics of Ca^{2+}-dependent polymerization and Ca^{2+}-binding capacities[9–12].

CASQ polymerization is classically viewed as a Ca^{2+}-driven sequential process, where monomer compaction enables dimerization, followed by tetramerization and the formation of a ribbon-like, linear polymers. However, this model does not justify how multiple missense mutations, spread all over the protein's surface[3], cause severe pathologies such as Tubular Aggregate Myopathies or Malignant Hyperthermia for the skeletal CASQ1 [13–16], or the highly lethal Catecholaminergic Polymorphic Ventricular Tachycardia type 2 (CPVT2) for the cardiac CASQ2 [8,17–20].

The CASQ polymerization model has been suggested mainly by *in vitro* turbidity measurements, which measure protein aggregation via light-scattering at 350 or 600 nm wavelengths, where absorption by proteins is minimal. Although turbidimetry captures the kinetics of protein multimerization it cannot discriminate the nature of the light-scattering bodies, such as soluble aggregates or linear fibers[21,22]. This has contributed to the prevailing view on CASQ polymerization as a linear cascade of Ca^{2+}-dependent events: folding, dimerization, tetramerization, and high-order polymerization[1,7,11,23,24].

Also, while the properties of CASQ have been widely studied with reference to the effects induced by Ca^{2+} [6–8,10,11,16,24,25] , the primary ion of interest in the jSR, the roles of other ions have been

far less evaluated. At the same time, recent findings reveal that low millimolar Mg^{2+} can unmask differences in Ca^{2+}-responsiveness across distinct CASQ2 variants[8,24]

Hence, the potential exists to incorporate the role played by other physiologically relevant ions in modulating CASQ folding and polymerization.

In this broad context we comprehensively examined the interplay between ionic strength, protein concentration, and Ca^{2+} abundance in shaping the polymerization of the cardiac isoform CASQ2. Using a combination of turbidimetry, mass photometry (MP), size-exclusion chromatography (SEC), dynamic light scattering (DLS), microscale thermophoresis (MST) and thermal stability assays, we show for the first time that dimerization is an intrinsic property of cardiac CASQ2 rather than being exclusively Ca^{2+}-dependent. Moreover, our data identify a previously uncharacterized Ca^{2+}-dependent switch-like transition from oligomeric to polymeric forms, challenging the traditional view of CASQ polymerization as a stepwise process. Our data indicate that CASQ2 dimers may identify the physiologically relevant, functionally active unit, whose responsiveness to Ca^{2+} integrates additional factors beyond Ca^{2+} abundance.

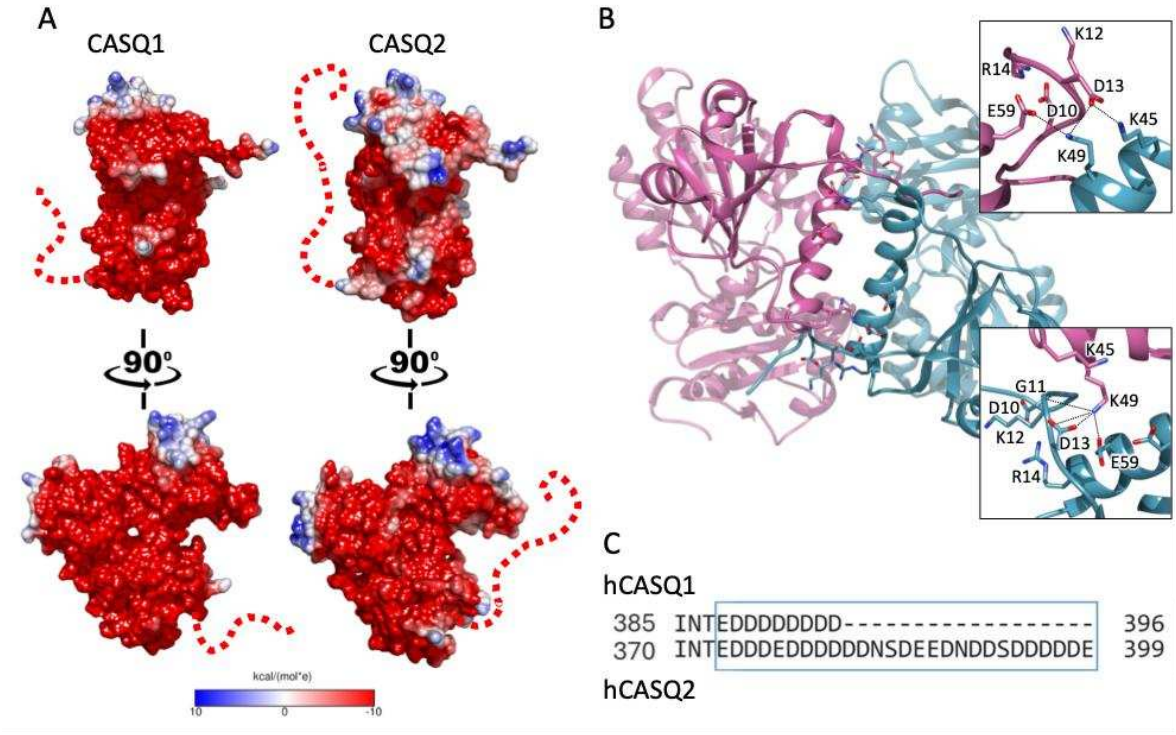

Figure 1. Structural and electrostatic comparison between CASQ1 and CASQ2. A) Electrostatic surface potential maps (±10 kcal/mol·e) of CASQ1 and CASQ2 show highly negative charge distribution across both proteins. The C-terminal tail (dashed red line) has not been modeled in the crystal structures due to its intrinsic disorder, but also includes extensive clusters of negative charges CASQ2 exhibits a more extended acidic tail compared to CASQ1. B) Ribbon representation of the CASQ2 dimer model highlighting two distinct dimeric interfaces (magenta and cyan monomers), with insets showing zoomed views of key interacting residues at the canonical interface regions shaped by the N-terminal segments.**C)** Sequence

alignment of the C-terminal regions of human CASQ1 and CASQ2 underscores the extensive aspartate/glutamate enrichment in CASQ2, which contributes to its highly acidic and disordered nature. The C-terminal, 18-residue long, portion is absent in the skeletal isoform CASQ1.

Results

1. Physiological quantities of K^+ ions support CASQ2 conformational compaction

Published NMR and CD spectra [9,15,26–30] show that Ca^{2+} is orders of magnitude more efficient than monovalent cations in promoting CASQ2 molecular compaction: under low ionic strength conditions (e.g. 20 mM NaCl), 0.3 mM Ca^{2+} triggers a large stabilizing effect on CASQ secondary structure, an effect which is matched by three orders of magnitude higher quantities of K^+ or Na^+ (300 mM). The mechanistic interpretation is that CASQ retains a molten globule state until its negative charges are adequately masked by Ca^{2+} levels comparable to those found within the jSR of muscle cells (0.3-1 mM) [31,32]. In light of accumulating evidence on a ionic-sensitive nature of CASQ2 Ca^{2+}-dependent polymerization[8,24], we sought to investigate the role of the physiologically abundant jSR ions. Among monovalent cations, K^+ is usually present within 120-225 mM range in the cardiomyocyte cytoplasm, whereas the cytosolic concentration of the second most abundant monovalent cation, Na^+, falls in the 5 to 15 mM range[31]. Thus, despite the limited knowledge on the ionic environment of the jSR, the assumption is that CASQ2 is exposed to higher amounts of K^+ rather than Na^+ ions. For this reason, this study focuses on the effect of K^+ ions on CASQ2 Ca^{2+}-dependent polymerization kinetics.

To dissect how K^+ ions affect the conformational compaction of CASQ2 molten globule state, we measured the apparent volume of the CASQ2 monomer by MP, in the presence of varying KCl concentrations. The MP method allows to calculate the size of CASQ2 indirectly, from the light scattering variation produced by single particles in solution that stochastically encounter a measurement surface. As for other experiments, the absence of contamination from Ca^{2+} or other divalent ions was ensured by dialysis in EDTA prior to measurements. Our MP data confirm the expected proportional collapse of CASQ2 size with respect to the ionic strength (Figure 2A, Figure S1). Increasing KCl levels, up to the 150-200 mM range, drive an evident compaction of CASQ2 monomer, so that the apparent solution volume decreases by about 6.4 ± 2.4 kDa with respect to the most relaxed CASQ2 conformation observed in 25 mM KCl (Figure 2A). A similar compaction of CASQ2 is observed when 10 mM $CaCl_2$ is added to a solution containing 50 mM KCl (Figure S2), supporting cooperative effects. Notably, the addition of millimolar amounts of $CaCl_2$ in 200 mM KCl does not trigger any detectable effect (Figure S2). Unexpectedly, the inverse relationship between ionic strength and CASQ2 hydrodynamic size is reversed beyond 200 mM: the apparent volume of CASQ2 increases with ionic strength (Figure 2A). This suggests that extensive charge screening at high salt concentrations may perturb either CASQ2 conformational architecture and/or its hydration shell and thus the apparent volume in solution.

We next explored thermal denaturation assays as a specular method to test the ionic dependence of CASQ2 conformational compaction. By tracking the change in the intrinsic fluorescence of the

protein's tryptophan residues (usually buried in a solvent-inaccessible environment) at increasing temperatures, thermal denaturation assays measure the kinetic of their exposure to the aqueous solvent, which usually mirrors the kinetic of thermally-induced protein unfolding. The temperature at which the highest slope of the denaturation curve is registered defines the melting temperature (t_m). Our analyses of CASQ2 thermal stability in varying KCl concentrations (Figure 2B) reveal a trend similar to that observed for size compaction: the t_m of CASQ2 increases with increasing KCl levels (from 25 to 200 mM). An inflection point in this positive trend is registered at 200 mM KCl, a condition in which the t_m of CASQ2 is higher by 4 °C than that registered in 50 mM KCl (Figure 2C). Taken together, both the volume variation measured by MP (Figures 2A, S2), and the thermal stabilization (Figures 2B-C) demonstrate that 200 mM K^+ maximally support the compaction of CASQ2 tertiary structure.

Counterintuitively, both the apparent volume occupied by CASQ2 (Figures 2A, S2) and the compaction of its hydrophobic core (Figures 2B-C) rise when the ionic strength increases above 200 mM KCl (Figures 2A, 2C). To facilitate the interpretation of these apparently contrasting results we investigated CASQ2's zeta (ζ)-potential, a proxy for exposed surface charges and ionic solvation shell of a particle in solution (Figure 2D). In 10 mM KCl, the abundant CASQ2 negative charges account for a ζ-potential of -400 mV, and become fully neutralized (0 mV) at the physiological concentration of 194 mM [K^+] [31]. Functionally, this implies that in the cellular context, even in the absence of Ca^{2+} ions, CASQ2 negative charges are mostly shielded, allowing proper hydrophobic collapse and conformational packing of the CASQ2 polypeptide chain. The behavior of the ζ-potential versus [K^+] curve is fitted well (R^2 = 0.9990) by a one-site saturation mathematical model, which supports a site-specific neutralization mechanism, where K^+ ions bind directly to a defined number of acidic residues on the CASQ2 surface, rather than diffuse screening. A similar saturable behavior is observed with Na^+ (R^2 = 0.9996, Figure 2D), though at lower than 100 mM concentrations, Na^+ is nearly twice more effective than K^+ at neutralizing the protein's negative surface charge, due to its higher charge density. At higher equimolar levels, both ions ultimately cause charge reversal, (positive ζ-potential values of +35 mV and +14 mV at 500 mM KCl and NaCl, respectively), a consequence of ion accumulation over densely charge surfaces beyond isoelectric neutralization and pairs with formation of a thicker solvation shell around the particles in solution[33]. This effect, observed for KCl concentrations above 200 mM, is consistent with the parallel increase in the apparent molecular volume of CASQ2 monomers (Figure 2A) and with the reduced solvent penetration into the hydrophobic core (Figures 2B-C). Together, all measurements on CASQ2 ion-dependent conformational fluctuations collectively indicate the 194-200 mM [K^+] condition as a critical switch point between insufficient neutralization of polypeptide charges (and reduced stability of the tertiary conformation), and excessive screening of the particle charges (and increased thickness of the solvation layer).

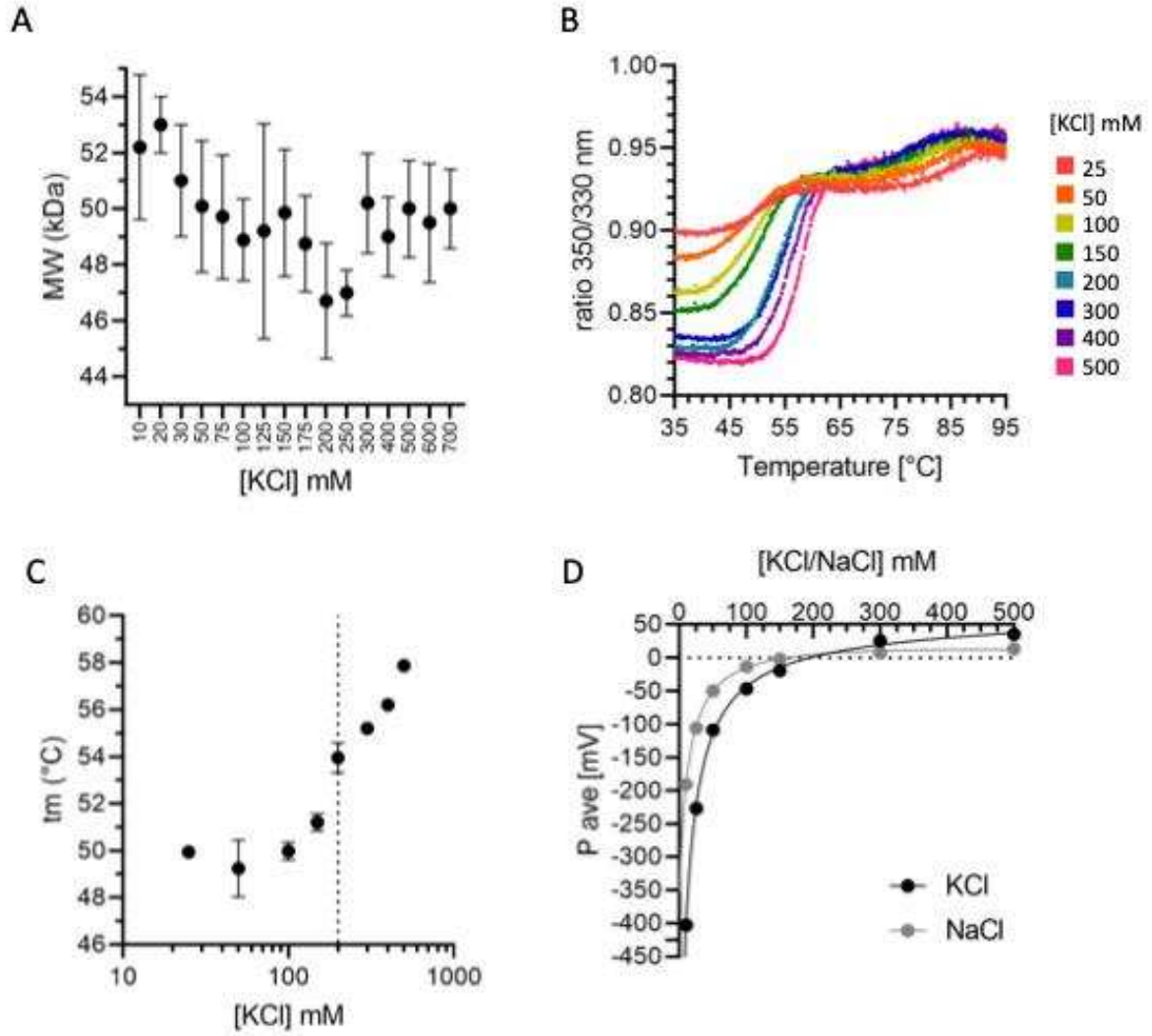

Figure 2. Monovalent cations modulate the tertiary structure and solvation shell of CASQ2. A) CASQ2 size distribution at varying KCl concentrations as determined by Mass Photometry (MP). Higher ionic strength promotes the compaction of the monomer, the smallest particle size being observed at 200 mM KCl (dotted line). Data are presented as median + range from at least three independent measurements. **B)** Thermal denaturation curves for CASQ2 samples under varying KCl concentrations, from which melting temperatures (t_m, expressed in °C) are extrapolated. Data are presented as mean from three independent measurements. **C)** The value of CASQ2 t_m increases rapidly with KCl concentrations up to 200 mM (dotted line), paralleling the increased stabilization of CASQ2 tertiary structure observed in MP experiments. At concentrations higher than 200 mM KCl, the t_m increases further because of the formation of a thicker ionic shell around CASQ2 monomers. Data are presented as mean ± SD from three independent measurements. **D)** ζ-potential measurements of CASQ2 at increasing KCl (black circles) and NaCl (grey circles) concentrations show a progressive reduction in surface charge. At 10 mM KCl and NaCl, the surface potential of CASQ2 is respectively on average -403 mV and -191 mV. A plateau in the positive range begins to emerge after 200 mM KCl and NaCl. At 500 mM KCl and NaCl, the ζ-potential of CASQ2 is respectively on average +35 mV and +13 mV. Data are presented as mean ± SD from three independent measurements.

2. CASQ2 forms dimers at physiological KCl concentrations in the absence of Ca^{2+}

From ζ-potential experiments it appears that repulsive forces among the abundant CASQ2 negative charges are at least partially masked at the physiological concentrations of K^+ of 140-225 mM [31]. Such charge screening might not only affect the monomeric state, but also reduce long-range electrostatic repulsion and thus facilitate inter-monomer interactions even without Ca^{2+}. Notably, most of the crystallographic dimer structures have been solved in the absence of Ca^{2+} or other divalent cations[3,13]. We thus explored whether K^+ ions alone (i.e. in the absence of Ca^{2+}) can support self-assembly of CASQ2. MP experiments confirmed this hypothesis. In 150 and in 200 mM KCl, and in the absence of Ca^{2+}, CASQ2 forms dimeric assemblies already at 10 nM protein concentrations (Figures 3, S1, S3). Lowering KCl increased dimer abundance, suggesting that incomplete electrostatic screening favors non-specific inter-monomer interactions (probably mediated by oppositely charged patches on the protein surface, Figure 1A), whereas neutralization of protein charges dampens these forms of electrostatic attractions, and the thickness of the protein's solvation shell increases their entropic cost. For K^+ levels higher than 150-200 mM, neither positive nor negative effects are observed on the equilibrium between CASQ2 monomers and dimers, and a stable population of Ca^{2+}-free dimers remains equally present (Figures 3A, S1, S3), possibly representing a structurally and functionally relevant CASQ2 pre-polymerization state.

To further characterize these assemblies, we inspected the Size-Exclusion Chromatography (SEC) profiles of CASQ2 at protein concentrations (45 μM) higher than those tested in MP, and under varying ionic conditions (Figures 3B, S4). SEC revealed the existence of multiple forms of Ca^{2+}-free CASQ2 oligomers (dimers, trimers, and tetramers) with distinct sensitivities to the ionic strength: dimers persist even at 200 mM KCl, whereas tetramers, and especially the previously unreported trimeric species, diminish or even vanish as the ζ-potential nears zero (Figures 2D, 4B), consistent with the interpretation that they arise from weak electrostatic interactions that dissolve with charge screening. Collectively, these findings support a model whereby CASQ2 can self- assemble in the absence of its canonical ligand, Ca^{2+}, particularly when its surface is partially but not fully neutralized. However, only a fraction of Ca^{2+}-free CASQ2 dimers is resistant to ionic strength, whereas all other form of Ca^{2+}-free oligomerization are non-specific assemblies rather than programmed intermediates in CASQ2 polymerization pathway.

The properties of CASQ2 self-assembly under physiological conditions were further dissected by MicroScale Thermophoresis (MST). MST quantifies how the thermal-dependent increase in the mobility of fluorescently labeled molecules in solution changes in the presence of a binding partner. A constant amount of fluorescently labeled CASQ2 was incubated with varying concentrations of non-labeled CASQ2 in PBS buffer (containing 137 mM NaCl and 2.7 mM KCl). Consistent with MP data (Figures 3A, S1, S3), MST experiments detected CASQ2 self-assembling within nanomolar levels

(Figure 3C). Remarkably, the MST response did not plateau, but instead increased steadily across the entire concentration range tested, extending into the high micromolar regime (Figure S6). Such continuous signal shift argues against a binary type of dimerization interaction between two specific interfaces, and instead suggests that CASQ2 self-associates via multiple weak, non-exclusive interfaces. This self-association process thus is not the sum of sequential, discrete steps, but a linear continuum of inter-monomer, additive binding events, where the probability of forming productive interactions almost linearly depends on the protein concentration. Supporting this view, SEC analyses showed that injection of identical quantities of CASQ2 at increasing concentrations (via proportionally lower injection volumes), resulted in progressive shifts of the quaternary species toward larger assemblies, consistent with concentration-dependent oligomerization (Figure 3D). This is in line with MP analysis showing that the relative abundance of CASQ2 dimers, trimers, and tetramers (with respect to monomers) is proportional to the experimental concentration (Figure S3B-C). Of note, no high-order polymers were observed neither in MP nor in SEC. Turbidimetric inspection of 2.5 μM CASQ2 under varying ionic conditions did not reveal the presence of any large, light-scattering species (Figure S7). Taken together, these findings indicate that CASQ2 undergoes Ca^{2+}-free self-association under physiological ionic conditions through a continuum of weak, multivalent interactions. Among the multiple electrostatic assemblies observed, a Ca^{2+}-free dimeric assembly form emrges as the most stable species, and may represent a poised structural state primed for rapid Ca^{2+}-induced polymerization.

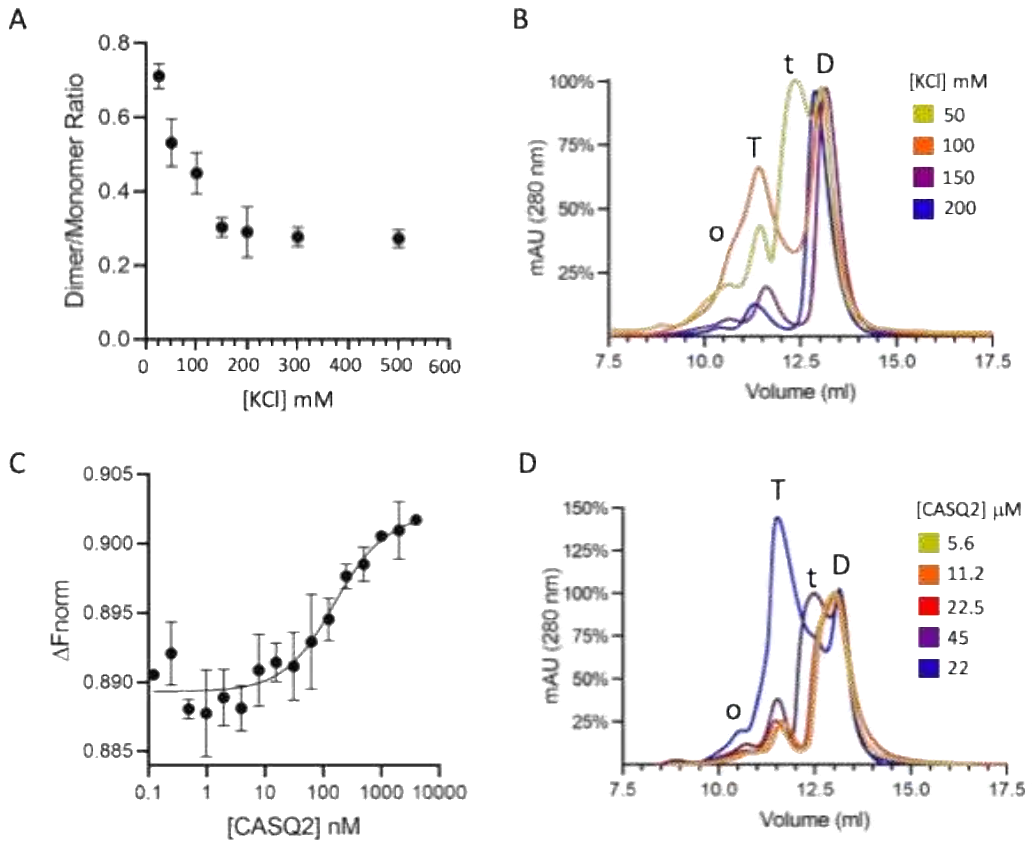

Figure 3. CASQ2 features an oligomerization propensity which is independent of the presence of Ca^{2+}. A) Quantification of dimer-to-monomer ratio from mass photometry (MP) across increasing [KCl], showing that a portion of CASQ2 dimers is significantly destabilized at higher than 100 mM salt concentrations. **B)** SEC analysis of CASQ2 (45 µM) (Superdex 200 10/300 GL column) at increasing KCl concentrations (50 mM, 100 mM, 150 mM, and 200 mM). The identity of elution peaks to dimers (D), trimers (t), tetramers (T), and oligomers (o), is based on the expected molecular weight of the eluted species, calculated from the column size calibration curve (Figure S5). **C)** MicroScale Thermophoresis (MST) analysis of the concentration-dependent self-association of CASQ2 in PBS buffer (containing 137 mM NaCl and 2.7 mM KCl). The increasing thermophoretic signal indicates that CASQ2 begins to form higher-order assemblies already in the nanomolar range. Data are presented as mean ± SD from three independent measurements. **D)** SEC profiles of CASQ2 samples (Superdex 200 10/300 GL column, see Figure S5) at varying protein concentrations (5.6 to 225 µM) running in a Ca^{2+}-free, 50 mM KCl buffer, showing progressive shift from monomers to dimers (D) and tetramers (T) in a concentration-dependent manner. The oligomeric species (o) eluted at volumes accounting for an apparent mass of 200 ± 17 kDa, consistent with CASQ2 pentamers.

3. *The CASQ2 Ca^{2+}-free oligomers compete with Ca^{2+}-driven quaternary assemblies*

The identification of electrostatically-independent Ca^{2+}-free dimers raised the question on their role in the Ca^{2+}-dependent CASQ2 polymerization process. To this aim, we tested the effect of Ca^{2+} on CASQ2 dimerization propensity in MP, at 10 nM protein (i.e. a concentration in which the dimeric species is not dominant). Addition of increasing amounts of Ca^{2+} to CASQ2 in a 50 mM KCl buffer, clearly shifted the equilibrium toward dimerization (Figure 4A), which becomes particularly evident at 20 mM and higher Ca^{2+} concentrations. However, for intermediate Ca^{2+} levels between 1 and 10 mM, there is a subtle dip in the dimer-to-monomer ratio (Figure 3A). This effect becomes more prominent when 25 nM CASQ2 is tested instead than 10 nM (i.e., in a condition in which CASQ2 electrostatically-dependent oligomerization is more favoured, red points in Figure 4B). This suggests a Ca^{2+}-induced destabilization of the electrostatic forms of dimers, similarly to the K+-dependent (Figure 3A). We thus tested whether, by inhibiting electrostatic dimers in higher ionic strength conditions, the positive effect of Ca^{2+} on CASQ2 dimerization would be more pronounced. Under this condition, Ca^{2+} promoted dimerization more strongly, reversing the negative trend seen at lower ionic strength, consistent with reduced competition from weak, electrostatic interactions (blue points in Figures 4B).

We next used SEC to assess the Ca^{2+}-responsivity of CASQ2 Ca^{2+}-free species formed at higher concentrations under increasing ionic conditions (Figure 4C-F). Of note, at these protein concentrations (45 μM), no monomeric species was detected, and the net effect of Ca^{2+} is observable as an increase in tetramers with respect to the dimeric species. Similarly to what is observed in MP, the electrostatic interactions that compete with Ca^{2+}-specific ones (i.e. tetrameric and trimeric species) are maximally inhibited at 200 mM KCl, confirming that these non-specific assemblies are actually not competent for Ca^{2+} binding. Overall, MP and SEC analyses clearly indicate that the Ca^{2+}-driven quaternary assembly of CASQ2 (proceeding from dimers to tetramers, Figure 4F) does not build upon pre-existing electrostatic assemblies, but is rather in competition with them. Taking into account the high physiological concentration of the CASQ2 protein within the jSR compartment (in the 1-4 mM range)[3,5,23], the competition between Ca^{2+}-specific and unspecific charge-driven interactions may be of relevance in shaping the onset of Ca^{2+}-dependent polymerization.

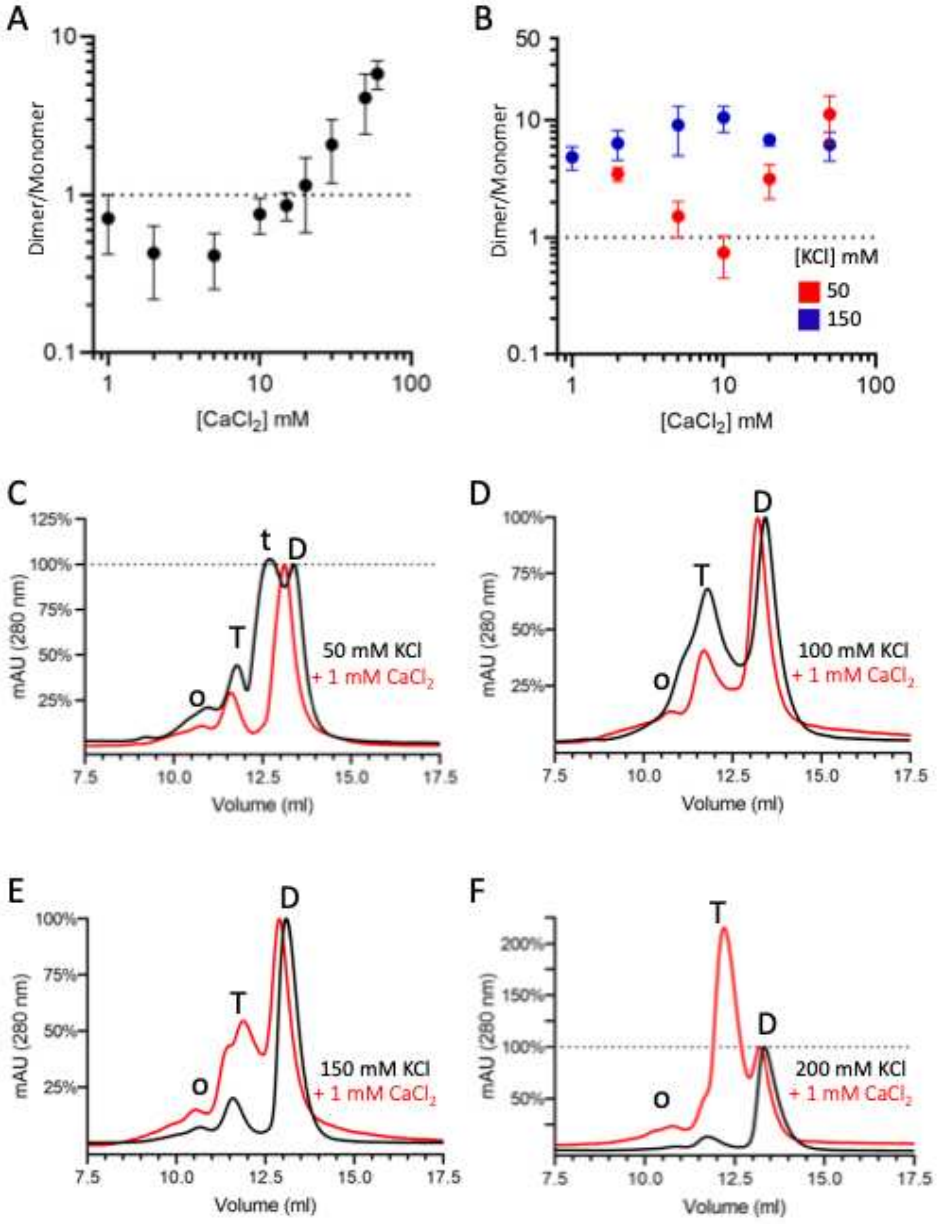

Figure 4. Electrostatic forms of CASQ2 assemblies compete with Ca^{2+}-dependent dimerization and tetramerization. A) Dimer-to-monomer ratio of 10 nM CASQ2 as a function of increasing Ca^{2+} concentrations, as measured by mass photometry (MP). A slight decrease in dimer abundance is observed in the 1–5 mM Ca^{2+} range, followed by a marked increase at concentrations above 10 mM, indicating a threshold for Ca^{2+}-dependent dimer stabilization. Data are presented as mean ± SD from at least two independent measurements performed with the same sample preparation, diluted in the same buffer. **B)** Dimer-to-monomer ratio of 25 nM CASQ2 as a function of increasing Ca^{2+} concentrations, in 50 mM and 200 mM KCl, as measured by mass photometry (MP). A decrease in dimer abundance is observed in the 10 mM Ca^{2+} range, followed by a marked increase at higher concentrations of Ca^{2+}. Data are presented as mean ± SD from at least two independent sample preparations. **C-F)** SEC chromatograms of CASQ2 injected at 2 mg/ml in buffer containing either 50 mM, 100 mM, 150 mM, or 200 mM KCl (black chromatograms). After 1 h incubation in each ionic condition with 1 mM $CaCl_2$, the sample was injected at 2 mg/ml into the SEC running in the respective buffer (containing either 50 mM, 100 mM, 150 mM, or 200 mM KCl and 1 mM $CaCl_2$, red chromatograms). The curves were normalized to the height of the peak of the dimer to facilitate comparison across species: dimer (D), trimer (t), tetramer (T), and oligomer (o).

4. *A complex interplay between electrostatic and Ca^{2+}-specific effects shapes CASQ2 polymerization*

To dissect the interplay between electrostatics and Ca^{2+}-dependent polymerization, we measured CASQ2 turbidity end-point values after exposure to varying Ca^{2+} concentrations under low (10 mM) and moderate (50 mM) KCl (Figure 5A). Polymerization onset occurred at lower Ca^{2+} concentrations in 50 mM KCl (0.1 mM Ca^{2+}) than in 10 mM KCl (0.4 mM Ca^{2+}), indicating that K^+ enhances CASQ2's Ca^{2+} sensitivity. The 0.3 mM difference in sensitivity matches the Ca^{2+} levels needed for CASQ2 folding under low ionic strength conditions[9,15,26–30], suggesting that K^+ facilitates Ca2+- responsiveness at least in part by promoting conformational compaction (Figure S2). In contrast, increasing K+ lowers the turbidimetric response to Ca^{2+} concentrations above 5 mM, a regime that also exhibits a pronounced Ca^{2+} -dependent decline in turbidity (Figure 5A). This convergence suggests that K^+ and Ca^{2+} share a common electrostatic mechanism that, when excessive, destabilizes Ca^{2+}-dependent CASQ2 polymers.

To capture both the positive and negative electrostatic contributions, we analyzed the kinetics of Ca^{2+}-dependent CASQ2 polymerization across a range of ionic strengths. The first prominent effect of K+ is a dual, positive/negative contribution to the maximal turbidity reached after 40 minutes (Figure 5B), whose multiple mechanistic causes became more evident when the experimental timing is extended to 150 minutes (Figure 5C). A sigmoidal growth model fitted all curves obtained at KCl concentrations below 112.5 mM (with an average $R^2 = 0.986 \pm 0.013$, Figure 5C), consistent with a cooperative, nucleation-dependent mechanism. Analysis of fitted plateaus reveals a linear K+-dependent decline in the number, and/or size of Ca2+-dependent polymers, with only the 50-75 mM KCl range showing similar values (Figure S8A), consistent with the fact that electrostatic screening destabilizes Ca2+-dependent polymers.

Not only the polymerization extent, but also the kinetics of polymerization is affected by electrostatics, as the nucleation lag phase is largely extended when [K+]>75 mM (Figure S8B). This effect indicates that polymer nucleation, sensitive to excessive K^+, is mechanistically distinct from CASQ2 conformational compaction, which instead benefits from cooperative interactions between Ca^{2+} and intermediate K^+ concentrations. Rather, polymerization nuclei may correspond to highly Ca^{2+}-sensitive quaternary states, presumably dimers, that compete with alternative K^+-stabilized assemblies. Strikingly, the condition beyond which both maximal turbidity is reduced and nucleation is prolonged (75 mM KCl, 1 mM $CaCl_2$; Figure 5C) corresponds to an estimated ζ-potential of -53.6 ± 13.1 mV (Figure 5D), closely matching the Ca^{2+}-dependent inflection in turbidity observed more sharply in 50 mM KCl (-45.7 ± 4.5 mV at 5 mM $CaCl_2$; Figure 5A). The convergence to a unique, critical ζ-potential value, suggests that long-range electrostatics dominates the onset of a negative effect by both K^+ and Ca2+ on the stability of CASQ2 Ca^{2+}-dependent polymers.

Adding a further layer of complexity, K^+ concentrations above 75 mM also enhanced the cooperativity of Ca^{2+}-dependent polymerization (Figure S8C). Hill slope analysis shows a transition from a poorly cooperative regime (Hill slope between 1 and 2) to a highly cooperative process (Hill slope >2) as [K^+]>75 mM. While apparently in contrast with the K^+-dependent reduction in the stability of Ca2+-dependent polymers and nucleation efficiency, the parallel increase in the productivity of CASQ2 interaction events aligns with the protein's conformational compaction and the reduction of inter-monomer electrostatic repulsion observed in the same range of K+ concentrations (Figure 2).

Despite the apparent complexity of these effects, our observations are fully consistent with published end-point turbidimetric data (Figure S9) [6,10,11,13,16,25,26,34]. Across studies, reducing monovalent cations enhances both the sensitivity and the amplitude of CASQ2 response to Ca^{2+}. The fact that no positive effect of monovalent can be identified is due to the fact that previous studies did not explore the critical ζ-potential window below –70 mV (corresponding to 20 mM NaCl and 50 mM KCl, Figure S9), where K^+ ions exert a positive effect on Ca^{2+}-dependent CASQ2 polymerization.

Overall, our data support a model in which Ca^{2+}-dependent CASQ2 polymerization is governed by a balance between competing electrostatic mechanisms. Increasing K+ up to 50-75 mM concentrations promotes Ca^{2+} sensitivity and polymerization cooperativity by favoring conformational compaction and reducing inter-monomer electrostatic repulsion. Beyond a critical threshold, however, excessive electrostatic screening interferes with the assembly of polymer nuclei and Ca^{2+}-dependent high order polymers. Together, these findings reconcile previously divergent observations and establish electrostatic tuning as a central principle governing the Ca^{2+}-dependent assembly of CASQ2. At the same time though, additional conformational or ion-specific effects cannot be excluded. An hint to this comes from the observation that a small hinge in the Ca^{2+}-dependent increase of CASQ2 turbidity observed between 0.8 and 2 mM $CaCl_2$ (Figure 5A), which was consistently reproduced in each single experimental replicate in 10 mM KCl (Figure S10). Intriguingly, a similar bi-phasic behavior, at the same Ca^{2+} concentrations, was previously and independently reported as a variation in the Ca^{2+}-binding affinities of recombinant CASQ1 and CASQ2 proteins[5]. Mirroring the existence of distinct Ca^{2+}-binding modes[5], the biphasic Ca^{2+}-dependent turbidity increase here observed may indicate a transition between distinct polymerization modes. This phenomenon does not relate to long-range electrostatic effects, as it alters the slope of polymerization (Figure S10), and hence the cooperativity of CASQ2 self-assembly.

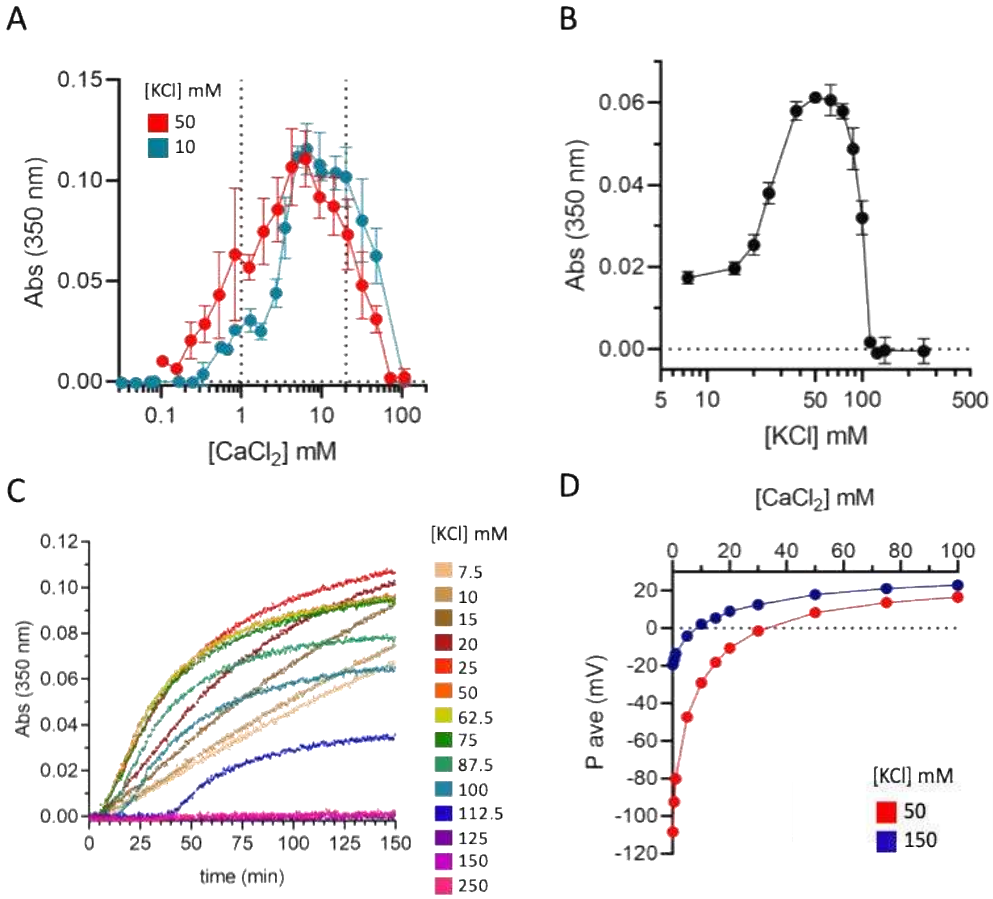

Figure 5. The Ca^{2+}-specific polymerization of CASQ2 is a non-linear, electrostatically modulated process. **A)** Turbidimetric end-point measurements of CASQ2 samples after 40 minutes since the exposure to varying concentrations of Ca^{2+} (0.01–100 mM) in buffers containing 10 mM (pink) and 50 mM (purple) KCl. In 10 mM KCl, CASQ2 exhibits a biphasic response with a maximal turbidity increase at ~1 mM Ca^{2+}, followed by a decrease and a secondary turbidity maximum at ~20 mM Ca^{2+}. In 50 mM KCl, the biphasic trend diminishes, suggesting competition between Ca^{2+} effects and ionic shielding by K^+ ions. Data are presented as mean ± SD from three independent experiments. The estimates for the physiological concentration of free (1 mM) and total (20 mM) Ca^{2+} ions in the jSR[31] are indicated by dotted lines. **B)** End-point turbidity of CASQ2 after 40 minutes since exposure to 1 mM $CaCl_2$ in varying ionic conditions (from 7.5 to 250 mM KCl). Data are mean ± SD from at least three independent experiments. **C)** Turbidity assays showing sigmoidal growth kinetics of CASQ2 in response to increasing Ca^{2+} concentrations under different KCl conditions. Data are mean from three independent experiments. Data are shown as single point measurements from three independent experiments. **D)** ζ-potential (expressed in mV) of CASQ2 as a function of $CaCl_2$ concentration. Increasing $CaCl_2$ from 0 to 100 mM reduces the surface charge, consistent with ionic shielding effects, stabilizing the CASQ2 fold and promoting multimerization. Data are presented as mean ± SD from at least three independent measurements. Of note, Ca^{2+} is markedly more efficient than K^+ at neutralizing CASQ2 charges: To reach a 0 mV ζ-potential, 30 mM Ca^{2+} is needed in 50 mM KCl, versus only 3 mM in 150 mM KCl. Moreover, 10 mM Ca^{2+} is sufficient to compensate for the ~75 mV difference brought by the 100 mM K^+ difference between the two salt conditions.

5. *CASQ2 polymerization is an ion-sensitive, Ca^{2+}-triggered switch*

To better characterize the kinetics of Ca^{2+}-dependent CASQ2 polymerization, we moved to perform a particle-size distribution (PSD) granulometric analysis of CASQ2 employing a custom Dynamic Light Scattering method which allows measurement of turbid samples. Intensity-weighted PSD measurements revealed that CASQ2 assembly does not proceed through a gradual, stepwise increase in particle size, as might be inferred from turbidimetric growth curves that reflect the formation of light-scattering bodies. Instead, once a critical Ca^{2+} concentration is reached, CASQ2 undergoes a sharp, highly cooperative transition between two distinct quaternary states (Figure 6A): a pre-existing oligomeric state, where CASQ2 exists as small oligomeric particles (6–12 nm, consistent with dimers, tetramers, and possibly octamers), and the Ca^{2+}-induced high-order polymeric states.

Notably, even under conditions that do not produce a measurable increase in turbidity—such as 150 mM KCl, where Ca^{2+}-dependent polymerization is strongly inhibited in bulk optical assays (Figures 5D, S8)—PSD analysis still revealed the formation of large CASQ2 assemblies. These assemblies did not increase further in size with time, suggesting that although long-range electrostatic screening suppresses the growth or stabilization of strongly scattering polymers, Ca^{2+} can still drive CASQ2 into a polymeric quaternary state. The lack of a corresponding turbidimetric signal likely reflects the formation of assemblies that are more hydrated, less compact, or possess lower refractive index. Overall, these data shed first light on the fact that CASQ2 Ca^{2+}-driven polymerization is not a linear, stepwise assembly of monomers into dimers, and then tetramers and multimers up to high-order polymers. Rather, CASQ2 operates as a Ca^{2+}-sensitive switch, oscillating cooperatively between an oligomeric phase and a high-order polymeric phase.

This switch-like behavior mirrors the qualitative observations in bulk solution. In cuvette experiments, exposure of 2.5 μM CASQ2 to 50 mM $CaCl_2$ triggers the immediate formation of a separated protein-rich phase (Figure S11). Moreover, thermal shift assays in 50 mM KCl reveal that the exposure to as little as 1 mM $CaCl_2$ is sufficient to preserve CASQ2's tryptophans in a hydrophobic environment even when the system is supplied with high thermal energy (Figure 6B). As in PSD granulometry, this transition occurs over a narrow Ca^{2+} concentration range in both 50 mM and 150 mM KCl (Figures 6B, 6C). Increasing K^+ concentration suppresses this effect: the T_m of CASQ2 in 1 mM $CaCl_2$ is 8°C lower in 150 mM KCl than in 50 mM KCl (Figures 6C, S12), whereas any thermal stability shift is completely abolished at 300–500 mM KCl (Figure 6D). These sharp changes in the biophysical properties of CASQ2 in response to a narrow range of Ca^{2+} concentrations likely reflects the involvement of multiple packing interfaces and strongly cooperative formation of a highly cross-linked polymer.

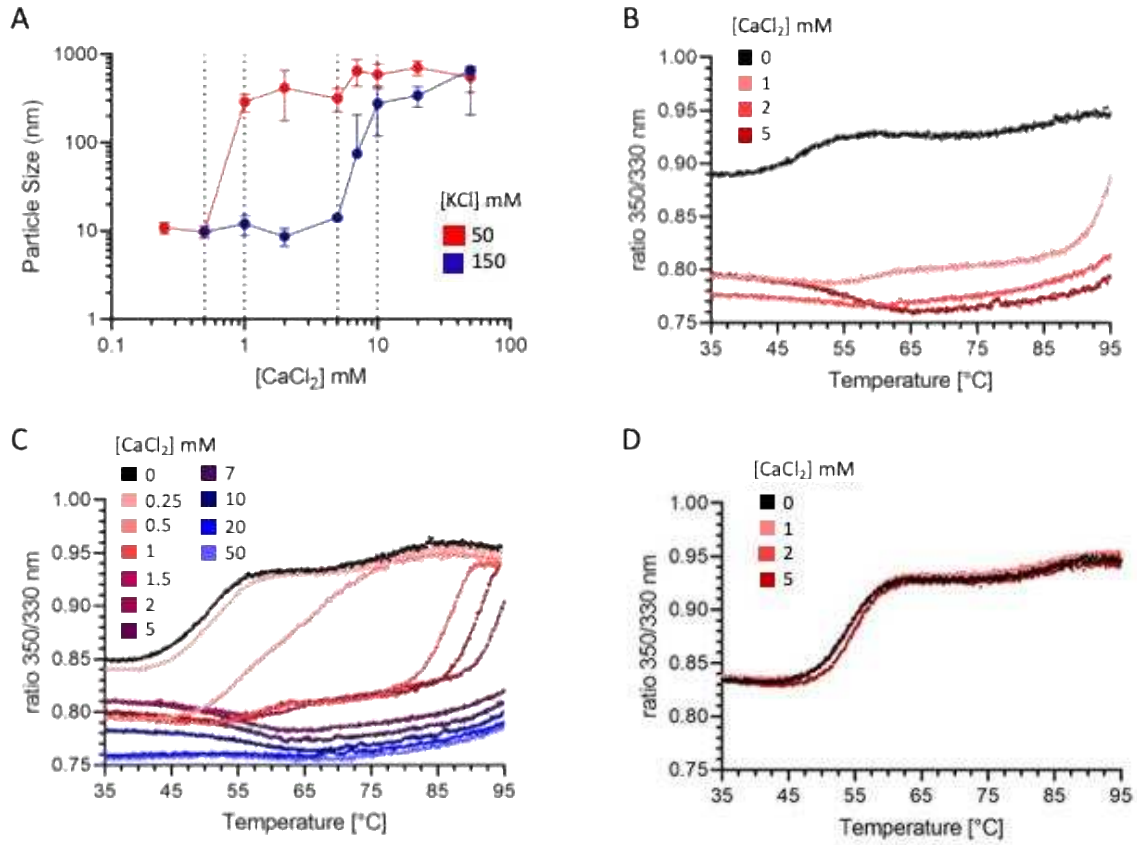

Figure 6. CASQ2 is a Ca^{2+}-sensor oscillating between an oligomeric and a high-order polymeric state. A) Average size of CASQ2 particles in solutions of varying Ca^{2+} and K^{+} concentrations, as determined by Dynamic Light Scattering (DLS). In 50 mM KCl, CASQ2 oligomeric particles grow in size in response to 0.5 mM and 1 mM Ca^{2+}, indicating polymerization. In the presence of 150 mM KCl, higher Ca^{2+} concentrations (5 to 10 mM) are required to promote particle size increase. Data are presented as mean ± SD from at least three independent measurements. **B-D)** Thermal denaturation curves, monitored by intrinsic tryptophan fluorescence (350/320 nm ratio), for CASQ2 samples in varying $CaCl_2$ concentrations, and either 50 mM KCl (B), 150 mM KCl (C), or 300 mM KCl (D). Data are presented as mean from three independent measurements.

Limitations

In cardiac myocytes CASQ2 is strongly glycosylated during transport to the jSR[6] and carries 0 to 2 phosphates per polypeptide[3,34], whereas the recombinant CASQ2 protein used here does not carry post-translational changes. These may alter the balance of the specific effects of K^+ and Ca^{2+} relative to those described herein, and/or the specific shape of the Ca^{2+}-dependent polymers. In addition, while the estimated physiological concentration of CASQ2 falls within the 1-4 mM range[35–37], the biochemical and biophysical properties of CASQ2 could be analyzed at much lower concentrations (with the exception of the MST data shown in Figure S6). Given the relevance of CASQ2 concentrations for its Ca^{2+}-free oligomerization properties, this parameter should be taken into consideration when extending our findings to the physiological setting. One final limitation is that all experiments herein were performed in the absence of Mg^{2+}. The effects of Mg^{2+} on CASQ2 Ca^{2+}-dependent polymerization, due to their complexity, are beyond the current study and will be the subject of future research.

Discussion

Our integrated experimental investigation redefines the molecular mechanism of cardiac CASQ2 polymerization by establishing three foundational advances: i) CASQ2 is a physiological dimer; ii) Ca^{2+}-dependent polymerization is electrostatically driven, and iii) CASQ2 polymerization is characterized by a switch-like transition.

Our results show for the first time that, under physiological ionic conditions, CASQ2 is intrinsically dimeric even at nanomolar concentrations and in the absence of its canonical ligand Ca^{2+}. The relative ionic stability of this dimer with respect to other electrostatic assemblies hints at a structure match with the crystallographic dimer, where a network of hydrogen-bonds stabilizes the N-terminal tail swapping between monomers (Asp32 with Lys68 and Lys64; Lys68 with Glu74 and Glu78, Figure 1B)[7]; Additionally, this dimer appears to be the functionally competent precursor of Ca^{2+}-dependent polymerization (Figure 4), ensuring rapid responsiveness to physiological Ca^{2+} fluctuations during excitation-contraction coupling.

Physiological amounts of K^+ ions modulate the equilibrium between functional and non-functional CASQ2 dimers (Figures 3 and 4). At concentrations below 50 mM, K^+ enhances CASQ2 sensitivity to Ca^{2+} and the efficacy of Ca^{2+}-dependent polymerization, likely by supporting protein folding and reducing inter-particle repulsion (Figures 5A, 5B). As the ionic strength increases and ζ-potential values approach 0 mV, unspecific inter-particle sticking (including non-specific forms of dimers, Figures 3A, 4A, 4B) are destabilized and the equilibrium shifts toward a non-electrostatically dependent, Ca^{2+}-free CASQ2 dimer, competent for Ca^{2+}-dependent quaternary assembly (Figures 4B-F). However, this same electrostatic effect also limits Ca^{2+}-dependent polymer growth (Figure 5),

reconciling the divergent effects of 50-200 mM K^+ across different biophysical assays (Figures 4B–D and 5A). Overall, the rapidity and magnitude of CASQ2 response to Ca^{2+} is optimal within a narrow electrostatic window between −60 and −40 mV, centered near −50 mV, suggesting a mechanism by which ionic homeostasis in the junctional SR may tune CASQ2 responsiveness during cyclic Ca^{2+} release (Figure 6A).

These experimental conclusions are independently corroborated by a theoretical model (Supplementary Text 1), which treats CASQ2 as a charge-regulated ion-binding electrolyte. This zero-dimensional electrostatic model simulates with impressive accuracy the interplay between electrostatic forces and the specific CASQ2 responsiveness to Ca^{2+}, confirming that the interaction between Ca^{2+} ions and CASQ2 is characterized by a strong electrostatic component.

Finally, our data also reveal that CASQ2 does not polymerize through a linear assembly, exclusively Ca^{2+}-driven, of monomers into dimers, tetramers and beyond. Instead, polymerization is the result of a Ca^{2+}-triggered switch, oscillating from a dimeric/oligomeric pool to a structurally distinct polymeric state. This transition is highly cooperative, as shown by granulometry, thermal denaturation, and turbidity, and is sensitive to both ionic and protein concentrations. These experimental data and theoretical model provide the long-awaited experimental evidence required to build a model for CASQ2 polymerization, and for the interpretation of the many missense mutations spread all over the surface of cardiac CASQ2 in CPVT2. Specifically, the existence of an equilibrium between non-functional and functional dimers carries important physio-pathological implications. In the biological context, CASQ2 dimerization shall occur readily after translation and before its transport to the jSR, even in the absence of Ca^{2+}. Building on the fact that CASQ2 trafficking is regulated by its quaternary assembly properties [4,34,38], and on published structural analysis of the missense mutations of CASQ1/2 [3], we propose that the dimerization competence of a mutant defines two distinct trafficking routes for either the dominant or recessive pathological mutants. While recessive mutations, affecting the stability of either the monomer or the dimeric state of CASQ2, are more easily recognized and not trafficked to the jSR or rapidly recycled from it, dominant negative mutations instead, by not altering the protein's competence to proper dimerization, are not recognized as non-wild-type and thus trafficked to the jSR. As a consequence, the dominant negative CASQ2 mutants, residing in the same biological compartment with the wild-type counterpart, sequester it into defective polymeric structures, ultimately leading to Ca^{2+}-leakage from the jSR and cardiac arrhythmias (Figure 7). This hypothesis fits with the fact that all published animal models of the recessive form of the CASQ2-related disease [17,39–42] feature a major loss of CASQ2 protein residing in the jSR, and a lower SR Ca^{2+} content, whereas the only dominant model for a CASQ2-related pathology [43] features a defect in the dynamics of SR Ca^{2+} exchange , but not any evident alteration of CASQ2 or Ca^{2+} content.

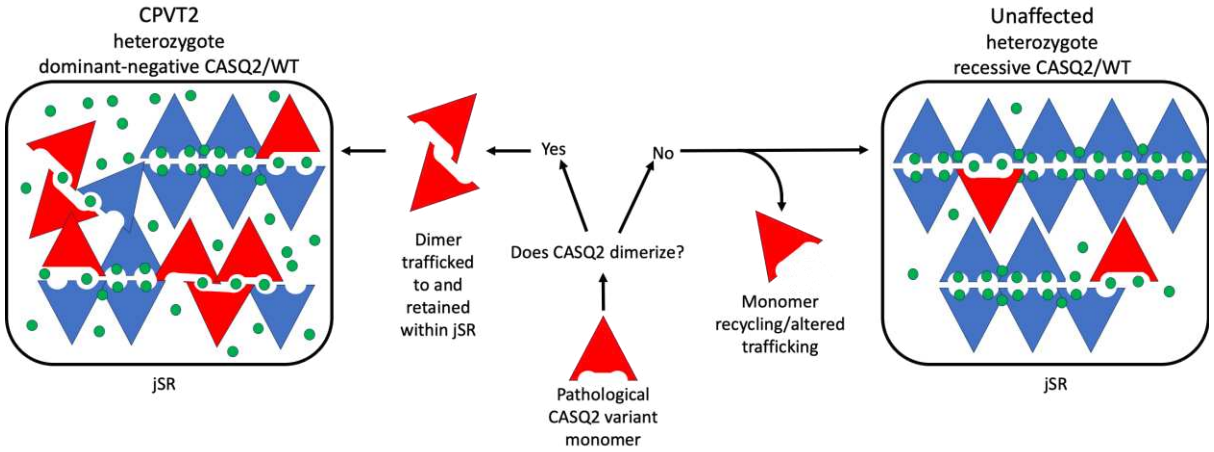

Figure 7. The proposed hypothesis on the distinct molecular pathways of recessive and dominant negative CASQ2 variants. Recessive CASQ2 mutations, affecting the stability of the protein monomer/dimer, and thus impeding necessary interactions for trafficking and retaining within the jSR, do not allow residence of the pathological protein variant within the jSR. For recessive CASQ2 mutations in heterozygosis, the wild-type counterpart can counteract the missing protein. Dominant negative CASQ2 variants, escaping the checkpoint for jSR delivery and/or residence, sequester the wild-type protein present within the jSR into a less-functional polymeric form. An altered hetero-polymeric mutant/WT-CASQ2-Ca^{2+} polymer may justify the slowly buffered, fast rise of free Ca^{2+}-ions in the jSR detected for the dominant negative CASQ2 variant K180R [43] and in turn the inappropriate opening of the RyR2 channels and the predisposition to arrhythmias. CASQ2 pathological variant is in red. WT CASQ2 is in blue. Calcium ions are green.

Bibliography

1. Perni, S., Close, M. & Franzini-Armstrong, C. Novel details of calsequestrin gel conformation in situ. *J. Biol. Chem.* **288**, 31358–31362 (2013).
2. Jones, L. R. *et al.* Regulation of Ca2+ signaling in transgenic mouse cardiac myocytes overexpressing calsequestrin. *J. Clin. Invest.* **101**, 1385–1393 (1998).
3. Marabelli, C., Santiago, D. J. & Priori, S. G. The Structural-Functional Crosstalk of the Calsequestrin System: Insights and Pathological Implications. *Biomolecules* **13**, 1693 (2023).
4. McFarland, T. P., Milstein, M. L. & Cala, S. E. Rough endoplasmic reticulum to junctional sarcoplasmic reticulum trafficking of calsequestrin in adult cardiomyocytes. *J. Mol. Cell. Cardiol.* **49**, 556–564 (2010).
5. Park, H. *et al.* Comparing skeletal and cardiac calsequestrin structures and their calcium binding: a proposed mechanism for coupled calcium binding and protein polymerization. *J. Biol. Chem.* **279**, 18026–18033 (2004).
6. Sanchez, E. J., Lewis, K. M., Munske, G. R., Nissen, M. S. & Kang, C. Glycosylation of skeletal calsequestrin: implications for its function. *J. Biol. Chem.* **287**, 3042–3050 (2012).
7. Bal, N. C. *et al.* The catecholaminergic polymorphic ventricular tachycardia mutation R33Q disrupts the N-terminal structural motif that regulates reversible calsequestrin polymerization. *J. Biol. Chem.* **285**, 17188–17196 (2010).
8. Ng, K. *et al.* An International Multicenter Evaluation of Inheritance Patterns, Arrhythmic Risks, and Underlying Mechanisms of *CASQ2* -Catecholaminergic Polymorphic Ventricular Tachycardia. *Circulation* **142**, 932–947 (2020).

9. Ohnishi, M. & Reithmeier, R. A. Fragmentation of rabbit skeletal muscle calsequestrin: spectral and ion binding properties of the carboxyl-terminal region. *Biochemistry* **26**, 7458–7465 (1987).
10. Beard, N. A. & Dulhunty, A. F. C-terminal residues of skeletal muscle calsequestrin are essential for calcium binding and for skeletal ryanodine receptor inhibition. *Skelet. Muscle* **5**, 6 (2015).
11. Bal, N. C. *et al.* The C-terminal calcium-sensitive disordered motifs regulate isoform-specific polymerization characteristics of calsequestrin. *Biopolymers* **103**, 15–22 (2015).
12. Shin, D. W., Ma, J. & Kim, D. H. The asp-rich region at the carboxyl-terminus of calsequestrin binds to Ca(2+) and interacts with triadin. *FEBS Lett.* **486**, 178–182 (2000).
13. Lewis, K. M., Ronish, L. A., Ríos, E. & Kang, C. Characterization of Two Human Skeletal Calsequestrin Mutants Implicated in Malignant Hyperthermia and Vacuolar Aggregate Myopathy. *J. Biol. Chem.* **290**, 28665–28674 (2015).
14. Gamberucci, A. *et al.* TAM-associated CASQ1 mutants diminish intracellular Ca2+ content and interfere with regulation of SOCE. *J. Muscle Res. Cell Motil.* **45**, 275–284 (2024).
15. He, Z., Dunker, A. K., Wesson, C. R. & Trumble, W. R. Ca(2+)-induced folding and aggregation of skeletal muscle sarcoplasmic reticulum calsequestrin. The involvement of the trifluoperazine-binding site. *J. Biol. Chem.* **268**, 24635–24641 (1993).
16. Barone, V. *et al.* Identification and characterization of three novel mutations in the CASQ1 gene in four patients with tubular aggregate myopathy. *Hum. Mutat.* **38**, 1761–1773 (2017).
17. di Barletta, M. R. *et al.* Clinical phenotype and functional characterization of CASQ2 mutations associated with catecholaminergic polymorphic ventricular tachycardia. *Circulation* **114**, 1012–1019 (2006).

18. Chopra, N. *et al.* Modest reductions of cardiac calsequestrin increase sarcoplasmic reticulum Ca2+ leak independent of luminal Ca2+ and trigger ventricular arrhythmias in mice. *Circ. Res.* **101**, 617–626 (2007).
19. Faggioni, M., Kryshtal, D. O. & Knollmann, B. C. Calsequestrin mutations and catecholaminergic polymorphic ventricular tachycardia. *Pediatr. Cardiol.* **33**, 959–967 (2012).
20. Priori, S. G. & Chen, S. R. W. Inherited dysfunction of sarcoplasmic reticulum Ca2+ handling and arrhythmogenesis. *Circ. Res.* **108**, 871–883 (2011).
21. Zhao, R. *et al.* Measurement of amyloid formation by turbidity assay—seeing through the cloud. *Biophys. Rev.* **8**, 445–471 (2016).
22. Pryor, N. E., Moss, M. A. & Hestekin, C. N. Unraveling the Early Events of Amyloid-β Protein (Aβ) Aggregation: Techniques for the Determination of Aβ Aggregate Size. *Int. J. Mol. Sci.* **13**, (2012).
23. Park, H., Wu, S., Dunker, A. K. & Kang, C. Polymerization of calsequestrin. Implications for Ca2+ regulation. *J. Biol. Chem.* **278**, 16176–16182 (2003).
24. Titus, E. W. *et al.* The structure of a calsequestrin filament reveals mechanisms of familial arrhythmia. *Nat. Struct. Mol. Biol.* **27**, 1142–1151 (2020).
25. Qin, J. *et al.* Luminal Ca2+ regulation of single cardiac ryanodine receptors: insights provided by calsequestrin and its mutants. *J. Gen. Physiol.* **131**, 325–334 (2008).
26. Bal, N. C. *et al.* Probing cationic selectivity of cardiac calsequestrin and its CPVT mutants. *Biochem. J.* **435**, 391–399 (2011).
27. Ostwald, T. J., MacLennan, D. H. & Dorrington, K. J. Effects of cation binding on the conformation of calsequestrin and the high affinity calcium-binding protein of sarcoplasmic reticulum. *J. Biol. Chem.* **249**, 5867–5871 (1974).

28. Aaron, B. M., Oikawa, K., Reithmeier, R. A. & Sykes, B. D. Characterization of skeletal muscle calsequestrin by 1H NMR spectroscopy. *J. Biol. Chem.* **259**, 11876–11881 (1984).
29. Yano, K. & Zarain-Herzberg, A. Sarcoplasmic reticulum calsequestrins: structural and functional properties. *Mol. Cell. Biochem.* **135**, 61–70 (1994).
30. Baksh, S. *et al.* Zn2+ binding to cardiac calsequestrin. *Biochem. Biophys. Res. Commun.* **209**, 310–315 (1995).
31. Bers, D. M. *Excitation-Contraction Coupling and Cardiac Contractile Force*. (Kluwer Academic Publishers, Dordrecht ; Boston, 2001).
32. Manno, C., Tammineni, E., Figueroa, L., Marty, I. & Ríos, E. Quantification of the calcium signaling deficit in muscles devoid of triadin. *PloS One* **17**, e0264146 (2022).
33. de Vos, W. M. & Lindhoud, S. Overcharging and charge inversion: Finding the correct explanation(s). *Adv. Colloid Interface Sci.* **274**, 102040 (2019).
34. Sanchez, E. J. *et al.* Phosphorylation of human calsequestrin: implications for calcium regulation. *Mol. Cell. Biochem.* **353**, 195–204 (2011).
35. MacLennan, D. H. & Wong, P. T. Isolation of a calcium-sequestering protein from sarcoplasmic reticulum. *Proc. Natl. Acad. Sci. U. S. A.* **68**, 1231–1235 (1971).
36. Royer, L. & Ríos, E. Deconstructing calsequestrin. Complex buffering in the calcium store of skeletal muscle. *J. Physiol.* **587**, 3101–3111 (2009).
37. Beard, N. A., Wei, L. & Dulhunty, A. F. Control of muscle ryanodine receptor calcium release channels by proteins in the sarcoplasmic reticulum lumen. *Clin. Exp. Pharmacol. Physiol.* **36**, 340–345 (2009).
38. A, G., Se, C. & Ls, S. Calsequestrin accumulation in rough endoplasmic reticulum promotes perinuclear Ca2+ release. *J. Biol. Chem.* **287**, (2012).

39. Katz, G. *et al.* The role of mutant protein level in autosomal recessive catecholamine dependent polymorphic ventricular tachycardia (CPVT2). *Biochem. Pharmacol.* **86**, 1576–1583 (2013).
40. Denegri, M. *et al.* Viral gene transfer rescues arrhythmogenic phenotype and ultrastructural abnormalities in adult calsequestrin-null mice with inherited arrhythmias. *Circ. Res.* **110**, 663–668 (2012).
41. Flores, D. J. *et al.* Conditional ablation and conditional rescue models for Casq2 elucidate the role of development and of cell-type specific expression of Casq2 in the CPVT2 phenotype. *Hum. Mol. Genet.* **27**, 1533–1544 (2018).
42. Kurtzwald-Josefson, E. *et al.* Alpha blockade potentiates CPVT therapy in calsequestrin-mutant mice. *Heart Rhythm* **11**, 1471–1479 (2014).
43. Wleklinski, M. J. *et al.* Impaired Dynamic Sarcoplasmic Reticulum Ca Buffering in Autosomal Dominant CPVT2. *Circ. Res.* **131**, 673–686 (2022).
44. Niebling, S. *et al.* Biophysical Screening Pipeline for Cryo-EM Grid Preparation of Membrane Proteins. *Front. Mol. Biosci.* **9**, 882288 (2022).

Supplementary Figures

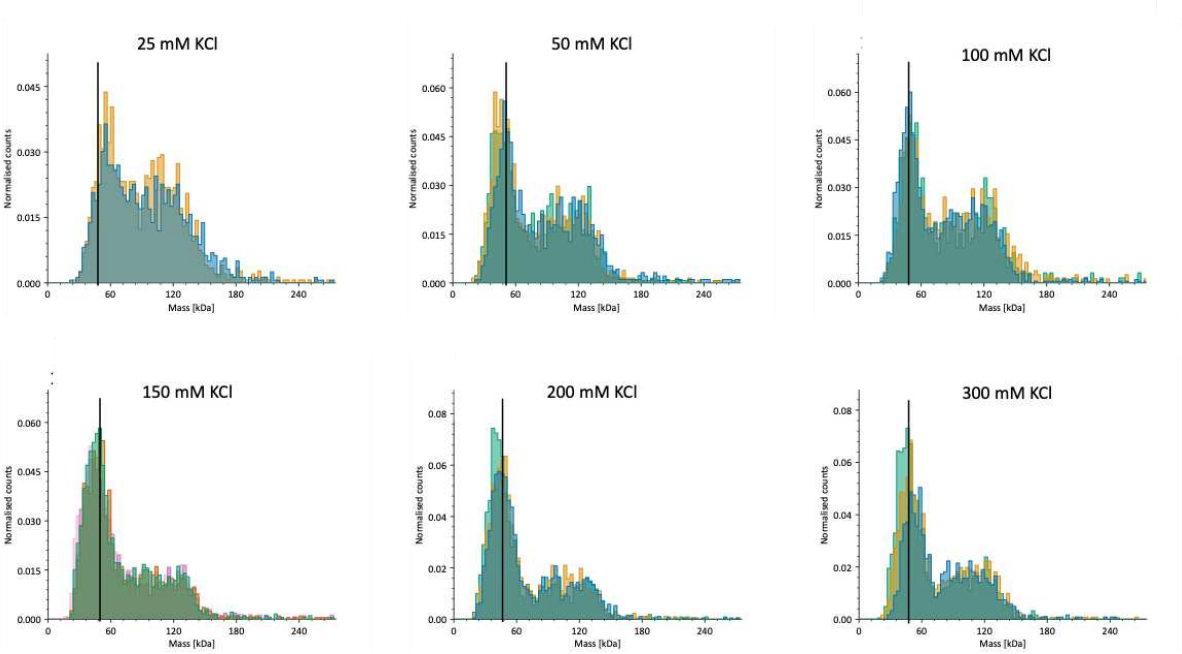

Supplementary Figure 1. Mass photometry (MP) of CASQ2 under increasing KCl concentrations. MP measurements reveal the relative abundance and distribution of CASQ2 monomers, dimers, and higher-order oligomers in buffer conditions with increasing KCl concentrations (25–300 mM). Three independent measurements are shown for each condition. The 48 kDa apparent mass value is highlighted by a black vertical bar, to facilitate comparison of the apparent volume registered for the monomer species across ionic conditions. Of note, quaternary assemblies corresponding to dimers, trimers, and tetramers, form in absence of Ca2+ and are progressively inhibited by increasing ionic conditions (in the 25 to 200 mM KCl range, see also Figure 3A). These results suggest a dynamic equilibrium between CASQ2 oligomeric states modulated by ionic strength, with K^+ ions influencing both the prevalence and stability of multimeric species.

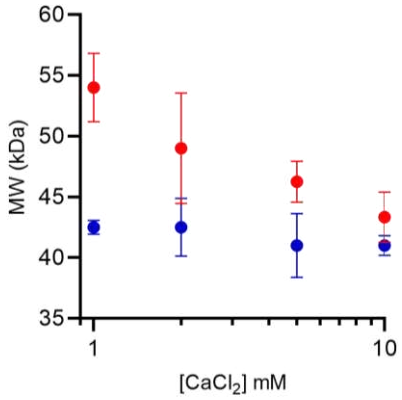

Figure S2. Mass photometry (MP) analysis of the size of CASQ2 monomer under increasing CaCl2 concentrations and in two distinct ionic strength conditions (50 mM and 200 mM KCl). The apparent volume occupied by CASQ2 monomers in 50 mM KCl solution (red) decreases with increasing CaCl2. In 200 mM KCl (blue points), CaCl2 does not compact any further the folding of CASQ2 polypeptide. At least three independent measurements, with CASQ2 25 nM, were considered for each condition.

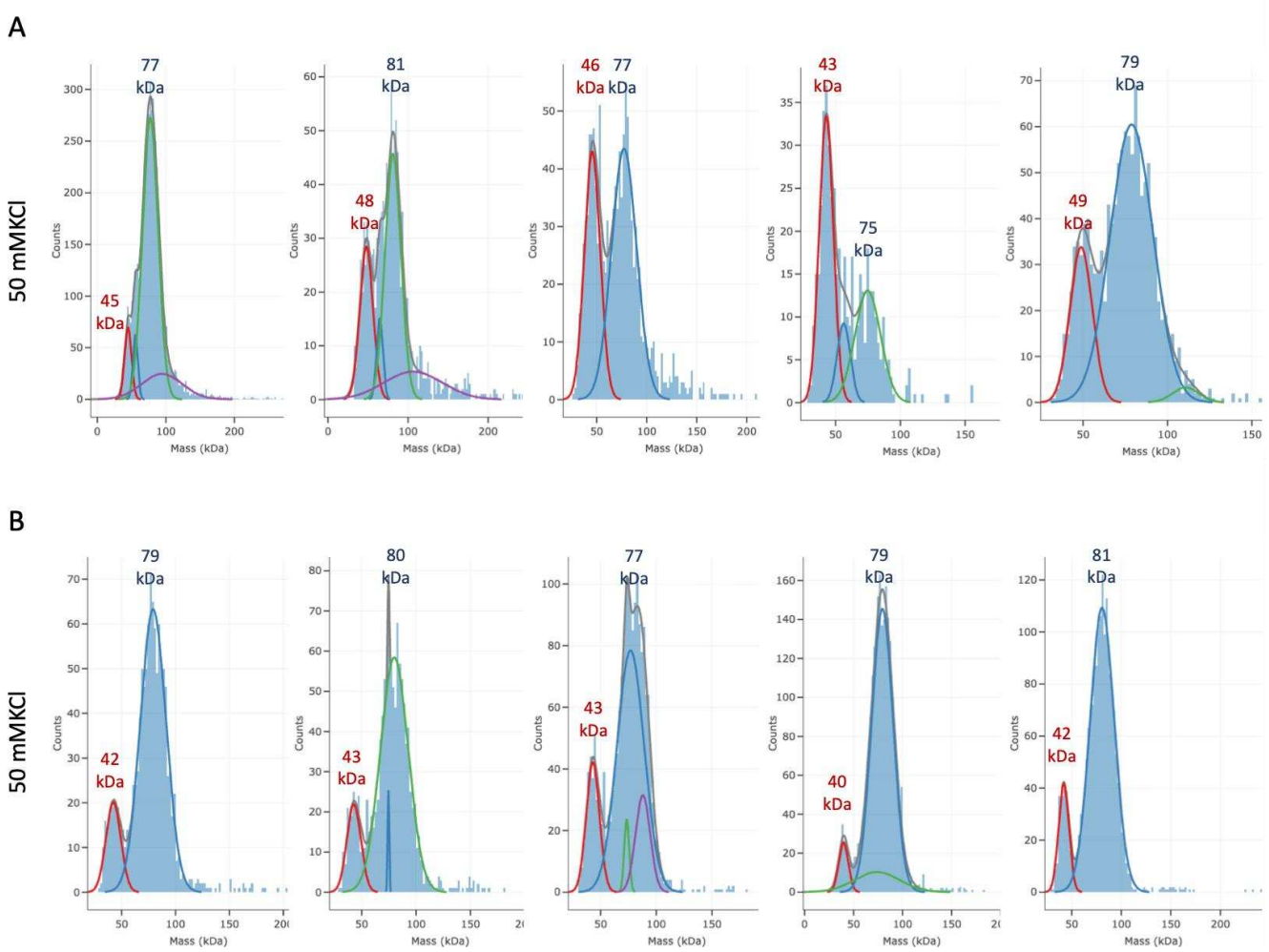

Figure S3. Representative Mass photometry raw data of CASQ2 multimerization at increasing Ca^{2+} concentrations. Distributions of detected particle masses for 25 nM wild-type CASQ2 incubated with increasing concentrations of $CaCl_2$, reveals a shift from monomer-dimer peaks with increasing Ca^{2+} levels. Data are fitted using automatic Gaussian distributions (PhotoMol [44]) to estimate peak centers and molecular mass assignments for the monomer (red) and dimer (blue) species.

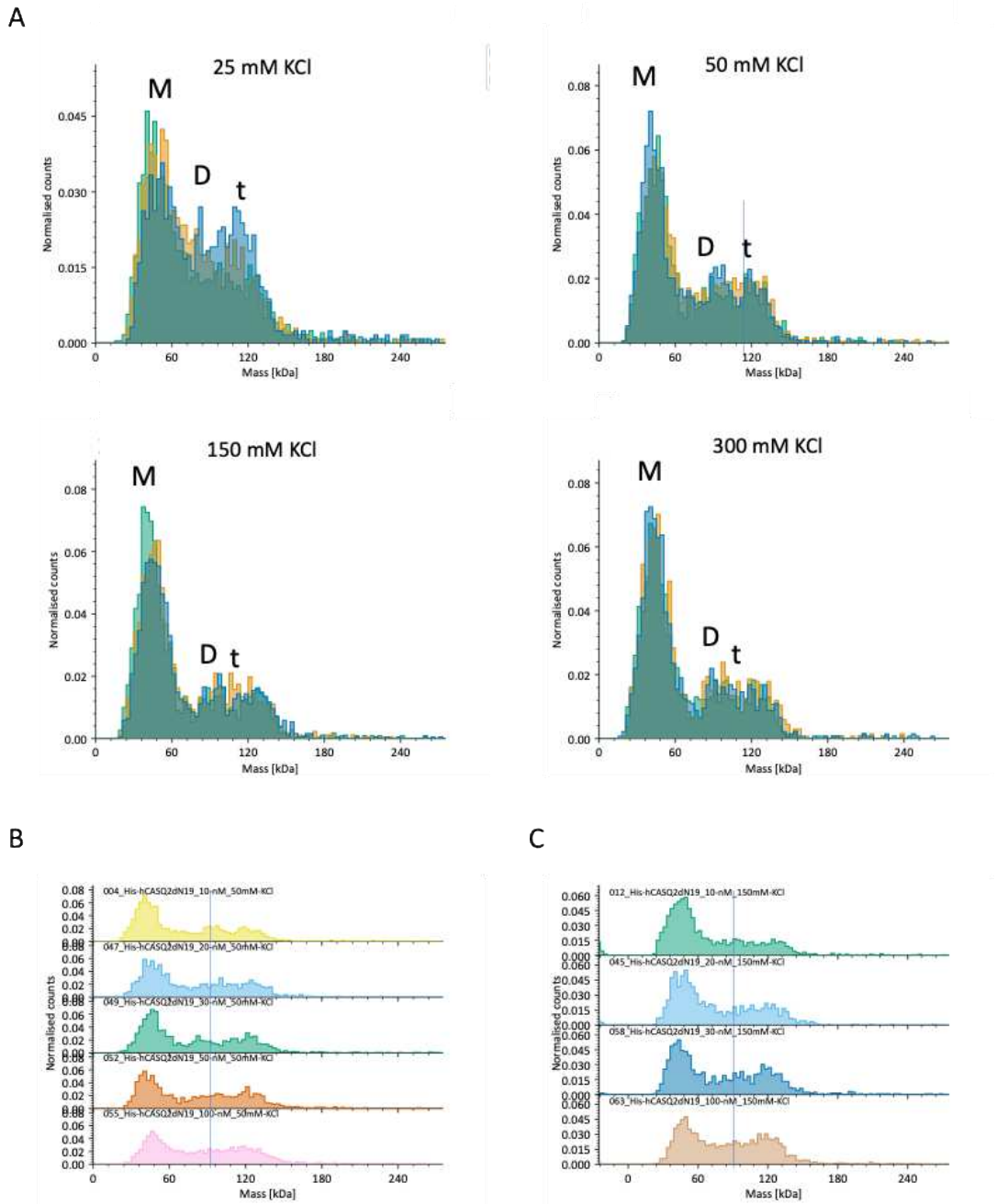

Figure S4. MP analysis of CASQ2 oligomer distribution as a function of KCl concentration. A) Normalized mass distributions for His-tagged CASQ2 at 10 mM protein concentration measured in 25, 50, 150, and 300 mM KCl. Mass distributions shift from broad, multimodal peaks at low salt toward narrower peaks centered around the size of dimeric (D) and trimeric (t) states, and a ashoulder at the approximate mass of the tetramer (T), with increasing ionic strength. Moving from 25 to 50 and 150 mM KCl, a decrease in the proportion of the dimeric quaternary assemblies is evident. Above 150 mM KCl, no significant change in the proportion of the dimeric Vs. monomeric species is observed. Data show the overlay of the measurements of three independent samples. **B-C)** Replicate datasets for varying concentrations of CASQ2 (10, 20, 30, 50, amd 100 nM) in 50 mM KCl buffer (B), and 200 mM KCl buffer (C). A vertical line positioned at the average mass of the dimeric species (80 kDa) is drawn as reference to facilitate visualization of the fact that supra-dimeric assemblies are sustained by increasing CASQ2 concentrations. These results support the interpretation that CASQ2 is able to form quaternary assemblies in absence of Ca2+, also at low protein concentrations.

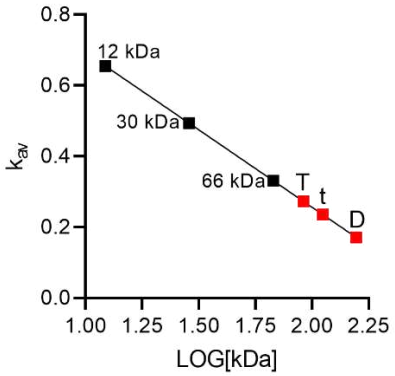

Figure S5. Correlation of molecular weight and elution profile in SEC (Superdex 200 10/300) calibration curve. Standard proteins of known molecular weight (black dots) were used to construct a calibration curve plotting the distribution coefficient (K_av) against the logarithm of their molecular weight (log_{10}[kDa]). Red squares represent the estimated molecular weights of CASQ2 species based on their elution volumes: 90 kDa (dimer, D), 110 kDa (trimer, t), and 152 kDa (tetramer, T), interpolated on the standard curve. This calibration was used to assess the quaternary state of CASQ2 under different ionic conditions.

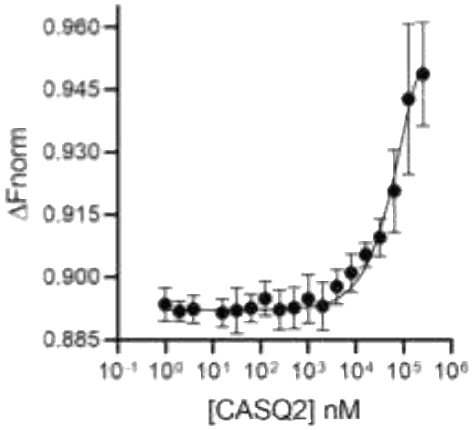

Figure S6. MST assay of CASQ2 self-association in PBS buffer, showing similar pronounced concentration-dependent CASQ2 self-association. Data are presented as mean ± SD from three independent measurement.

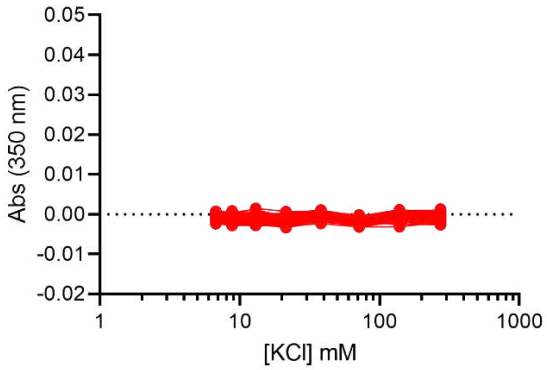

Figure S7. Turbidimetric analysis of CASQ2 multimerization in the absence of divalent ions. Absorbance at 350 nm was measured for 45 minutes since the incubation of CASQ2 with increasing concentrations of KCl, in the absence of Ca^{2+} or Mg^{2+}. The lack of significant turbidity changes across the tested ionic strengths confirms that CASQ2 does not efficiently form large multimers without the presence of divalent cations. These results support the requirement of Ca^{2+} or Mg^{2+} to promote higher-order assembly of CASQ2.

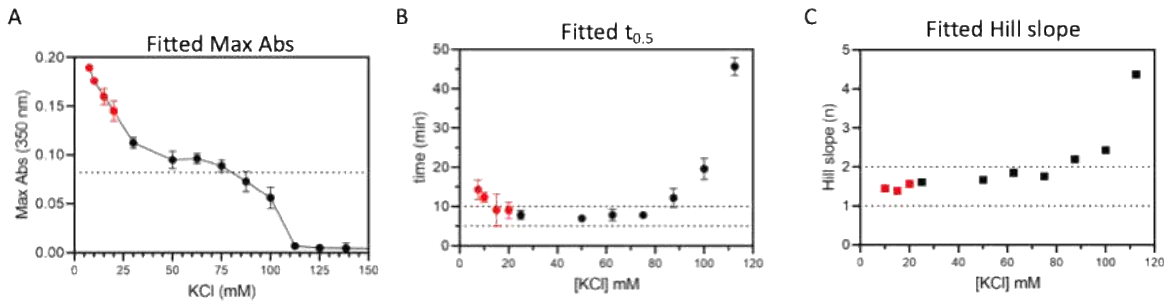

Figure S8. Parameters calculated from the fitted sigmoidal growth curves for Ca^{2+}-dependent polymerization. For [KCl] < 15 mM, the values are highlighted in red, as only the initial linear growth phases were captured, limiting the accuracy of the mathematical model for those conditions, especially for the maximal absorbance level reached at plateau. **A)** Maximal absorbance levels reached at pleateau. **B)** Hill slope values show positive cooperativity of polymerization at moderate ionic strengths (25–75 mM KCl), rapidly increasing above 100 mM KCl**. C)** The nucleation phase, defined as the time required to reach half the maximum turbidity, increases for [KCl] > 90 mM.

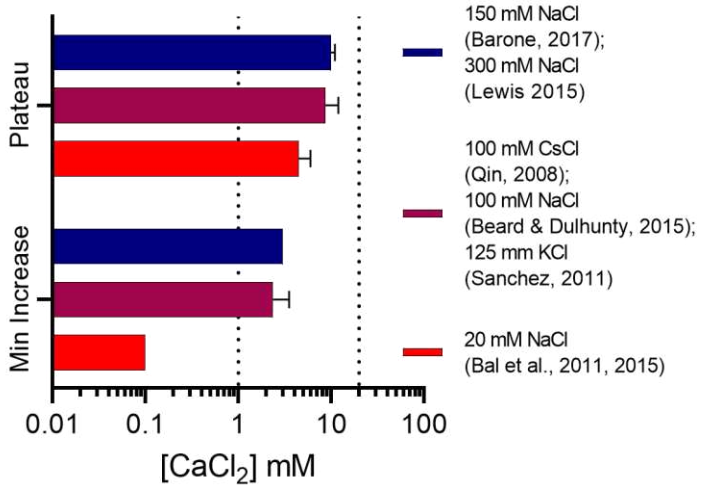

Figure S9. Overview of the Ca^{2+}-dependent CASQ2 polymerization main parameters extracted from published data: i) the minimal Ca^{2+} concentrations required to elicit the onset of turbidimetric increase, and ii) the minimal Ca^{2+} concentrations required to reach the the maximal responsiveness plateau phase. Data are divided according to the ionic strength of the published experiment, as reported in the legend. The estimates for the physiological concentration of 1 mM free and 20 mM total Ca^{2+} ions in the junctional Sarcoplasmic reticulum (jSR) [31] are indicated by dotted lines. The ζ-potential of the lowest ionic strength condition reported in literature (20 mM NaCl, corresponding to -105.7 mV, Figure 2D) is matched by our 50 mM KCl condition (–108.4 mV, Figure 2D), which explains the fact that no positive effect is observed for K+ on CASQ2 Ca2+-dependent polymerization.

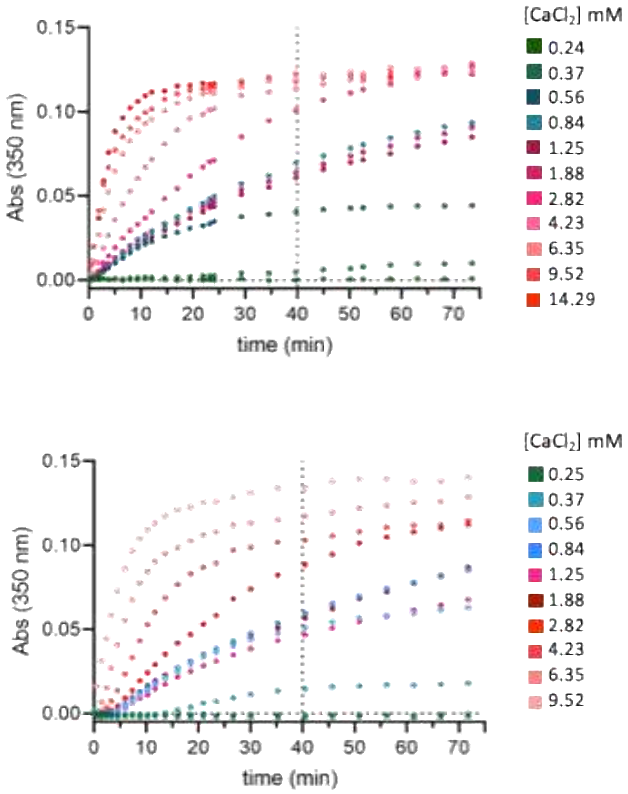

Figure S10. Turbidity of CASQ2 protein in response to the addition of varying concentrations of $CaCl_2$. For each experimental condition, the absorbance measurements are reported as the average of three measurements from three independent samples at defined timepoints. The legend on the right refers to the final concentration of $CaCl_2$ once added to the sample. In the range 0.5-1.25 mM $CaCl_2$, the initial turbidity slope is reproducibly higher than the response to 1.88 mM $CaCl_2$.

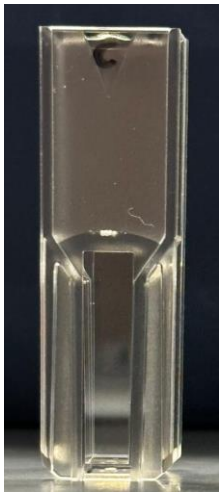

Figure S11. CASQ2 polymerization at high Ca^{2+} concentrations results in visible phase separation. Representative image of a cuvette containing 2.5 µM CASQ2 in 50 mM KCl buffer exposed to 50 mM $CaCl_2$, showing a visible phase-separated system. The appearance of a dense, turbid layer indicates the formation of polymeric CASQ2 condensates, supporting the occurrence of a macroscopic phase transition upon calcium-induced polymerization. In addition, measurement of the absorbance at 280 nm of samples from all three liquid phases (above, within, and below the turbid phase), demonstrated that only in the turbid phase an absorbance curve appropriate for a protein was clearly detected (corresponding to a protein concentration of about 20 µM). This visual evidence complements turbidimetry, DLS, and thermal shift assays in demonstrating the sharp transition between oligomers and high-order CASQ2 polymers.

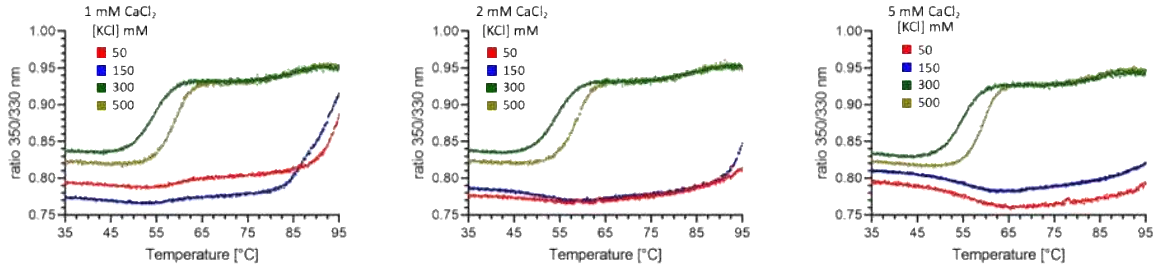

Figure S12. Thermal stabilization of CASQ2 by Ca^{2+} is progressively inhibited by increasing KCl concentrations. Thermal denaturation profiles of CASQ2 (6 μM) after 1 h incubation with 1, 2, or 5 mM $CaCl_2$ in buffers containing 50, 150, 300, or 500 mM KCl. In 50 mM KCl, Ca^{2+} induces a pronounced upward shift in melting temperature (Tm), consistent with formation of highly stabilized CASQ2 polymers. This Ca^{2+}-induced thermal stabilization is reduced in 150 mM KCl and abolished at 300–500 mM KCl, demonstrating that high concentrations of monovalent cations antagonize the formation of the Ca^{2+}-dependent polymeric state.

Expression and Purification of cardiac Calsequestrin

The pET28a-based expression construct codig for N-terminally tagged His-CASQ2 [deleted of its first 19 residues] was transformed into the BL21 (DE3) *E. coli* strain. Overnight starter cultures were used to inoculate large-scale cultures (750 mL of broth per 2.8 L flask), which were grown at 37 °C to an optical density (OD) of 0.5 before induction with 1 mM IPTG. Following induction, cultures were incubated for an additional 3 hours at 30 °C. All cultures were grown in standard LB medium supplemented with 25 µg/mL kanamycin and 50 µg/mL chloramphenicol. Cells were harvested by centrifugation at 4,000 g for 20 minutes, and the resulting cell pellets were collected and stored at -80 °C.

Frozen cell pellets were resuspended in resuspension buffer (20 mM Potassium Phosphate, pH 7.4, 500 mM NaCl, 1 mM EDTA, 5 mM imidazole, 1 mM β-mercaptoethanol) and lysed mechanically using a Minilys® bead-beater (Bertin Technologies) at maximum speed (5000 rpm) for four cycles of 30 seconds each. The lysate was clarified by centrifugation at 8,900 × *g* for 1 hour at 4 °C. The supernatant was then filtered through a 0.45 µm membrane, and calsequestrin-containing fractions were isolated via immobilized metal affinity chromatography (IMAC) using a 5 mL HisTrap FF column on an ÄKTA go FPLC system. The IMAC buffers were as follows: Buffer A (20 mM KPi, pH 7.4, 300 mM NaCl, 20 mM imidazole) and Buffer B (20 mM KPi, pH 7.4, 300 mM NaCl, 300 mM imidazole). After a wash in 20% Buffer B, the protein was eluted in 100% Buffer B and subsequently dialyzed overnight at 4 °C in 2 L of Dialysis Buffer (20 mM HEPES, pH 7.3, 100 mM NaCl, 5 mM EDTA, 1 mM β-mercaptoethanol).

Anion exchange chromatography was performed using a 5 mL HiTrap Capto Q column with Buffer A (20 mM HEPES, pH 7.3, 100 mM NaCl) and Buffer B (20 mM HEPES, pH 7.3, 1 M NaCl). Protein was eluted using a continuous gradient up to 100% Buffer B, with calsequestrin consistently eluting at 40–50% Buffer B. The calsequestrin-rich fractions were pooled and concentrated using an Amicon® centrifugal filter unit with a 10 kDa molecular weight cut-off.

Size-exclusion chromatography (SEC) was performed by loading the sample into a 10 mL loop using a 5 mL syringe and allowing it to flow through a HiLoad 26/600 Superdex 200 pg column equilibrated with gel filtration (GF) buffer (20 mM HEPES, pH 7.3, 50 mM KCl). Calsequestrin-rich fractions were pooled, concentrated, aliquoted, and stored at -80 °C.

Turbidity assays

The response of CASQ2 to $CaCl_2$ (0.01 mM to 100 mM) or $MgCl_2$ (0.01 mM to 100 mM) in the presence of 10 or 50 mM KCl was assessed using a Tecan Infinite 200® Pro plate reader by measuring absorbance at 350 nm. The assays were conducted in a 96-well plate, with each well containing a final volume of 140 µL. CASQ2 was buffer-exchanged to 20 mM HEPES (pH 7.3) and either 10 or 50 mM KCl. Prior to $CaCl_2$ or $MgCl_2$ addition, the plate containing CASQ2 sample was left at room temperature for 20 minutes and baseline turbidity was measured for blank determination. $CaCl_2$ or $MgCl_2$ was then manually added using a multichannel micropipette, and the sample was rapidly mixed by pipetting five times (avoiding the formation of air bubbles). Absorbance was recorded immediately after $CaCl_2$ or $MgCl_2$ addition. All measurements were performed at room temperature in triplicate for each condition.

Mass photometry measurements

Mass photometry measurements were performed using a Refeyn TwoMP mass photometer (Refeyn Ltd). To prepare samples, CASQ2 was first buffer-exchanged into a measurement buffer containing 20 mM HEPES (pH 7.3) and a KCl concentration ranging from 25 mM to 500 mM. Each condition was

incubated on ice for 45 minutes before being diluted in the equilibration condition to 100 nM CASQ2 in the first dilution and 10 nM CASQ2 in the final assessed drop. Data acquisition was initiated immediately after sample loading and resuspension by pipetting and recorded for 60 seconds. Molecules landing on the glass–buffer interface were visualized as changes in the interferometric scattering signal, which were automatically detected and quantified using AcquireMP software.
To determine molecular mass, recorded contrast values for individual landing events were converted using a calibration curve established with protein standards. Data analysis was conducted using DiscoverMP software (Refeyn Ltd.), generating mass distribution histograms and applying Gaussian fits to determine the average molecular mass and sample heterogeneity. All experiments were performed at room temperature.

Size-exclusion chromatography
A Superdex 75 10/300 GL column (Cytiva), connected to an ÄKTA go FPLC system, was equilibrated with a gel filtration (GF) buffer containing 20 mM HEPES (pH 7.3) and different concentrations of KCl (ranging from 50 mM to 200 mM) depending on the experimental condition being tested. A 100 µL sample of CASQ2 at 1 mg/mL, preincubated with the respective KCl concentrations, was injected into a 500 µL loop immediately after the addition of 1 mM $CaCl_2$. To evaluate the effect of CASQ2 concentration, the same column was used with a consistent GF buffer composition (20 mM HEPES, pH 7.3, 50 mM KCl) across all conditions. CASQ2 samples (100 µL) at varying concentrations (ranging from 5.6 µM to 225 µM) were injected, with 1 mM $CaCl_2$ added immediately prior to injection.
All experiments were conducted at 4 °C, and elution profiles were monitored using the UV-Vis detection module integrated into the ÄKTA go system.

Thermal stability assay
Protein samples were prepared in a buffer containing 20 mM HEPES (pH 7.3) with varying KCl concentrations (ranging from 25 mM to 500 mM) to achieve a final CASQ2 concentration of 2.5 µM. Approximately 10 µL of each sample was loaded into disposable Tycho capillaries (NanoTemper Technologies, cat# TY-C001). Thermal stability was assessed using the Tycho NT.6 instrument (NanoTemper Technologies). The system applied a temperature ramp from 35 °C to 95 °C at a controlled rate of 30 °C/min while recording the intrinsic tryptophan fluorescence at 330 nm and 350 nm. The fluorescence intensity ratio (350 nm/330 nm) was continuously monitored and used to generate an unfolding profile. Inflection temperatures (Ti), which indicate the temperature at which significant unfolding occurs, were determined automatically by the Tycho software. Each curve is the average of three independent measurements.

Micro Scale Thermophoresis (MST)
MST experiments were carried out using a Monolith NT.115 instrument (NanoTemper Technologies) with premium Monolith capillaries. Protein labeling and binding assays were conducted using the Monolith His-Tag Labeling Kit RED-tris-NTA 2nd Generation (Cat. No. MO-L018) following the manufacturer's instructions. The target protein was fluorescently labeled and diluted in PBS-T buffer. Prior to measurement, samples were incubated at room temperature for 30 minutes to allow binding equilibrium to be reached. The MST was performed at 25°C. Data analysis was conducted using MO.Affinity Analysis software.

Dynamic light scattering and Z-potential measurements
Particle size analysis was performed using the NANOTRAC Flex (Microtrac) instrument, which employs a unique dynamic light scattering method with a flexible probe, in batch mode. CASQ2 samples were diluted in a buffer containing 20 mM HEPES (pH 7.3) and either 50 mM or 150 mM KCl

to achieve a final protein concentration of 2.5 µM. Before each measurement, a blank reading was recorded using the buffer alone. Particle size was assessed using the same CASQ2 sample, with $CaCl_2$ added stepwise. The sample was continuously agitated by a piston before and during each measurement. At least six independent measurements were recorded for each $CaCl_2$ concentration.
The Z-potential of CASQ2 at varying $CaCl_2$ and KCl concentrations was determined using a STABINO ZETA (Microtrac) ζ-potential analyzer. Similar to the particle size analysis, CASQ2 samples were diluted in a buffer containing 20 mM HEPES (pH 7.3) and varying KCl concentrations, ensuring a final protein concentration of 2.5 µM. For Z-potential measurements in the absence of $CaCl_2$, separate samples were used for each ionic strength condition. In contrast, to assess the effect of $CaCl_2$, measurements were performed stepwise on the same sample, recording changes in ζ-potential after each sequential addition of $CaCl_2$. A piston with a cutoff size of 200 nmwas employed in this case.

Author Contributions: Conceptualization C.M. and S.D.J.; methodology C.M., C.D.A. and P.E; investigation C.D.A., C.M. and P.E.; writing C.D.A., C.M. and E.P.; supervision F.F. and S.G.P.; funding acquisition S.G.P. All authors have read and agreed to the published version of the manuscript.

Conflicts of Interest: The authors declare no conflicts of interest.

APPENDIX: A 0-D theoretical formulation describing the formation of dimeric and polymeric CASQ2 assemblies, based purely on electrostatics.

SCOPE:

The following approach, while guided by physical intuition, is phenomenological. It is aimed at qualitatively accounting for the most important experimentally observed effects of different ionic environments (containing K^+, Na^+ and/or Ca^{2+}) on the **equilibrium self-association properties of wild-type human Calsequestrin 2 (CASQ2) without post-transcriptional modifications**.

No mathematical fitting of parameters has been attempted. All values used in this model have either been calculated or set by hand.

PREMISES:

The current theoretical scheme is built under the following premises:

(1) Depending on the ionic environment, CASQ2 molecules partition between 2 states: *optimally folded* molecules (capable of dimerization and Ca^{2+}-dependent polymerization, see next premise) and *non-functionally folded* ones (capable of forming electrostatic dimers, non-competent for Ca^{2+}-dependent polymerization). Electrostatically-driven oligomers, described in this manuscript, are neglected from this theoretical scheme for convenience.
(2) CASQ2 polymerization can only occur among optimally folded molecules
(3) CASQ2 dimerization can occur only between molecules in the same state, i.e. mixed dimers are not allowed.
(4) CASQ2 polymerization occurs by sequential addition of dimers.

REACTION SCHEME:

CASQ2 is modeled as following the set of reactions below. These reactions are treated separately for convenience, as they try to reflect different aspects of the CASQ2 behavior: dimerization vs. polymerization

$$D_{nf} \rightleftharpoons 2M_{nf} \rightleftharpoons 2M_o \rightleftharpoons D_o \qquad [1]$$

Where D refers to a dimer, M to a monomer, the subscript *nf* refers to non-functionally folded CASQ2 monomers/dimers and the subscript *o* refers to optimally folded monomers/dimers. Reaction [1] has 3 equilibrium constants, named *K1* (reaction $D_{nf} \rightleftharpoons 2M_{nf}$), *K2* ($2M_{nf} \rightleftharpoons 2M_o$) and *K3* ($2M_o \rightleftharpoons D_o$).

Sequential addition of D_o dimers leads to oligomers and polymers. At this point, we impose a maximum number of D_o molecules per polymer, *N*, due to the otherwise difficult tractability of the equations.

$$ND_o \rightleftharpoons (N\text{-}2)\,D_o + T_o \rightleftharpoons (N\text{-}3)\,D_o + H_o \ldots \rightleftharpoons P_o\,(N\text{-}1) + D_o \rightleftharpoons P_o\,(N) \qquad [2]$$

Note that in the current formulation we have not allowed for polymers to form by addition of oligomers (e.g. an octamer may be obtained by combination of a dimer and a hexamer, as modelled, or by combination of two tetramers). We did not allow this second form of combination, due to the complexity in tracking individual reactions when N becomes high, and the lack of certainty regarding the equilibrium constants.

The equilibrium constants for reaction [2] are assumed to take the form:

$$K_{n\ dimers} = K_{tetramerization} \cdot \alpha^{(n-2)} \qquad [3]$$

Where *n* refers to the number of D_o dimers involved in the reaction. For example, when $n = 2$ (i.e. tetramer formation), $K_{n=2}$ reduces to $K_{tetramerization}$. For the formation of a hexamer ($n = 3$), $K_{n=3} = K_{tetramerization} \cdot \alpha$, and so

on until the maximum polymer forms, $K_{n=N} = K_{tetramerization} \cdot \alpha^{(N-2)}$. Note that α denotes the cooperativity of the process (i.e. positive when α > 1).

The total concentration of CASQ2 is given in terms of $[M_o]$, the equilibrium constants, α and N. Once $[M_o]$ is known, the fractions of all other species are calculated. We will return to the numeric value of the equilibrium constants *K1*, *K2*, *K3*, $K_{tetramerization}$ and α at a later stage. At this point in time, we first need to discuss what are the driving processes of CASQ2's optimal folding in the current theory.

PROCESSES:

Process 1: The neutralization of CASQ2 net charge depends on ionic environment

This process builds on the intuition that proteins cannot be optimally folded unless their charge is neutralized by counter-ions. We used the canonical human CASQ2 sequence (Uniprot ID O14958-1) to determine the CASQ2 net charge at pH 7.3 (the pH used in the experiments of the current manuscript). Charges for each individual amino-acid were calculated based on the pKa values of the amino acids [REFS 1-2], and are shown here in summarized form:

Amino-acid charges: {'A', 'R', 'N', 'D', 'C', 'E', 'Q', 'G', 'H', 'I', 'L', 'K', 'M', 'F', 'P', 'S', 'T', 'W', 'Y', 'V'}, [0, 1, 0, -1, 0, -1, 0, 0, 0.17, 0, 0, 1, 0, 0, 0, 0, 0, 0, 0, 0].

Note that histidine (H) was given a charge of 0.17 due to partial protonation at pH 7.3. The calculated net charge of CASQ2 was (-57.98).

Ions were considered to neutralize CASQ2 charges depending on their charge density relative to K^+. The following formula accounted for the amount of cationic charge available to neutralize CASQ2 in any given ionic environment containing K^+, Na^+ and/or Ca^{2+}:

$$cationic\_charge = [K^+] \cdot (K\_r/K\_r) + [Na^+] \cdot (K\_r/Na\_r) + 2 \cdot [Ca^{2+}] \cdot (K\_r/Ca\_r) \quad [4]$$

where K_r is the ionic radius of K^+ (133 pm), Na_r is the ionic radius of Na^+ (95 pm) and Ca_r is the ionic radius of Ca^{2+} (65 pm). CASQ2 neutralization was expressed as a percentual value of its net charge:

$$\text{Non-neutralized charges (\%)} = 100 \cdot (CASQ2\_charge + cationic\_charge/3.35) / abs(CASQ2\_charge) \quad [5]$$

In other words, a non-neutralized CASQ2 (as if there were no ions around it) would render a (-100%) value in [6], whereas a fully neutralized one would render a 0% value. Note the denominator that divides *cationic_charge:* it was set at 3.35 to match the $[K^+]$ leading to zero ζ-potential at the experimental concentration of 194.2 mM (see Figure 2D within the manuscript and Footnote 1 within this appendix).

Footnote 1: Experiments indicate that, when CASQ2 dwells within an environment containing KCl alone, ζ-potential equals 0 when $[K^+]$ = 194.2 mM. We can use equations [4] and [5] (setting non-neutralized charges = 0) to estimate the value of X, the denominator of *cationic_charge* in equation [5].

$$cationic\_charge = [K^+] \cdot (K\_r/K\_r) = 194.2 \quad [4\text{-special}]$$

$$0 = 100 \cdot (CASQ2\_charge + cationic\_charge/X) / abs(CASQ2\_charge) \quad [5\text{-special}]$$

Replacing equation [4-special] into equation [5-special] and rearranging, we get

$$X = cationic\_charge / (- CASQ2\_charge) = 194.2 / (-(-57.98)) = 3.34943$$

Also note that, by applying an analogous reasoning, we can roughly estimate the maximum number of Ca^{2+} moles that can be bound to a fully neutralized mole of CASQ2 molecules. We show the end-stage of the calculation

$$Ca^{2+}_{Max\text{-}bound} = (-CASQ2\_charge) \cdot (3.35/2) \cdot (Ca\_r / K\_r) = 57.98 \cdot 1.675 \cdot (65 / 133) = 47.45$$

The number agrees with the experimentally estimated maximum Ca^{2+}-binding capacity of CASQ2 of 40-50 ions per molecule [3].

Process 2: the fraction of optimally folded CASQ2 is proportional to charge neutralization

The process above, charge neutralization, was assumed to drive the optimal folding of CASQ2. To model this, we used the following ascending sigmoidal equation:

$$Promoted\_folding = ((1 + (EC50_{Folding} / \text{ionic\_strength})^{1.5}))^{(-1)} \quad [6]$$

Where $EC50_{Folding}$ was defined to be the amount of *cationic_charge* (formula [4]) needed for 50% of the CASQ2 charges to be neutralized. Applying formula [5] with Non-neutralized charges = (-50%), we obtain:

$$EC50_{Folding} = 3.35 \cdot ((-0.5) \cdot \text{abs}(\text{CASQ2\_charge}) - \text{CASQ2\_charge}) = 97.0991 \text{ mM}$$

On what concerns ionic strength, it was calculated as dependent on charge density (i.e. not all ions count the same for ionic strength purposes, even if they have the same charge). Once again, K^+ was set as reference

$$\text{ionic strength} = 0.5 \cdot \sum (K\_r / Ion\_r) \cdot [Ion] \cdot Ion\_charge^2 \quad [7]$$

Process 3: Excessive ionic strength promotes non-functional foldings of CASQ2

Beyond a certain amount (mM) of ionic strength, proteins leave their optimal functional configuration due to excessive charge-screening from hydration shells, hampering electrostatic (and Ca^{2+}-dependent) interactions. We modeled this process as a descending sigmoidal curve with an $EC50_{Loss}$ defined to be the amount of *cationic_charge* (formula [4]) needed to revert 50% of the CASQ2 charges. Applying formula [5] with Non-neutralized charges = (+50%), we obtain:

$$EC50_{Loss} = 3.35 \cdot (0.5 \cdot \text{abs}(\text{CASQ2\_charge}) - \text{CASQ2\_charge}) = 443.3034 \text{ mM}$$

And the descending sigmoidal curve representing this process is

$$Loss = ((1 + (\text{ionic\_strength}/EC50_{Loss})^{1.5}))^{(-1)} \quad [8]$$

Process 4: Ca^{2+}/K^+ competition right-shifts $EC50_{Loss}$

The current manuscript presents strong evidence of K^+/Ca^{2+} discrimination in the polymerization reaction of CASQ2 (see reaction [2]), plus a competitive reaction between K^+ and Ca^{2+} in favor of the latter which leads to the dissipation of non-functionally folded structures. In order to account for these effects, the model calculates the Ca^{2+}-dependent ionic strength relative to the total ionic strength provided by cations (each calculated by formula [7])

$$bivalent\_related\_folding = (Ca\_is) / (\text{ionic\_strength} - Cl\_is) \quad [9]$$

and $EC50_{Screen/Loss}$ is right-shifted depending on the Ca^{2+} levels present in solution, thus spanning the stability of the protein in the presence of Ca^{2+}:

$$EC50_{Loss} = EC50_{Loss\text{-no bivalents}} \cdot (1 + bivalent\_related\_folding) \quad [10]$$

Note that, depending on the levels of environmental Ca^{2+}, a right-shift occurs in *Screen/Loss* that leads to higher *FOF* as compared to environments where monovalent cations are present.

RESULTANT OF MODEL PROCESSES 1-4: CASQ2 fraction that is optimally folded

The fraction of CASQ2 that is optimally folded/functional (*FOF*) critically depends on ionic conditions, and is calculated by the equation:

$$FOF = Promoted\_folding \cdot Loss \quad [11]$$

Since the process of charge neutralization defines the EC50s for *Promoted_folding* and *Loss*, this process is fully present in equation [11] even if not mentioned explicitly.

EQUILIBRIUM CONSTANTS OF THE CHEMICAL REACTION [1]:

K1 ($D_i \rightleftharpoons 2M_i$) was defined to ensure that weak ionic strengths promote the formation of D_{nf} whereas high ionic strengths (by rising the value of *K1*) lead to formation of M_{nf} monomers.

$$K1 = 1 / (1 + 0.25 \cdot \text{ionic\_strength}) \quad [12]$$

In order to assign a numeric value to *K2* ($2M_{nf} \rightleftharpoons 2M_o$), we made the conjecture that the folding-unfolding reaction of monomers is much faster than the formation of dimers, and that we start reaction [1] with all CASQ2 molecules being monomers. From the definition of $K2 = M_o / M_{nf}$ and these special conditions, we get that:

$$K2 = FOF / (1 - FOF) \quad [13]$$

K3 ($2M_o \rightleftharpoons D_o$) was given a fixed numerical value. This was done because the experiments within the current manuscript demonstrate that CASQ2 dimers do occur independently of the presence of Ca^{2+}, and because no obvious dependency on KCl levels could be extracted from the data for this type of dimerization.

$$K3 = 0.25 \quad [14]$$

$K_{tetramerization}$ was parametrized as being directly proportional to *bivalent_related_folding* (i.e. the Ca^{2+} contribution to cationic ionic strength; see [9]) and inversely proportional to the 4th power of *Loss* (see [8]). This definition is purely phenomenological, reflecting the facts that (a) CASQ2 does not form multimers in the absence of divalent cations (Supplementary Figure 6 in the manuscript) and that (b) polymers are destabilized by ionic strengths above those needed for ζ-potential close to neutrality (descending curve in Figure 6A).

$$K_{tetramerization} = bivalent\_related\_folding \cdot Loss^{4} \quad [15]$$

Finally, α was given a fixed numerical value.

$$\alpha = 1.1 \quad [16]$$

Note that, despite the numerical value of α is small, the value of the equilibrium constants for polymerization reactions follow an exponential dependency on the number of dimers involved (see [3]). Therefore, such equilibrium constants can reach large values when the number of dimers is large. For example, when $n = 20$ dimers/polymer, the equilibrium constant becomes five times and a half the tetramerization constant

$$K_{n=20} = K_{tetramerization} \cdot \alpha^{18} = K_{tetramerization} \cdot 5.56$$

SIMULATION METHODOLOGY

All simulations were performed in MATLAB R2021b (Mathworks Inc., Natick, MA, United States) on a Windows 11 Pro HD desktop computer. The function *fsolve* was called to solve for $[M_o]$, with options 'TolFun' =1e-12 and 'TolX' = 1e-12. The initial guess used by *fsolve* was $[M_o]_{initial\_guess} = [CASQ2_{Total}] \cdot FOF$. Calsequestrin 2 total concentration is input in the model in μM units, while ionic concentrations are input in mM units. The value of the equilibrium constants varies with each environment tested, according to the equations and formulas discussed above.

Each specific environment can be tested within a few seconds, so that complete sets of simulations can be performed in less than a minute.

Use of artificial intelligence: Meta AI (Meta, USA) was used to device the MATLAB code that calculates the molecular weight and the net charge (pH 7.3) of the CASQ2 monomer.

MODEL OUTCOMES

Model Outcome 1: Ionic environments needed for zero ζ-Potential

When the model replicates the ionic environments used in the experiments, the application of equations [4] and [5] (setting "Non-neutralized charges = 0 %") renders that the ionic concentrations needed to neutralize CASQ2 approximate the observed ionic conditions experimentally needed to obtain a ζ-potential ≈ 0 (Table 1).

Composition of ionic environment	MS. Fig.	Observed: [Salt] for ζ-potential ≈ 0	Predicted by model: [Salt] needed to neutralize CASQ2
Variable (1 to 600 mM) KCl	2D	194.2 mM KCl	Same as observed, since this value was used to obtain X in eq. [5]
Variable (1 to 600 mM) NaCl		159.7 mM NaCl	139 mM NaCl
50 mM KCl, variable (1 to 40 mM) $CaCl_2$	5C	35.2 mM $CaCl_2$	35.3 mM $CaCl_2$
150 mM KCl, variable (1 to 40 mM) $CaCl_2$		10 mM $CaCl_2$	10.8 mM $CaCl_2$

Table 1: Observed vs. calculated salt concentrations at which z-potential ≈ 0 in different ionic environments.

From the table it is clear that the theory is in excellent agreement with the experiment on what pertains the CASQ2 behavior in environments containing K^+ and Ca^{2+}. In environments containing solely NaCl, the theory some refinements may be necessary to fully account for the CASQ2 behavior.

Model Outcome 2: Apparent molecular weight of CASQ2 monomers as a function of [KCl]

The molecular weight (MW) of individual amino-acids was obtained from [1,2] and added, using the canonical human CASQ2 sequence (Uniprot ID O14958-1). Using this approach, it was obtained that the MW of CASQ2 monomers is 46.407 KDa. The weights used for each amino-acid were, in summarized form:

Amino-acid weights = {'A', 'R', 'N', 'D', 'C', 'E', 'Q', 'G', 'H', 'I', 'L', 'K', 'M', 'F', 'P', 'S', 'T', 'W', 'Y', 'V'}, [71.03711, 156.10111, 114.04293, 115.02694, 103.00919, 129.04259, 128.05858, 57.02146, 137.05891, 113.08406, 113.08406, 128.09496, 131.04049, 147.06841, 97.05276, 87.03203, 101.04768, 186.07931, 163.06333, 99.06841]

To explain the experimentally observed changes in the CASQ2's apparent molecular weight, it was assumed that optimal folding of the CASQ2 monomer leads to a reduction of its apparent molecular weight, following a simple linear relationship.

$$app\_MW = MW - \text{apparent\_compaction\_due\_to\_proper\_folding} * FOF \quad [16]$$

where *app_MW* is the apparent molecular weight of the CASQ2 monomer, *MW* is the molecular weight of the unfolded CASQ2 monomer as calculated from its constituent amino-acids (see above), and apparent_compaction_due_to_proper_folding = 13 KDa.

Figure A.1, panel A, displays the processes used by the model to calculate *FOF* (equations [5] to [11]), whereas panel B compares the output of the model to Figure 2A within the manuscript. The qualitative agreement with the experimental data is remarkable.

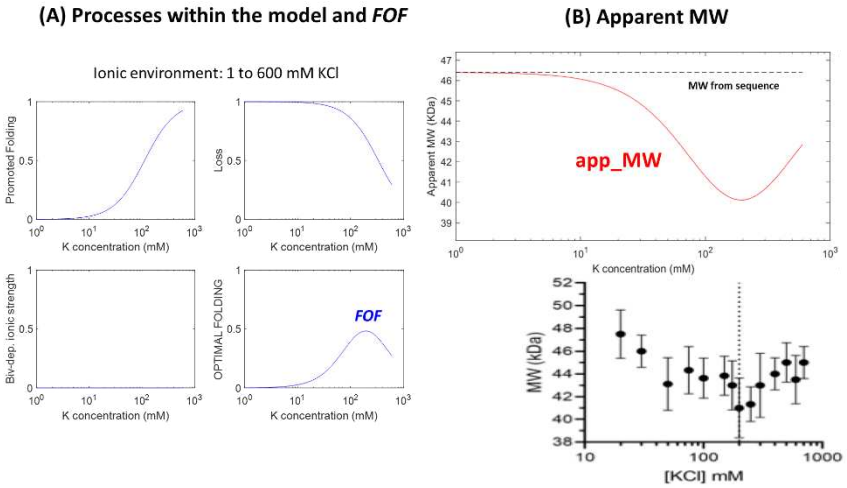

Figure A.1: Apparent molecular weight of CASQ2 monomers in variable [KCl].

<u>Model Outcome 3: Apparent molecular weight of CASQ2 monomers as a function of [$CaCl_2$] at different ionic strengths</u>

Figure S2 within the manuscript shows that, when CASQ2 dwells in an environment with 50 mM KCl, the addition of 1 to 10 mM $CaCl_2$ leads to an increase in ionic strength which itself leads to molecular compaction of the CASQ2 monomer. This effect is not observed in 200 mM KCl, where molecular compaction is already maximal.

In order to understand whether the current theoretical formulation can also simulate this behavior, we performed simulations as in *Model outcome 1* above, adjusting the concentrations of KCl and $CaCl_2$ to match the different experimental environments. Results are summarized by Figure A.2: Panel A.2-left replicates Figure S2 from the manuscript, whereas panels A.2-center and A.2-right compare, respectively, the theoretical predictions in 50 mM vs. 200 mM KCl. It can be seen that, as occurs in the experiments, a monomer compaction progressively develops with increasing levels of Ca^{2+} in 50 mM KCl, whereas at 200 KCl the compaction of the CASQ2 monomer is already completed.

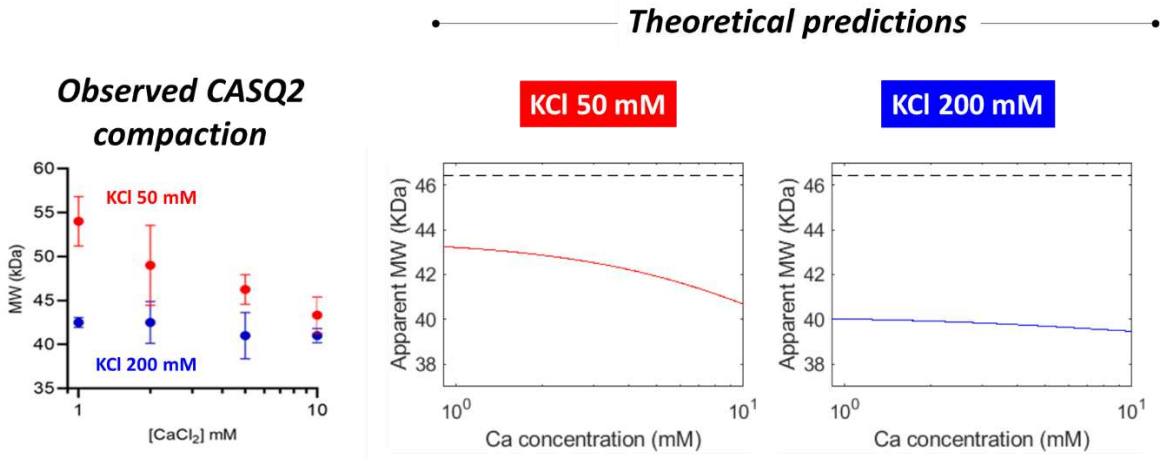

Figure A.2: Apparent molecular weight of CASQ2 monomers in variable [$CaCl_2$] at low vs. optimal ionic strengths.

Model Output 4: [Dimer]-to-[Monomer] (D/M) ratio as a function of [KCl]

Figure 3A within the manuscript shows that a non-negligible proportion of CASQ2 dimers are observed at any [KCl] in the absence of bivalents at [$CASQ2_{Total}$] = 2.5 μM. Furthermore, no polymers were detected using turbidometry (Figure S6). The D/M ratio is highest when the ionic strength is lowest, suggesting that the excess of dimers at low ionic strengths originates via non-specific electrostatic interactions due to incomplete charge shielding of the CASQ2 molecule.

To understand whether the current theory could simulate this behavior, N = 20 was set in the model and [$CASQ2_{Total}$] = 2.5 μM. The processes and *FOF* calculated by the model are shown in Figure A.1A above. Figure A.3A shows the concentration of the different chemical species, whereas Figure A.3B compares the predicted D/M ratio vs. Figure 3A within the manuscript. The qualitative agreement between theory and experiment is close, and adds value to the hypotheses presented in the manuscript: (a) at low ionic strengths and in the absence of bivalents, most dimers are non-functionally folded; (b) at high ionic strengths and in the absence of bivalents, the dimers observed are mostly folded in an optimal (i.e. polymerization-ready) fashion. No polymers are observed.

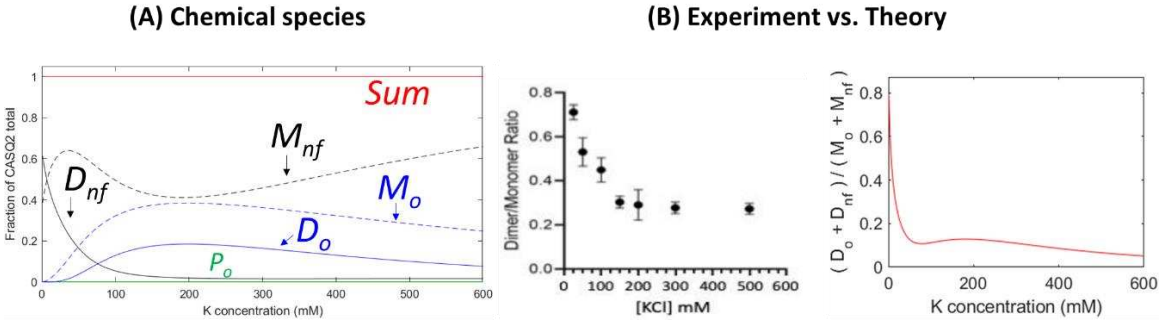

Figure A.3: Behavior of the [Dimer]-to-[Monomer] in variable [KCl] and no added Ca^{2+}.

Model Output 5: [Dimer]-to-[Monomer] ratio as a function of [$CaCl_2$] in environments with 50 mM [KCl]

Figure 5A within the manuscript shows that, at [KCl] = 50 mM, the addition of $CaCl_2$ (1-60 mM) leads to non-monotonic behaviors of the D/M ratio. We tested this behavior by setting in the model [KCl] = 50 mM, N = 20 and [$CASQ2_{Total}$] = 2.5 μM.

Figure A.4A shows the processes within the model, Figure A.4B shows the chemical species and Figure A.4C compares the experimental observation in the manuscript (Figure 4A) to the theoretical predictions. While the curve calculated by the model clearly fails in replicating the quantitative CASQ2 behavior, it replicates with excellent accuracy its qualitative behavior (expressed by the Ca^{2+} levels at which the different experimental effects are observed): (a) 1-5 mM Ca^{2+} rapidly leads to lesser fraction of non-functionally folded molecules in favor of optimally folded ones, decreasing the overall number of D_{nf} dimers and the D/M ratio; (b) between 5 and 10 mM, the increase in optimally folded molecules is not yet high enough, and so the D/M ratio remains at a valley; (c) above 10 mM, the monomers and dimers that now predominate are optimally folded, and the D/M ratio rises above its value in 1 mM Ca^{2+}.

At 50 and 60 mM Ca^{2+}, the qualitative theoretical behavior deviates from the experiment, since in the theory the D/M ratio flattens. This fact, and the quantitative disagreement highlighted above, indicate that further refinements of the theory are needed when describing the CASQ2 behavior in the presence of bivalents. That said, it should also be noted that, at high Ca^{2+} concentrations (50–60 mM), Mass Photometry measurements become intrinsically less reliable due to the concurrent formation of higher-order oligomers. This phenomenon,

which also occurs at elevated K^+ concentrations, increases background noise and reduces the precision of assignment of counts to the dimeric species. Therefore, the apparent flattening of the experimental D/M ratio at high Ca^{2+} levels may also reflect, at least in part, methodological limitations rather than a genuine deviation from the theoretical prediction.

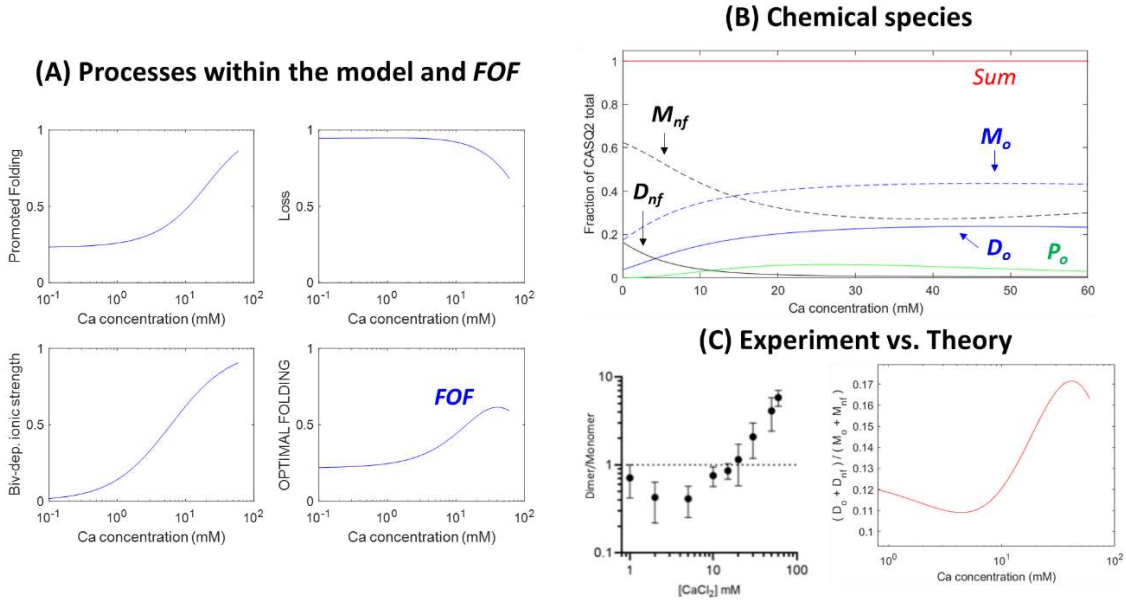

Figure A.4: Behavior of the [Dimer]-to-[Monomer] in 50 mM [KCl].

<u>Model Output 6: [Dimer]-to-[Monomer] ratio as a function of $[CaCl_2]$ in 50 vs. 150 mM [KCl]</u>

Figure 4B within the manuscript shows that, when KCl concentration equals 150 mM, the Ca^{2+}-dependent decrease in D/M ratio (seen in 50 mM KCl at low millimolar Ca^{2+}) flattens due to attenuation of the K^+ vs. Ca^{2+}competition in favor of potassium. To see whether the theory could qualitatively replicate this behavior, we performed new simulations by setting in the model [KCl] = 150 mM, N = 20 and $[CASQ2_{Total}]$ = 2.5 µM

Figure A.5 compares the theoretical D/M ratios at 50 mM (left) and 150 mM KCl (center) vs the experiments shown in Figure 4B of the manuscript (right). The model qualitatively replicates the behavioral shift shown by the experiments (note arrowheads inserted within the theoretical predictions).

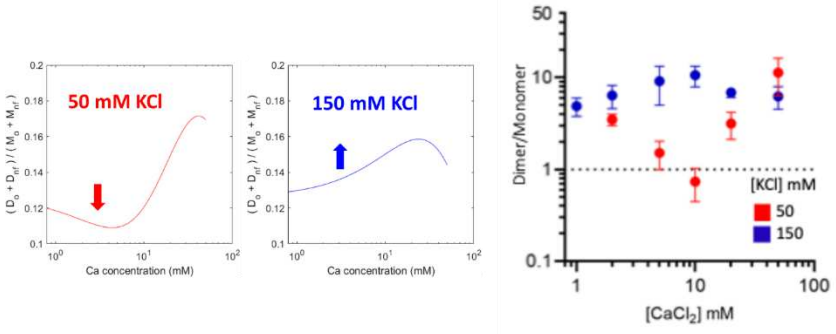

Figure A.5: Behavior of the [Dimer]-to-[Monomer] ratio in 50 mM vs. 150 mM [KCl]

Model Output 7: CASQ2 polymerization is a Ca^{2+}-dependent switch in which K^+ shows mixed effects

The experiments shown within the current manuscript are aimed at studying the K^+ vs. Ca^{2+} relationship in shaping CASQ2 polymerization. 3 effects are clearly seen:

- In the absence of Ca^{2+} ions, K^+ ions alone are not capable of leading to CASQ2 polymerization, regardless of their amounts (Figure S6)
- CASQ2 polymerization starts at lower Ca^{2+} concentrations when K^+ levels are higher (a sensitizing effect on the part of K^+) (Figure 6A)
- At high K^+ levels, Ca^{2+}-dependent CASQ2 polymerization displays a lower cooperativity (a negative effect on the part of K^+) (Figure 6A)

The lack of polymerization in the absence of Ca^{2+} can be already been seen in the simulations from Figure A.2 ($[CASQ2_{Total}] = 2.5$ µM).

To simulate the two latter CASQ2 behaviors, we set $[CASQ2_{Total}] = 45$ µM (as in the experiments) and $N = 20$. Two KCl-containing environments were simulated (either 10 mM or 50 mM, as in the experiment), to which Ca^{2+} ions were added within the concentration range 1-200 mM. Figure A.5, left, replicates the experiments shown in Figure 6A of the manuscript. Theoretical results are shown to the right. The green traces in the right (theoretical) panels, which indicate the compounded sum of tetramers, hexamers, octamers, etc (up to 40 monomers) represent well the experimental behavior: there are both an ascending and a descending phase. The model replicates both the lower threshold $[Ca^{2+}]$ and the smallest steepness of the polymerization curve in 50 mM vs. 10 mM KCl. Of additional importance is the formation of M_{nf} monomers and D_o dimers concomitantly to the dissipation of polymers during the descending phase of the curve, implying that polymer folding has become impeded by the high ionic strength. The model, however, right-shifts the descending phase of both polymerization curves relative to those of the experiment, and it right-shifts the ascending curve of the 10 mM KCl environment, indicating once again that theory refinement is needed.

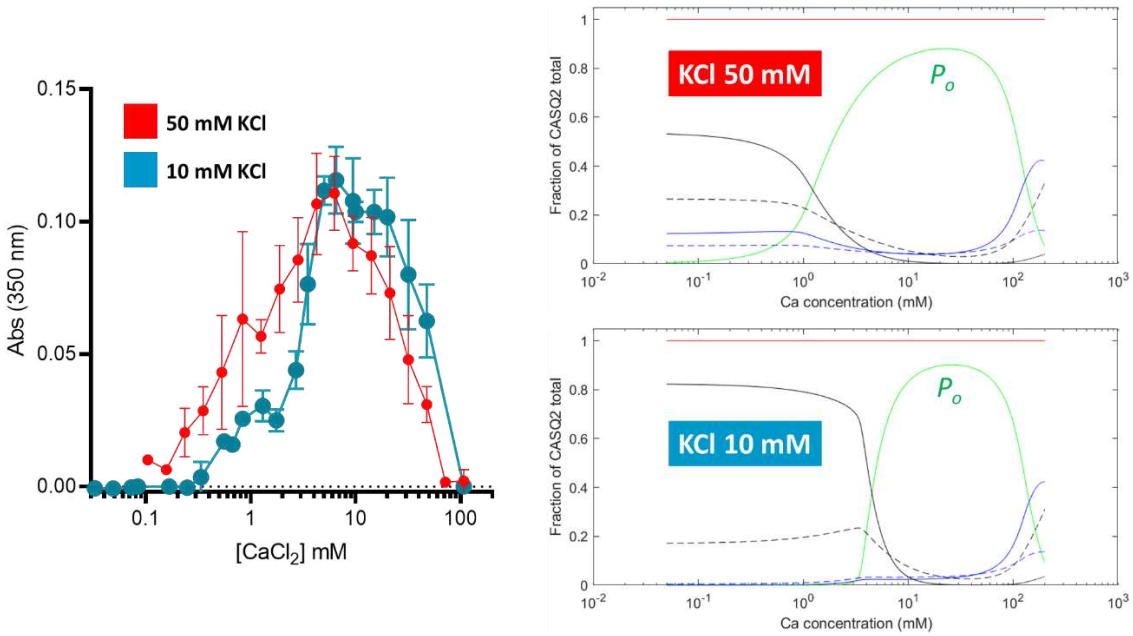

Figure A.6: Ca^{2+}-dependent CASQ2 polymerization (green line) in environments with low [KCl].

Model Output 8: Ca^{2+}-dependent CASQ2 polymerization occurs suddenly

Figure 7A within the manuscript highlights the Ca^{2+}-dependent switch-like behavior of CASQ2 polymerization, by testing the size of CASQ2 particles at either 50 or 150 mM environmental KCl. It is observed that polymerization occurs suddenly, indicating a switch-like event of extreme cooperativity, which threshold [Ca^{2+}] depends on [K^{+}]. The experiments were not conducted beyond 40 mM Ca^{2+}, so a descending phase cannot be visualized.

We tested whether the theory can simulate this behavior (Figure A.6) by setting [$CASQ2_{Total}$] = 45 μM and N = 20. The left panel in Figure A.6 is the experiment. The central and right panels are the predicted CASQ2 behaviors at, respectively, 50 and 150 mM KCl. Within these theoretical behavior panels, the graphs separately display the individual fractions of M_o, D_o and each species P_o, up to a [Ca^{2+}] = 15 mM, for any given environmental [Ca^{2+}]. It can be seen that, in both environments, a polymerization reaction occurs suddenly, with few polymer species in-between the size of the dimer (2 M_o/polymer) and the maximum size allowed (40 M_o/polymer). Furthermore, for the 50 mM KCl environment the formation of very large polymers is about 75% ended at 5 mM Ca^{2+}, closely resembling the experiment. For the 150 mM KCl environment, formation of very large polymers starts around 3-4 mM Ca^{2+}, and by a level of 10 mM such polymerization is nearly completed. Again, no polymers of intermediate sizes are observed.

It can be concluded that the theoretical 0-D CASQ2 behavior, as simulated herein, reproduces the experimental observation by which a Ca^{2+}-dependent switch triggers the formation of very large polymers in a cooperative fashion.

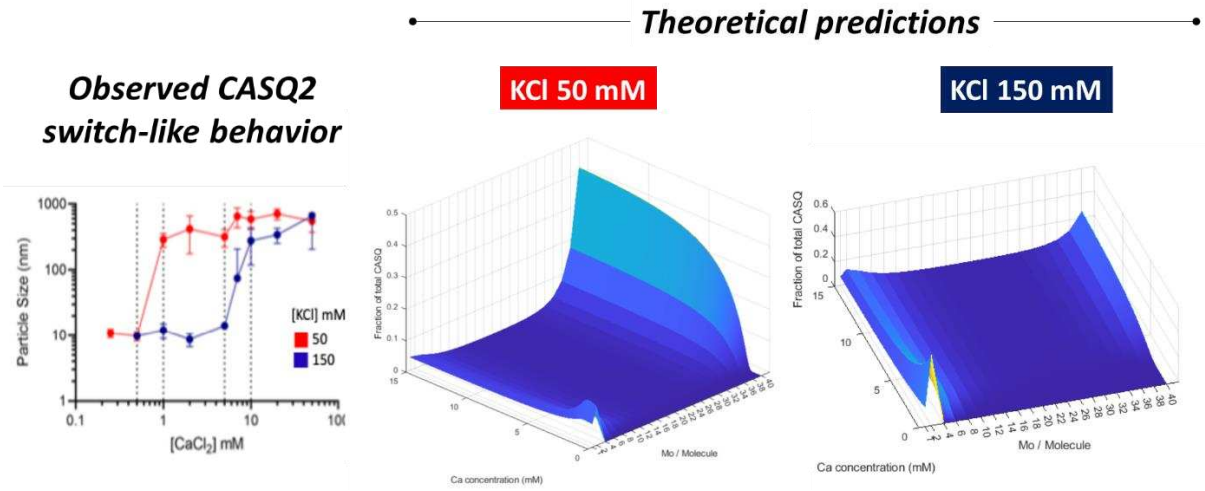

Figure A.7: CASQ2 polymerization occurs suddenly

CONSISTENCY OF THE 0-D CASQ2 MODEL vs. PREVIOUSLY PUBLISHED DATA

The 0-D theoretical formulation presented herein focuses solely in the equilibrium folding behavior of CASQ2. This leaves unanswered the key question of what happens to Ca^{2+} binding by CASQ2, and in particular the question of whether the current theoretical formulation is (or not) consistent with previously published Ca^{2+} binding experiments. Note that the current manuscript (and this appendix) present evidence suggesting that CASQ2 is able to dimerize even in the absence of Ca^{2+}. This is, however, apparently contradictory to experiments such as those from Park et al. (2004) [4], which were interpreted to indicate that there is a strict $M_o \rightarrow D_o \rightarrow P_o$ sequence, and that dimerization is very strongly dependent on [Ca^{2+}]. Therefore, the question

arises: Is the current theory capable of reconciling the experiments from both publications and provide a unified interpretation?

In order to address the question, it was first assumed that Ca^{2+} binding to CASQ2 can only occur in optimally folded molecules (i.e. M_o, D_o and P_o of any size). Maximum Ca^{2+}-binding capacity of CASQ2 was set to 47.45, obtained as explained in Footnote 1. It was assumed that Ca^{2+}-binding capacity was independent of polymer size, since the theory has no way of calculating bound Ca^{2+} other than based on the charge neutralization principle (see Footnote 1). Therefore, the role of Ca^{2+} as a bridging element between monomers has been omitted in this calculation. All the above implies that:

$$\text{binding\_sites\_monomer} = 47.45$$

$$\text{binding\_sites\_dimer} = 2 \cdot \text{n\_binding\_sites\_monomer}$$

$$\text{binding\_sites\_polymer}_n = n \text{ dimers} \cdot \text{binding\_sites\_dimer}$$

where n is the number of dimers in the polymer of size n. Dissociations constants were set, for the monomer, $K_{D\text{-mono}} = 0.25$ mM, and for species with 2 or more monomers, $K_{D\text{-higher}} = 5$ mM. Hill coefficients were assumed to be $H_{mono} = 1$ and $H_{high} = 4$, respectively, for monomers or species with more than one monomer. Occupancy was defined as the moles of Ca^{2+} bound per total CASQ2 present, as in Park et al. In the simulations, $[CASQ2_{Total}]$ was 45 µM (about 2 mg/ml, mid-range of Park et al. experiments) and N, the maximum number of dimers allowed within individual polymers, was 20. The environment was set to [KCl] = 300 mM, as in Park et al. We did not modify the pH of our simulation (7.3), which is slightly different from that of Park et al. (7.5).

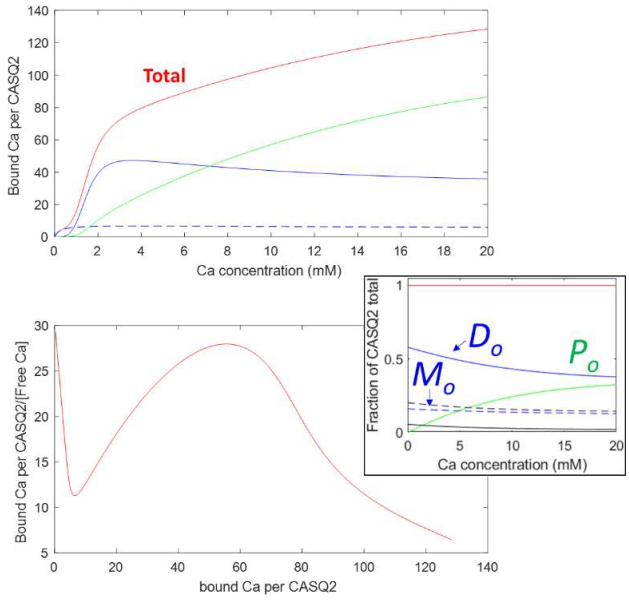

Figure A.8: Ca^{2+}-binding properties of 0-D simulated CASQ2 as a function of free $[Ca^{2+}]$

Figure A.8 shows the theoretical prediction. The top and bottom panels were built similarly to Figures 5A (binding curve) and 5B (Scatchard-like plot) from Park et al. (2004) [4]. An insert further contains the proportion of D_{nf}, M_{nf}, M_o, D_o, and all combined P_o molecules (note that the proportion of D_o dimers, as predicted by the current 0-D electrostatic theory, is very large even in the absence of Ca^{2+}). Within the top panel of Figure A.8,

the dashed blue line represents Ca^{2+} that is bound to CASQ2 M_o monomers, whereas the solid blue line is Ca^{2+} bound to D_o dimers. The green line is the combined Ca^{2+} that is bound to all other polymers (i.e. tetramers, hexamers, octamers, and so on). Finally, the red curve labelled with "Total" is the sum of the above 3 curves, and the one that needs to be compared to Figure 5 in Park et al. (2004).

There is a good qualitative agreement: It is evident in the binding curve that sequential binding phases occur (first to monomers, then to dimers, then to polymers). Furthermore, the theoretical Scatchard-like plot shows a similar behavior vs. the one observed experimentally, with varying slopes as a function of occupancy. However, what explains the different phases according to the current theory are key differences in K_D, Hill coefficient and monomer/dimer/polymer abundances, rather than a strict coupling between binding and polymerization.

Areas of disagreement include the maximum Ca^{2+} bound ions per CASQ2 molecule, with was shown experimentally to be 36 by Park et al., vs. 47.45 ions calculated by the 0-D theory. This is in part because the 0-D theory only assumes electrostatics, without structural distinctions of what constitutes (or not) a Ca^{2+}-binding site in three-dimensional space.

All the above said, we conclude that our theoretical frame can qualitatively replicate both the experiments from the current manuscript and those from Park et al. (2004). Therefore, we see no contradiction among the two sets of experimental data.

THE NEAR-PHYSIOLOGICAL ENVIRONMENT

As a last simulation, we applied the current theory to understand what would be the expected aggregation status of CASQ2 within environments as close as possible to the physiological cardiac environment. We set as near-physiological conditions 140 mM KCl, 5 mM NaCl and variable free Ca^{2+}, ranging from 0 to 1.25 mM. $[CASQ2_{Total}]$ was set to 1000 μM, the concentration believed to occur within the junctional sarcoplasmic reticulum of striated muscle [5]. *N* was set to 20, as in prior simulations.

Figure A.9 summarizes the theoretical expectation. The left panel indicates that at free Ca^{2+} levels of 1 mM (i.e. similar to levels found in the junctional sarcoplasmic reticulum during diastole) approximately 5% of the total CASQ2 would be in the form of D_o dimers, whereas most CASQ2 (about 95%) would be expected to form oligomers and high-order polymers. A very small fraction (less than 1%) would be monomeric, of either optimal or non-functional configurations. Figure A.9, right panel, dissects which optimally folded forms would predominate: the vast majority of CASQ2 protein (about 90%) would form the highest polymers allowed by the simulation, whereas the remaining fraction would form tetramers, hexamers and octamers, with few polymers of intermediate order. Together, the theoretical predictions agree well with the observation (by electron microscopy) of large CASQ2 polymers in the junctional sarcoplasmic reticulum from wild-type cells [6]. In diseases such as Catecholaminergic Polymorphic Ventricular Tachycardia type 1, where the sarcoplasmic reticulum Ca^{2+} content is similar or slightly reduced (due to Ca^{2+} leak) vs. healthy cells, the theory still predicts that CASQ2 will be highly polymerized. This is in agreement with the visualization of polymers in electron micrographs from affected animals [7].

It would be tempting to speculate about the predictions at free Ca^{2+} levels consistent with the nadir of sarcoplasmic reticulum depletions during a heartbeat. However, due to the equilibrium nature of the current theory, and because the time lapse where the sarcoplasmic reticulum remains depleted during a heartbeat is narrow, we prefer to refrain from such speculation.

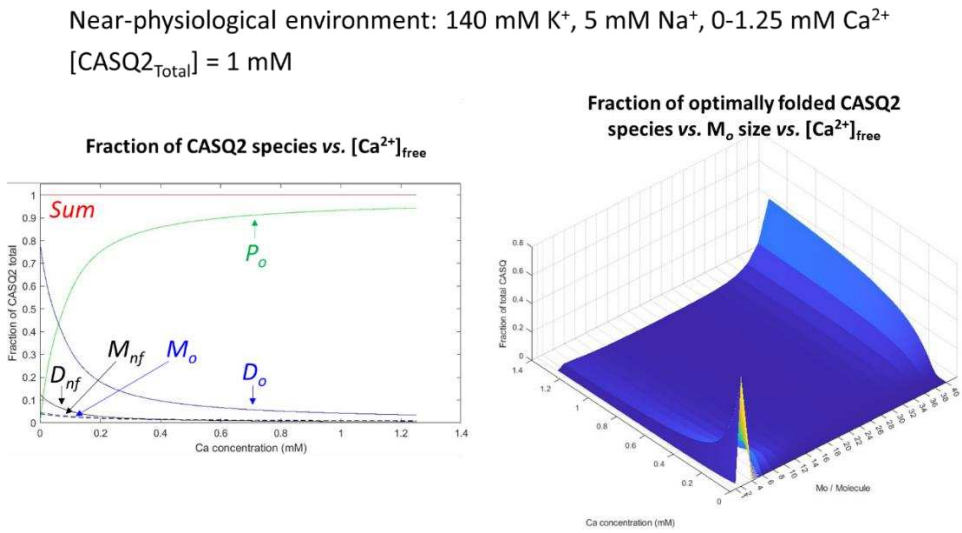

Figure A.9: Predicted CASQ2 aggregation status in simulated near-physiological junctional sarcoplasmic reticulum ionic environment

An additional question faced by the theory is, if the ionic environment within the entire sarcoplasmic reticulum is similar, why does CASQ2 not polymerize in the vicinity of the transcription sites [8]. We believe it is because, at transcription sites, the CASQ2 concentration is not high-enough to promote strong polymerization. We are aware of the fact that CASQ2 concentration may not be the only determinant of its polymerization state at transcription. However, this model is not currently suited for incorporating the effect of post-translational modifications. To illustrate this point, we have repeated the simulation shown by Figure A.9 but using an arbitrarily low [$CASQ2_{Total}$] value equal to 10 µM. Figure A.10, analogous in structure to Figure A.9, shows the results. Figure A.10, left, confirms the expectation by showing that at 1 mM free Ca^{2+} the fraction of P_o molecules is very small. Figure A.10, right, further shows that the totality of P_o molecules are tetramers. While the levels of CASQ2 chosen for this simulation were arbitrarily set to illustrate a point, it is worth noting that the simulation outcome replicates the accumulation of tetrameric DsRed-CASQ2 at the CASQ2 transcription sites as shown by the Cala group [8].

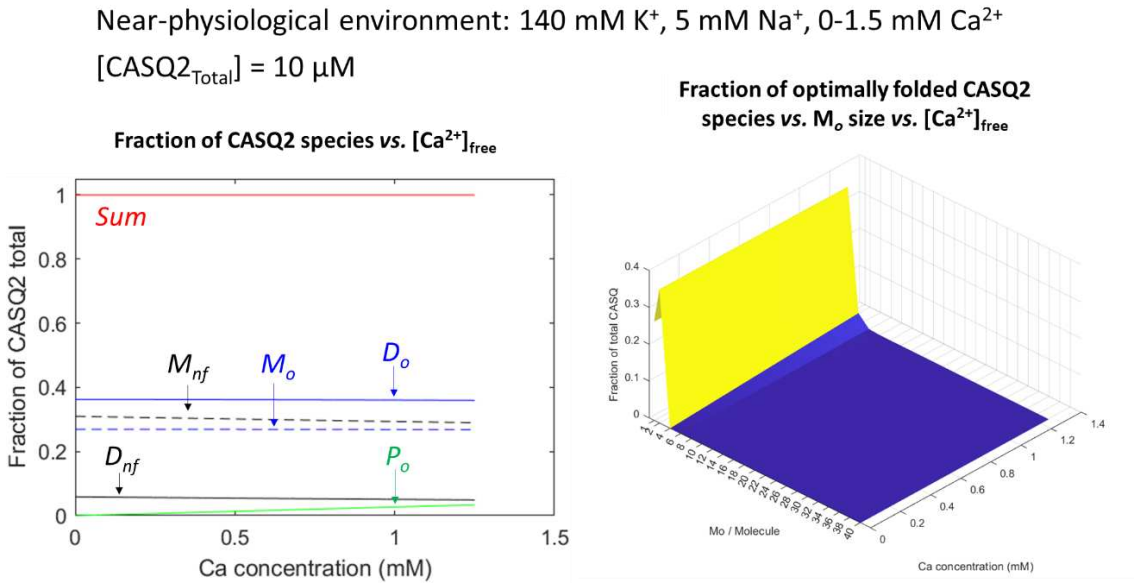

Figure A.10: Predicted CASQ2 aggregation status in simulated near-physiological transcription site environment

LIMITATIONS

The 0-D nature of this theory allows for interested users to perform a very fast and efficient exploration of the CASQ2 behavior in a plethora of ionic environments, in such a way that it can be used predictively, at least in qualitative terms. However, this same 0-dimensionality creates difficulties when predicting the precise number of Ca^{2+} binding sites, as it does not consider the 3-D structure of the protein: Bound Ca^{2+} can only be calculated based on electrostatics (see Footnote 1), and, while the calculation agrees well with some experimental estimates [3], it does not agree with others [4]. One further limitation is that the theory does not contemplate the effects of post-transcriptional modifications, nor of Mg^{2+}-rich environments, on CASQ2 aggregation dynamics, since the experimental data that were used to create the theory were not generated in those conditions.

CONCLUDING REMARKS

Despite being phenomenological and 0-dimensional, the theoretical formulation presented in this appendix retains a glimpse of physical intuition, is quite simple, and approximates very important qualitative *in vitro* behaviors of CASQ2, including monomer compaction, dimerization and polymerization behavior in different ionic environments, and Ca^{2+} binding studies. Thus, this theoretical framework has the potential, if properly refined and extended, to aid in the scientific understanding about CASQ2 and Ca^{2+}-dependent cardiac arrhythmias.

REFERENCES

[1] Lehninger AL, Nelson DL, Cox MM. (2008). Lehninger Principles of Biochemistry (5th ed.). W.H. Freeman and Company.

[2] Berg JM, Tymoczko JL, Stryer L. (2012). Biochemistry (8th ed.). W.H. Freeman and Company.

[3] Mitchell RD, Simmerman HK, Jones LR. (1988) Ca2+ binding effects on protein conformation and protein interactions of canine cardiac calsequestrin. *J Biol Chem.* 263(3):1376-81

[4] Park H, Park IY, Kim E, Youn B, Fields K, Dunker AK, Kang C. (2004) Comparing skeletal and cardiac calsequestrin structures and their calcium binding: a proposed mechanism for coupled calcium binding and protein polymerization. *J Biol Chem.* 279(17):18026-33.

[5] Manno C, Tammineni E, Figueroa L, Marty I, Ríos, E. (2022) Quantification of the calcium signaling deficit in muscles devoid of triadin. *PloS One* 17, e0264146.

[6] Denegri M, Avelino-Cruz JE, Boncompagni S, De Simone SA, Auricchio A, Villani L, Volpe P, Protasi F, Napolitano C, Priori SG. (2012) Viral gene transfer rescues arrhythmogenic phenotype and ultrastructural abnormalities in adult calsequestrin-null mice with inherited arrhythmias. *Circ Res.* 110(5):663-8

[7] Bongianino R, Denegri M, Mazzanti A, Lodola F, Vollero A, Boncompagni S, Fasciano S, Rizzo G, Mangione D, Barbaro S, Di Fonso A, Napolitano C, Auricchio A, Protasi F, Priori SG. (2017) *Circ Res.* 121(5):525-536.

[8] McFarland TP, Milstein ML, Cala SE. (2010) Rough endoplasmic reticulum to junctional sarcoplasmic reticulum trafficking of calsequestrin in adult cardiomyocytes. *J Mol Cell Cardiol.* 49(4):556-64